Control of Upconversion Luminescence for Photovoltaics using Photonic Structures

Zur Erlangung des akademischen Grades eines

DOKTOR-INGENIEURS

von der KIT-Fakultät für
Elektrotechnik und Informationstechnik
des Karlsruher Instituts für Technologie (KIT)

genehmigte

DISSERTATION

von

M.Sc. Clarissa Lea Maja Hofmann

geb. in Gießen

Tag der mündlichen Prüfung: 24. November 2021

Hauptreferent: Prof. Bryce S. Richards
Korreferenten: Prof. Dr. rer. nat. Stefan W. Glunz
Prof. Dr. rer. nat. Jan Christoph Goldschmidt

Durchgeführt am

Fraunhofer Institut für
Solare Energiesysteme ISE

Gefördert durch

das Promotionsstipendien Programm
der Heinrich Böll Stiftung

CONTENTS

ABSTRACT

Upconversion (UC) constitutes an approach to increase the efficiency of solar cells by making use of the otherwise non-utilized sub-bandgap photons. Photonic structures can influence the properties of luminescence phenomena. This is of particular interest when tuning the properties of non-linear luminescence processes, such as photon UC, thus increasing the UC efficiency. Tuning the photonic structure design to maximize UC enhancement requires a careful design optimization, for which an adequate modeling framework has been missing throughout literature. The objective of this work is to develop a comprehensive theoretical framework to understand the photonic effects on the UC dynamics, furthermore to experimentally realize optimized photonic upconverters and finally validate the model's predictions in large scale parameter scans.

To this end, the UC dynamics within β-$NaYF_4$:Er^{3+} are investigated and the potential improvement of UC efficiency by embedding the upconverter into a one-dimensional photonic structure is investigated. The photonic structure consists of alternating layers of Poly(methyl methacrylate) with embedded upconverting nanoparticles and a high refractive index spacer layer. The model describes the photonic effects of the local energy density enhancement and of the modified local density of optical states on the internal UC dynamics within a rate equation modeling framework. Additionally, the model accounts for production inaccuracies via Monte Carlo simulations. The analysis of this work shows that the effect of the modified local density of optical states can, with an optimized design, change the spontaneous emission probabilities such that the maximum possible UC quantum yield (UCQY) is increased significantly, by 0.8% absolute for a high refractive index within the Bragg structure of 1.8, or more for a higher refractive index contrast. Furthermore, by using the the local optical energy density enhancement, the structure can be tailored such that the maximum UCQY occurs at a much lower incident irradiance.

To verify the modeling framework, Bragg structures with embedded core-shell upconverter nanoparticles are realized in high precision. The predicted trends of the UC photoluminescence (UCPL) enhancement due to the modeled interaction of the optical energy density enhancement and local density of optical states with the internal UC dynamics are clearly visible in all experimentally performed parameter scans. In total, 2480 separate parameter combinations were analyzed, scanning through the incident irradiance as well as the excitation wavelength on 40 different sample designs. The measured UCPL enhancement

reaches 82±24% of the simulated enhancement, in the mean of all 2480 separate parameter combinations.

The findings of this work identify Bragg structures as suitable and promising to use in photonic upconverter devices for a target application in photovoltaics, as *i*) the amount of upconverter material is flexible and therefore the overall upconverter absorption can be high, *ii*) a high UCPL enhancements of over 300-fold can be reached at one sun irradiance, with a production accuracy of σ = 1 nm, *iii*) at any incident irradiance, down to about 10 suns, a Bragg structure design can be found that yields close to the maximum possible UCQY, *iv*) the spectral width of the enhancement effects can be tailored to cover the core absorption range of the upconverter material Er^{3+}, in a trade off with the absolute enhancement factors reached and *v*) efficient in-coupling of light is possible up to large incident half angles up to 30 °.

The basic findings of this work can be transferred to any upconverter material with a similar set of energy levels. While the investigations were performed for a 1-dimensional photonic structure in this work, the description of the photonic effects on UC can be transferred to any photonic structure, including 2- and 3-dimensional designs. Therefore, the validated modeling framework now enables a precise optimization of photonic structure designs for various upconverting materials and target applications.

DEUTSCHE ZUSAMMENFASSUNG

Der Prozess der Hochkonversion ist ein Ansatz zur Effizienz-Steigerung von Solarzellen. Photonen, deren Energie unterhalb der Bandlücke der Solarzelle liegt, können durch die Hochkonversion zur Stromerzeugung in der Solarzelle nutzbar gemacht werden. Bei der Hochkonversion werden mehrere niederenergetische Photonen absorbiert und ein hochenergetisches emittiert. Im Weiteren können photonische Strukturen die Eigenschaften von Lumineszenzphänomenen beeinflussen. Diese Möglichkeit ist insbesondere für nichtlineare Lumineszenzprozesse von Interesse, wie für die Photonen-Hochkonversion, und kann deren Effizienz erhöhen. Die Anpassung des Designs der photonischen Struktur im Hinblick auf eine Maximierung der Hochkonversions-Effizienz-Erhöhung, erfordert eine gezielte Designoptimierung, für welche bisher kein passendes Simulationsmodell in der Literatur zur Verfügung stand. Gegenstand dieser Arbeit ist die Weiterentwicklung eines umfassenden theoretischen Modells zur Analyse der photonischen Effekte auf die Hochkonversionsdynamik, zudem die experimentelle Realisierung von photonischen Hochkonvertern und die Validierung des theoretischen Modells in weit gefassten Parameter-Scans.

Zu diesem Zweck wird die Hochkonversionsdynamik in β-$NaYF_4$:Er^{3+} untersucht und die potenzielle Erhöhung der Hochkonversionseffizienz durch die Einbettung des Hochkonverters in eine eindimensionale (1D) photonische Struktur. Diese photonische Struktur besteht aus alternierenden Schichten von Poly(methyl methacrylat) mit eingebetteten Hochkonverter-Nanopartikeln und einer Zwischenschicht mit höherem Brechungsindex. Das Modell beschreibt die photonischen Effekte der lokalen Energiedichteerhöhung und der modifizierten lokalen optischen Zustandsdichte auf die interne Hochkonversionsdynamik in einem Ratengleichungsmodell. Zudem berücksichtigt das Modell Produktionsungenauigkeiten über Monte-Carlo Simulationen. Die Analyse dieser Arbeit zeigt, dass der Effekt der modifizierten lokalen optischen Zustandsdichte in einem optimierten Design die Wahrscheinlichkeit von spontanen Emissionsprozessen derart beeinflussen kann, dass die maximal mögliche Hochkonversionsquantenausbeute (UCQY) signifikant erhöht wird, um 0.8% absolut für einen hochbrechendes Medium innerhalb der Bragg Struktur mit einem Brechungsindex von 1.8, und mehr für einen höheren Brechungsindex Kontrast. Darüber hinaus kann die Struktur angepasst werden, sodass durch die lokale Energiedichteerhöhung die maximale UCQY bereits bei einer deutlich niedrigeren einfallenden Bestrahlungsstärke auftritt.

Um eine Validierung des Simulationsmodells durchzuführen, werden Bragg-Strukturen mit

eingebetteten Core-Shell Hochkonverter-Nanopartikeln untersucht und in hoher Präzision experimentell hergestellt. Die simulierte Wirkung der lokalen Energiedichteerhöhung und der modifizierten lokalen optischen Zustandsdichte auf die interne Hochkonversionsdynamik ist in allen durchgeführten Parameter-Scans sichtbar. Insgesamt wurden 2480 verschiedene Paramter Kombinationen untersucht, in einem Scan der Bestrahlungsstärke, sowie der Anregungswellenlänge an 40 verschiedenen Proben-Designs. Die gemessene Erhöhung der Hochkonversionsphotolumineszenz (UCPL) beträgt 82$\pm$24% der simulierten Erhöhung, im Mittel der 2480 untersuchten verschiedenen Parameter-Kombinationen.

Die Ergebnisse dieser Arbeit lassen Bragg-Strukturen als sinnvoll und vielversprechend für photonische Hochkonverter für eine Anwendung in der Photovoltaik erscheinen, da *i*) die Menge des Hochkonverter-Materials flexibel angepasst werden kann und somit eine hohe Gesamtabsorption durch den Hochkonverter erreicht werden kann, *ii*) eine hohe UCPL Erhöhung von über 300-fach bei nur einer Sonne Bestrahlungsstärke erreicht werden kann, mit einer angenommenen Produktionsungenauigkeit von σ = 1 nm, *iii*) Bei jeder Bestrahlungsstärke bis hinunter zu etwa 10 Sonnen, ein Bragg-Struktur-Design gefunden werden kann durch welches annähernd die maximal mögliche UCQY erreicht wird, *iv*) die spektrale Breite der Erhöhungseffekte angepasst werden kann, sodass der Kernbereich der Absorption des Hochkonverters in den Erhöhungsbereich fällt und *v*) eine effiziente Licht-Einkopplung bis hin zu hohen Einfallswinkeln von ca 30° möglich ist.

Die Kernaussagen dieser Arbeit können auf jedes Hochkonvertermaterial mit einer ähnlichen Konfiguration von Energiezuständen angewendet werden. Die Analyse im Rahmen dieser Arbeit bezieht sich auf eine 1D photonische Struktur, kann allerdings auf jede photonische Struktur, auch 2D und 3D Designs angewendet werden. Daher eröffnet das validierte Simulationsmodell nun die Möglichkeit eine präzise Optimierung des Designs von photonischen Strukturen für diverse Hochkonverter-Materialien und Zielanwendungen durchzuführen.

ACKNOWLEDGEMENTS

I would like to thank all people who contributed to this work at both, the Fraunhofer Institute for Solar Energy Systems (ISE) and the Karlsruhe Institute of Technology (KIT):

Fraunhofer ISE

My very special thanks go to Prof. Jan Christoph Goldschmidt for being an amazing supervisor in the group Novel Solar Cell Concepts at Fraunhofer ISE throughout the time of my PhD, for all the fun in depth scientific discussions on upconversion, for all his highly valuable input and ideas, for always trusting in my abilities, always supporting my decisions, both for science and for my personal path.

Thanks to Prof. Stefan Glunz, as second assessor of my thesis, for all his valuable input.

Special thanks go to Barbara Herter, Johannes Gutmann and Stefan Fischer for always answering my questions and all the amazing work they established during their PhDs in the group Novel Solar Cell Concepts that I was able to built up on: Barbara Herter on taking photonic effects on upconversion into account in simulation, as well as fabricating thin upconverting layers; Johannes Gutmann on simulating the (fractional) local density of optical states as well as fabricating Bragg structures; and Stefan Fischer on the simulation of upconversion dynamics and the upconversion photoluminescence measurement setup, and later for fabricating super efficient custom made upconverter naoparticles that I could use for the experiments of my work.

My very special thanks go to Emil Eriksen, who I spent the most fun, productive and intensive three moths of my phd with, while he was visiting from Aarhus University, creating so much science together as the perfect team. Thanks to Emil for being such a super fast and precise brilliant programmer and for rewriting the complete simulation code in python, implementing many new features.

Many thanks to Benedikt Bläsi for all his valuable input and always helping out when questions on optics arose, in simulations, ellipsometric data analysis and photoluminescence measurements and data interpretation.

Many thanks to Oliver Höhn for always helping out and answering so many little detailed questions on simulations, IT, software, and also atomic force microscopy measurements.

Thanks to Deniz Yazicioglu for all the work he established during his master's thesis, constructing the setup for UC photoluminescence measurements for a varied incident angle, for performing all measurements at this setup and also numerous UC luminescence measurements at the integrating sphere setup for parameter scans. Thanks to Volker Kübler and Andrew Mondon for scanning electron microscopy measurements; to Felicia Volle for spin-coating many thin layers for me for process optimization; to Kristina Winkler and Fabian Gerspacher for spectroscopic ellipsometry measurements and to those two as well as Felix Martin for spectrophotometer measurements.

To Alexander Bett and Patricia Schulze for being the greatest "officemates" and to all Team Novel for for hiking in the snowstorm and through deep valleys, for icecream on the rooftop and for always helping each other out.

My thanks further go to Fabian Spallek and Thomas Wellens from the University of Freiburg, for all the exchange on theoretical approaches to the photonic effects on UC within the project NaLuWiLeS.

Karlsruhe Institute of Technology

Special thanks go to Prof. Bryce Richards for supervising my PhD thesis as an external PhD student within his group Nanophotonics for Energy at KIT, for all his highly appreciated scientific input and for always trusting in my way of doing my work.

More special thanks go to Ian Howard and Dmitry Busko for their guidance and for always supporting my work with their wide knowledge on how to optimize and interpret photoluminescence measurements.

Many thanks to Christian Reitz for adapting and running the atomic layer deposition process for fabrication of the TiO_2 layers of my Bragg structures with me, for all his support and explanations around this topic and the fun time in the lab.

Further, I would like to thank Nicolo Baroni for XRD measurements of my structures, to Stefan Dottermusch, Michael Adams, Michael Olderburg and all the others of the group for always helping out with my questions and for the fun time together, especially at the group days.

And of course to my family and friends

Thanks to my friends Lena, Andi, Leo, Laura and Christian and all the others for being such an amazing physics crew for such a long time.

A big thanks to my family for all their support, to Flora, Ute and Alma for always helping looking after the little ones, to Mirella and Andieas for co-creating the space for this time, and Frieder and Marja-Lena and all their kids for all their inspiration.

And of course, my warmest heartfelt thanks go to my amazing husband Nils for all his support, his humor, all the long evening discussions such that he turned into an expect of upconversion himself and for always being the backbone of the family. These warmest thanks also go to my wonderful children Sora and Jaro for being as great as they are, filling my life with so much joy and giving me so much freedom to be with them amazing beings, and do my own.

LIST OF PUBLICATIONS

Publications in peer-reviewed journals

C. L. M. Hofmann, S. Fischer, E. H. Eriksen, B. Bläsi, C. Reitz, D. Yazicioglu, I. A. Howard, B. S. Richards and J. C. Goldschmidt. Experimental validation of a modeling framework for upconversion enhancement in 1D-photonic crystals. *Nature Communications* **12**, 1-10 **(2021)**.

E. H. Eriksen, S. P. Madsen, B. Julsgaard, **C. L. M. Hofmann**, J. C. Goldschmidt and P. Balling. Enhanced upconversion via plasmonic near-field effects: role of the particle shape, *Journal of Optics* **21**, 035004 **(2019)**.

C. L. M. Hofmann, E. H. Eriksen, S. Fischer, B. S. Richards, P. Balling and J. C. Goldschmidt. Enhanced upconversion in one-dimensional photonic crystals: a simulation-based assessment within realistic material and fabrication constraints, *Optics Express* **26**, 7537-7554 **(2018)**.

H. Hauser, B. Herter, **C. L. M. Hofmann**, O. Höhn, V. Kübler, S. Fischer, S. Wolf, S. Fasold, F. C. J. M. van Veggel, J. C. Goldschmidt and B. Bläsi. Soft thermal nanoimprint of PMMA doped with upconverter nanoparticles, *Microelectronic Engineering* **187-188**, 154-159 **(2018)**.

C. L. M. Hofmann, B. Herter, S. Fischer, J. Gutmann and J. C. Goldschmidt. Upconversion in a Bragg structure: photonic effects of a modified local density of states and irradiance on luminescence and upconversion quantum yield. *Optics Express* **24**, 14895-14914 **(2016)**.

Published simulation code

C. L. M. Hofmann, E. H. Eriksen, B. Bläsi, F. Hallermann, S. Fischer, B. Fröhlich, J. Gutmann, B. Herter, P. Löper, H. Steinkemper and J. C. Goldschmidt. remUCPS - rate equation model of upconversion dynamics including photonic structure effects. *Fordatis* **(2020)**. `http://dx.doi.org/10.24406/fordatis/110.2`.

Oral conference contributions

C. L. M. Hofmann, E. H. Eriksen, D. U. Yazicioglu, S. Fischer, B. Bläsi, C. Reitz, B. S. Richards and J. C. Goldschmidt. Upconversion performance enhancement in real 1D photonic crystals: simulation, experiment and perspectives for photovoltaics. *OSA Optical Society of America, Advanced Photonics Congress, San Francisco, USA* (August **2019**). (**Invited**)

C. L. M. Hofmann, S. Fischer, C. Reitz, B. S. Richards and J. C. Goldschmidt. Bragg stacks enhancing upconversion for photovoltaics: a theoretical and experimental analysis. *OSA Optical Society of America, Light, Energy and the Environment Congress, Leipzig, Germany* (November **2016**).

C. L. M. Hofmann, S. Fischer, C. Reitz, B. S. Richards and J. C. Goldschmidt. Bragg stacks for enhanced upconversion: theoretical optimization and experimental characterization of photonic effects, *EMN International Conference on Energy, Materials and Nanotechnoligy, Meeting on Photonics, Barcelona, Spain* (September **2016**). (**Invited**)

C. L. M. Hofmann, B. Herter, S. Fischer, J. C. Goldschmidt. Enhancing upconversion with a Bragg structure, *DPG German Physical Society Conference, Focus Session: Nanophotonic Concepts and Materials for Energy Harvesting - Plasmonics, Transformation Optics, Upconversion, and beyond II, Berlin, Germany* (March **2015**).

Conference proceedings

C. L. M. Hofmann, E. H. Eriksen, D. U. Yazicioglu, S. Fischer, B. Bläsi, C. Reitz, B. S. Richards and J. C. Goldschmidt. Upconversion performance enhancement in real 1D photonic crystals: simulation, experiment and perspectives for photovoltaics. *In Proceedings of the OSA Optical Society of America Advanced Photonics Congress*, PT1C.2 **(2019)**.

E. H. Eriksen, **C. L. M. Hofmann**, S. Fischer and J. C. Goldschmidt. Upconversion in a finite, one-dimensional photonic crystal: a simulation-based assessment of the potential for increasing the upconversion efficiency of β-$NaYF_4$:Er^{3+}. *In Proceedings of the OSA Optical Society of America, Light, Energy and the Environment Congress*, PW2A.1 **(2017)**.

C. L. M. Hofmann, S. Fischer, C. Reitz, A. Mondon, D. Busko, I. Howard, B. S. Richards and J. C. Goldschmidt. Bragg stacks enhancing upconversion for photovoltaics: a theoretical and experimental analysis. *In Proceedings of the OSA Optical Society of America, Light, Energy and the Environment Congress*, PTh4A.5 **(2016)**.

C. L. M. Hofmann, S. Fischer, C. Reitz, B. S. Richards and J. C. Goldschmidt. Comprehensive analysis of photonic effects on upconversion of β-$NaYF_4$:Er^{3+} nanoparticles in an organic-inorganic hybrid 1D photonic crystal. *In proceedings of SPIE the International Society of Optics and Photonics* **9885**, 98851A, 1-9 **(2016)**.

Poster presentations

C.L.M. Hofmann, S. Fischer, C. Reitz, B.S. Richards, J.C. Goldschmidt, Comprehensive analysis of photonic effects on upconversion of β-$NaYF_4$:Er^{3+} nanoparticles in an organic-inorganic hybrid 1D photonic crystal. *SPIE the International Society of Optics and Photonics, SPIE Photonics Europe, Meeting on Optics and Photonics, Photonic Crystal Materials and Devices XII, Brussels, Belgium*, 9885-46, (April **2016**).

CHAPTER 1

INTRODUCTION

1.1. Motivation

The energy consumption of mankind is growing rapidly due to the growth in world population and an increase in living standards linked to powered devices. Fossil fuels and coal are clearly no long term solution to provide this power as they are limited, harvesting causes severe harm to nature and extracting energy releases carbon dioxide and other greenhouse gases that harm the quality of the atmosphere and contribute to global warming. Nuclear energy also does not provide a solution, as it constitutes the risk of enormous long term and large area catastrophes for nature in the case of an accident and additionally, there is no long term solution how to handle nuclear waste. Renewable energy sources like solar energy, wind energy and hydro power are available and can be harvested without exploiting the nature of this planet. Above all, the sun provides an enormous amount of energy and the technology of photovoltaics provides the possibility to directly convert solar radiation into electricity. Lowering the prices of solar electricity increases the potential to increase its market share. Addressing major optical loss channels is one promising approach to lower the costs. One major optical loss channel are sub-bandgap losses, the photons with an energy too small to bridge the bandgap and to be absorbed by the solar cell. In a silicon solar cell, the sub-bandgap losses make up 20% of the energy of the solar spectrum, as illustrated in Fig. 1.1a.

One approach to exploit these sub-bandgap losses is upconversion (UC), the spectral conversion of low energy photons into higher energy photons. When an upconverter is placed behind a bifacial solar cell (illustrated in Fig. 1.1b), the sub-bandgap photons can be absorbed by the upconverter material and can be converted to photons with a higher energy above the solar cells bandgap energy. When these higher energy photons are emitted back towards the solar cell, they can be absorbed by the solar cell and can therefore contribute to charge generation. The concept of UC in the context of photovoltaics is of major interest and has been studied widely [4–10]. For a crystalline silicon solar cell, the fundamental efficiency limit lies around 29.4% [11, 12]. In a fundamental work, Trupke *et al.*, calculated a potential increase of silicon solar cell efficiency to 40.2%, assuming an ideal upconverter transforming the region of sub-bandgap losses within the AM1.5G solar spectrum to usable

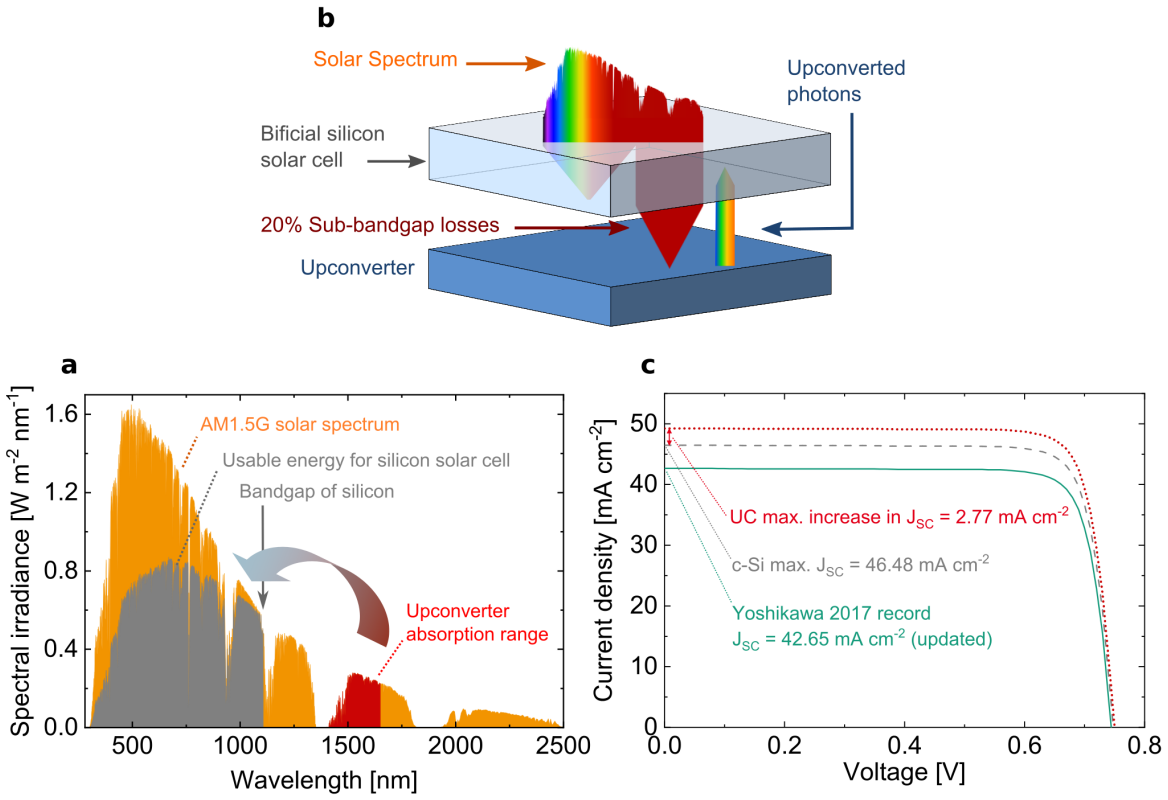

Figure 1.1.: Potential of upconversion (UC) for silicon photovoltaics. **a** AM1.5G solar spectrum, the range that can efficiently be harvested by a silicon solar cell with a bandgap energy of 1.12 eV. Upconverting the complete range between 1400 nm and 1650 nm with an ideal UC efficiency of 50% could gain a 6% efficiency increase for a silicon solar cell [1]. **b** The sub-bandgap losses that are transmitted through a silicon solar cell can, via an upconverter placed behind, be converted to photons above the silicon bandgap and subsequently contribute to charge generation. **c** Current-voltage (IV) curve of the record crystalline silicon solar cell [2] with a short circuit current (J_{SC}) of 42.65 mA cm^{-2}(updated J_{SC}) [3], record IV curve scaled to the potential maximum J_{SC} of 46.48 mA cm^{-2} for a silicon solar cell [1] and the maximum potential increase in J_{SC} of 2.77 mA cm^{-2} due to UC [1] as illustrated in graph **b**. The IV-curves are calculated from the record cell IV-curve [2] by adding the difference in J_{SC}.

energy for the silicon solar cell. A very recent paper by Richards *et al.* has estimated up to 6% absolute solar cell efficiency increase of a silicon solar cell, using an idealized Er^{3+} upconverter (which is one of the most suitable UC materials in combination with a silicon solar cell, as discussed below). To illustrate this possible enhancement, Fig. 1.1c shows the IV-curve of the current most efficient laboratory-scale crystalline silicon solar cell, with a short circuit current (J_{SC}) of 42.65 mA cm^{-2} [2,3]. The theoretical maximum J_{SC} of a crystalline silicon solar cell lies at 46.48 mA cm^{-2} [1]. Using an idealized Er^{3+} upconverter, this J_{SC} can be enhanced by 2.77 mA cm^{-2}, which represents a 6% absolute efficiency increase [1]. It includes that *i*) all photons within the Er^{3+} absorption range between 1400 nm and 1650 nm are absorbed, *ii*) the UC process functions at its maximum possible quantum efficiency of 50% (neglecting reverse processes), meaning that two lower energy photons always create one higher energy photon and *iii*) that the collection efficiency of the bifacial solar cells rear side functions without optical losses at an external quantum efficiency of unity.

The principle of UC itself has been of rapidly growing interest in various fields of physics and materials chemistry within the past 50 years [13]. Intensive research has been carried out on understanding the basic principles of the UC process [13–16], as well as on upconverter material development, predominantly in the shape of nanocrystals [4, 5, 17–25]. Rare earth ions are efficient upconverter materials that provide a suitable set of energy levels to exploit sub bandgap losses in the context of silicon photovoltaics. Figure 1.2c and 1.2d show the

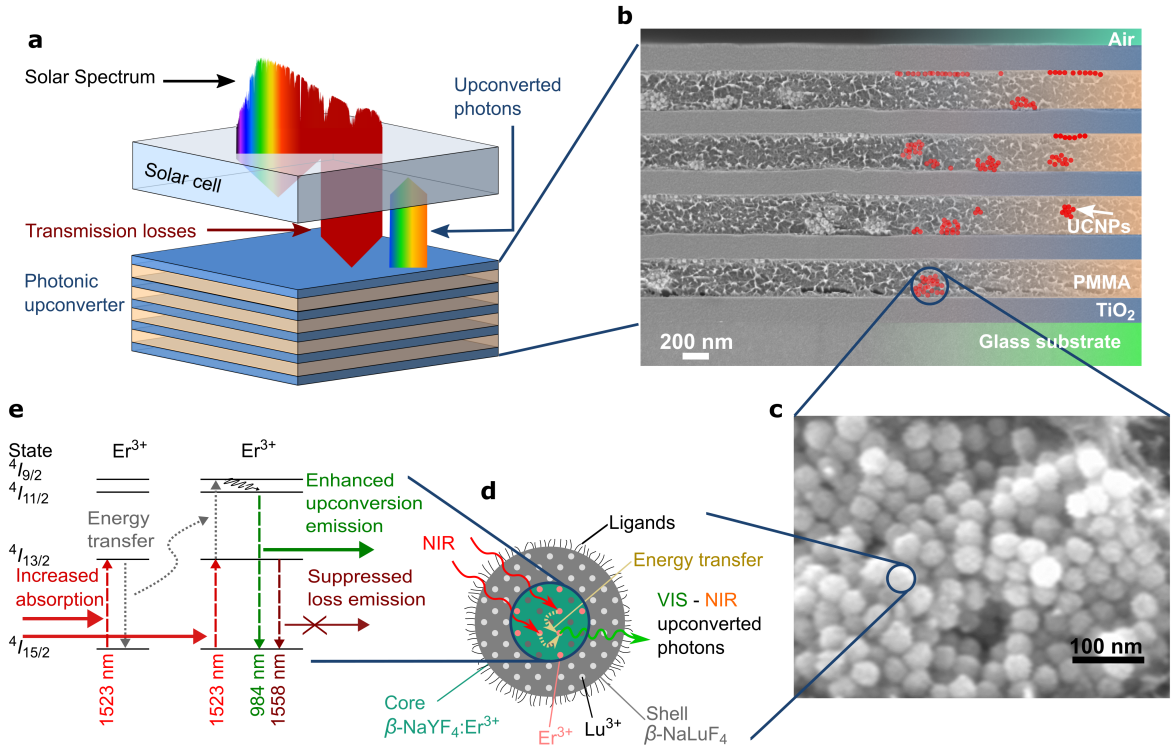

Figure 1.2.: Motivation of the investigated photonic upconverter device. **a** Approach of utilizing sub-bandgap photons for charge generation in a solar cell by a photonic upconverter on the rear side. **b** Scanning electron microscope (SEM) image of the realized 1D-photonic structure made of TiO_2 and PMMA with embedded upconverter nanoparticles (UCNPs). **c** SEM image of upconverter nanoparticles. **d** Schematics of core-shell upconverter nanoparticles of β-$NaYF_4$:Er^{3+}, converting near infrared (NIR) to NIR and up to visible (VIS) photons in the active core. The inert shell prevents losses due to surface quenching. **e** Energy levels in the upconverter Er^{3+} and the upconversion (UC) process influenced by photonic effects of the surrounding structure: increased absorption due to a locally enhanced energy density, non-linearly increasing the probability of an energy transfer UC process, followed by UC emission from a higher level that can be enhanced due to a modified local density of optical states. (Figure adapted form [26])

β-$NaYF_4$:Er^{3+} core-shell upconverter nanoparticles, as used in this work. The ground state absorption of Er^{3+} lies at 1523 nm wavelength, with a subsequent dominant UC emission around 980 nm, which is just above the energy of the bandgap of silicon. In rare earth ions, the dominant UC process is energy transfer UC, as illustrated in Fig. 1.2e. In this process, two low energy photons are absorbed, lifting two ions into an excited energy level. Subsequently, the energy from one excited ion is non-radiatively transferred to another excited ion, lifting the latter into a higher energy level, followed by the emission of one photon with higher energy. The process of energy transfer UC therefore requires two excited ions

in close vicinity in space and time [27]. Consequently, the probability of an energy transfer process to take place is non-linearly dependent on the incident irradiance. The irradiance is decisive for the density of excited ions that are available to participate in an energy transfer UC process. Consequently, the low irradiance incident in photovoltaic applications constitutes a challenge due to the low UC efficiency in the low irradiance regime.

One approach to increase UC efficiency, particularly in the low irradiance regime, is embedding the upconverter into a photonic structure (Fig. 1.2a in the context of photovoltaics and Fig. 1.2b depicting the investigated photonic upconverter within this work). Within photonic structures, there are two effects that act on an UC process, as illustrated in Fig. 1.2e. A locally enhanced optical energy density alters all stimulated processes within the UC process. With a tuned photonic structure design, it can increase the absorption within the upconverter material, which non-linearly increases the probability of an energy transfer UC process to take place. Furthermore, within the photonic structure, the local density of optical states is modified. This modified environment acts on all spontaneous emission processes and can therefore, with a tuned design, increase the number of photonic states being available for a particular spontaneous emission process to take place. Throughout literature, photonic structure enhanced UC is being investigated for a broad range of photonic structures and upconverter materials. The state of the art of photonic structure enhanced UC is comprehensively addressed in section 2.2.5. A careful design of the photonic structure is crucial in order to obtain a positive effect of the photonic structure on UC and further, to maximize UC efficiency through photonic structure effects. However, throughout literature, none or very little focus is put on optimizing the photonic structure design by means of comprehensive simulation models in order to maximize the UC efficiency enhancement.

1.2. Objectives of this work

The objective of my work is to fill the gap in literature of a knowledge-based optimization process of photonic structure enhanced UC. Within this thesis I investigate photonic effects on UC, both in simulation and experiment, reaching a validation of the modeling framework in large parameter scans that are relevant for an application in photovoltaics. The topic of this thesis is therefore placed in the intersection of three large research fields that are *i*) UC, *ii*) photonic structures and *iii*) photovoltaics (Fig. 1.3).

As upconverter material, β-$NaYF_4$ doped with Er^{3+} is investigated, because it is an efficient upconverter material with suitable energy levels to reduce sub-bandgap losses of silicon photovoltaics. The photonic structure analyzed in this thesis is a Bragg structure, a simple one-dimensional photonic structure with a small number of design parameters. The simplicity of the structure allows for understanding the impact of each single design parameter and to tune each parameter individually. The Bragg structure consists of two alternating layers of different refractive index. Each layer features the same optical thickness d_i that is given by the design wavelength λ_{design}, as $d_i = {}^{\lambda_{\text{design}}}/_{4n_i}$ for each layer with refractive index n_i. In this work, the upconverter is embedded into the low refractive index layer to match refractive indices and prevent scattering.

This work has three main objectives, *i*) the simulation of photonic upconverters, *ii*) the experimental realization of optimized photonic upconverters and *iii*) the experimental evaluation

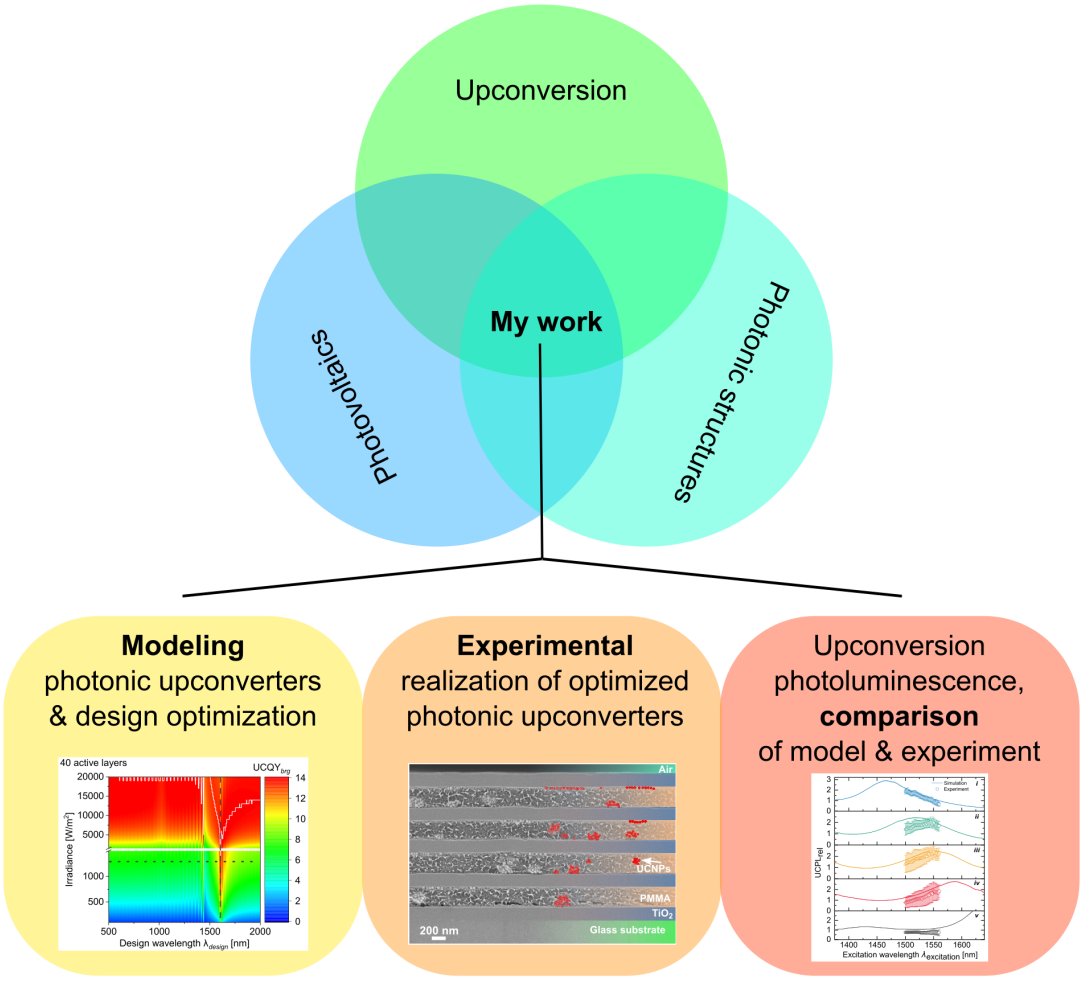

Figure 1.3.: Thematic classification and scope of my work.

of photonic effects on UC and comparison to the model (Fig. 1.3).

Simulation

Over the past 15 years, a modeling framework has been developed in the group Novel Solar Cell Concepts at Fraunhofer ISE to describe photonic effects on UC theoretically [28–31]. The theoretical part of this thesis builds up on this excellent pioneer work of the group. Using an adapted version of the modeling framework, the impact of each single photonic effect, the local optical energy density and the modified local density of optical states, on the UC photoluminescence (UCPL) and UC quantum yield (UCQY) is investigated [32]. In a cooperation with the visiting PhD student Emil H. Eriksen, we transferred the model into a more efficient simulation environment in python. In this final version, we also included the impact of layer thickness variations within the Bragg structure, as they occur in any real fabrication process and largely influence the strength of the photonic effects. Based on the work by Gutmann *et al.* on luminescent concentrators [33] within our group, the directionality of emission was included in the model, which is important to consider in the context of

photovoltaics, to answer the question whether the upconverted photons can be absorbed by a solar call placed above the photonic upconverter. Using this efficient final modeling framework, large-scale parameter scans are performed within this work in order to thoroughly understand the photonic effects on UC, not only at some specific parameter combinations but in a large-scale and interdependent context. The parameters investigated in this work are key parameters when wanting to optimize a photonic upconverter for an application in photovoltaics, varying *i*) the refractive index of the high-refractive index layer, *ii*) the number of layers of the Bragg structure, *iii*) the design wavelength and *iv*) production accuracy of the Bragg structure. Furthermore, the impact of *v*) a varied incident irradiance, *vi*) excitation wavelength and *vii*) angle of incidence is investigated, as well as *viii*) the directionality of UC emission. As an important output of this work, the final model is published in Hofmann, Eriksen *et al.* 2018 [34] and has been made available open access on the Fraunhofer platform Fordatis [35].

Experiment

To measure the effect of optimized Bragg structures on UC, such structures were experimentally realized in high precision, in order to prevent a reduction of the photonic effect due to production inaccuracies. Great care was taken to optimize the composition, layer thickness control and roughness of the single layers. The low refractive index layer was made of Poly(methyl methacrylate) with embedded upconverter nanoparticles. This layer is referred to as the active layer. The high refractive index layer was made of TiO_2, fabricated via atomic layer deposition to ensure a maximal refractive index contrast and therefore to maximize the photonic effects. The final stacks were composed of four active layers with fife surrounding TiO_2 layers (Fig. 1.2b). The reference samples for an optimized multilayer stack contain the active layers only. The comparably small layer number of the Bragg structures was chosen to ensure that the production accuracy reached in the single layer fabrication was sufficient in order not to diminish the photonic effects in the final multilayer stack. 40 sample designs with various design wavelengths were fabricated, such that the photonic effects were at the expected maximum UC enhancement, closely around this maximum as well as in the region of no expected UC enhancement. The final design wavelength was analyzed to a precision of 1 nm by matching the measured and simulated characteristic reflectance of the Bragg structure.

Comparison of model and experiment

To validate the modeling framework, within this work, the photonic effects on UC were determined in UCPL measurements of the Bragg structures relative to the respective reference structure. A comprehensive comparison of simulation and experiment of photonic structure enhanced UC was performed in large-scale parameter scans: *i*) 40 samples with different design wavelengths were analyzed *ii*) in a large-scale scan of the excitation wavelength, which is a highly relevant parameter for a broad-band application of photovoltics. *iii*) The incident irradiance was scanned in a low irradiance regime applicable in photovoltaic applications. *iv*) The effect of a varied incident angle was studied, which is important both for regular photovoltaics systems, with a varying incident angle of the sun, as well as in

concentrator systems using tracking with light incident from a fixed angle cone. All parameter scans comprise of 5225 different parameter combinations, allowing for a validation of the modeling tool in a large parameter range.

1.3. Outline of this work

Chapter 2 introduces the fundamental theory on light matter interaction, photonic crystals and the interaction between electromagnetic fields and atoms. Based on this theory, the UC process is described and the effect of a photonic structure on the UC dynamics. Subsequently, a comprehensive discussion on the state of the art of photonic structure enhanced UC of rare earth upconverter materials is given.

In chapter 3, firstly the modeling framework for photonic structure enhanced UC is introduced in detail, going from the simulation of the single photonic effects to the UC dynamics and further to the impact of a photonic structure environment on the UC dynamics. Secondly, the experimental methods are discussed with respect to the details applied in fabrication and nanostructural characterization. Furthermore, the used photoluminescence measurement setup is explained.

The fabrication and characterization of the photonic upconverters is comprehensively discussed in chapter 4. The choice of composition, fabrication process, refractive index determination and design optimization are explained for the active layers and subsequently for the TiO_2 layers. Finally, the design and structural characterization of the Bragg structures, the multilayer photonic upconverters, is discussed.

The modeling of photonic upconverters makes up chapter 5. In the beginning, the simulation results of the single photonic effects, the optical local energy density, then the local density of optical states and based on the latter the fractional local density of optical states are presented and discussed. After the presentation of the results concerning the UC process in homogeneous media, the impact of each photonic effect is studied, followed by an analysis of how to maximize the efficiency of UC by a Bragg structure. Subsequently, the impact of a varied refractive index of the high-refractive index layer is studied under the influence of different production accuracies and finally the combined impact of the Bragg structure on UC. Finally, the directionality of the UC emission is investigated.

Chapter 6 connects the two previous results chapters: the comparison of the modeling framework to measured UCPL enhancements is drawn in large-scale parameter scans. First, the UCPL in a Bragg structure and reference is introduced. Subsequently, the parameters that are varied in experiment are introduced with respect to their significance in an application in photovoltaics. The comparison between simulation and experiment is drawn for each varied parameter, the design wavelength, excitation wavelength, incident irradiance and the angle of excitation. The chapter is closed by discussing the experimental, and partly the modeling results of this thesis in the context of literature.

The general conclusion on the results of this thesis is given in chapter 7 as well as an outlook on perspectives and possible future work.

CHAPTER 2

FUNDAMENTALS

The first part of this chapter introduces the fundamental theory of photonic crystals, relevant for this work. In the second part, upconverting materials and the upconversion process is discussed, followed by a brief historical background on upconversion for photovoltaics. Furthermore, the impact of a photonic structure environment on the upconversion process is introduced and the state of the art of photonic structure enhanced upconversion is discussed comprehensively.

The section 2.2.5 within this chapter is based on parts of the supplementary information of the following publication:

C. L. M. Hofmann, S. Fischer, E. H. Eriksen, B. Bläsi, C. Reitz, D. Yazicioglu, I. A. Howard, B. S. Richards and J. C. Goldschmidt, Experimental validation of a modeling framework for upconversion enhancement in 1D-photonic crystals, *Nature Communications* **12**, 1-10 **(2021)**

2.1. Photonic crystals

Photonic crystals are structures with a periodic variation of the refractive index n (or relative permittivity $n = \sqrt{\varepsilon}$). Figure 2.1 shows how the periodicity can be in one, two or three dimensions, thus naming the photonic crystal, 1D, 2D or 3D. In this section, the properties of photonic crystals are introduced, which are required for an understanding of this work.

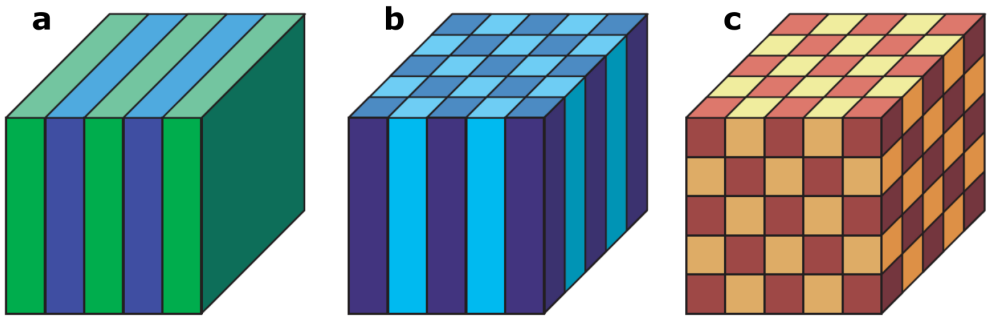

Figure 2.1.: Sketch of photonic crystals that are one-, two or three dimensional. [36].

2.1.1. Electromagnetic fields and waves in media

The propagation of light, as an electromagnetic wave is described by the well known Maxwell equations. In the following, the master equation, as it is often referred to in the context of photonic crystals, is derived from the Maxwell equations. The solution of the master equation enables calculating the properties of a photonic crystal. The following derivation is based on one of the standard works on photonic crystals by Joannopoulos *et al.* [36]. Based on this theory Johnson and Joannopoulos developed the simulation program MIT Photonic Bands [37] which is used in my work to calculate the photonic crystal properties.

The materials of interest in the context of photonic crystals give certain boundary conditions: *i*) Photonic crystals, in general, are made up by mixed dielectric media, materials with regions of different dielectric media, that do not vary in time. Therefore, the medium can be described in dependence on a position vector $\mathbf{r}$. These media do not feature free charges or currents, resulting in a charge density $\rho = 0$ and current density $\mathbf{j} = 0$. *ii*) The materials are macroscopic and isotropic and usually feature a relative magnetic permeability $\mu(\mathbf{r})$ very close to unity, hence for simplicity $\mu(\mathbf{r})$ can be set to unity; *iii*) There is no explicit material dispersion, therefore the relative permittivity is $\varepsilon(\mathbf{r}) \neq \varepsilon(\mathbf{r}, \omega)$. *iv*) The material is non-absorbing, therefore $\varepsilon(\mathbf{r})$ is real and positive. Consequently, the refractive index is given by $n(\mathbf{r}) = \sqrt{\varepsilon(\mathbf{r})}$. Taking into account all the above restrictions, the Maxwell equations take

on the form

$$\nabla \cdot \mathbf{H}(\mathbf{r},t) = 0 \tag{2.1}$$
$$\nabla \cdot [\varepsilon(\mathbf{r})\mathbf{E}(\mathbf{r},t)] = 0 \tag{2.2}$$
$$\nabla \times \mathbf{E}(\mathbf{r},t) + \mu_0 \frac{\partial \mathbf{H}(\mathbf{r},t)}{\partial t} = 0 \tag{2.3}$$
$$\nabla \times \mathbf{H}(\mathbf{r},t) - \varepsilon_0 \varepsilon(\mathbf{r}) \frac{\partial \mathbf{E}(\mathbf{r},t)}{\partial t} = 0 \tag{2.4}$$

whereby $\mathbf{E}(\mathbf{r},t)$ and $\mathbf{H}(\mathbf{r},t)$ are the electric and magnetic field, respectively, ε_0 the vacuum permittivity, μ_0 the vacuum permeability.

Solutions to the linear Maxwell equations can be found using the Ansatz of an harmonic time dependence of the fields, whereby the space and time dependence can be separated as

$$\begin{aligned} \mathbf{H}(\mathbf{r},t) &= \mathbf{H}(\mathbf{r}) \cdot e^{-i\omega t} = \mathbf{H} \cdot e^{i\mathbf{kr}} \cdot e^{-i\omega t} \\ \mathbf{E}(\mathbf{r},t) &= \mathbf{E}(\mathbf{r}) \cdot e^{-i\omega t} = \mathbf{E} \cdot e^{i\mathbf{kr}} \cdot e^{-i\omega t}. \end{aligned} \tag{2.5}$$

$\mathbf{k}$ describes the wave vector and ω the angular frequency. Inserting equation 2.5 into the divergence equations 2.1 and 2.2 results in the constraint that the solutions are transverse electromagnetic waves. Inserting the Ansatz of equation 2.5 into the curl equations 2.3 and 2.4, yields expressions that relate $\mathbf{E}(\mathbf{r})$ to $\mathbf{H}(\mathbf{r})$

$$\nabla \times \mathbf{E}(\mathbf{r}) - i\omega\mu_0 \mathbf{H}(\mathbf{r}) = 0 \tag{2.6}$$
$$\nabla \times \mathbf{H}(\mathbf{r}) + i\omega\varepsilon_0 \varepsilon(\mathbf{r}) \mathbf{E}(\mathbf{r}) = 0 \tag{2.7}$$

Dividing equation 2.7 by $\varepsilon(\mathbf{r})$, taking the curl and inserting equation 2.6 finally yields the so called master equation that is only dependent on $\mathbf{H}(\mathbf{r})$

$$\nabla \times \left(\frac{1}{\varepsilon(\mathbf{r})} \nabla \times \mathbf{H}(\mathbf{r}) \right) = \left(\frac{\omega}{c_0} \right)^2 \mathbf{H}(\mathbf{r}) \tag{2.8}$$

with c_0 being the speed of light in vacuum $c_0 = {}^1/_{\sqrt{\mu_0 \varepsilon_0}}$. Equation 2.8 thereby defines an eigenvalue problem, with an Hertitian operator $\hat{\Theta}$ for a given structure $\varepsilon(\mathbf{r})$, that can be solved to find the eigenfrequency ω and eigenvector $\mathbf{H}(\mathbf{r})$

$$\hat{\Theta}\mathbf{H}(\mathbf{r}) = \left(\frac{\omega}{c_0} \right)^2 \mathbf{H}(\mathbf{r}) \tag{2.9}$$

The electric field component $\mathbf{E}(\mathbf{r})$ can be recovered from equation 2.7 as

$$\mathbf{E}(\mathbf{r}) = \frac{i}{\omega\varepsilon_0 \varepsilon(\mathbf{r})} \nabla \times \mathbf{H}(\mathbf{r}). \tag{2.10}$$

In a homogeneous medium with constant refractive index, so without variations in ε, the solution to equation 2.8 are simple plane waves with $\mathbf{H}(\mathbf{r}) = \mathbf{H}_0 e^{i\mathbf{kr}}$. This results in a linear dispersion relation

$$\omega = \frac{c_0}{n} |\mathbf{k}|, \tag{2.11}$$

linking ω to $\mathbf{k}$ via the refractive index of the medium $n = \sqrt{\varepsilon}$. In a photonic structure, however, the refractive index is not constant and the linear dispersion relation is not longer valid.

2.1.2. Photonic bandstructure

The descriptions in this section are again based on ref. [36]. The translational symmetry in space, imposed by the periodic variation of $\varepsilon(\mathbf{r})$, can be expressed as $\varepsilon(\mathbf{r}) = \varepsilon(\mathbf{r} + \mathbf{R})$, with $\mathbf{R}$ being a linear combination of the primitive lattice vectors $\mathbf{r}$. In solid state physics, the translational symmetry of charges in real crystals results in an electronic band structure and the definition of a Winger-Seitz unit cell [38]. In an analogous way, the translational symmetry of $\varepsilon(\mathbf{r})$ defines a photonic crystal. As a result of the translational symmetry, the fields can be expressed by Bloch states $\mathbf{u}_{b,\mathbf{k}}(\mathbf{r})$ that are periodic on the photonic crystal lattice with $\mathbf{u}_{b,\mathbf{k}}(\mathbf{r})$ = $\mathbf{u}_{b,\mathbf{k}}(\mathbf{r} + \mathbf{R})$ such that

$$\mathbf{H}_{b,\mathbf{k}}(\mathbf{r}) = e^{i\mathbf{kr}}\mathbf{u}_{b,\mathbf{k}}(\mathbf{r}) \tag{2.12}$$

whereby *b* describes the photonic band index. Inserting the Ansatz of equation 2.12 into equation 2.8 yields the expression

$$(i\mathbf{k} + \nabla) \times \frac{1}{\varepsilon(\mathbf{r})}(i\mathbf{k} + \nabla) \times \mathbf{u}_{\mathbf{k}}(\mathbf{r}) = (\omega(\mathbf{k})/c)^2\mathbf{u}_{\mathbf{k}}(\mathbf{r}) \tag{2.13}$$

The software package MIT Photonic Bands, used in my work, solves this eigenvalue problem numerically, applying the plane wave expansion method [39].

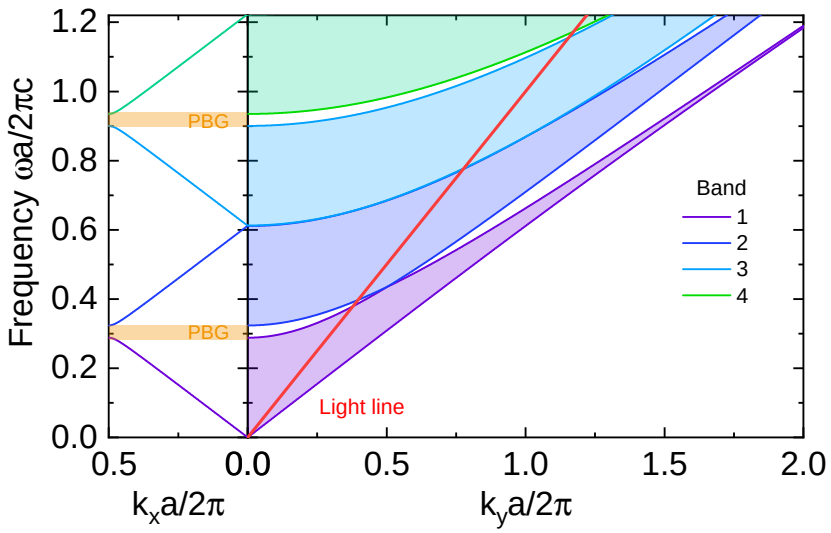

Figure 2.2.: Photonic band structure of a Bragg structure with low and high refractive indices n_{low} = 1.5 and n_{high} = 1.8, respectively. The band structure in on-axis direction (k_x) shows the linear dispersion relation, deviating from linearity at the edge of the FBZ to form the photonic bandgaps (PBG). In k_y direction, which represents the parallel wave vector $\mathbf{k}_{\parallel}$, the bands are depicted at $k_x a/2\pi$ = 0 and 0.5. The shaded region in between the two cases indicates where the continuum of bands lies for intermediate k_x. The red line indicates the light line $\omega = c_0 k_y$ for modes that can be coupled out into air (addressed in section 2.1.3). For clarity, only the transverse electrical modes are plotted, which only slightly differ from the transverse magnetic modes.

Figure 2.2 depicts the photonic band structure of a Bragg structure. The linear dispersion relation $\omega(k) = c_0/nk$ (equation 2.11) describes the basic relation between ω and k_x in

on-axis direction (which is the direction of periodically varying n, see Fig. 2.2. Thereby the band is folded back, each time it reaches the edge of the first Brillouin zone (FBZ). The slope is governed by n, which, in this case, is given by the effective refractive index of the structure (see equation 2.27). At the edges of the FBZ, the slope deviates from linearity, giving rise to the formation of photonic bandgaps in on-axis direction. The bandgaps can exist in one, two or three dimensions, depending on the dimensionality of the photonic crystal. In a Bragg structure, the bandgap is one-dimensional, meaning that within the bandgap, light cannot traverse through the Bragg structure inside the bandgap in the direction of periodicity, however, in the other two dimensions, there are modes that can traverse through the structure.

In direction of the parallel wave vector k_y, the bands extend. In the plot, the bands along k_y are shown at $k_x a/2\pi$ = 0 and 0.5. The shaded region in between depicts the continuum of bands along k_y for all intermediate values of k_x.

The origin of the photonic bandgap can be understood by considering the energy of the modes in the high- and low-ε regions. I want to give a short explanation for the example of a 1D photonic crystal, for which the photonic band structure is plotted in Fig. 2.2. At the edge of the FBZ, at $k = \pi/a$, the photonic bandgaps form as frequency regions in which no solutions exist to equation 2.8. The corresponding modes have a wavelength of $2a$. Due to the required symmetry of the unit cell about its center, there are two possible ways to center a mode with wavelength $2a$ within the unit cell: *i*) either the maximum is centered in the low-, *ii*) or in the high-ε region, as illustrated in Fig. 2.3. According to the electromagnetic

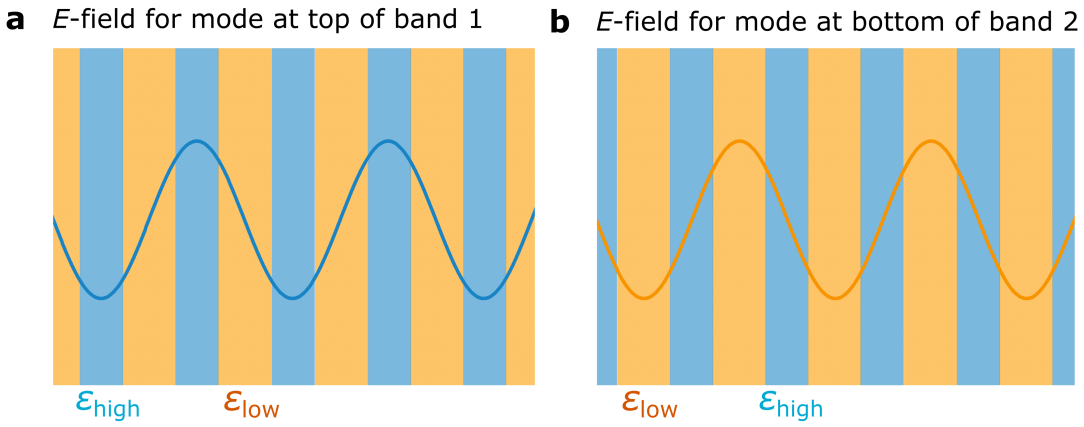

Figure 2.3.: Electric field distributions for the modes right below and above the lowest photonic bandgap. The electric field distribution is shown in a Bragg structure of a high ε-medium $\varepsilon_{\text{high}}$ and a low ε-medium ε_{low}. Electric field at the top of band 1 (compare to Fig. 2.2), centered in the $\varepsilon_{\text{high}}$ medium. **b** Electric field at the bottom of band 2, centered in the ε_{low} medium. Figure adapted from ref. [36].

variational theorem, the energy of low-frequency modes is concentrated in the high-ε regions, while a large fraction of the energy of high-frequency modes is located in the low-ε regions [1]. Consequently, the two different cases stated above result in slightly different energies at the same k, which gives rise to the formation of the photonic bandgap. *i*) When the maximum

[1] The localization of the energy for the low-and high-frequency modes is derived from considering small perturbations in the magnetic field $\mathbf{H}$. A detailed derivation can be found in ref. [36]

of the mode is centered in the low-ε region, the energy, and therefore the frequency ω of the mode is slightly higher. This corresponds to the band above the photonic bandgap (sometimes referred to as the air band). *ii*) When the maximum is centered in the high-ε region, ω is slightly lower, corresponding to the band below the photonic bandgap (referred to as the dielectric band). The formation of a photonic bandgap therefore appears each time the band is 'folded back' at the edge of the FBZ, at $k = {}^{\pi}/_{a}$.

Based on the reasoning above, the difference in ω for the air and dielectric band (above and below the photonic bandgap) increases with an increasing contrast in ε. Consequently, a larger contrast in ε between the low- and high- index layer results in a widening of the photonic bandgap.

2.1.3. Light at interfaces

Other than in ideal photonic crystals, which are infinitely periodic in $\varepsilon(\mathbf{r})$, real structures are finite. In this work, I refer to these finite structures as photonic structures. Finite structures have boundaries to other media, e.g. to a substrate and a surrounding medium. At these interfaces, the light obeys criteria that define whether the light is coupled out of the photonic structure into another medium. These criteria are: *i*) The conservation of energy imposes a conservation of the modes' frequency ω. *ii*) The continuous translational symmetry along the interface imposes that the wave vector component $\mathbf{k}_{\parallel}$ parallel to the interface is conserved [36, 40].

For the case of plane waves at the interface of two homogeneous media, these criteria result in Snells law of refraction [41]

$$n_i \sin(\theta_i) = n_t \sin(\theta_t), \tag{2.14}$$

whereby n_i and n_t denote the refractive indices of the medium that the light is incident from and transmitted into, respectively, and θ_i and θ_t the angles of propagation of the corresponding modes $\mathbf{k}$ (see Fig. 2.4a). For the case of $n_i > n_t$, there is a critical angle $\theta_c = \arcsin({}^{n_t}/_{n_i})$ from which on total internal reflection occurs, such that no modes can be coupled out of the medium n_i into n_t.

Light coupling out of a photonic structure into a homogeneous medium, however, needs to be described in a more complex manner via the parallel wave vector $\mathbf{k}_{\parallel}$. Listed above as criteria *ii*), $\mathbf{k}_{\parallel}$ needs to be conserved in the incident and transmission medium:

$$\begin{aligned} |\mathbf{k}_{\parallel,i}| &= |\mathbf{k}_{\parallel,t}| \\ \Leftrightarrow |\mathbf{k}_{\parallel}| &= |\mathbf{k}_i| \sin\theta_i = |\mathbf{k}_t| \sin\theta_t, \end{aligned} \tag{2.15}$$

from geometrical reasoning (see Fig. 2.4a). Additionally, in the transmission medium, the linear dispersion relation (equation 2.11) holds.

The modes that are able to couple out, need to have real solutions for $\mathbf{k}_{\perp,t}$. Consequently, using equations 2.11 and 2.15, for a mode to couple out, $\mathbf{k}_{\parallel}$ must fulfill the criteria [36]

$$\begin{aligned} |\mathbf{k}_{\parallel,t}| &\leq \omega n_t / c_0 \\ \text{with } |\mathbf{k}_{\perp,t}| &= \sqrt{(\omega n_t / c_0)^2 - |k_{\parallel,t}|^2} \end{aligned} \tag{2.16}$$

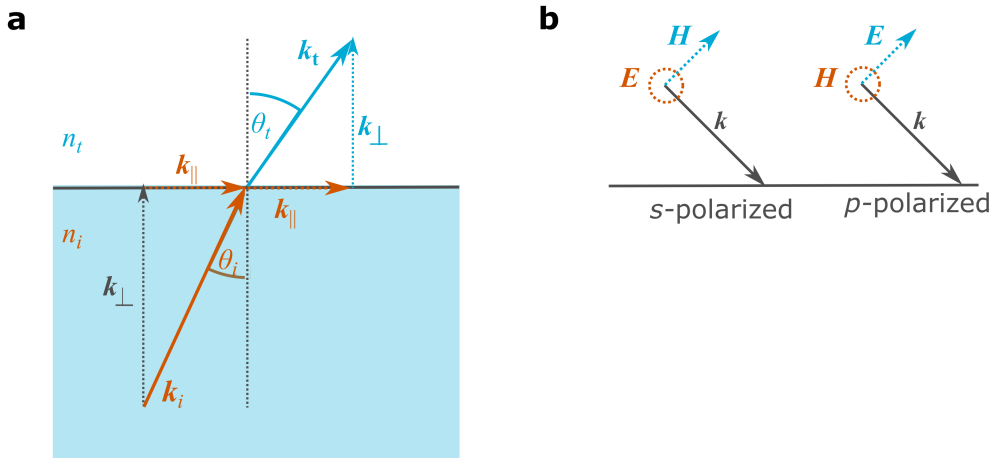

Figure 2.4.: Light refraction at a planar interface. a For a mode $\mathbf{k}$ propagating from an incident medium into a transmission medium, the frequency ω and the parallel wave vector $\mathbf{k}_\parallel$, described by the angle θ, need to be conserved. The perpendicular wave vector component $\mathbf{k}_{\perp,t}$ changes. **b** Definition of s and p-polarization, with the E and H field, respectively, being parallel to the interface plane.

These states can expand in free space and are continuous.

The case of $|\mathbf{k}_\parallel| = \omega n_t/c_0$ describes the so called light line, the equivalent to the critical angle in Snells law (equation 2.14), up to which light can be coupled out [36]. The red line in Fig. 2.2 represents the light line for modes being coupled out of a Bragg structure into air.

Modes with $|\mathbf{k}_\parallel| > \omega n_t/c_0$ cannot couple out and expand, as there are no real solutions for the perpendicular component $\mathbf{k}_\perp$. Instead, these index-guided modes are confined within the photonic structure, analogous to total internal reflection described by Snells law. Due to their localization in one direction, they form a set of discrete frequencies. These discrete frequencies represent the discrete photonic bands below the light line [36] (see Fig. 2.2).

Fresnel coefficients

Because the field components parallel to the interface, illustrated in Fig. 2.4a are conserved, the polarization of the mode has an impact on the reflection and transmission properties. Figure 2.4b illustrates the two polarizations as they are defined throughout this work: in s-polarization, the E-field is parallel to the interface, while in p-polarization, the H-field is parallel to the interface. From the constraints on $\mathbf{k}_\parallel$ and $\mathbf{k}_\perp$ at an interface, the amplitudes of the reflected and transmitted waves for s- and p-polarization can be derived from the Maxwell equations (2.1 to 2.4). The amplitudes of the reflected and transmitted wave relative to the

amplitude of the incident wave and are given by the Fresnel coefficients [41]

$$\begin{aligned} r_s &= \frac{n_t \cos\theta_i - n_i \cos\theta_t}{n_t \cos\theta_i + n_i \cos\theta_t} \\ r_p &= \frac{n_i \cos\theta_i - n_t \cos\theta_t}{n_i \cos\theta_i + n_t \cos\theta_t} \\ t_s &= \frac{2n_i \cos\theta_i}{n_t \cos\theta_i + n_i \cos\theta_t} \\ t_p &= \frac{2n_i \cos\theta_i}{n_i \cos\theta_i + n_t \cos\theta_t} \end{aligned} \tag{2.17}$$

The reflected and transmitted power, which is detected in a measurement, are given by the reflectivity and transmittivity, respectively, which can be obtained from the amplitudes via [41]

$$R = |r|^2 \tag{2.18}$$

$$T = \frac{n_t}{n_i}\frac{\cos\theta_t}{\cos\theta_i}|t|^2 \tag{2.19}$$

2.1.4. Local density of optical states

The total number of states at a certain frequency ω within the FBZ are counted by the density of optical states (DOS) [42]

$$\rho(\omega) = \sum_b \int_{FBZ} \delta(\omega - \omega_{b,\mathbf{k}}) d\mathbf{k}. \tag{2.20}$$

Thereby, a sum rule applies, which states that the total number of states is conserved [43,44]. Consequently, when in a photonic bandgap there are less (or no) photonic states, these states are shifted to adjacent frequencies at the band edges.

The DOS counts all states with equal weight, however, the distribution of the local fields varies significantly throughout the FBZ. This spatial dependence, as well as the weighting by the local field distribution $\mathbf{E}_{b,\mathbf{k}}(\mathbf{r})$ is accounted for by the local density of optical states (LDOS), defined as [42]

$$\rho(\mathbf{r},\omega) = \sum_b \int_{FBZ} |\mathbf{E}_{b,\mathbf{k}}(\mathbf{r})|^2 \delta(\omega - \omega_{b,\mathbf{k}}) d\mathbf{k} \tag{2.21}$$

The LDOS alters spontaneous emission probabilities, which is described by Fermi's golden rule (see equation 2.35). In the context of photonic structures altering the properties of upconversion (UC), the LDOS is the final value that is needed to quantify the impact of the photonic structure on spontaneous emission processes.

2.1.5. The Bragg structure

Figure 2.5 shows the phase difference δ of an electromagnetic wave incident under the angle α, which is reflected at two parallel interfaces with distance d, given by

$$\delta = 2 \cdot d \cdot \cos\alpha. \tag{2.22}$$

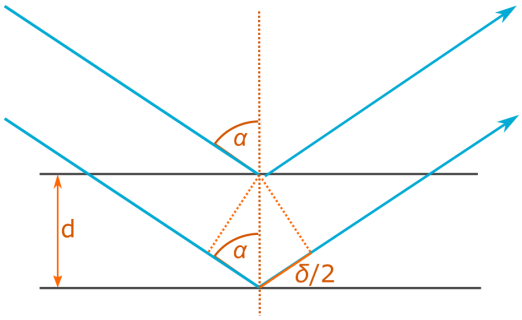

Figure 2.5.: Illustration of the Bragg condition. An incident electromagnetic wave under the angle α, refracted at two interfaces with distance d depicts the phase difference δ.

The two reflected waves show constructive interference, if the Bragg condition is fulfilled [41]

$$2 \cdot d \cdot \cos\alpha = m \cdot \lambda (m = 1, 2, 3, ...). \tag{2.23}$$

If there is a medium with refractive index n between the two interfaces, the angle α can be rewritten according to Snells law (equation 2.14) and the Bragg condition can be expressed by

$$2 \cdot d \cdot \cos\left[\arcsin\left(\frac{1}{n_{\text{eff}}}\sin\alpha\right)\right] = m \cdot \frac{\lambda_0}{n_{\text{eff}}}. \tag{2.24}$$

This can be expressed in a simpler geometric term to describe the angle dependent Bragg condition [45]

$$2 \cdot d \cdot \sqrt{(n_{\text{eff}}^2 - \sin^2\alpha)} = m \cdot \lambda_0, \tag{2.25}$$

with λ_0 being the vacuum wavelength and n_{eff} the effective refractive index (see equation 2.27).

The Bragg structure is perhaps the simplest realization of a photonic structure. It is built up by alternating layers of a low refractive index n_{low} and high refractive index n_{high}. Each layer features the same optical thickness, with a thickness d_i, such that the Bragg condition of equation 2.25 is fulfilled at $\alpha = 0°$ for a design wavelength λ_{design} [46]

$$d_i = \frac{\lambda_{\text{design}}}{4 \cdot n_i} \tag{2.26}$$

whereby i denotes the index 'low' or 'high'. Due to the reflection at all the interfaces of the Bragg structure, a very high reflectance up to one can be reached at and around the design wavelength λ_{design} (see Fig. 4.9). This spectral region of total reflectance is the photonic bandgap. In this context, the photonic bandgap might be easier to understand than in the exact derivation by localization of modes as described above. If total reflectance occurs at a particular wavelength, modes of this wavelength are not able to traverse within the Bragg structure in the direction of periodicity, which represents the 1D photonic bandgap.

Equation 2.25 describes the Bragg condition in dependence on the wavelength and the incident angle. The spectral region of the photonic bandgap therefore shifts for a varied incident angle. As the incident angle α increases, the photonic bandgap shifts to smaller

wavelength. This behaviour is investigated in simulation and experiment, presented in Fig. 6.9.

The effective refractive index of the Bragg structure is given by the average refractive index of the two components of the structure, weighted by their filling fraction within the unit cell a

$$n_{\text{eff}} = n_{\text{low}} \cdot \frac{d_{\text{low}}}{a} + n_{\text{high}} \cdot \frac{d_{\text{high}}}{a} = \frac{2n_{\text{low}}n_{\text{high}}}{n_{\text{low}} + n_{\text{high}}} \tag{2.27}$$

2.2. Upconversion

Upconversion (UC) describes anti-Stokes processes, where an emitted photon exceeds the excitation energy by 10 $k_B\mathcal{T}$ to 100 $k_B\mathcal{T}$ [13]. This energy cannot be provided by phonons and therefore the UC process relies on the absorption of two or more photons that excite an upconverter ion into a higher electronic state from which a photon with a higher energy can be emitted. The principle of UC has become a topic of interest in various fields of physics and materials chemistry over the past 50 years [13]. The theoretical foundation of the UC process has been studied in many journal publications, such as [13–16], and fundamental text books, such as [47, 48].

In this section, the UC process is elaborated including the details that are relevant for the upconverter material used in this work and the representation in the rate equation modeling framework.

2.2.1. Upconverting materials

Several materials, both organic and inorganic show UC properties. Among the inorganic, rare earth ions are the most studied [13]. In this introduction, I want to give an overview over the most important properties of the upconverter material Er^{3+} that is analyzed in this work.

Er^{3+} was the first ion that was investigated and showed UC properties [49]. Up to now it is still one of the most studied materials in the context of inorganic UC. Er^{3+} is a trivalent lanthanide ion with an outer electronic configuration of $5s^25p^64f^{11}$ [47]. The valence electrons that can undergo the optical transitions, are in the $4f^{11}$ shell. The outer lying, energetically lower $5s^2$ and $5p^6$ shell shield the optically active $4f^{11}$ shell. As a consequence, the energy levels of the electronic states of the free ion are very similar to those in a host crystal lattice [47]. The absorption and luminescence spectra therefore do not significantly change for different host crystal materials. Between the electronic states of the $4f^{11}$ shell, many optical transitions possible.

In a free Er^{3+} ion, selection rules apply, according to which electric dipole transitions are forbidden between states with the same parity and magnetic dipole transitions are forbidden between electronic states with different parity [38]. Electric dipole transitions are the ones of interest, as they are by a factor of 10^5 more probable than magnetic dipole transitions [48] (see section 2.2.2 "Electric dipole transition probability"). When an Er^{3+} ion is embedded in a host crystal, a mixing of parity for an electronic state can occur. This can be the case when the active ion occupies a cite of the host lattice where point symmetry is lacking and even when the ion occupies a cite of the host lattice that satisfies point symmetry [48]. As a result of the parity mixing for electronic states of an Er^{3+} ion in a crystal host lattice, electric dipole

transitions are possible even between electronic states with equal parity, which would be forbidden in a free ion [48]. Taking into account parity mixing effects, Judd [50] and Ofelt [51] reformulated the selection rules for electric dipole transitions between states of the $4f^n$ shell of trivalent lanthanides. For the case of Er^{3+}, these selection rules for the spin momentum S, the angular orbital momentum L and the total angular momentum J are

$$\begin{aligned} \Delta S &= 0 \\ \Delta L &\leq 6 \\ \Delta J &\leq 6. \end{aligned} \tag{2.28}$$

Consequently, the host lattice plays an important role in the UC efficiency. One of most promising host lattices for Er^{3+} is β-$NaYF_4$ [13]. β-$NaYF_4$ provides very similar lattice constants to Er^{3+}, such that a negligible lattice mismatch of only 0.13% and 0.25% occurs in the different dimensions of the hexagonal unit cell [52]. Additionally, the phonon energies in the host lattice β-$NaYF_4$ are very suitable for an efficient UC process: Suyver *et al.* found that in β-$NaYF_4$ phonon energies lie between 0.0347 eV to 0.0558 eV with an average phonon energy of 0.0446 eV [53]. Auzel *et al.* also calculated that the optimal phonon energy for a host material to gain efficient UC from infrared to blue lies at 0.0459 eV [54] (the probability of a multi-phonon relaxation process based on these numbers is discussed in section 2.2.2 "Multi-phonon relaxation").

In terms of UC efficiency, bulk upconverter materials are the best choice as they feature largely extended lattice structures to enable efficient energy transfer and few impurities to prevent quenching. However, the study of photonic structure enhanced UC requires for the upconverter to be in a form that can be embedded into the photonic structure. Consequently, the upconverter material has to be small to enable embedding it into layers with a thickness in the range of 100 nm or smaller. Both, a bulk and a micro-crystalline form of the upconverter material is not an option. Bulk materials are not flexible and in the range of mm to cm. Also micro-crystalline powders are in the range of 1 µm to 3 µm [55]. A direct implantation of the upconverter ion into a photonic structure leads to very low UC efficiencies due to severe quenching and non-optimized energy transfer processes because of random distances between the upconverter ions [56–58]. The most flexible and by now intensely improved option are upconverter core-shell nanoparticles. Synthesized upconverter nanoparticles allow for a controlled environment, a core that contains the chosen host lattice and upconverter dopant. A protective and well designed shell prevents surface quenching effects. Due to the flexibility of this approach it has gained major attention in research, starting from about 15 years ago. In 2004, Krämer *et al.* investigated systhesis routes for Er^{3+} doped upconverter materials in microcrystalline form [55]. Auzel *et al.* contributed an important review in 2004 [13]. Since then, a large number of works have been dedicated to core-shell upconverter nanocrystal material development, as published in [4, 5, 17–25], to name a few. This optimization includes the size of the active core and shell, co-doping materials for higher absorptance as well as embedding organic luminescent dyes, which spectrally contentrate a larger fraction of light into the absorption range of the upconverter.

In this work, I use upconverter nanoparticles of pure β-$NaYF_4$:Er^{3+} because this material configuration is analyzed in the REM. The upconverter nanoparticles are purpose built by Stefan Fischer as published in Fischer *et al.* [59]. The approach of my work is to validate the

modeling framework with respect of photonic effects on UC. Therefore, it is most important to match simulation and experiment as precisely as possible.

2.2.2. The upconversion process

Figure 2.6 depicts the seven first electronic states of the upconverter β-$NaYF_4$:Er^{3+}, in the notation $^{2S+1}L_J$. In this thesis, the UC process is studied for excitation at 1523 nm, which

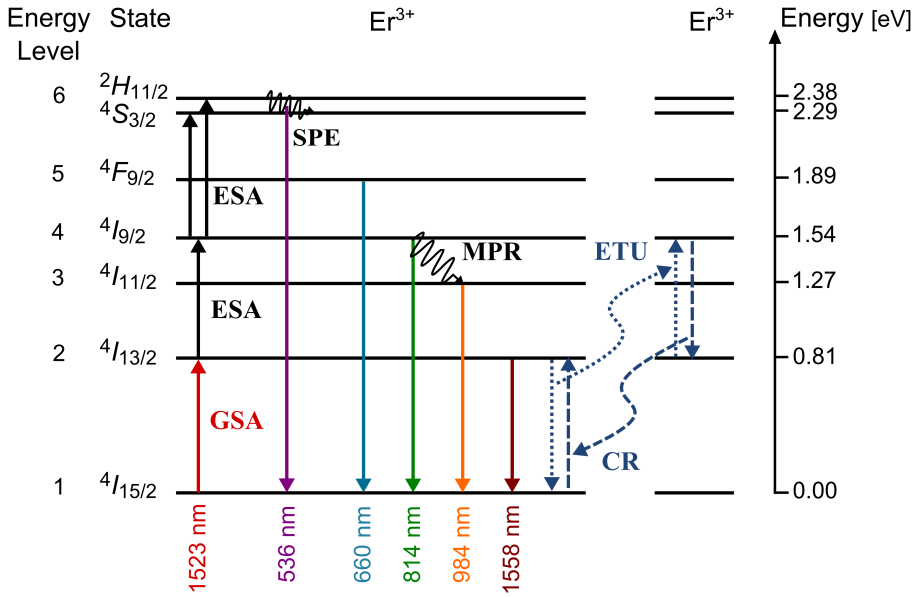

Figure 2.6.: Schematic of the first seven energy levels in β-$NaYF_4$:Er^{3+}, along with most important transitions for the UC process: ground- and excited state absorption (GSA, ESA), multi-phonon relaxation (MPR), energy transfer upconversion (ETU) (one exemplary ETU process shown) and spontaneous emission (SPE). For the considered excitation of the GSA at 1523 nm wavelength, the main UC emission lies at 984 nm. [34]

represents the ground state absorption. When two Er^{3+} ions in close proximity in space and time are in their first excited state, one ion can transfer its energy to the other, thereby the donor ion relaxes to the ground state, while the acceptor ion is lifted into a higher excited state. This process is called energy transfer upconversion. Due to the close proximity in energy of the $^4I_{9/2}$ and $^4I_{11/2}$ electronic states, there is a high probability that the acceptor ion non radiatively relaxes to the $^4I_{9/2}$ electronic state, transferring the excess energy to the crystal lattice in a multi photon relaxation process. The high probability of multi-phonon relaxation to take place significantly lowers the probability of the reverse process of cross relaxation to energy transfer upconversion. From the higher excited state $^4I_{9/2}$ spontaneous emission of a photon can take place.

There are other pathways to excite an ion into a higher state, such as second harmonic generation, that is the absorption of two photons within one ion, undergoing ground state absorption directly followed by excited state absorption. However, the efficiency of this process is about two orders of magnitude less than excited state absorption [13]. Other possibilities are yet orders of magnitude less efficient [13]. Energy transfer upconversion can take place in various ways between the energy levels, when the spacing in energy is

sufficiently similar. Consequently, spontaneous emission can take place from any state, as shown in Fig. 2.6.

In the following, the theoretical description of all components of the upconversion process is elaborated.

Radiative transitions

Einstein coefficients

In 1917, Albert Einstein introduced the so-called Einstein coefficients to describe the interaction between electromagnetic waves and atoms [60]. The following representation is mainly based on ref. [38]. An atom has discrete electronic energy states, between which a radiative transition can occur when a photonic state with an energy $\hbar\omega_{if}$ is available that matches the energy difference between the energy E_i of an initial and the energy E_f of a final electronic state

$$\hbar\omega_{if} = E_i - E_f. \tag{2.29}$$

Einstein differentiated between three possible transitions: *i*) The absorption of a photon, lifting the atom into a higher excited energy level. *ii*) A mode causing the stimulated emission of another photon into the same mode. Consequently, the direction, frequency and phase of the two photons are identical. *iii*) The spontaneous emission of a photon into a none-occupied mode and therefore into any direction.

The Einstein A-coefficient A_{if} gives the probability P_{SPE} per unit time t that an electron (or ion) in an initial state i will return spontaneously to a final state f by emitting a photon with energy $\hbar\omega_{if}$

$$P_{\mathsf{SPE}} = A_{if}. \tag{2.30}$$

The probability of the stimulated processes is described by the Einstein B-coefficients, B_{if}^{ABS} for absorption (ABS) and B_{if}^{STE} for stimulated emission (STE) processes. Additionally, as there are external photons involved, the spectral energy density $u(\omega_{if})$ also influences the probability

$$P_{\mathsf{ABS}} = B_{if}^{\mathsf{ABS}} \cdot u(\omega_{if}) \tag{2.31}$$

$$P_{\mathsf{STE}} = B_{if}^{\mathsf{STE}} \cdot u(\omega_{if}) \tag{2.32}$$

From the Ansatz of the system being in thermal equilibrium, a Boltzmann distribution to describe the population of the energy levels and Planck's law describing the thermal radiation field in equilibrium, the relation between the Einstein coefficients can be derived for a simple two-level system

$$g_2 \cdot B_{21}^{\mathsf{STE}} = g_1 \cdot B_{12}^{\mathsf{ABS}} \tag{2.33}$$

$$A_{21} = \frac{\hbar\omega^3}{\pi^2 c^3} \cdot B_{21}^{\mathsf{STE}} \tag{2.34}$$

Thereby, $c = {}^{c_0}/_{n}$ the speed of light in medium. The parameters g_1 and g_2 describe the degeneracies of energy level 1 and 2, which is defined via the total angular momentum quantum number $g_i = (2J_i + 1)$. Consequently, in case of $g_1 = g_2$, the Einstein B-coefficients are equal. A concise derivation can, for example, be found in ref. [38].

Electric dipole transition probability

Fermi's golden rule describes the transition rate $P_{\mathsf{if}}(\mathbf{r})$ between two energy eigenstates of a system when the transition involves decoherence, which is the case in a relaxation process as spontaneous emission [61, 62]

$$P_{if}(\mathbf{r}) = \frac{2\pi}{\hbar} |\langle \mathsf{f}|H|\mathsf{i}\rangle|^2 \rho(\mathbf{r}, \omega_{if}). \tag{2.35}$$

The transition matrix element describes the perturbation Hamiltonian H between the initial and final state $\langle i|$ and $\langle f|$, respectively. For an ion in a crystal lattice, the Hamiltonian H is composed of three parts, the Hamiltonian of the free ion, of the interaction with the crystal field and of the interaction of the electronic center with the electromagnetic field [48]. The sum of the Hamiltonians can be expressed in a series expansion and using suitable approximations, it can be expressed in terms of an electric dipole term, a magnetic dipole term and an electric quadrupole term. The relative ratio of these three terms is approximately $1 : 10^{-5} : 10^{-6}$ [48]. Therefore, optical transitions are often expressed only by the electric dipole term [48]. In this so called electric dipole approximation, the probability of a spontaneous emission process can be expressed in terms of the electric dipole transition element $|\mu_{if}|^2$. Based on equation 2.35, using another suitable set of assumptions, the spontaneous emission probability takes on the form [48]

$$P_{\mathsf{SPE}} = \frac{1}{4\pi\varepsilon_0} \cdot \frac{4n\omega_{if}^3}{3\hbar c^3} \cdot \left(\frac{\mathbf{E}_{\mathsf{loc}}}{\mathbf{E}}\right)^2 \cdot \frac{1}{g_i} \cdot |\mu_{if}|^2, \tag{2.36}$$

with the electronic states degeneracy of the initial state g_i. Additionally, the local field correction factor $(\mathbf{E}_{\mathsf{loc}}/\mathbf{E})^2$ for solids now enters the equation. It describes that radiation has a polarizing effect on neighboring atomic environments. Therefore differences in the local field and macroscopic field can occur. In crystals with a high local symmetry the field correction is often used in the form [48]

$$\left(\frac{\mathbf{E}_{\mathsf{loc}}}{\mathbf{E}}\right)^2 = \left(\frac{n^2+2}{3}\right)^2. \tag{2.37}$$

The advantage of this representation is that the needed parameters $|\mu_{if}|^2$ can be determined more precisely in experiment than the Einstein coefficients. While for a formulation via the Einstein coefficients, the exact absorption frequencies of all transitions would need to be known to calculate induced radiative processes. In a formulation via the $|\mu_{if}|^2$, it is sufficient to have precise knowledge of the absorption coefficient. Using Smakula's formula for electric dipole absorption [47], the $|\mu_{if}|^2$ for all emissions with the ground state as the final state can be determined from the absorption coefficient. Furthermore, applying the Judd-Ofelt theory [50, 51] all other required $|\mu_{if}|^2$ of transitions with final states not being the ground state can be determined. The experimental determination of all parameters $|\mu_{if}|^2$ is elaborated by Fischer [63].

Radiative transition probabilities

According to equation 2.36, the Einstein A-coefficients directly represent the probability of a spontaneous emission process. Consequently, the link between the Einstein A-coefficient

and $|\mu_{if}|^2$ can be expressed as

$$A_{if}^{\mathsf{SPE}} = \frac{1}{4\pi\varepsilon_0} \cdot \frac{4n\omega_{if}^3}{3\hbar c^3} \cdot \left(\frac{n^2+2}{3}\right)^2 \cdot \frac{1}{g_i} \cdot |\mu_{if}|^2. \tag{2.38}$$

Via equation 2.34 the Einstein B-coefficient of stimulated emission can be expressed in terms of $|\mu_{if}|^2$ in a generalized form

$$B_{if}^{\mathsf{STE}} = \frac{\pi}{3n^2\hbar^2\varepsilon_0} \cdot \left(\frac{n^2+2}{3}\right)^2 \cdot \frac{1}{g_i} \cdot |\mu_{if}|^2, \tag{2.39}$$

and also the Einstein B-coefficient for absorption processes including equation 2.33

$$B_{if}^{\mathsf{ABS}} = \frac{\pi}{3n^2\hbar^2\varepsilon_0} \cdot \left(\frac{n^2+2}{3}\right)^2 \cdot \frac{1}{g_i} \cdot |\mu_{if}|^2. \tag{2.40}$$

Multi-phonon relaxation

Multi-phonon relaxation describes the relaxation of an ion into a lower electronic state, whereby the excess energy is transferred to the crystal lattice as phonons. The probability of a multi-phonon relaxation process scales with the number of involved phonons to bridge the energy gap ΔE_{if} between the respective initial and final electronic state. The host crystal properties also play a significant role. According to the energy gap law formulated by Weber [64, 65] and Riseberg [66], the probability of a multi-phonon relaxation process can be expressed as

$$P_{\mathsf{MPR}} = C_{\mathsf{MPR}} \cdot e^{-\kappa \Delta E_{if}}. \tag{2.41}$$

Thereby, C_{MPR} and κ are empirical material specific parameters. Also material specific is the effective phonon energy $E_{\mathsf{phonon,eff}}$, which defines how many phonons N_{phonon} are involved to bridge the energy gap with $N_{\mathsf{phonon}} = \Delta E_{if}/E_{\mathsf{phonon,eff}}$. Shalav *et al.* found that for small energy gaps, multi-phonon relaxation is the dominant process if the number of involved phonons is $N_{\mathsf{phonon}} < 6$ [67]. The energy gap between the $^4I_{9/2}$ and $^4I_{11/2}$ electronic states corresponds to 0.27 eV (see Fig. 2.6). Therefore, the average phonon energy of 0.0446 eV in β-$NaYF_4$ [53] (discussed in section 2.2.1) is just high enough to provide a large probability of the needed multi-phonon relaxation $^4I_{9/2} \rightarrow^4 I_{11/2}$, while at the same time providing a very low probability of unwanted phonon assisted processes for the larger energy gaps between other electronic states.

Energy transfer processes

In the context of rare-earth ions, energy transfer upconversion is the most probable process to reach a higher electronic state [13]. Förster [68] and Dexter [69] first theoretically described the process for multipolar coupling. The probability of an energy transfer process to take place can be described via the interaction Hamiltonian $\hat{H}_{\mathsf{int}}$ between a donor D upconverter ion with an initial and final state i and f and an acceptor ion A with an initial and final state i' and f' [48]

$$P_{\mathsf{ET},dd}^{if,i'f'} = \frac{2\pi}{\hbar} \cdot \left|\langle D_f, A_{f'}| \, \hat{H}_{\mathsf{int}} \, |D_i, A_{i'}\rangle\right|^2 \int g_{if}^{em}(E) g_{i'f'}^{abs}(E) dE. \tag{2.42}$$

Another important aspect are the spectral line shape functions of the donor emission g_D^{em} and the acceptor absorption g_A^{abs}. If the overlap integral of g_D^{em} and g_A^{abs} is non-zero, an ET process can take place, increasing in probability for an increasing overlap. Again, equation 2.42 can be expressed in terms of the electric dipole interaction, as the dominant term in a series expansion. The probability for an energy transfer process then reads [48]

$$P_{\mathsf{ET},dd}^{if,i'f'} = \frac{4\pi}{3\hbar} \cdot \left(\frac{1}{4\pi\varepsilon_0 n^2}\right)^2 \cdot \frac{1}{d^6} \cdot |\mu_{if}|^2 |\mu_{i'f'}|^2 \int g_{if}^{em}(E) g_{i'f'}^{abs}(E) dE \tag{2.43}$$

A more detailed description can be found in ref. [63]. The line shape functions of absorption and emission are not the same. Consequently, the probability of energy transfer UC can be significantly different from the probability of the reverse process cross relaxation. The distance d between the two ions undergoing an energy transfer process is crucial, as the probability has been found to decay with the sixth power of d.

The upconversion process shows a non-linear dependence on the incident irradiance. Theoretically, this was first described by Pollnau *et al.* [70] and later extended by Soyver *et al.* [71]. who investigated the power dependence of UC for different irradiance scenarios and excitation routes. Within the low power limit, they described the relation between the occupation N_j of the j-th energy level and the irradiance I_{in} by the power law [70]

$$N_j(I_{\mathsf{in}}) \propto I_{\mathsf{in}}^j. \tag{2.44}$$

Thereby, the exponent j can be seen as the number of photons that are required to populate the j-th energy level. In the high power limit, this non-linear dependence merges into a linear dependence [70]

$$N_j(I_{\mathsf{in}}) \propto I_{\mathsf{in}}. \tag{2.45}$$

These limits are not precisely valid in a real upconverter, with many different energy levels between which numerous processes are possible, but only in an idealized system. Also the exact irradiance at which the low power limit merges into the high power limit is strongly material dependent and occurs at a different irradiance for each energy level. The linear relation of the high power limit occurs when necessary absorption to populate the j-th energy level saturates and the population of higher energy levels becomes more probable (compare to Fig. 5.9a).

2.2.3. Upconversion for photovoltaics

The efficiency of a silicon solar cell is limited to 30% mainly due to spectral losses [72]. Photons that are energetically below the bandgap of silicon, the so called sub-bandgap losses, make up 20% of the energy of the solar spectrum [73]. Making this large spectral range accessible for charge generation carries high potential. Figure 2.7 shows how an upconverter can be placed behind the solar cell, such that the transmitted photons are absorbed, converted to photons with a higher energy that is above the silicon bandgap and emitted back to the solar cell. Thereby, the solar cell and upconverter only need to be matched in their optical properties, which enables a separate optimization in terms of electrical properties of both devices.

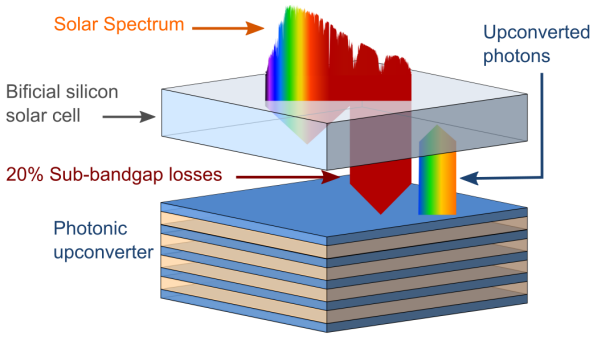

Figure 2.7.: Schematics of the photonic upconverter placed behind a bificial silicon solar cell. The sub-bandgap losses that are transmitted through a silicon solar cell can, in the photonic upconverter, be converted to photons above the silicon bandgap and subsequently contribute to charge generation. (Figure adapted from [26])

Trupke *et al.* first presented a comprehensive theoretical study of the potential efficiency increase of a silicon solar cell due to upconversion, first under black-body radiation [74]. In 2006 Trupke *et al.* included illumination with the standard solar spectrum air mass 1.5 global (AM1.5G), and reported a maximum silicon solar cell efficiency of 40.2% for an ideal upconverter transforming the sub-bandgap losses into usable photons above the bandgap of silicon [75]. In 2012 Johnson *et al.* further extended the model to also take into account the real absorption of silicon. They reported a possible efficiency increase of a silicon solar cell to 38.6% in an ideal upconverter solar cell device [27]. Recently in 2021, Richards *et al.* determined a 6% possible absolute increase in silicon solar cell efficiency by the use of an Er^{3+} upconverter. This estimate includes that the complete absorption range between 1400 nm and 1650 nm within the AM1.5G solar spectrum is absorbed. Further, the UC process is taken to function at 50% quantum efficiency, thus creating one higher energy photon out of each two absorbed photons (neglecting any reverse processes). The collection efficiency of the bifacial solar cell is taken to feature no optical losses with an external quantum efficiency of unity.

Among the first to experimentally demonstrate a solar cell efficiency increase due to UC were Gibart *et al.* in 1996 [76]. In 2007, Strümpel *et al.* published an overview of available upconverter materials for silicon solar cell enhancement, identifying Er^{3+} as the most suitable upconverter [77]. Er^{3+} provides a number of close to equidistant energy levels, particularly ${}^4I_{15/2} \rightarrow {}^4I_{13/2}$ and ${}^4I_{13/2} \rightarrow {}^4I_{9/2}$. This allows for the excitation of ions into higher electronic states with a high probability and little loss of energy. The close vicinity of the energy levels ${}^4I_{9/2}$ and ${}^4I_{11/2}$ makes multi-phonon relaxation the dominant process. Consequently, a non-radiative relaxation into the ${}^4I_{11/2}$ state is very probable, which prevents self-quenching in form of cross relaxation. The ground state absorption lies below the silicon bandgap at 1523 nm and subsequent UC emission around 984 nm (${}^4I_{11/2} \rightarrow {}^4I_{15/2}$), just above the bandgap of silicon. Shalav and Richards *et al.* experimentally demonstrated a silicon solar cell efficiency increase due to Er^{3+} upconversion in 2005 [78] and 2007 [79]. By now, experimental realizations of upconverter solar cell devices have been the focus of a large number of works, as discussed in numerous review articles [4–9]. The highest reported efficiency increase was published by Fischer *et al.* in 2015. They realized a monocrystalline

BaY_2F_8:30%Er^{3+} upconverter, coupled to a bifacial silicon solar cell. The upconverter itself depicted a high external UC quantum yield of 9.5% under illumination at 1520 nm and 4740 W m^{-2}. Measurements under a sun simulator at a concentration of 95 suns were reported to yield an 0.55% relative increase of the short-circuit current [80].

The main challenge to gain high efficiency increases in upconverter solar cell devices is the low UC efficiency in the low irradiance range, which is the range of interest for photovoltaic applications.

2.2.4. Increasing upconversion performance via photonic structure effects

There are different approaches to increase upconversion efficiency in the low irradiance regime: *i*) Geometric concentrator optics within a module can be designed to increase the irradiance incident on the upconverter [81]. *ii*) Spectral concentration can be applied, e.g. by implementing downshifting materials that concentrate a larger spectral range of the sub-bandgap region into the absorption range of the upconverter [82–84]. *iii*) Plasmonic field enhancement effects in the vicinity of metal nanoparticles can be utilized to gain very high local electric field enhancement effects, which in a small volume can drastically increase the absorption and therefore UC efficiency. However, at the metal nanoparticles, severe quenching effects occur [85, 86]. *iv*) Photonic structure effects can be utilized to reach local electric field enhancements over a larger area and additionally the modified local density of optical states can be used to modify spontaneous emission probabilities. The latter is the approach that is investigated in this work. Photonic structures alter the properties of light in two essential ways (see section 2.1), illustrated in Fig. 2.8. As a result, the properties of an embedded upconverter can be tuned and significantly enhanced.

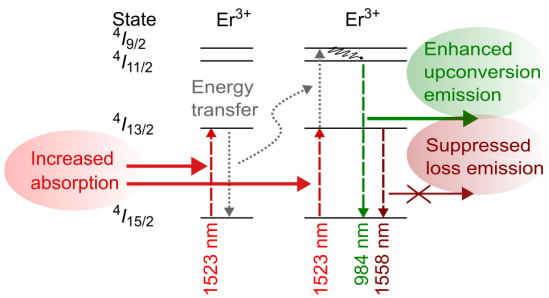

Figure 2.8.: Simplified scheme of the energy transfer upconversion process in the upconverter Er^{3+}. The photonic effect of a locally increased optical energy density acts on all stimulated processes. The photonic effect of the modified local density of optical states alters the probability of spontaneous emission processes. Thus, with a tuned photonic structure design, absorption can be increased and the wanted upconversion emission enhanced. (Figure adapted from [26])

Modified optical energy density altering stimulated radiative processes

The optical energy density is locally enhanced within or at the surface of a photonic structure. How this energy density enhancement influences the UC process can be understood from the relation of the Einstein coefficients. In equations 2.31 and 2.32, the probability of a stimulated process is linearly proportional to the energy density. Therefore, a change in the energy density alters the probability of all stimulated processes. The main aspect is that absorption, particularly the ground state absorption, are linearly enhanced by an energy density enhancement. This, in turn, non-linearly increases the probability of an energy transfer UC process to take place, as there are two excited upconverter ions needed in immediate vicinity in space and time. Consequently also the UC emission is non-linearly increased.

Modified local density of optical states altering spontaneous emission probabilites

Within a photonic structure, a photonic band structure forms and the local density of optical states (LDOS) is modified. Again, the effect on the UC process can be understood from the relation of the Einstein coefficients. In the case of equal degeneracies $g_1 = g_2$, the Einstein B-coefficients in equation 2.33 are equal. In equation 2.34, the term $\omega^3/\pi^2 c^3$ represents the density of optical states (DOS) $\rho(\omega)$. A change in the DOS cannot influence the correlated Einstein B-coefficients. Consequently, a modified DOS has an impact on the Einstein A-coefficient and therefore only on spontaneous emission processes. As described by Fermi's golden rule, it is the LDOS that has to be taken into account, as the exact LDOS at each emitter position is decisive for the probability of a spontaneous emission processes. Consequently, with a tuned photonic structure design, the modified LDOS has the potential to increase the probability of the wanted UC emission and /or to decrease the probability of loss emissions, such as the direct de-excitation of the first excited electronic state.

Photonic effects on energy transfer processes

It has been discussed in the past, whether Förster energy transfer processes are also influenced by changes in the local photonic environment [87–89]. As already stated by [87, 90], I follow the path that the photonic environment does not influence energy transfer processes. Our project partners Spallek and Wellens also showed the latter theoretically in an unpublished work [91].

2.2.5. State of the art of photonic structure enhanced upconversion

The field of photonic structure enhanced UC has been extensively investigated for many different target applications. Each target application has different requirements on the research questions, properties of the photonic structure and upconverter material and investigated parameters. Therefore, a large variety of photonic structures and upconverter materials, both organic and inorganic, have been investigated. Plasmonic structures for UC enhancement are yet another promising research branch. Due to the many different research

communities involved, targeting different applications, and the varying requirements, there is no standardized way of an analysis of a photonic upconverter. The missing standardization makes a direct comparison or ranking of photonic upconverters from literature reports impossible. Yet, perhaps the most important aspect for my work, is that a knowledge-based approach of optimizing the photonic structure design, to maximize UC enhancement for a specific application, is missing in the vast majority of literature reports.

In this section, I want to give an overview over a selection of literature reports that are high quality in both, the reported experiments and in the way of scientific reporting, including experimental details. Furthermore, the chosen literature reports cover the most important types of photonic structures that have been investigated. To narrow it down, I do not include literature on organic upconverter materials and also no literature on plasmonic structures.

Tables 2.1 to 2.4 give an overview over the selected reports to discuss the state of the art, the variety of photonic upconverters and reported UC photoluminescence (UCPL) enhancement factors. The tables include a list of parameters that are highly important to consider when trying to compare different reported UCPL enhancement factors. Furthermore, they include the simulation methods that have been applied for optimizing the photonic structure design and to understand the experimental results. In the following, the summary tables are discussed in detail.

Photonic structure

The photonic structures, which have been investigated for UC enhancement throughout literature are 1D, 2D or 3D and all have their benefits and drawbacks. The investigated 3D photonic structures are mostly opal photonic crystals, as reported by Shi *et al.* [92], Niu *et al.* [93] and Yin *et al.* [94] (Table 2.1) or inverse opal photonic crystals, as analyzed by Xu *et al.* [95] and Zhang *et al.* [96](Table 2.2). 2D photonic structures that are being analyzed for UC enhancement are mostly metasurface structures, as reported by Wang *et al.* [97], Würth *et al.* [98] and Mao *et al.* [99] (Tables 2.2 and 2.3). Interesting 1D Photonic structures are of three types, waveguide structures, as investigated by Lin *et al.* [100], cavitiy designs, as reported by Rojas-Hernandez *et al.* [101] or multilayer stacks, as analyzed by Johnson *et al.* [58] and in my own work [26]. To be able to judge the effect that a particular type of photonic structure has on the UCPL, it is beneficial to compare a number of structures that either have different designs or have been fabricated separately. Many reports only investigate one single design and structure [58, 99, 100], others analyze 2-5 different structures [92–96,98]. Investigating more designs is an exception, Rojas-Hernandez *et al.* investigated 9 structures [101] and Wang *et al.* $\sim$25 structures [97]. Therefore, in my work, I put an emphasis on analyzing a large number of 40 different designs that are chosen to cover the expected maximum photonic effect on UCPL, the regions around this peak enhancement and also the region of no expected enhancement.

Upconverter material

The upconverter material that is used in a photonic upconverter has a large impact on the measured enhancement factors. If the upconverter on its own in a reference sample already

depicts a high efficiency, the measured enhancement factor will be considerably lower than for an upconverter material that has a very low efficiency.

As mentioned before, the tables only include reports on rare-earth upconverter materials. However, there is still a large deviation in UC efficiency, depending on the exact combination of materials and especially the form of the upconverter material. A bulk upconverter material has the highest efficiency, however, it is not flexible in shape and therefore cannot be used in micro- or nano-scale photonic structures. Therefore, the development of efficient upconverter nanoparticles (UCNPs) has been in focus of research and has led to major improvements [4, 5, 17–25]. Usually, the UCNPs are built up of an active core, surrounded by one or more inert shells that prevent quenching at the surface. The most efficient host crystal, which is used almost exclusively throughout literature is β-$NaYF_4$. The active upconverter material is mostly Er^{3+}, often co-doped with Yb^{3+} or Tm^{3+} as a more efficient sensitizer when exciting at 980 nm (see section 2.2.1 for details). However, Yb^{3+} or Tm^{3+} only are also used as active upconverter material [92–94, 102]. My own work is done with β-$NaYF_4$:Er^{3+}, slightly less efficient than including a co-doping, because the modeling environment, the rate equation model, is currently set up for this material and the main focus of my work was to reach a exact as possible comparison of simulation and experiment [26]. It is also possible, to dope other materials with the upconverter, Rojas-Hernandez *et al.* use Tm^{3+}/Yb^{3+} co-doped aluminosilicate glass [101] and Johnson *et al.* Er^{3+} doped porous silicon [58]. However, the UC efficiency is mostly very low for these directly doped compositions because of quenching effects.

Not only the form of upconverter material is important to consider but also the amount of upconverter material that can be embedded into or onto a particular photonic structure within the range of enhancement effects. In many applications, the absolute UCPL will be of major interest, therefore, the amount of upconverter material is a highly relevant factor. Opal photonic crystals depict a high electric field enhancement at the surface. Therefore, thin layers of UCNPs are deposited on top of the opal [92–94]. This, however, limits the amount of upconverter material for which one can expect a photonic effect to layers of about 200 nm [93] or a maximum of 1 µm [92]. A design using inverse opal photonic crystals allows for embedding the UCNPs in the voids of the inverse opal structure. Thus, the amount of upconverter material is not limited by this design. Most 2D metasurfaces also exploit surface effects, again with UCNP layer thicknesses ranging from $\sim$100 nm [98] to 1.3 µm [97]. Another option is to embed the UCNPs in the voids of the surface structure, with a height of 300 nm [99]. In the case of 1D photonic structures, the waveguide structure exploits surface effects in immediate vicinity of the surface, with a UCNP layer thickness of 200 nm [102]. A benefit of multilayer stacks is that the amount of upconverter material is not limited, but can be increased by adding more layers to the stack, which, in turn increases the photonic effects. For stacks with few layers, as in my work, the summed up thickness of upconverter layers is 1.2 µm [26], while Johnson *et al.* report a 60 layer stack with a total upconverting layers thickness of 15 µm [58].

It is therefore a trade-off between the enhancement factors that can be reached in a particular structure and the amount of upconverter material that can be used in the photonic upconverter.

Reference structure

The choice of reference structure is, of course, crucial for the resulting UCPL enhancement factors. While the choice of reference was very diverse in literature from over ten years ago, by now a standard developed more and more: the reference is a separate sample consisting of the upconverter material, fabricated the same way and in the same shape as in the photonic upconverter. Thereby, the reference is mostly either fabricated to feature the same amount of upconverting material as in the photonic upconverter [26, 92, 93, 97, 101], or scaled to the same unit volume [99]. These two approached yield a comparable result. Other approaches do not guarantee a comparability, like with the same approach as above but not controlling the thickness of the reference sample (or the control is not reported) [94–96]. Yet others define their reference as the unstructured part at the edges of the photonic upconverter sample [98, 102] or define the enhancement factor relative to the lowest UCPL signal measured at another excitation angle [58].

Within each literature report, it is important that the reference is clearly defined. For comparability of reached enhancement factors throughout literature, it would be a large benefit if the community agreed on a common reference.

Excitation and detection parameters

The excitation parameters play a significant role in the UC dynamics, particularly under the influence of photonic structure effects. The irradiance that is applied in a measurement is decisive because the UC process is non-linearly dependent on the irradiance. Therefore, both, the efficiency of the pure upconverter material and based on that the enhancement factor due to a photonic surrounding will be given by the applied irradiance. However, still now in high quality literature reports, the parameter of the incident irradiance is often not reported but only the incident power [58, 92, 94, 96, 101]. The irradiances applied in experiments range from 10^6 W cm^{-2} [95] to medium irradiances of 4 W cm^{-2} [93] and down to almost solar irradiance in my work (see section 6.6 and 6.5). The strong dependence of the measured UCPL enhancement factor can be seen in the rare reports in which a scan of the incident irradiance is performed, as done by Würt *et al.* [98] and, in a particularly large range, by Mao *et al.* [99].

The excitation wavelength also needs to be linked to the target application. The vast majority of studies investigate excitation at 980 nm wavelength, which is efficient with an Er^{3+} and Yb^{3+} or Tm^{3+} co-doped upconverter. For an application in silicon photovoltaics, however, the excitation at 1523 nm and subsequent UC emission at 980 nm, right above the bandgap of silicon, is of interest. Johnson *et al.* also investigate this transition for an application in photovoltaics [58]. In my work, I additionally scan a the core domain of the absorption spectrum of the upconverter material for the ${}^4I_{15/2} \rightarrow {}^4I_{13/2}$ transition from 1500 nm to 1560 nm to gain the best possible comparison to the broad-band excitation sunlight [26].

The angle of excitation and detection is often not reported at all [92, 96, 101] and many studies simply excite at normal incidence and detect at one distinct angle [93, 95, 97, 99]. However, there are reports in which the angle dependence is considered in experiment for the incident angle [26, 58, 94], or precisely varying both, the excitation and detection angle, as done by Würt *et al.* [98] and Lin *et al.* [100]. The outcome, as also known from

simulations, is that photonic structures are highly angle dependent, both in the in-coupling and out-coupling of light. Therefore, the detected UCPL enhancement factors are also highly angle dependent.

It is therefore highly important to consider all excitation and detection parameters in an experiment with respect to the target application. To sum it up, the incident irradiance and excitation wavelength range, as well as the excitation and detection angle range all play a significant role in the analysis of a photonic upconverter and need to be chosen such that the parameter ranges are covered that are important for a target application.

Upconversion enhancement factor

Almost all studies of photonic structure enhanced UC aim at presenting one high enhancement factor. However, as described in the sections above, there are a large number of parameters that largely influence this factor. It is therefore not possibly to simply judge a type of photonic structure by a reported enhancement factor or compare to other literature reports. Having the discussions above in mind, I do want to draw a comparison of reported UCPL enhancement factors at this point. For the three opal photonic structures, similar UCPL enhancement factors of $\sim$30 are reported for the 450 nm to 800 nm emission [92, 92–94] (table 2.1). For the inverse opal photonic structures, the reported UCPL enhancement factors differ by an order of magnitude from 43-fold [95] to 4.6-fold [96], for the 300 nm to 800 nm UC emission (2.2). Between the different types of photonic structures, 2D metasurfaces clearly yield the highest UC enhancement factors in the three listed, very careful reports. Wang *et al.* report a 50 and 130-fold UCPL enhancement of the green and red UC emission, respectively [97] and Mao *et al.* report 130 and 340-fold enhancement of the green and red emission, respectively [99]. Würt *et al.* report an up to 1000-fold enhancement of both green and red UC emission [98]. Additionally, these are probably the most comparable three reports, as the experimental details, especially the incident irradiance, cover a similar range. Würt *et al.* find a spectral range of roughly $\pm$20 nm and an excitation angle range of about $\pm5^\circ$ in which the enhancement factor occurs [98] (defined as the enhancement dropping to about half of the maximum). An extreme example of a high enhancement is reported by Lin *et al.* for a grating waveguide structure. However, this enhancement only occurs in a very narrow angle range: while the maximum UCPL enhancement of 10 for the 450 nm to 650 nm emission occurs at 31.5° incidence, it drops by three orders of magnitude within 0.75° [100]. Depending on the target application, this can be a major drawback, like for photovoltaics, or a benefit, possibly for anticounterfeiting. The UCPL enhancement factors in multilayer stack designs differ quite largely. Rojas-Hernandez *et al.* report a 25-fold enhancement of the green emission under 980 nm excitation by a 21-layer stack cavity design [101], while Johnson *et al.* report a five and 26-fold enhancement of the 980 nm and green UC emission, respectively, under 1550 nm excitation [58]. In my own work, I found a 4-fold enhancement of the 980 nm emission under 1523 nm excitation for a 9 layer Bragg structure [26]. However, in the first two examples, the upconverter layer is made of doped aluminosilicate glass [101] and porous silicon [58], which can be expected to have a much lower UC quantum yield due to quenching effects, which results in higher UC enhancement factors due to photonic structure effects. Additionally, the regarded transitions and choice of reference differs, so comparability is not given. However, the approximate

range of enhancement factors is evident. In my work, I put an emphasis on analyzing the spectral and angle range, in which the enhancement factors occur, as this is highly important for a target application in photovoltaics. The investigated Bragg structure with 9 layers allows enhancing UC in a large angle and spectral range of about 30° and 60 nm, respectively [26].

In conclusion, one can say that all parameters of the upconverter material, the photonic structure, reference and experimental setup largely influence the measured UCPL enhancement factors and it is important to consider all when judging the efficiency of a particular photonic structure for a target application.

Simulation

Photonic structures, in general, depict a high spectral selectivity. The exact design of the structure determines the spectral position of the photonic band structure and therewith the spectral position of the appearing effects. That makes a careful design of the photonic structure for a particular upconverter and application very important. However, in many literature reports, the exact design is not within the focus of the work. Often, the position of the photonic bandgap is simulated and used as an orientation for the photonic structure design, as in the listed reports for the opal and inverse opal photonic crystals [92–94, 96]. A detailed design via the simulated reflectance or transmittance characteristics, including a comparison to the measured enhancement factors is performed by Rojas-Hernandez *et al.* for the microcavity design [101] and by Johnson *et al.* for the multilayer stack [58]. The reflectance or transmittance gives evidence of the position of the photonic bandgap and it is known that enhancement factors occur at the band edges, the width and exact position of these enhancement factors is not covered. A simulation of the electric field intensity (or optical energy density as it is called in my work) is the next step, as the exact spectral position of electric field enhancements is known from it. This simulation, and based on it a design optimization and comparison to the spectral position of measured UCPL enhancement factors, is only rarely included in literature. The three listed reports of the 2D-metasurfaces [97–99] and the 1D-waveguide structure [102] all include a comprehensive analysis of the electric field intensity. This largely improves the theoretical understanding of the appearing effects.

To cover all major effects in simulation, at least three aspects need to be included: optical energy density enhancement, the modified local density of optical states and the dynamics of the UC process. Apart from the work of our team, the approach of implementing the effects of an optically active surrounding on UC dynamics has been used for plasmonic effects on UC in a simulation based approach. Shao *et al.* also investigated the effects of an inverse opal photonic crystal, coupled with plasmonic resonances on embedded UCNPs and used a simplified rate equation modeling approach [103]. Based on a cooperation and the rate equation model developed in our group, a research group from Aarhus university derived a simplified rate equation model coupled with plasmonic effects and investigated the effects with respect to the nanoparticle shape in a work by Eriksen *et al.* [104]. Their model has since been used to design experiments [10]. A research group from the university of Boulder (USA), developed a simplified rate equation modeling framework for the UC dynamics under the influence of plasmonic effects [85, 105]. Recently, they adapted this model to additionally include photonic effects on UC. The energy density enhancement is taken into account as an

absorption enhancement factor, while the local density of optical states is considered via the Purcell factor [99]. Additionally, the model considers quenching effects of heat dissipation on the metal nanoparticles [99]. In the work by Mao *et al.* their model was used to design a photonic metasurface structure for UC enhancement. They measured one sample design, scanning through a large range of the incident irradiances from 1W cm^{-2} to 10^4 W cm^{-2} [99] (Table 2.3).

Because of the sensitivity of the UC process with respect to internal parameters and in a photonic or plasmonic surrounding, our research group at Fraunhofer ISE, as the pioneers developed a modeling approach. First a rate equation framework was established for modeling the UC dynamics in homogeneous media [28]. Later, the environment of a plasmonic structure was added to the model [29,30] and based on the plasmonic interactions, the photonic environment was integrated [31, 32] and the final version [34] was published open access on the Fraunhofer platform Fordatis [35]. My final publication Hofmann *et al.* 2021 builds up on this work: a comprehensive comparison of simulation and experiment of photonic structure enhanced UC is drawn in large-area scans of experimental parameters and large statistics in measurements to compare to different parameter combinations in simulation. Therewith, a validated modeling tool is provided to the research community for a knowledge based optimization process of photonic upconverters [26].

Coupled plasmonic and photonic effects for upconversion enhancement

Plasmonic resonances of metal nanostructures can produce very high enhancements of the optical near field within a very small volume. If an upconverter is positioned within this near field, it experiences an extremely high absorption enhancement. However, the drawback of these structures is that the high quenching rate, that is, the transfer of energy from the upconverter to the metal, where the energy is dissipated as heat. The coupling of plasmonic and photonic effects combines the possibility to reach very high electric field enhancements in the near field by plasmonic resonances and simultaneously the large area, but lower photonic enhancement effects. To name a few important works, the coupled effects where investigated in refs. [103, 106–112].

From their research on both plasmonic and photonic structures for UC enhancement, Mao *et al.* conclude that the very high optical near field enhancement due to plasmonic resonances is offset partially by the inevitable luminescence quenching to the metal. In purely dielectric photonic structures, the optical field enhancement is not as high, however, on the other hand, there is no significant luminescence quenching. An additional advantage of photonic structures is that the optical enhancement occurs over a large area. Plasmonic resonances cause extreme optical hotspots within a very small volume, which leads to a very high peak enhancement. However, achieving an enhancement over a large area is difficult with purely plasmonic structures. Therefore, Mao *et al.* conclude that photonic structures, as opposed to plasmonic structures, provide an excellent alternative that is suitable for other applications that may require a larger active area, like lighting, displays or sensors, and, what I can add from my own research, photovoltaics.

		3D - opal PC	3D - opal PC	3D - opal PC
Publication		Y. Shi *et al.* (2019) [92]	W. B. Niu *et al.* (2014) [93]	Z. Yin *et al.* (2013) [94]
Photonic structure	**Photonic Structure**	SiO_2 opal	3D PC of monodisperse carboxylate-modified polystyrene spheres	PMMA opal PC
	Number of designs investigated	2	3	5
UC material	**UC material**	β-$NaYF_4$:Yb/Er and β-$NaYF_4$:Yb/Tm	Yb/Er and Yb/Tm co-doped β-$NaYF_4$	β-$NaYF_4$:Yb^{3+}, Tm^{3+}/Er^{3+}
	Form of UC material	UCNPs	UCNPs	UCNPs
	Amount of UC material in structure	$\sim$1 µm thin layer on top of opal PC	$\sim$200 nm thin layer on top of opal PC	One thin layer in spaces around opal colloids on top layer, thickness not reported
	Limited by PC design	Yes	Yes	Yes
Reference	**Reference structure**	Thin UC nanoparticle film on glass substrate	Thin UC nanoparticle film on glass substrate	Thin UC nanoparticle film on glass substrate
Excitation	**Irradiance**	-	4 W cm^{-2}	-
	Power	400 mW	-	5 mW
	Wavelength	980 nm	980 nm	980 nm
	Angle (to surface normal)	-	0°	65° - 90° (0° - 25° off surface plane)
Detection	**Angle (to surface normal)**	-	-	180° transmission
UCPL enhancement	**Wavelength/emission**	450 nm / 541 nm	540 nm / 650 nm	"Overall UC" of emissions between 400 nm and 800 nm
	Enhancement factor	34 /23	30 / 30	30
	Spectral width	-	-	-
	Angle width	-	-	-
Simulation	**R/T for PBG**	Yes	Yes	Yes
	Electric field intensity	-	-	-
	Local density of optical states	-	-	-
	Upconversion dynamics	-	-	-

Table 2.1.: Literature overview of upconversion photoluminescence (UCPL) enhancement of embedded upconverter nanoparticles (UCNPs) in opal photonic crystal (PC) structures. "R/T for PBG" abbreviates "Reflectance/transmittance to determine position of bandgap" . [113]

		3D - inverse opal PC	3D - inverse opal PC	2D - metasurface
Publication		S. Xu *et al.* (2014) [95]	F. Zhang *et al.* (2010) [96]	H. Wang *et al.* (2016) [97]
Photonic structure	**Photonic Structure**	TiO_2 inverse opal PCs	polystyrene inverse opal PCs	anodic aluminum oxides two-dimensional photonic crystal
	Number of designs investigated	5	3	∼25
UC material	**UC material**	β-$NaYF_4$:Yb^{3+},Tm^{3+}(Er^{3+})	β-$NaYF_4$:Yb^{3+}/Er^{3+}	β-$NaYF_4$:Yb^{3+} Er^{3+}
	Form of UC material	UCNPs	UCNPs	UCNPs
	Amount of UC material in structure	UCNPs are embedded in the voids of TiO_2 IOPCs, thickness not reported	Inside the voids of the IOPC 1 cm path-length sample investigated in cuvette	1.3 µm thin film on top of 2D PC
	Limited by PC design	no	no	yes
Reference	**Reference structure**	Thin UC nanoparticle film on glass substrate	UCNPs in cuvette	Thin UC nanoparticle film on glass substrate
Excitation	**Irradiance**	$4.8{\cdot}10^6$ W cm^{-2} (48 mW mm^{-2})	-	33 W cm^{-2}
	Power	0.1 - 0.9 W	800 mW	-
	Wavelength	980 nm	978 nm	980 nm
	Angle (to surface normal)	0°	-	0°
Detection	**Angle (to surface normal)**	180° transmission	-	∼45°
UCPL enhancement	**Wavelength/emission**	"Overall UC" of emissions between 300 nm and 800 nm	515 nm, 565 nm, 640 nm, 675 nm	"Overall UC" of emissions of red and green / red /green
	Enhancement factor	43 (decreasing for higher power)	4.6 (same for each emission reported)	65 / 130 / 50
	Spectral width	-	-	-
	Angle width	-	-	-
Simulation	**R/T for PBG**	-	Yes	Yes
	Electric field intensity	-	-	Yes
	Local density of optical states	-	-	-
	Upconversion dynamics	-	-	-

Table 2.2.: Literature overview of upconversion photoluminescence (UCPL) enhancement of embedded upconverter nanoparticles (UCNPs) in inverse opal photonic crystal (PC) structures and 2D-metasurface photonic structures. "R/T for PBG" abbreviates "Reflectance/transmittance to determine position of bandgap". [113]

		2D - metasurface	2D - metasurface	1D - waveguide
Publication		C. Würth *et al.* (2020) [98]	C. Mao *et al.* (2019) [99]	J. H. Lin *et al.* (2015) [102]
Photonic structure	**Photonic Structure**	2D silicon metasurface with layer of PMMA/UCNPs or PLMA/UCNP on top	2D Si_3N_4 metasurface with UCNPs filled in voids on quartz substrate	Waveguide structure
	Number of designs investigated	2	1	1
UC material	**UC material**	β-$NaYF_4$:Yb^{3+}/Er^{3+}	β-$NaYF_4$:Yb^{3+}/Er^{3+}	β-$NaYF_4$:Yb^{3+},Tm^{3+}
	Form of UC material	UCNPs	UCNPs	UCNPs
	Amount of UC material in structure	Thin layers of 125 nm and 200 nm thickness	Filled voids in structure, 300 nm high, $\sim$300 nm diameter	$\sim$200 nm thin layer on top of waveguide structure
	Limited by PC design	Yes	Yes	Yes
Reference	**Reference structure**	Unstructured parts of the sample at the edges	UCNPs on substrate. For analysis, scaled to same unit cell area as UCNPs in the photonic structure	None-patterned area of the sample
Excitation	**Irradiance**	7.5 - 20 W cm^{-2}	1 - 10^4 W cm^{-2}	65 W cm^{-2} (scanned $\sim$10-70 W cm^{-2})
	Power	-	-	-
	Wavelength	976 nm (800 nm - 1100 nm)	980 nm	976 nm
	Angle (to surface normal)	0° - 50°	0°	0° - 50°
Detection	**Angle (to surface normal)**	0° - 50°	0°	0° - 50°
UCPL enhancement	**Wavelength/emission**	Red and green	Red / green	650 nm / 480 nm / 450 nm
	Enhancement factor	Up to 1000 (for 125 nm thin UC layer at 12.5 W cm^{-2}) and up to 300 (for 200 nm thin UC layer at 7.5 W cm^{-2})	340 (at 10 W cm^{-2}) / 130 (at 2 W cm^{-2})	$1.6 \cdot 10^4$ / $8.8 \cdot 10^4$ / $6.8 \cdot 10^4$
	Spectral width	Roughly $\pm$20 nm	Roughly ± 10 nm	Only very specific wavelengths
	Angle width	$\sim \pm 5$ °	-	Extremely narrow: 10^4 at 31.5° dropping to 1.4 at 30.75°
Simulation	**R/T for PBG**	-	Yes	Yes
	Electric field intensity	Yes (comprehensively)	Yes (comprehensively)	Yes
	Local density of optical states			-
	Upconversion dynamics	-	Simplified and flexible rate equation model including absorption enhancement and quenching	-

Table 2.3.: Literature overview of upconversion photoluminescence (UCPL) enhancement of embedded upconverter nanoparticles (UCNPs) in 2D-metasurface and 1D-waveguide photonic structures. "R/T for PBG" abbreviates "Reflectance/transmittance to determine position of bandgap". [113]

		1D - microcavity structure	1D - multilayer stack	1D - multilayer stack
Publication		R. E. Rojas-Hernandez *et al.* (2018) [101]	C. M. Johnson *et al.* (2013) [58]	C. L. M. Hofmann *et al.* (2021) [26]
Photonic structure	**Photonic Structure**	Microcavity structure with 21 layers: two Bragg reflectors of TiO_2 and Tb^{3+}/Yb^{3+}-doped aluminosilicate glass, spacer layer: Tb^{3+}/Yb^{3+}-doped aluminosilicate glass	Multilayer stack of 60 layers of Er^{3+}-doped porous silicon with alternating refractive index (all layers are doped)	Bragg structure of 4 active layers of PMMA with embedded UCNPs and 5 surrounding TiO_2 layers
	Number of designs investigated	9	1	40
UC material	**UC material** **Form of UC material**	Tb^{3+}/Yb^{3+} UC doped aluminosilicate glass	Er^{3+} UC doped porous silicon	β-$NaYF_4$:25%Er^{3+} UCNPs
	Amount of UC material in structure	11 layers with a summed up thickness of 1 µm	Thin layers with ∼15 µm summed up thickness	∼1.2 µm summed up thickness of all UC layers
	Limited by PC design	No	No	No
Reference	**Reference structure**	Layer stack of only the Tb^{3+}/Yb^{3+}-doped aluminosilicate layers. Seperate reference for each microcavity design	None. The enhancement is calculated relative to the lowest measured UC emission at 38°	Layer stack of only the UC layers on glass to gain the same total thickness as the UC layers in each Bragg structure
Excitation	**Irradiance**	-	-	Max at 1.48 W cm^{-2} (scan ∼0.18 W cm^{-2} - 1.5 W cm^{-2})
	Power	2 W (scan 1 W to 4 W)	200 mW	1 mW - 10 mW
	Wavelength	975 nm	1550 nm	1523 nm for max UC enh. 1500 nm - 1560 scan
	Angle (to surface normal)		Max UC enhancement at 34°, scanned: 21° - 38°	4° for max, and scanned 0° - 75°
Detection	**Angle (to surface normal)**	One distinct detection angle (not given which)	0°	Integrating sphere
UCPL enhancement	**Wavelength/emission**	Green	980 nm / Green	984 nm / 814 nm
	Enhancement factor	25	5 / 26.5	Max 4.1 (mean 2.4) / ∼5
	Spectral width	-	-	∼60 nm
	Angle width	-	∼ ±2° (at 34°), dropping by factor of 5 within 2°	∼30° half angle
Simulation	**R/T for PBG**	Yes	Yes	Yes
	Electric field intensity	-	-	Yes
	Local density of optical states	-	-	MIT Photonic bands & histogramming method for local density of optical states
	Upconversion dynamics	-	-	Rate equation model of UC dynamics including photonic effects and production accuracy

Table 2.4.: Literature overview of upconversion photoluminescence (UCPL) enhancement of embedded upconverter nanoparticles (UCNPs) or upconverter-doped materials in 1D microcavity and multilayer stack photonic structures. "R/T for PBG" abbreviates "Reflectance/transmittance to determine position of bandgap". [113]

CHAPTER 3

METHODS

In the first part of this chapter, the methods to model the photonic effects in a Bragg structure are presented and subsequently, the rate equation modeling framework, describing the upconversion (UC) dynamics under the influence of photonic structure effects. The modeling framework has been developed in the research group over the past 15 years. Within this work, it has been further developed, photonic effects on UC have been experimentally verified and the model has been published open access at `http://dx.doi.org/10.24406/fordatis/110.2`.

The second part of this chapter gives an overview over the experimental techniques and setups used in this work, as well as experimental data evaluation.

This chapter is based on parts of the following publications:

C. L. M. Hofmann, S. Fischer, E. H. Eriksen, B. Bläsi, C. Reitz, D. Yazicioglu, I. A. Howard, B. S. Richards and J. C. Goldschmidt, Experimental validation of a modeling framework for upconversion enhancement in 1D-photonic crystals, *Nature Communications* **12**, 1-10 **(2021)**

C. L. M. Hofmann, E. H. Eriksen, S. Fischer, B. S. Richards, P. Balling, and J. C. Goldschmidt, Enhanced upconversion in 1D photonic crystals: a simulation-based assessment within realistic material and fabrication constraints, *Optics Express* **26**, 7537-7554 **(2018)**

Contributions to this chapter of the author, co-authors and others can be found in section 3.3.

3.1. Modeling

3.1.1. Transfer matrix formalism

The transfer matrix method (TMM) is an analytical and one of the simplest approaches to calculate the field components of an electromagnetic wave traversing through a 1D structure. This structure is composed of multiple planar layers, each featuring a homogeneous refractive index. The implementation of the TMM used in this work was written in python by E.H. Eriksen [114, 115]. It is based on the approach published by Katsidis *et al.* [116]. The TMM package is now implemented into the remUCPS model [35] for modeling the UC dynamics. In this section, I want to give a concise overview over the TMM based on ref. [116], a thorough description of the method can be found in the original work by Katsidis *et al.*

Figure 3.1 illustrates how an electromagnetic wave that traverses through the structure

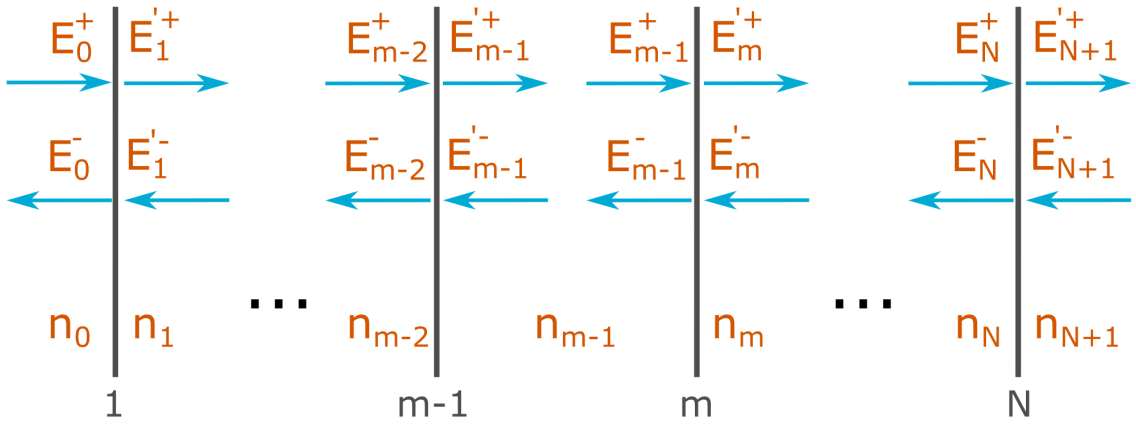

Figure 3.1.: Notation of the electric field amplitudes in a multilayer stack.

is being reflected or transmitted at every interface. Here, only the coherent calculation is considered that applies for layers that are thin with respect to the wavelength of the incident light. The electric field component at any point in this structure can therefore be expressed as a superposition of a forward ($^+$) and backward ($^-$) traveling plane wave. Within the TMM, the electric field amplitudes in each layer can be related via a sequence of 2 $\times$ 2 matrices. Thereby, the interaction at each interface is represented by a refraction or transmission matrix $\mathbf{D}_i$. The propagation within each layer is accounted for via the propagation matrix $\mathbf{P}_i$. The electric field amplitudes on the left hand side of the interface m, E^+_{m-1} and E^-_{m-1}, can be linked to the field amplitudes on the right hand side of the interface, E'^+_m and E'^-_m, via the refraction or transmission matrix $\mathbf{D}_{m-1,m}$ as

$$\begin{aligned}\begin{pmatrix} E^+_{m-1} \\ E^-_{m-1} \end{pmatrix} &= \mathbf{D}_{m-1,m} \begin{pmatrix} E'^+_m \\ E'^-_m \end{pmatrix} \\ &= \frac{1}{t_{m-1,m}} \begin{bmatrix} 1 & r_{m-1,m} \\ r_{m-1,m} & 1 \end{bmatrix} \begin{pmatrix} E'^+_m \\ E'^-_m \end{pmatrix}. \end{aligned} \tag{3.1}$$

$r_{m-1,m}$ and $t_{m-1,m}$ represent the complex Fresnel coefficients (see equation 2.17) of the mth

interface for reflection and transmission, respectively. The matrix $\mathbf{D}_i$ is identical for s- and p polarized waves.

The field amplitudes on the left hand side of the (m-1)th homogeneous layer are related to the field amplitudes on the right hand side of the same layer via the propagation matrix $\mathbf{P}_{m-1}$ in the form

$$\begin{aligned}\begin{pmatrix} E_{m-1}^{\prime +} \\ E_{m-1}^{\prime -} \end{pmatrix} &= \mathbf{P}_{m-1} \begin{pmatrix} E_{m-1}^{+} \\ E_{m-1}^{-} \end{pmatrix} \\ &= \begin{bmatrix} e^{i\delta_{m-1}} & 0 \\ 0 & e^{-i\delta_{m-1}} \end{bmatrix} \begin{pmatrix} E_{m-1}^{+} \\ E_{m-1}^{-} \end{pmatrix}. \end{aligned} \tag{3.2}$$

The phase shift δ_{m-1} is imposed on the electromagnetic wave when it traverses through the homogeneous layer (m-1). This phase shift can be expressed including the angle of incidence θ as [117]

$$\delta_{m-1} = \left(\frac{2\pi d_{m-1} n_{m-1}}{\lambda} \right) \cos\theta. \tag{3.3}$$

with the layer thickness d_{m-1}, refractive index n_{m-1}, and the vacuum wavelength λ_0.

Finally, when the incident wave traverses through N layers and N-1 interfaces, a product of transformations leads to the systems transfer matrix $\mathbf{T}$

$$\begin{aligned}\begin{pmatrix} E_0^{+} \\ E_0^{-} \end{pmatrix} &= \mathbf{D}_0^{-1} \left[\prod_{m=1}^{N} \mathbf{D}_m \mathbf{P}_m \mathbf{D}_m^{-1} \right] \mathbf{D}_{N+1} \begin{pmatrix} E_{N+1}^{\prime +} \\ E_{N+1}^{\prime -} \end{pmatrix} \\ &= \mathbf{T} \begin{pmatrix} E_{N+1}^{\prime +} \\ E_{N+1}^{\prime -} \end{pmatrix} \\ &= \begin{bmatrix} T_{11} & T_{12} \\ T_{21} & T_{22} \end{bmatrix} \begin{pmatrix} E_{N+1}^{\prime +} \\ E_{N+1}^{\prime -} \end{pmatrix}. \end{aligned} \tag{3.4}$$

By the transfer matrix coefficients T_{ij}, the net complex reflection and transmission coefficients are defined as

$$\begin{aligned} r = r_{0,N+1} &= \left. \frac{E_0^{-}}{E_0^{+}} \right|_{E_{N+1}^{\prime -}=0} = \frac{T_{21}}{T_{11}} \\ t = t_{0,N+1} &= \left. \frac{E_{N+1}^{\prime +}}{E_0^{+}} \right|_{E_{N+1}^{\prime -}=0} = \frac{1}{T_{11}} \\ r^{\prime} = r_{N+1,0} &= \left. \frac{E_{N+1}^{-}}{E_{N+1}^{+}} \right|_{E_0^{+}=0} = -\frac{T_{12}}{T_{11}} \\ t^{\prime} = t_{N+1,0} &= \left. \frac{E_0^{-}}{E_{N+1}^{+}} \right|_{E_0^{+}=0} = \frac{\mathrm{Det}(T)}{T_{11}} \end{aligned} \tag{3.5}$$

whereby $\mathrm{Det}(T) = T_{11}T_{22} - T_{12}T_{21}$. r and t ($r^{\prime}$ and $t^{\prime}$) describe the net reflection and transmission coefficients for a plane wave traveling in forward (backward) direction and passing through all layers and interfaces. The total front and back reflectance R and $R^{\prime}$, respectively, and transmittance T and $T^{\prime}$, respectively, can be obtained as the square of

the coefficients r, r', t and t'. Rearranging terms, using the coefficients in equation 3.5, the transfer matrix (equation 3.4) can be expressed as

$$\begin{pmatrix} E_0^+ \\ E_0^- \end{pmatrix} = \frac{1}{t_{0,N+1}} \begin{bmatrix} 1 & -r_{N+1,0} \\ r_{0,N+1} & (t_{0,N+1}t_{N+1,0} - r_{0,N+1}r_{N+1,0}) \end{bmatrix} \begin{pmatrix} E'^+_{N+1} \\ E'^-_{N+1} \end{pmatrix}. \tag{3.6}$$

Within this work, the superstrate air and substrate glass are both simulated as half infinite mediums with refractive index n = 1.0 and n = 1.5, respectively. All layers of the Bragg structure are thin, therefore a coherent simulation is used. However, the TMM can be expanded to non-coherence and also partial coherence and is therefore widely applicable [116].

3.1.2. Optical local energy density in multilayer stacks

The local energy density of the electric field, $u(x)$, can be calculated as

$$u(x) = \frac{1}{2}\varepsilon(x)\left|\mathbf{E}(x)\right|^2, \tag{3.7}$$

with $\varepsilon(x)$ being the electrical permittivity. The relative local energy density $u_{\text{rel}}(\tilde{x})$ of the Bragg structure is calculated relative to the reference as a half-infinite low refractive index material

$$u_{\text{rel}}(\tilde{x}) = \frac{u_{\text{brg}}(\tilde{x})}{u_{\text{ref}}(\tilde{x})}, \tag{3.8}$$

where for the Bragg structure the $\tilde{x}$ coordinate runs inside the active layers only, as shown in Fig. 3.2. $u_{\text{rel}}(\tilde{x})$ is the exact calculation of the energy density at each position in the

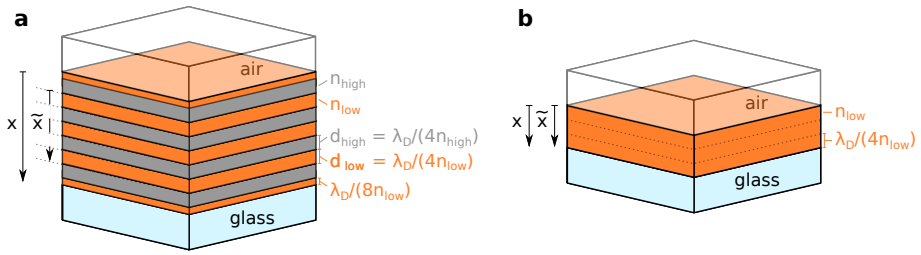

Figure 3.2.: Structural sketches of the Bragg structure (a) and the reference structure (b). The Bragg structure consists of alternating quarter-wave layers, with respect to a design wavelength λ_{design}, of an active and a spacer material with refractive indices n_{low} and n_{high}, with the corresponding layer thicknesses d_{low} and d_{high}. The outermost layers have a reduced optical thickness of $\lambda_{\text{design}}/8n$ and are assumed passive. The reference structure consists of a single, homogeneous layer containing the same amount of active material as the corresponding Bragg structure. [34]

Bragg structure. Visualizing this value within a varied structure design is, however, difficult. Therefore, an average value is needed in only the active layers of the Bragg structure, to be able to easily visualize the dependence of $u_{\text{rel}}(\tilde{x})$ on a varied design wavelength. The average relative energy density $\bar{u}_{\text{rel}}$ is thus defined as

$$\bar{u}_{\text{rel}} = \frac{\int u_{\text{brg}}(\tilde{x})d\tilde{x}}{\int u_{\text{ref}}(\tilde{x})d\tilde{x}}. \tag{3.9}$$

These quantities are very sensitive to structural imperfections. To account for final production tolerances, Monte Carlo simulations are carried out. A number of calculations are performed where for each layer the thickness d is modified as

$$d \to d + \delta d, \tag{3.10}$$

where δd is drawn from a Gaussian distribution with a standard deviation σ representing the production accuracy. Finally, the energy density is determined from the (incoherent) average across all calculations. [34]

3.1.3. Calculating the local density of optical states

For infinite periodic structures, i.e. ideal photonic crystals, the local density of optical states (LDOS) can be derived from eigenmode calculations, as presented in section 2.1.4. In this work, the MIT Photonic Bands [37] software package was used for calculating the eigenmodes and bandstructure of the Bragg structure. While the ideal crystal assumption is not accurate for Bragg structures with only a small number of layers [118, 119], the impact is not large. In this work, the comparison to experiment is drawn for a Bragg structure with four active layers and good agreement is found. However, for future applications, with Bragg structures with more active layers, featuring much larger photonic effects, should be considered. For these structures, the uncertainty stemming from the LDOS calculation is even smaller. The benefit of the eigenmode approach is that it permits the calculation of an angularly resolved LDOS, introduced in section 5.1.3.

Due to the scale invariance of the problem, dimensionless quantities are considered

$$\mathbf{k}' = \frac{\mathbf{k}a}{2\pi}, \quad \omega' = \frac{\omega a n}{2\pi c_0}, \tag{3.11}$$

where $\mathbf{k}$ is the wave vector, a the size of the Wigner-Seitz unit cell of the photonic crystal, n the refractive index and c_0 the speed of light in vacuum. For a given eigenvector $\mathbf{k}'_j$, an eigenmode calculation yields the mode frequency $\omega'_{b,\mathbf{k}'_j}$ and the electric field profile $\mathbf{E}_{b,\mathbf{k}'_j}(x)$ with b being the band index.

Gutmann *et al.* developed a calculation of a quasi-3D LDOS, by calculating the 2D LDOS by applying the histogramming method and subsequently exploiting the in-plane symmetry of the Bragg structure to expand to the third dimension.The quasi-3D LDOS can thus be calculated as [33]

$$\begin{aligned} \mathrm{LDOS}(x,\omega') &= \sum_b \sum_{\mathbf{k}' \in \mathbf{K}_{b,\omega'}} |\mathbf{E}_{b,\mathbf{k}'}(x)|^2 \cdot 2\pi k'_y \\ \text{with } \mathbf{K}_{b,\omega'} &= \left\{ \mathbf{k}'_j \middle| \omega' \leq \omega'_{b,\mathbf{k}'_j} \leq \omega' + \Delta\omega' \right\}, \end{aligned} \tag{3.12}$$

where $\mathbf{k}'_j$ is sampled mode on an equidistant grid with spacing $\Delta k'$ in the first quadrant of the xy-plane in reciprocal space, as illustrated in Fig. 3.3. While the sampling in the x-direction is bound by the edge of the First Brillouin Zone at $k'_x = 0.5$, k'_y is unbound due to the lack of translational symmetry. [34]

In order to cover the complete spectral range of interest, a certain range of k-vectors has to be calculated. In this work, k_x is always calculated within the first Brillouin Zone, $0 < k'_x < 0.5$.

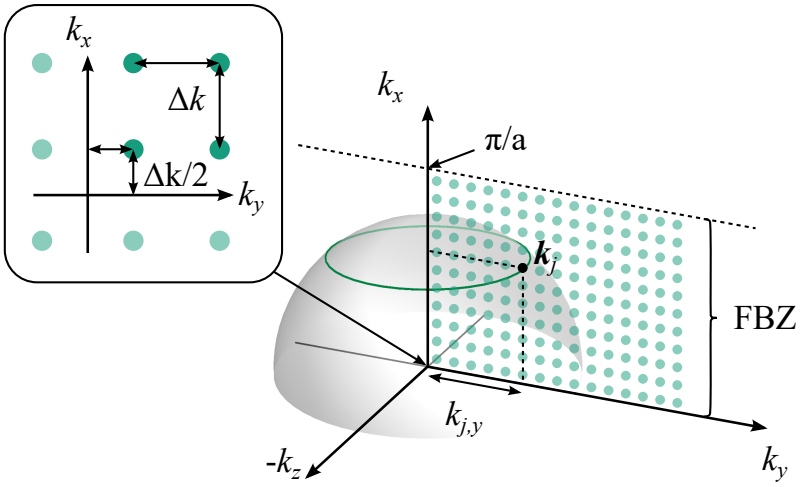

Figure 3.3.: Sketch of the sampled $\mathbf{k}$-space for the quasi-3D calculation of the local density of optical states (LDOS). The eigenmodes $\mathbf{k}$ are sampled on an equidistant 2D-grid in reciprocal space with a binning width of Δk. Due to the in-plane symmetry, the quasi-3D LDOS can be obtained by weighting each mode with its circumference of a circle around the x-axis with radius $\mathbf{k}_y$. Figure from ref. [120]

k_y however, does not have a Brillouin Zone boundary and hence a maximum value needs to be chosen. This maximum k_y needs to be calculated up to a value such that all modes are included within the needed ω'-range. Finally, the ω'-range has to be chosen such that ω' can be rescaled to the required emission- and design wavelength range, via equation 3.18. Therefore, for comparison with experiment in this work, the range $0 < \omega' < 1.2$ is required to allow for rescaling the LDOS to the design- and emission wavelength range of interest. To include all modes in this ω'-range, the fist five bands of the photonic band structure are required and $0 \leq k'_y \leq 2.4$. These ω' and k_y parameters are used for all calculations with refractive indices n_{low} = 1.47 and n_{high} = 2.28 in chapter 5 and all calculations in chapter 6.

The following passage is in large parts taken from my publication, ref. [34]. For all other simulations, shown in chapter 5, all modes across the first seven bands in the range $0 < \omega' < 1.4$ were calculated. To obtain all contributing modes for the relevant emission frequencies and material combinations, the range $0 \leq k'_y \leq 5.4$ was considered. An optional output in MIT Photonic bands is the electric field energy density, from which the squared amplitude of the electric field can be computed,

$$|\mathbf{E}_{b,\mathbf{k}'}(x)|^2 = \frac{2u_{b,\mathbf{k}'}(x)}{\varepsilon(x)}. \tag{3.13}$$

The LDOS can then be calculated via Eq. (3.12). For all calculations presented in this work, a discretization of $\Delta k' = 10^{-3}$ and $\Delta\omega' = 10^{-3}$ was used. The limited resolution in k-space caused a significant amount of binning noise. To reduce the noise, the LDOS was smoothed along the frequency axis using a Gaussian filter with $\sigma = 5$. As the reference is homogeneous, the LDOS is independent of the position. Hence, it is equal to the DOS up to a multiplicative constant which depends on the discretization of the Wigner-Seitz unit cell.

The DOS for a homogeneous medium has an analytical form [120],

$$\mathrm{DOS3D}(\omega') = \frac{4\pi n^3}{\Delta k'^2}\omega'^2. \tag{3.14}$$

Applying the same binning procedure as in the numerical calculation for the Bragg structure, the binned reference LDOS can be calculated as

$$\begin{aligned}\mathrm{LDOS}_{\mathrm{ref}}(\omega') &= \int_{\omega'}^{\omega'+\Delta\omega'} \mathrm{DOS3D}(\omega'')d\omega'' \\ &= \frac{4\pi n^3 \Delta\omega'}{\Delta k'^2}\left(\omega'^2 + \omega'\Delta\omega + \frac{\Delta\omega'^2}{3}\right)\end{aligned} \tag{3.15}$$

with $n = n_{\mathrm{low}}$ [33]. The relative LDOS in the Wigner-Seitz unit cell is defined as

$$\mathrm{LDOS}_{\mathrm{rel}}(x,\omega') = \frac{\mathrm{LDOS}_{\mathrm{brg}}(x,\omega')}{\mathrm{LDOS}_{\mathrm{ref}}(\omega')}. \tag{3.16}$$

For visualization purposes I define also the average relative LDOS across the active layers of the Bragg structure,

$$\overline{\mathrm{LDOS}}_{\mathrm{rel}}(\omega') = \frac{\int \mathrm{LDOS}_{\mathrm{brg}}(\tilde{x},\omega')d\tilde{x}}{\int \mathrm{LDOS}_{\mathrm{ref}}(\omega')d\tilde{x}}. \tag{3.17}$$

The relative LDOS for a particular transition $i \to f$, characterized by the transition wavelength λ_{fi} and for a particular design, characterized by the design wavelength $\lambda_{\mathrm{design}}$, is mapped to the dimensionless transition frequency ω'_{fi} as [32]

$$\omega'_{fi} = \frac{n_{\mathrm{low}} + n_{\mathrm{high}}}{4n_{\mathrm{low}}n_{\mathrm{high}}}\frac{\lambda_{\mathrm{design}}}{\lambda_{fi}}. \tag{3.18}$$

3.1.4. Calculating the fractional local density of optical states

The change in emission rates is altered by the LDOS, that contains all eigenmodes of the photonic crystal. However, not all modes are able to couple out of the photonic crystal. To describe the out-coupling condition and the directionality of out-coupled modes, the fractional local density of optical states (FLDOS) has been developed within our team by Gutmann *et al.* [33, 120]. To find the FLDOS, the calculation of the LDOS is restricted to the subset of modes, that fulfill the requirements to describe either the light guiding efficiency or directionality of out-coupled modes. In my work, the case of the out-coupled modes is of interest. In a configuration with the solar cell above the photonic-upconverter, it is important to understand which fraction of the upconverted light can reach the solar cell and can therewith contribute to charge generation.

The subset of modes that are able to couple out of the photonic crystal is given by $|\mathbf{k}'_{\parallel}| \leq \omega'_{b,\mathbf{k}'} n_{\mathrm{out}}/c_0$ (see equation 2.16), where $\mathbf{k}'_{\parallel}$ is the wave vector component parallel to the surface plane and n_{out} is the refractive index of the surrounding medium that the mode is coupled out into. The FLDOS contains the modes that are associated with a certain emission direction. This corresponds to a detection cone with a half-angle θ_d, as it would be detected in a photoluminescence measurement. The FLDOS can then be calculated for

each detection cone, tilted by an angle ϕ_d with respect to the surface normal. In the quasi-3D approach, used in this work, the calculation is first carried out in a 2D xy-plane, as illustrated in Fig. 3.4a. In this plane, the modes that lie within the detection cone can be found by checking the criteria [120]

$$\phi_d - \theta_d < \phi_k < \phi_d + \theta_d, \tag{3.19}$$

with ϕ_k being the angle of an out-coupled mode $\mathbf{k'}_{\text{out}}$ with respect to the surface normal, given by $\phi_k = \arcsin(|\mathbf{k}'_{\parallel}|/|\mathbf{k'}_{\text{out}}|)$. Figure 3.4b shows the expansion to the third dimension,

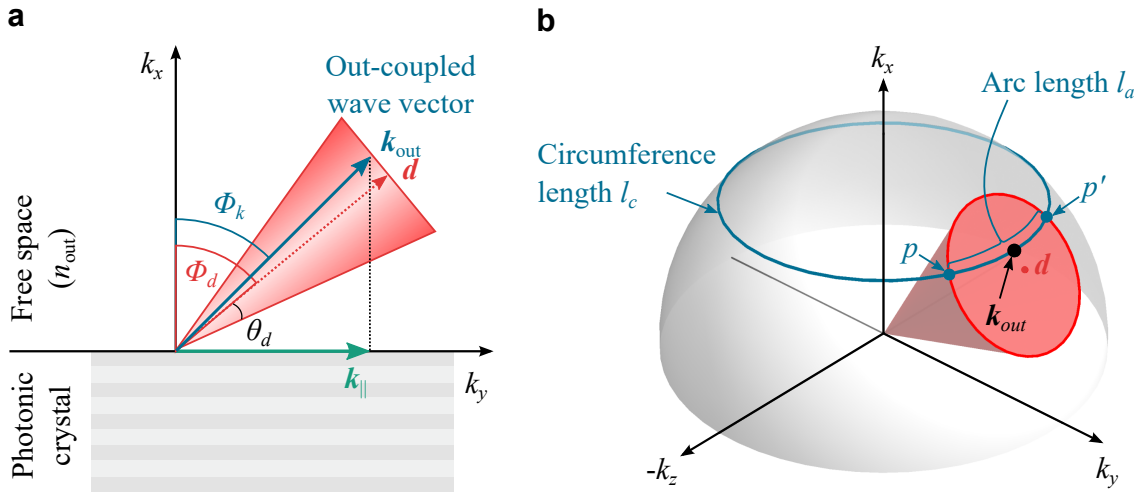

Figure 3.4.: Sketch of the method to calculate the fractional local density of optical states (FLDOS) to understand the directionality of UC emission. a In the quasi-three-diomensional approach used in this work, first the modes with wave vector $\mathbf{k}_{\text{out}}$ that are coupled out into a detection cone with half angle θ_d that is tilted by the angle ϕ_d with respect to the surface normal are selected in 2D. **b** To expand to the third dimension, the modes $\mathbf{k}_{\text{out}}$ contribute to the FLDOS according to the ratio of the arc length l_a to the circumference length l_c. The fraction l_a/l_c is calculated via the intersection points $\mathbf{p}$ and $\mathbf{p}'$. Figures from [120] are adapted to match the nomenclature of this work.

taking in the yz-plane. In the quasi-3D LDOS, the expansion is done by multiplying with the factor $2\pi k_y$. Now, the fraction of symmetric modes of $\mathbf{k}_{\text{out}}$ that lie within the detection cone, depends on the relative position of $\mathbf{k}_{\text{out}}$ to ϕ_d. The fraction can be found by considering the arc length l_a within the total circumference length l_c that enters the cone at point p and leaves the cone at point p'. This then gives the factor $2\pi k_y \cdot l_a/l_c$ to expand to the third dimension. From the quasi-3D LDOS (3.12), taking into account both criteria from the modes $\mathbf{k}_{\parallel}$ that can couple out (equations 2.16) and equation 3.19, the quasi-3D FLDOS is given by [120]

$$\begin{aligned} \text{FLDOS}(x,\omega') &= \sum_b \sum_{\mathbf{k}' \in \mathbf{F}_{b,\omega'}} |\mathbf{E}_{b,\mathbf{k}'}(x)|^2 \cdot 2\pi k'_y \cdot \frac{l_a}{l_c} \\ \text{with } \mathbf{F}_{b,\omega'} &= \left\{ \mathbf{k}' \in \mathbf{K}_{b,\omega'} \;\middle|\; |\mathbf{k}_{\parallel}| \leq \omega_{b,\mathbf{k}} n_{\text{out}}/c_0 \right\} \\ \text{and } \mathbf{F}_{b,\omega'} &= \left\{ \mathbf{k}' \in \mathbf{K}_{b,\omega'} \;\middle|\; \phi_d - \theta_d < \arcsin(|\mathbf{k}_{\parallel}|/|\mathbf{k}_{\text{out}}|) < \phi_d + \theta_d \right\}. \end{aligned} \tag{3.20}$$

The factor l_a/l_c can be calculated as follows: the vector $\mathbf{k} = \begin{pmatrix} \cos\phi_k \\ \sin\phi_k \\ 0 \end{pmatrix}$ is, per rotation matrix

$R_x(\theta_p) = \begin{pmatrix} 1 & 0 & 0 \\ 0 & \cos\theta_p & \sin\phi_k \\ 0 & \sin\theta_p & \cos\phi_k \end{pmatrix}$, rotated around the x-axis until it intersects the cone at point $\mathbf{p}$ with

$$\mathbf{p} = R_x(\theta_p) \cdot \mathbf{k} = \begin{pmatrix} \cos\phi_k \\ \cos\theta_p \cdot \sin\phi_k \\ \sin\theta_p \cdot \cos\phi_k \end{pmatrix}. \tag{3.21}$$

Next, the half cone angle θ_d is given by the angle between the vector $\mathbf{p}$ and $\mathbf{d}$, and therefore $\cos\theta_d = {}^{\mathbf{p}\cdot\mathbf{d}}/_{|\mathbf{p}|\cdot|\mathbf{d}|}$ with $\mathbf{d} = \begin{pmatrix} \cos\phi_d \\ \sin\phi_d \\ 0 \end{pmatrix}$. The arc length ${}^{l_a}/_{l_c}$ is then given by the fraction of the half angle θ_p of the circumference as ${}^{l_a}/_{l_c} = {}^{\theta_p}/_{\pi}$ and finally

$$\frac{l_a}{l_c} = \frac{1}{\pi} \cdot \arccos\left(\frac{\cos(\theta_d) - \cos(\phi_d) \cdot \cos(\phi_k)}{\sin(\phi_d) \cdot \sin(\phi_k)}\right). \tag{3.22}$$

In the case of the Bragg structure regarded in this work, $k_\parallel$ is in the surface plane, that the light is coupled out of and therefore, $k_\parallel = k_y$. For all calculations in this work, the surrounding medium is taken as air with $n = 1.0$, as it is in experiment. The step width of the dimensionless parameters are identical as in the LDOS calculation with $\Delta k' = 10^{-3}$ and $\Delta\omega' = 10^{-3}$. The FLDOS calculations in this work are performed up to $\omega_{\text{max}} = 1.2$, in the range $0 \leq k'_x \leq 0.5$ and $0 \leq k'_y \leq 2.4$ for the first five bands of the photonic band structure, to sufficiently display the range of interest. The reference sample is calculated the same way as the Bragg structure to ensure an identical binning. It is possible to simulate a reference sample in MIT Photonic bands, when the difference in the refractive indices is smaller than the precision of the program of 10^{-7} [121]. Therefore, the reference is calculated with $n_{\text{low}} = 1.474$ and $n_{\text{high}} = 1.474 + 10^{-8}$. This returns a homogeneous material without bandgaps, or to put it in a different way, the bandgaps are too small to exist.

To display the angle dependence, the fractional density of optical states (FDOS) is calculated as the average over all emitter positions $\tilde{x}_i$ within the active layer. I define the normalized FDOS ($\text{FDOS}_{\text{norm}}$) as the modes coupled out into the angle ϕ_d and the surrounding half cone θ_d, relative to all emitted modes:

$$\text{FDOS}_{\text{norm}}(\omega', \phi_d) = \frac{1}{m} \sum_{i=1}^{m} \frac{\text{FLDOS}(\tilde{x}_i, \omega', \phi_d)}{\text{LDOS}(\tilde{x}_i, \omega')}. \tag{3.23}$$

To understand how the directionality of emission is changed relative to the reference sample, I define the relative FDOS (FDOS_{rel}) as the quotient of the FDOS in the Bragg structure ($\text{FDOS}_{\text{norm,brg}}$) to the FDOS in the reference structure ($\text{FDOS}_{\text{norm,ref}}$)

$$\text{FDOS}_{\text{rel}}(\omega', \phi_d) = \frac{\text{FDOS}_{\text{norm,brg}}(\omega', \phi_d)}{\text{FDOS}_{\text{norm,ref}}(\omega', \phi_d)} \tag{3.24}$$

In experiment, FDOS_{rel} is observed when dividing the measured Bragg structure by the measured reference sample. For convenience in plotting, for both $\text{FDOS}_{\text{norm}}$ and FDOS_{rel}, all values of infinity are set to zero.

3.1.5. Modeling upconversion

In this section, the modeling framework describing the dynamics of the UC process in a rate equation model is presented. The initial development of the model was published by Fischer

et al. 2012 [28] for homogeneous media. Based on coupling plasmonic effects with the rate equation model, by Fischer *et al.* in 2012 [122] and 2013 [30], the model was extended for a photonic environment by Herter *et al.* 2013 [31] and Hofmann *et al.* 2016 [32]. The model version mainly used in this work is published in Hofmann, Eriksen *et al.* 2018 [34]. The new components in the version from 2018 are a transfer from Matlab to a python environment, speeding up the calculations and solving the rate equation more precisely. Additionally, the variation of the incident angle and directionality of emission is included. The experimental validation of the photonic effects on UC is published in Hofmann *et al.*2021 [26].

The description in this section serves the purpose to precisely elaborate the model as it is published open access at `http://dx.doi.org/10.24406/fordatis/110.2`. The theory that the final formulas presented in this section are based on is given in section A thorough description of the UC process can be found in section 2.2.2. All experimentally determined input parameters can be found in the Appendix in section A.1.

The occupation density vector

The model considers the first seven energy levels of β-$NaYF_4$:Er^{3+}, as shown in Fig. 2.6. The energy levels of the ${}^2H_{11/2}$ and the ${}^2S_{3/2}$ states are treated as one effective energy level, due to their close proximity. The occupation of each level is described by an element of the occupation density vector $\mathbf{n}$. The linear processes included in the rate equation model are ground state absorption (GSA), excited state absorption (ESA), stimulated emission (STE), spontaneous emission (SPE) and multi-phonon relaxation (MPR). Additionally, the non-linear Förster energy transfer processes, energy transfer upconversion (ETU) and cross relaxation (CR), are considered. The most important processes are indicated in Fig. 2.6. [34]

The rate of change of the occupation density vector yields

$$\dot{\mathbf{n}} = \left[M_{\mathsf{GSA}} + M_{\mathsf{ESA}} + M_{\mathsf{STE}} + M_{\mathsf{SPE}} + M_{\mathsf{MPR}}\right]\mathbf{n} + \nu_{\mathsf{ETU}}(\mathbf{n}) + \nu_{\mathsf{CR}}(\mathbf{n}). \tag{3.25}$$

The transition matrices M and vector functions $\mathbf{v}$ are conducted via the transition dipole matrix elements $|\mu_{if}|^2$, which have been experimentally determined by Fischer [63] (see Appendix equation A.1). In the following, the form of all matrices is given for the individual types of processes.

The transition matrices are based on column and row one to six correspond to the energy levels one to six as depicted in Fig. 2.6.

Stimulated radiative processes

From equations 2.31 and 2.40, the matrix describing population of the energy levels due to ground state absorption and excited state absorption processes takes on the form

$$M_{\mathsf{ABS}} = \alpha_{\mathsf{trans}} \cdot \begin{bmatrix} -|\mu_{12}|^2 K_{12}/g_1 & 0 & 0 & 0 & 0 & 0 \\ +|\mu_{12}|^2 K_{12}/g_1 & -|\mu_{24}|^2 K_{24}/g_2 & 0 & 0 & 0 & 0 \\ 0 & 0 & 0 & 0 & 0 & 0 \\ 0 & +|\mu_{24}|^2 K_{24}/g_2 & 0 & -|\mu_{46}|^2 K_{46}/g_4 & 0 & 0 \\ 0 & 0 & 0 & 0 & 0 & 0 \\ 0 & 0 & 0 & +|\mu_{46}|^2 K_{46}/g_4 & 0 & 0 \end{bmatrix} \tag{3.26}$$

with the pre-factor

$$\alpha_{\text{trans}} = \frac{\pi}{3n^2\hbar^2\varepsilon_0} \cdot \left(\frac{n^2+2}{3}\right)^2 \cdot \frac{n}{c_0} I. \tag{3.27}$$

Thereby, g describes the degeneracy, in this case of the initial state i, n the refractive index, c_0 the vacuum speed of light, ε_0 the vacuum permittivity, $\hbar$ the reduced Planck constant and I the incident irradiance. The term $(n/c_0)IK_{if}$ is included in the equation in the case of monochromatic irradiance [63] whereby K_{if} is a fit parameter which represents how resonant the respective transition if is with the monochromatic excitation energy (given in the Appendix in equation A.4). The refractive index used in the rate equation calculation is $n = 1.5$.

The matrix M_{STE} describing population due to stimulated emission processes can be drawn from equations 2.32 and 2.39 to yield

$$M_{\text{STE}} = \alpha_{\text{trans}} \cdot \begin{bmatrix} 0 & +|\mu_{21}|^2 K_{21}/g_2 & 0 & 0 & 0 & 0 \\ 0 & -|\mu_{21}|^2 K_{21}/g_2 & 0 & 0 & 0 & 0 \\ 0 & 0 & 0 & 0 & 0 & 0 \\ 0 & 0 & 0 & 0 & 0 & 0 \\ 0 & 0 & 0 & 0 & 0 & 0 \\ 0 & 0 & 0 & 0 & 0 & 0 \end{bmatrix}. \tag{3.28}$$

Spontaneous emission

Spontaneous emission is directly linked to the Einstein A-coefficients A_{if} (equation 2.38) depopulating the initial state and populating the final states

$$M_{\text{SPE}} = \begin{bmatrix} 0 & A_{21} & A_{31} & A_{41} & A_{51} & A_{61} \\ 0 & -A_{21} & A_{32} & A_{42} & A_{52} & A_{62} \\ 0 & 0 & -A_{31} - A_{32} & A_{43} & A_{53} & A_{63} \\ 0 & 0 & 0 & -A_{41}.. - A_{43} & A_{54} & A_{64} \\ 0 & 0 & 0 & 0 & -A_{51}.. - A_{54} & A_{65} \\ 0 & 0 & 0 & 0 & 0 & -A_{61}.. - A_{65} \end{bmatrix} \tag{3.29}$$

Thereby, the individual Einstein coefficients are calculated from the electric dipole transition elements $|\mu_{if}|^2$, see equation 2.38.

Multi phonon relaxation

The probability of multi-phonon relaxation processes is described by the energy gap law (see equation 2.41). It depends on the host crystals' phonon energies, described by the material constants C_{MPR} and κ. Multi-phonon relaxation takes place between two neighboring electronic states of the upconverter material and scales with their energy distance ω_{if}.

According to equation 2.41, the matrix for multi-phonon relaxation can be expressed as

$$M_{\mathsf{MPR}} = C_{\mathsf{MPR}} \cdot \begin{bmatrix} 0 & +e^{-\kappa\hbar\omega_{21}} & 0 & 0 & 0 & 0 \\ 0 & -e^{-\kappa\hbar\omega_{21}} & +e^{-\kappa\hbar\omega_{32}} & 0 & 0 & 0 \\ 0 & 0 & -e^{-\kappa\hbar\omega_{32}} & +e^{-\kappa\hbar\omega_{43}} & 0 & 0 \\ 0 & 0 & 0 & -e^{-\kappa\hbar\omega_{43}} & +e^{-\kappa\hbar\omega_{54}} & 0 \\ 0 & 0 & 0 & 0 & -e^{-\kappa\hbar\omega_{54}} & +e^{-\kappa\hbar\omega_{65}} \\ 0 & 0 & 0 & 0 & 0 & -e^{-\kappa\hbar\omega_{65}} \end{bmatrix} \tag{3.30}$$

The material constants C_{MPR} and κ were determined from a fit on the experimental data by Fischer *et al.*, as elaborated in ref. [28] and are given in the Appendix in equation A.2. The transition frequencies ω_{if} have been determined experimentally in an unpublished work by Fröhlich and are given in the Appendix in equation A.3.

Energy transfer

The vectors $\nu_{\mathsf{ET}}(\mathbf{n})$ describe the impact of all energy transfer processes on the occupation density $\mathbf{n}$. Energy transfer processes occur between a donor upconverter ion with initial and final state i and f and an acceptor upconverter ion with initial state i' and final state f'. The probability is governed by the electric dipole-dipole transition $P^{if,i'f'}_{\mathsf{ET},dd}$ (see equation 2.43) and the occupation of donor and acceptor ion in their initial states N_i and $N_{i'}$

$$\nu_{\mathsf{ET}}(\mathbf{n}) = P^{if,i'f'}_{\mathsf{ET},dd} \cdot \mathbf{e}^{if,i'f'}_{\mathsf{ET}} \cdot N_i N_{i'} \tag{3.31}$$

$$= \frac{4\pi}{3\hbar} \cdot \left(\frac{1}{4\pi\varepsilon_0 n^2}\right)^2 \cdot \frac{1}{d^6_{\mathsf{Er}}} \cdot |\mu_{if}|^2 |\mu_{i'f'}|^2 \cdot \kappa^{if,i'f'}_{\mathsf{ET}} \cdot \mathbf{e}^{if,i'f'}_{\mathsf{ET}} \cdot N_i N_{i'} \tag{3.32}$$

$\kappa^{if,i'f'}_{\mathsf{ET}}$ represents the spectral overlap integral of the two considered transitions defined as (see equation 2.43)

$$\kappa^{if,i'f'}_{\mathsf{ET}} = \frac{1}{\hbar} \int g^{\mathsf{em}}_{if}(\omega) g^{\mathsf{abs}}_{i'f'}(\omega) d\omega \tag{3.33}$$

Within the work of Fischer, the parameters $\kappa^{if,i'f'}_{\mathsf{ET}}$ have been determined experimentally. They are given in the Appendix in table A.1. The energy is transferred between two ions, thus there are electron states being populated and other that are being depopulated, which is accounted for via $\mathbf{e}^{if,i'f'}_{\mathsf{ET}}$ as a plus or minus sign for each transition. To clarify the calculation, I want to give one example for the energy transfer UC process of the main UC emission: both, the donor and acceptor ion start at level 2. The donor transfers its energy, relaxing to the ground state of level 1, while the acceptor is lifted into the 4th state. This process is shortened by (2,2 $\rightarrow$ 1,4) and the vector $\nu^{22,14}_{\mathsf{ET}}(\mathbf{n})$ takes the form

$$\nu^{22,14}_{\mathsf{ET}}(\mathbf{n}) = \frac{4\pi}{3\hbar} \cdot \left(\frac{1}{4\pi\varepsilon_0 n^2}\right)^2 \cdot \frac{1}{d^6_{\mathsf{Er}}} \cdot \kappa^{22,14}_{\mathsf{ETU}} \cdot \begin{bmatrix} +|\mu_{21}|^2 |\mu_{24}|^2 N_2^2 \\ -2|\mu_{21}|^2 |\mu_{24}|^2 N_2^2 \\ 0 \\ +|\mu_{21}|^2 |\mu_{24}|^2 N_2^2 \\ 0 \\ 0 \end{bmatrix} \tag{3.34}$$

The distance d_{Er} between the two ions that are involved in the energy transfer process critically depends on the doping concentration c_{Er} of the upconverter Er^{3+} in the host lattice. β-$NaYF_4$:Er^{3+} can be described with a hexagonal unit cell with a volume $\sqrt{3}/2 \cdot \mathcal{A}^2\mathcal{C}$ and the lattice constants $\mathcal{A}$ and $\mathcal{C}$ [123]

$$d_{\mathrm{Er}} = \left(\frac{\sqrt{3}/2 \cdot \mathcal{A}^2\mathcal{C}}{1.5 \cdot c_{\mathrm{Er}}} \right)^{1/3}, \tag{3.35}$$

In β-$NaYF_4$, these lattice constants are $\mathcal{A} = \mathcal{B} = 5.9757\ \mathring{A}$ and $\mathcal{C} = 3.5305\ \mathring{A}$ [55]. The dopant Er^{3+} and the host lattice β-$NaYF_4$, which is regarded in this work, depict very similar lattice constants, such that the lattice mismatch between β-$NaYF_4$ and β-$NaErF_4$ is as small as 0.13% for the lattice constant $\mathcal{A}$ and 0.25% for the lattice constant $\mathcal{C}$ and therefore negligible [124]. The Er^{3+} doping concentration c_{Er} can be varied within the modeling framework. The constants are summarized in the Appendix in equation A.6.

In this work, I examine photonic effects on UC and not the UC process itself. Therefore, a constant doping concentration is chosen that yields a high UC quantum yield in a large range of incident irradiances, as shown by Fröhlich [125]. This serves the purpose to be able to study a variety of different Bragg structure designs with a varying optical energy density enhancement effect.

3.1.6. Modeling photonic effects on upconversion

The impact of photonic effects on UC is introduced in section 2.2.4. The modifications of the rate equation model due to the changes in the photonic environment imposed by the photonic structure have been developed in [31].

Photonic effects on stimulated radiative processes

The probability of stimulated radiative processes scale with the local energy density $u(x, \omega'_{fi})$. This can be taken into account by scaling the transition matrices for stimulated radiative processes with the relative change in the local energy density $u_{\mathrm{rel}}(x, \omega'_{fi})$

$$\begin{aligned} M_{\mathrm{GSA}} &\rightarrow M_{\mathrm{GSA}} u_{\mathrm{rel}}(x, \omega'_{fi}), \\ M_{\mathrm{ESA}} &\rightarrow M_{\mathrm{ESA}} u_{\mathrm{rel}}(x, \omega'_{fi}), \\ M_{\mathrm{STE}} &\rightarrow M_{\mathrm{STE}} u_{\mathrm{rel}}(x, \omega'_{fi}). \end{aligned} \tag{3.36}$$

Photonic effects on spontaneous emission processes

The probability P_{fi} of a spontaneous emission process is governed by Fermi's golden rule, introduced in equation 2.35. According to Fermi'S golden rule, it is the local density of optical states (LDOS) $\rho(\mathbf{r}, \omega_{if})$ that influences the probability of a spontaneous emission process. The local dependence of the LDOS is important to include, because the exact density of optical states at each emitter position is decisive. To incorporate the effect of the modified

LDOS into the rate equation model, the Einstein coefficients for spontaneous emission are scaled as

$$A_{fi} \rightarrow A_{fi}\mathrm{LDOS}_{\mathrm{rel}}(x, \omega'_{fi}). \tag{3.37}$$

Calculation of upconversion photoluminescence and quantum yield

The following passage is taken from my publication, ref. [34]. The output of the rate equation model is a steady-state occupation density vector $\mathbf{N}$ from which the main figures of merit, the UC photoluminescence (UCPL) and the internal UC quantum yield (UCQY), can be calculated. The photoluminescence (PL) for each transition is

$$\mathrm{PL}_{if} = \int_{x_0}^{x_m} A_{if}(x) N_i(x) dx \tag{3.38}$$

where N_i is the steady-state occupation density of level i. The energy level numbering scheme is shown in Fig. 2.6. In the UCPL, we consider only the main UC emission of the $3 \rightarrow 1$ transition,

$$\mathrm{UCPL} = \mathrm{PL}_{31}. \tag{3.39}$$

This approximation enables a simpler analysis going forward, and the associated error is small, as the $3 \rightarrow 1$ transition accounts for more than 95% of the emitted, upconverted photons. To obtain the UCQY, the UCPL is divided by the number of absorbed photons,

$$\mathrm{UCQY} = \frac{\mathrm{UCPL}}{N_1 M_{\mathrm{GSA},12} + N_2 M_{\mathrm{ESA},24} + N_4 M_{\mathrm{ESA},46}}. \tag{3.40}$$

To enable clear visualization of the effect of the Bragg structure, I define also the relative UCPL

$$\mathrm{UCPL}_{\mathrm{rel}} = \frac{\mathrm{UCPL}_{\mathrm{brg}}}{\mathrm{UCPL}_{\mathrm{ref}}}. \tag{3.41}$$

Implementation of the fractional local density of optical states (FLDOS)

The effect of the FLDOS has to be linked to the final results of the rate equation model in a different way than the LDOS effect. The reason is *i*) that the FLDOS only takes into account the modes that are coupled out and *ii*) the FLDOS is calculated separately for each detection angle. The UC process, however, is affected by all modes within the active layer simultaneously, no matter whether they are coupled out or which detection cone they are directed into. Therefore, the rate equation model is solved under the influence of the LDOS effect, as per equation 3.37. Subsequently, there are two ways to calculate an FDOS result from the UCPL. To understand which fraction of the total modes within the active layer is coupled out and directed into a detection cone at the angle ϕ_d relative to the surface normal with an opening half cone angle of θ_d, $\mathrm{FDOS}_{\mathrm{norm}}$ is needed. The total emission from the active layer of a Bragg structure is given by the UCPL. Therefore, when the frequency dependent $\mathrm{UCPL}(\omega')$ (equation 3.39) is multiplied with $\mathrm{FDOS}_{\mathrm{norm}}(\omega', \phi_d)$ (equation 3.23), the result is the $\mathrm{UCPL}_{\mathrm{FDOS}}$

$$\mathrm{UCPL}_{\mathrm{FDOS}}(\omega', \phi_d) = \mathrm{UCPL}(\omega') \cdot \mathrm{FDOS}_{\mathrm{norm}}(\omega', \phi_d) \tag{3.42}$$

that describes which fraction of the total UCPL can be detected at each angle. The second approach is to analyze the UCPL off the Bragg structure relative to the reference structure in a certain detection cone. This is given by the product of $UCPL_{rel}$ (equation 3.41) and $FDOS_{rel}$ (equation 3.24) as $UCPL_{rel,FDOS}$

$$UCPL_{rel,FDOS}(\omega', \phi_d) = UCPL_{rel}(\omega') \cdot FDOS_{rel}(\omega', \phi_d). \tag{3.43}$$

$UCPL_{rel,FDOS}$ is the parameter that is later compared to the outcomes of the experiment. Analogously, both the $UCPL_{FDOS}$ and $UCPL_{rel,FDOS}$ can be calculated as a function of $\lambda_{excitation}$ or λ_{design} by rescaling ω' via equation 3.18.

3.2. Experimental

3.2.1. Fabrication methods

Spin-coating

The upconverting layers are composed of Poly(methyl methacrylate) (PMMA) (120,000 g mol^{-1}, purchased from Sigma-Aldrich), with embedded 25wt% of the purpose built core-shell upconverter nanoparticles β-$NaYF_4$:Er^{3+}, fabricated as reported in [59].
In the following, these layers are referred to as active layers. For the production, a stem solution of 10wt% PMMA in toluene and a stem solution of upconverter nanoparticles in toluene were mixed to give a final relation of 25wt% of upconverter nanoparticles with respect to the PMMA content, and 5wt% of PMMA with respect to the toluene content. A second solution was composited the same way but containing 4wt% of PMMA with respect to the toluene content. The 5wt% and 4wt% solutions were used to fabricate single and double active layers, respectively (see Section 4.1).
Thin layers were produced via spin-coating with a spin-coater SCS G3P-8 from Specialty Coating Systems (Alura Group BV). As a substrate, borosilicate glass (Borofloat 33, Schott AG) with a surface roughness smaller 1 nm was used. The substrates were cleaned for 15 minutes in acetone in an ultrasonic bath, then in isopropanol for 15 minutes in an ultrasonic bath. Directly prior to the spin-coating process, each substrate was dried with a nitrogen gun. 250 µL of solution were added within the first seconds of the spin-coating process with a total length of 60 s. The spin-speed was varied between 500 rpm and 3000 rpm for layer thickness adaption. Afterwards the samples were annealed at 40°C for 5 minutes. [113]

Atomic layer deposition

TiO_2 is used as high refractive index layer of the Bragg structure. The TiO_2 layers are produced with atomic layer deposition (R-200 Advanced, Picosun, Finland) from molecular precursors $TiCl_4$ (purchased from Sigma-Aldrich ($\geq$ 99% $TiCl_4$)) and H_2O. A low temperature process at 100°C allows for compatibility with PMMA. In the deposition process, rinsing and pulse times were: 0.1 s $TiCl_4$ pulse, 4 s rinsing with Ar, 0.1 s H_2O pulse, 6 s rinsing with Ar. [113]
The total number of pulses was 4000 to gain a layer thickness of around 200 nm, whereby

an inhomogeneity of the layer thickness was found within the deposition chamber. However, this inhomogeneity was well analyzed and used for fabricating Bragg structures with different designs in one deposition run.

3.2.2. Nanostructural characterization methods

Spectrophotometer measurements

Reflectance and Transmittance measurements were performed with a spectrophotometer (Lambda 950, PerkinElmer, Germany) from 500 nm to 2445 nm with a step width of 5 nm. An integrating sphere setup was used with a tilt of the sample of 8° to the incident light beam. For calculating the normalized absorptance of the upconverter nanoparticles (Fig. 4.1c) spectrophotometer measurements were performed on the upconverter nanoparticles in toluene solution and in plain toluene. The normalized absorption of the upconverter nanoparticles was calculated from the transmittance and reflectance data, with plain toluene subtracted. The absorptance within 1 µm PMMA (Fig. 4.2), which approximately resembles the total thickness of the active layers in a Bragg structure and reference sample, was calculated via the absorption coefficient extracted from the reflectance and transmittance of a 4.9 mm thick PMMA sample. For the Bragg structure reflectance and design wavelength determination (Fig. 4.9), the incident light beam of the spectrograph was reduced with an aperture to feature a spot of approximately 1 mm diameter on the sample.

Design wavelength determination of Bragg structures

The design wavelength of the Bragg structures was analyzed by fitting the measured reflectance of each analyzed sample point (Fig. 4.9a) to the simulated reflectance (Fig. 4.9b). The reflectance simulation was carried out in an implementation of the transfer matrix method [34]. The determined refractive indices served as input parameters. The angle of incidence was simulated as 8 °, as in the reflectance measurement. [113]

The design wavelength λ_{design} of each measured point on the Bragg structure samples was analyzed by the squared difference $\Delta R(\lambda_{\text{design}})$ of the measured reflectance $R_{\text{exp}}(\lambda)$ to the simulated reflectance curves $R_{\text{sim}}(\lambda)$ at each wavelength λ

$$\Delta R(\lambda_{\text{design}}) = \int_{\lambda=500\,\text{nm}}^{2500\,\text{nm}} \left(R_{\text{exp}}(\lambda) - R_{\text{sim}}(\lambda, \lambda_{\text{design}})\right)^2 d\lambda. \tag{3.44}$$

$\Delta R(\lambda_{\text{design}})$ was calculated for each design wavelength separately, with a binning of 1 nm in λ_{design}. The minimum of all $\Delta R(\lambda_{\text{design}})$, at which simulated and measured reflectance match best, then defines the design wavelength $\lambda_{\text{design}}(R_{\text{exp}})$ of the measured sample point. Figure 4.9c shows $\Delta R(\lambda_{\text{design}})$ for all analyzed sample points.

Spectroscopic ellipsometry

The refractive index of the thin active layers, as well as the refractive index and thickness of the thin TiO_2 layers were determined on a silicon substrate via spectral ellipsometry (Fig. 4.5

and 4.7). The used ellipsometer (M-2000, J.A.Woollam Co.) covers the wavelength range 245 nm to 1700 nm. Ellipsometry measurement cover the angles of 65° to 80° in steps of 5°. For fitting the data the software Complete Ease [121] was used. [113]

Atomic force microscopy

The surface quality, roughness and layer thickness, of the active layers were analyzed with an atomic force microscope (Dimension Edge, Bruker). For the surface roughness determination (Fig. 4.4a), the layer topography was measured with a scan rate of 0.7 Hz, a scan range of 2 µm with 512 lines in x and y direction.
The thickness measurements (Fig. 4.4b and c) were performed by scratching a small cut into the layer and measuring the depth of the valley. The measurement was performed with a scan rate of 0.7 Hz, a scan range of 20 µm with 128 lines along the valley in x-direction and 1/16 of range and lines in y-direction. The depth was calculated as the difference between the mean of the area on the bottom of the valley and of the area on the layer surface. It is important to include the surface roughness in the thickness adaption for a multilayer stack. Taking the mean of all heights worked out very well to gain an overall thickness control for the final production of multilayer stacks. For various spin speeds, mean and standard deviation of the resulting thickness, three to five measurements for each spin speed were fitted. [113]
The surface roughness of complete Bragg structures (Fig. 4.10d) was measured for a 50 µm scan range with 1024 lines in x- and y direction and a scan rate of 0.2 Hz.

Scanning electron microscopy

Single active layer and Bragg structure cross sections were analyzed with a scanning electron microscope (SEM) (Auriga 60, Zeiss). An in-lens detector and 1 kV voltage of the electron beam EHT was used. For single active layer analysis (Fig. 4.3), a thin platinum film was deposited on top of the sample, to ensure good conductivity. Subsequently, focused ion beam was applied to cut into the layer and reveal a cross section. The Bragg structure samples (Fig. 4.10a-c) were first broken mechanically and subsequently sputtered with a thin 3 nm platinum film.

X-Ray diffraction

The crystallinity of thin TiO_2 films (Fig. 4.6) was determined in X-ray diffraction (XRD) measurements (XRD D8, Bruker, equipped with an x-ray source of Cu-anode with a Cu K$\alpha_{1,2}$ radiation (λ = 0.15419 nm). The measurements were performed in the range of 10° to 80° in steps of 0.05°. [113]

3.2.3. Photoluminescence measurements

Upconversion photoluminescence measurement setup

For the UC photoluminescence measurements of the design wavelength scan (Fig. 6.3), excitation wavelength scan (Fig. 6.5) and incident irradiance (Fig. 6.7) scan, an integrating

sphere setup was used (Figure 3.5). A tunable low power 20 mW infrared laser (TSL-510,

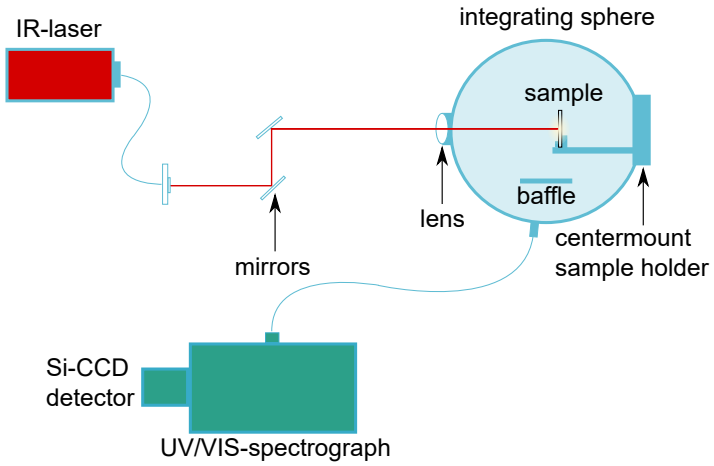

Figure 3.5.: Sketch of photoluminescence measurement setup. [113]

Santec) served as excitation source. All samples were measured in an integrating sphere (819C-SL-5.3, Newport), placed in a center mount holder with a tilt of 4° relative to the incident laser beam. A 75 mm focal length lens was additionally installed at the entrance port of the integrating sphere to avoid unwanted coherence effects in the glass substrate. The signal was detected with a spectrograph (SP2300i, Princeton Instruments, USA), equipped with a blazed grating (150 grooves/mm at a blaze wavelength of 800 nm) and a silicon CCD detector (PIXIS:256E, Princeton Instruments, USA).
To extract the real emitted spectrum of a measured sample, the signal is corrected for the spectral response of setup components like grating, detector and lens. A calibrated tungsten halogen lamp served as excitation source for measuring the spectral response correction function of the setup. [26]

Irradiance determination

For all laser powers and excitation wavelengths used in the experiments of this work, the irradiance of the excitation beam was determined at the sample position. A beam profiler (BP209-IR/M, Thorlabs) was used to measure the laser beam area and a photodiode sensor (PD300-IR, Ophir Photonics) to determine the laser power. Figure 3.6a, shows the Gaussian-shaped beam profile at 1.48 W cm^{-2} irradiance and 1523 nm excitation wavelength. The difference of diameter in x- and y-direction of the Gaussian profile of all measurements is smaller than 0.7%. The laser irradiance was calculated only from the FWHM region in x-direction. Because of the non-linear dependence of UC on the irradiance, the higher irradiance region within the gaussian-shaped laser profile contributes significantly more to the measured UC signal. Therefore, a more exact determination of the effective irradiance is given with this approach. Figure 3.6a displays a FWHM area of 0.27 mm^2, corresponding to a diameter of 0.59 mm. The diameter slightly varies for a varied power and excitation wavelength in the range of 0.57 mm and 0.61 mm. To resemble the same region as the

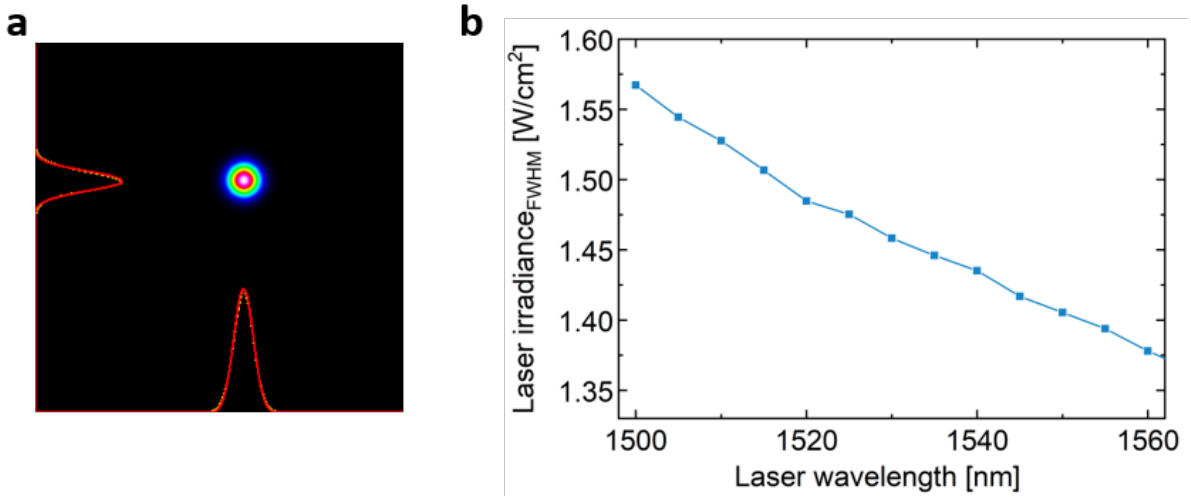

Figure 3.6.: Determination of laser irradiance. **a** Laser beam profile. **b** Determined laser irradiance for varied laser wavelength. [113]

FWHM laser area, the total laser power P_{total} was scaled to the fraction of power P_{FWHM} within the FWHM region of a circular normal distribution, given by:

$$P_{\text{FWHM}} = P_{\text{total}} \cdot 0.5 \tag{3.45}$$

Additionally scaling the area by the tilt of the samples of 4°, the irradiance is given by

$$I_{\text{in,FWHM}} = \frac{P_{\text{FWHM}}}{A_{\text{FWHM}}/\cos(4°)} \tag{3.46}$$

At 1523 nm excitation wavelength, the irradiance was determined for the power range from 1 mW to 10 mW in steps of 0.5 mW and at an excitation power of 10 mW in the excitation wavelength range 1500 nm to 1560 nm in steps of 5 nm (Figure 3.6b). All needed values between these measurements were interpolated. [26]

Upconversion photoluminescence measurements

The UCPL measurement was performed at the same five points on each sample that were characterized in spectrophotometer measurements (Figure 4.9a). For both, design wavelength scan (Section 6.3) and irradiance scan (Section 6.5), UCPL spectra were performed with 200 s integration time, for the excitation wavelength scan (Section 6.4) with 60 s integration time and for the The UCPL$_{\text{rel}}$ was evaluated as the ratio of integrals over the UCPL spectra of Bragg structure and reference within the wavelength range of 930 nm to 1020 nm (compare to Fig. 6.3a). [26] For the higher UC emission around 814 nm, the UCPL spectra are integrated in the spectral range of 775 nm to 850 nm.

Calculation of mean agreement of measurement and simulation

To quantify the mean agreement of measured and simulated enhancement of the UC photoluminescence (UCPL$_{\text{rel}}$) for all 2480 measurements with separate parameter combinations,

the measured $UCPL_{(rel,measured)}$ is compared to the exact same parameters in simulation $UCPL_{(rel,simulated)}$, with a binning of 1 nm in design wavelength and featuring the exact irradiance of the experiment. The mean and standard deviation of $UCPL_{(rel,measured,i)}$ divided by $UCPL_{(rel,simulated,i)}$ is then calculated for all measurements i within the evaluated group of the measurements.

Upconversion photoluminescence measurements under a varied incident angle

For UC photoluminescence measurements with a varied incident angle the same excitation and detection device was used as described in the integrating sphere measurement setup, however, now no integrating sphere was used. A 25.4 mm focal length lens was installed 110 mm in front of the sample to avoid unwanted oscillations in the signal caused by oscillations in the glass substrate. The excitation angle is scanned from 0° to 75° in steps of 5° and the excitation wavelength from 1500 nm to 1560 nm in steps of 1 nm. Detection is performed at 18° relative to the surface normal of the sample, while the signal is coupled in for an opening half cone of 7°. The data is again corrected with a spectral response correction function. From the laser characterization the FWHM irradiance at 1523 nm excitation wavelength, including the beam widening due to the lens, is 0.2546 W cm^{-2} on the sample surface. [113]

Correction of simulation and experiment for upconversion photoluminescence under a varied incident angle

To be able to compare simulation and experiment, both data needs to be corrected to finally feature a common output:
i) The simulation is carried out for at a number of binning points, which are identical at each incident angle α. Therefore, the measured UCPL signal $S_{measured}(\alpha)$ is normalized to feature at every α the same area and light path as at α = 0°. The normalized signal is thus calculated as $S_{normalized}(\alpha) = S_{measured}(\alpha) \cdot \cos^2(\alpha)$.
ii) In experiment, the irradiance reduces by a factor of $\cos(\alpha)$ towards higher angles, as the laser spot on the sample grows larger. This is accounted for by simulating the UCPL at each excitation angle with the adapted irradiance $I(\alpha) = I(0°) \cdot \cos(\alpha)$ for 0° < α < 75° in steps of 1°.
The following differences are neglected to simplify the analysis:
iii) The excitation wavelength is varied in simulation from 1500 nm to 1560 nm in steps of 1 nm, all with the same irradiance as at $\lambda_{excitation}$ = 1523 nm $I(0°) = 0.2546$ W cm^{-2}. The slight difference in irradiance of approximately +6% at 1500 nm and -7% at 1560 nm in experiment (see Fig. 3.6) is neglected in simulation.
iv) The simulation is carried out for an ideal Bragg structure, thus neglecting the production inaccuracies. However, from section 5.1.1 it is known that this has only little impact on the simulation result.

3.3. Contributions to this chapter

Modeling (in chronological order)

Stefan Fischer

- developed the rate equation modeling framework for upconversion in homogeneous media [28], together with many people in the team Novel Solar Cell Concepts, led by Jan Christoph Goldschmidt at Fraunhofer ISE
- measured the experimental input parameters of the upconversion process for the rate equation model [28]
- developed the first concepts of coupling plasmonic effects with the rate equation model [30, 122]

Barbara Herter

- extended the rate equation model for a photonic environment [31]

Johannes Gutmann

- developed the histogramming method for calculating the local density of optical states (LDOS) and fractional local density of optical states (FLDOS) [33]

Clarissa L. M. Hofmann (Author)

- implemented a more precise way of calculating the LDOS, based on Gutmanns work [32]
- implemented production in inaccuracies of the single layers within the Bragg structure

Emil H. Eriksen

- rewrote the complete simulation code in Python, optimizing speed, precision, way of calculating production inaccuracies, output format and compatibility of the different simulation steps, as well as implementing new varied parameters, such as the incident angle and directionality of emission
- this version of the code can be found in the publication with shared first authorship Hofmann, Eriksen *et al.* [34]

Clarissa L. M. Hofmann (Author)

- developed the final evaluation of the upconversion emission, taking into account directionality of emission
- published the final simulation code open access to the research community on the Fraunhofer database Fordatis `http://dx.doi.org/10.24406/fordatis/110.2`

Jan Christoph Goldschmidt

- conceived of research questions that led to the development of all the above works
- supervised and significantly contributed to the development of all simulation code

Experimental

Contributions to experimental processes can be found in Section 4.5, the contributions to the chapter Fabrication and characterization of photonic upconverter devices.

CHAPTER 4

FABRICATION AND CHARACTERIZATION OF PHOTONIC UPCONVERTER DEVICES

The main purpose of this work is to experimentally validate a theoretical modeling framework describing photonic effects on upconversion (UC) dynamics. These photonic effects are complex and they strongly depend on material parameters and production accuracy. Therefore, as a photonic structure, a simple Bragg structure was chosen in order to be able to precisely control all parameters of the structure. Within the experimental part of this work, the main emphasis is on an exact characterization of all material parameters that enables a careful design and characterization of fabricated photonic upconverter devices. This chapter presents the design and characterization, first of the active layer of the Bragg structure that contains the upconverter material, secondly of the high refractive index layer and finally of the Bragg structure samples with embedded upconverter nanoparticles.

This chapter is based on parts, especially of the supplementary information of the following publication:

C. L. M. Hofmann, S. Fischer, E. H. Eriksen, B. Bläsi, C. Reitz, D. Yazicioglu, I. A. Howard, B. S. Richards and J. C. Goldschmidt, Experimental validation of a modeling framework for upconversion enhancement in 1D-photonic crystals, *Nature Communications* **12**, 1-10 **(2021)**

Contributions to this chapter of the author, co-authors and others can be found in section 4.5.

4.1. Design of active layers

4.1.1. Core-shell upconverter nanoparticles

The upconverter material for this work above all has to feature a high UC quantum yield in order to absorb as much sunlight as possible and subsequently emit a large fraction as upconverted photons. Furthermore, it needs to be in a form such that it can be embedded into thin layers of a nanoscale multilayer structure. The most efficient and best to process choice is using the upconverter in the form of core-shell upconverter nanoparticles (UCNPs). The UCNPs used in this work are custom made as reported in [59], featuring a high UC quantum yield (UCQY) of 2.0% [59] at a low incident irradiance of 0.43 W cm^{-2}. Throughout literature, to my knowledge, no other UCQY of UCNPs is published, measured at such a low irradiance. This makes a reliable comparison difficult. Hudry *et al.* discuss properties of UCNPs in detail in their review paper [25]. A measured UCQY of 5% at 30 W cm^{-2} incident irradiance for β-$NaYF_4$:Yb,Er core shell UCNPs reported by Homann *et al.* [126] ranges among the highest reported UCQYs. Even when extrapolating the UCQY curve from Homann *et al.* down to the very low irradiance regime to 0.43 W cm^{-2}, a lower UCQY is found than the 2% reported by Fischer *et al.* [59]. Therefore, while I detailed ranking is not possible due to the variety of materials and characterization parameters of UCNPs, I can assume that the particles I worked with range among the best performing UCNPs available. The UCNPs are made of hexagonal sodium yttrium tetraflouride (β-$NaYF_4$) with a 25% doping of trivalent erbium (Er^{3+}) (β-$NaYF_4$:Er^{3+}). An inert β-$NaLuF_4$ shell prevents quenching of excited ions at the core surface and thus increases the efficiency. Oleic acid ligands are attached to the shell to improve embedding the UCNPs into the polymer layer (Fig. 4.1a).

Figure 4.1b shows a scanning electron microscopy image of the used UCNPs, featuring a large and uniform diameter of ≈ 40 nm.

In simulations, the UC process of β-$NaYF_4$:Er^{3+} is modeled inside the photonic structure. The model has been developed for a bulk upconverter material [28]. In Fig. 4.1c, the normalized absorption of the bulk material, that serves as input in simulations, as well as of the UCNPs used in experiment is plotted (Methods Section 3.2.2). One can see that the spectral dependence of both materials agrees very well. [113]

4.1.2. Layer composition

The host material for the UCNPs is required *i)* to ideally have no, or realistically no significant, absorption in the range of the UC absorption and emission, *ii)* to allow for embedding of the UCNPs into the layer and achieve a reasonably uniform distribution within the layer, *iii)* to allow for a simple and precise solution based production process with the possibility to produce layers of different thicknesses. *iv)* to feature a very similar refractive index as the UCNPs to avoid scattering effects within the active layers, which would diminish the photonic effects.

A material that fulfills all these requirements, not ideally but sufficiently, is Poly(methyl methacrylate) (PMMA). The active layers of PMMA with embedded UCNPs were produced via spin-coating from a toluene based solution (Methods Section 3.2.1). Via spin-coating, very high layer uniformity and thickness control can be reached, while at the same time a

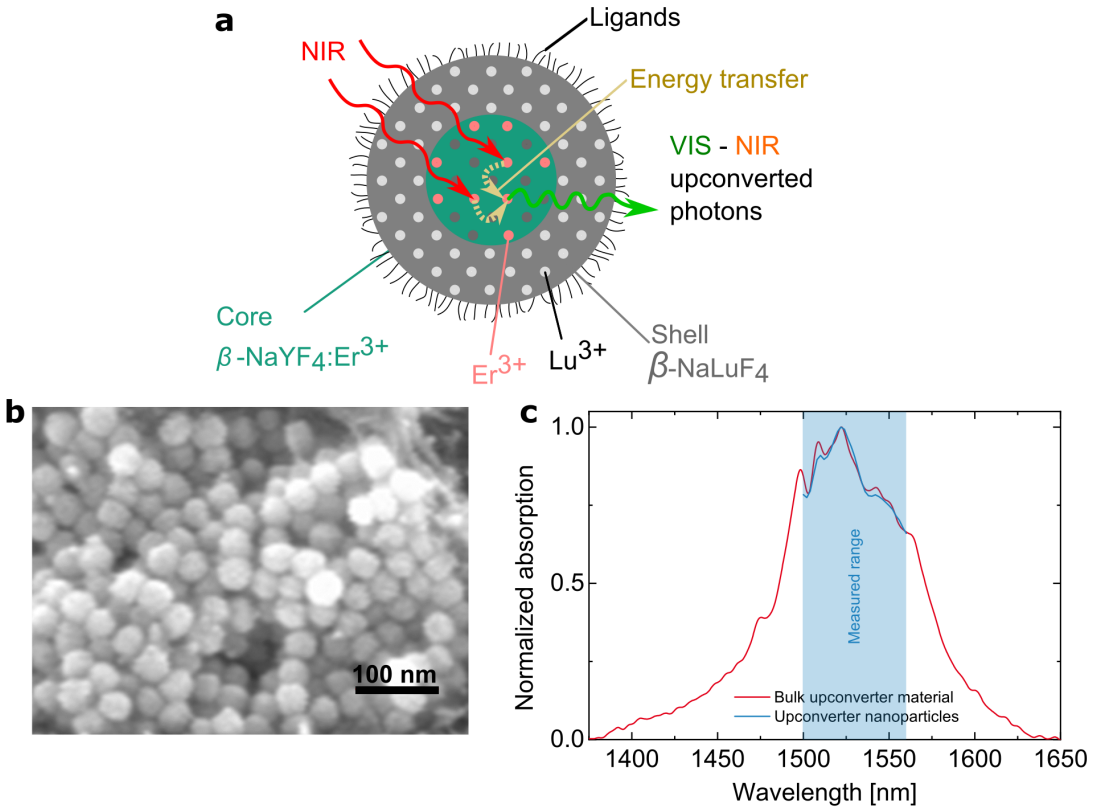

Figure 4.1.: Custom made core-shell upconverter nanoparticles (UCNPs). **a** Schematics of the core-shell UCNPs made of β-$NaYF_4$:Er^{3+}, converting near infrared (NIR) to NIR and up to visible (VIS) photons in the active core. The inert shell made of $NaLuF_4$ prevents losses due to surface quenching. **b** Image of the UCNPs taken with a scanning electron microscope (SEM). **c** Normalized absorptance of β-$NaYF_4$:Er^{3+} for the simulated bulk material and the UCNPs used in experiment. (Graph **a** and **b** adapted from [26], graph **c** adapted from [113])

variation of the layer thickness can be easily done. In the following, the material analysis, fabrication details and layer characterization is presented.

4.1.3. PMMA absorption

Fig. 4.2 shows the absorptance in a 1 µm thin PMMA layer (Methods Section 3.2.2), which approximately is the total thickness of the active layers in the Bragg structures which are experimentally realized in this work. Within the absorption range of the upconverter around 1523 nm, PMMA depicts a negligible absorption of maximally $1.4 \cdot 10^{-4}$ in the complete absorption range and maximally $2.1 \cdot 10^{-5}$ in the range that the UC photoluminescence measurements were performed in. In the emission range of the upconverter around 984 nm and 814 nm, the PMMA absorptance is also negligible. Therefore, for our experiments, the PMMA absorption does not have a significant influence. However, if the number of layers within the Bragg structure is significantly increased, one might want to consider using a different polymer.

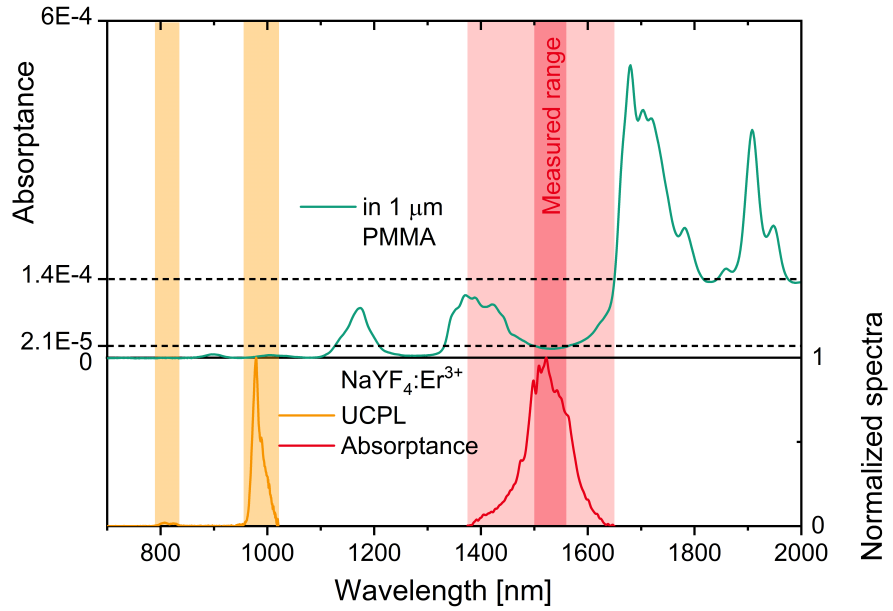

Figure 4.2.: Spectral position of absorptance and upconversion (UC) photoluminescence in the active layer. Absorptance in a 1 µm thin PMMA layer; normalized UC photoluminescence (UCPL) and absorptance in the upconverter β-$NaYF_4$ doped with 25% Er^{3+} for the 984 nm and 814 nm emission. [113]

4.1.4. Layer uniformity and nanoparticle distribution

To investigate the effects of a photonic structure on UC and compare these to a modeling framework, the photonic structure needs to be fabricated as precise as possible. Therefore, all layers within the structure need to be uniform. The photonic effects differ significantly at different positions in the active layers. The simulation describes the UC process as an average over all positions within the active layers. To gain a fair comparison, the UCNPs also need to be distributed randomly within the active layers. Therefore, the distribution of the UCNPs was analyzed with a scanning electron microscope (SEM) on layer cross sections (Methods Section 3.2.2). In Fig. 4.3 the layer homogeneity and distribution of UCNPs within

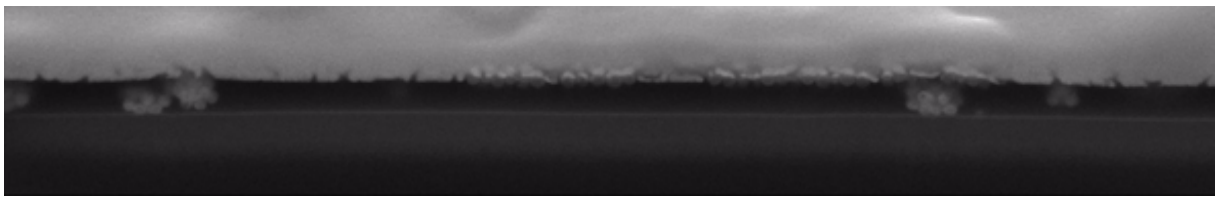

Figure 4.3.: Distribution of upconverter nanoparticles (UCNPs) in an active layer cross section measured with a scanning electron microscope (SEM). This image is provided without a scale bar, as it was taken as a series of images to create a 3D film of the UCNPs distribution within the layer, with no scale bar provided. The approximate diameter of the UCNPs is 40 nm.

a single active layer can be seen. The UCNPs form small clusters and are positioned at the surface of the layer. A reason for this behaviour could be the polymerisation when the layer dries within the spin-coating process. Exposing the solution to an ultrasonic bath directly prior to spin-coating led to a better layer quality with smaller nanoparticle clusters in the final

production of Bragg structures.

The same analysis, also with respect to the UC photoluminescence was performed with different amounts of UCNPs with respect to the PMMA, varying from 10wt% to 70wt%. As no significant improvement could be found, I kept the initial composition with 25wt% UCNPs. Furthermore, Chlorobenzene was tested as solvent with respect to the smoothness and precision of layer thickness, compared to layers produced form a Toluene based solution. Again, no significant difference was found, such that I proceeded working with Toluene as the environmentally more reasonable solution.

To try and exploit the UCNPs' position on the surface of the layer, two different types of layers were produced: one simple single layer and a double layer made of two active layers, spin-coated right on top of each other, with an annealing step in between. Both layers together make up one active layer. The reason for testing this procedure was to see whether the UCNPs in the first layer stay on the surface and thus in the final layer are positioned right in the center of the layer. Also, the overall distribution of UCNPs within the double active layer is different and possibly more favorable with respect to the photonic effects of the Bragg structure. From simulations it is known that in the center of the active layers, the photonic effects are strongest. Thus, a positioning of the UCNPs more towards the center could increase the UC photoluminescence due to stronger photonic effects. The distribution of the UCNPs in the single layer and the double layer is shown in scanning electron microscopy images of Bragg structure cross sections in Fig. 4.10.

4.1.5. Layer thickness adjustment and roughness

To investigate the surface quality, the roughness and layer thickness, atomic force microscopy measurements were performed on single layers (Methods Section 3.2.2). Figure 4.4a shows a surface topography of an active layer with 25wt% UCNP content. The UCNPs form islands of hexagonally organized monolayers that partly stick out of the PMMA layer surface. The measured roughness of the surface within the displayed graph is 5.2 nm. Considering that the UCNPs have a diameter of about 40 nm, this is a good achievement. Apart from this roughness due to UCNPs, the layer surface is very smooth.

To achieve highly uniform layers with an even distribution of UCNPs, it was best to choose a spin-speed in the range of 500 rpm to about 3000 rpm. The target thickness around 300 nm for the single active layers was found in the needed rpm range with a solution with 5wt% PMMA with respect to the toluene content. The double active layers, made up by two active layers spin-coated on top of each other, each spin-coated layer needs to be half the thickness. Therefore, a less viscose solution with 4wt% was chosen to stay within the required rpm range. In the later fabrication of Bragg structure samples, the spin-coated layers are annealed within the atomic layer deposition process of the high refractive index layers. Annealing affects therefore need to be considered in the thickness adaption. The annealing time of the spin-coated layers was varied between 5 minutes and 240 minutes and no significant change in the layer thickness was found before and after annealing. Therefore a short annealing time of 5 minutes was chosen for the thickness adaption process.

Furthermore, the thickness of a spin-coated layer significantly depends on the adhesion to the substrate material. For the production of a Bragg structure, the adaption is therefore needed on a TiO_2 layer. For the production of reference samples, the first active layer is

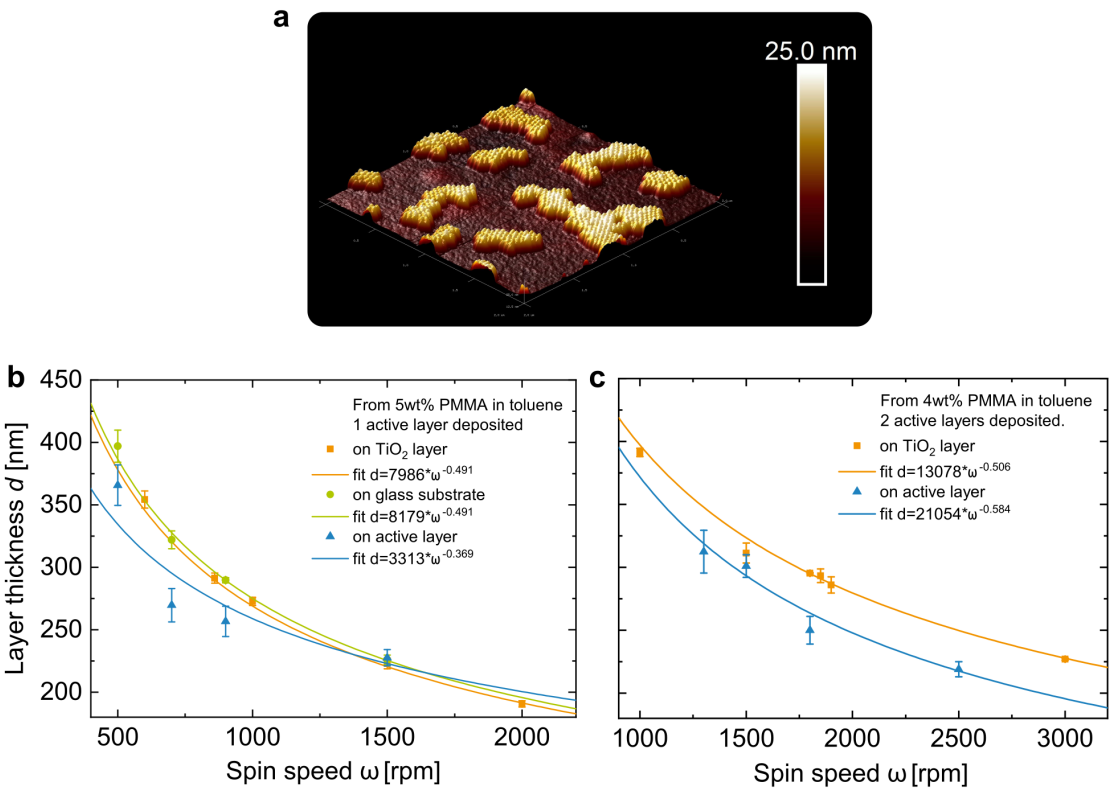

Figure 4.4.: Thickness adaption of active layers. a Topography of single active layer measured with an atomic force microscope (AFM), showing a small roughness of 5.2 nm due to upconverter nanoparticles (UCNPs) at the layer surface for a 2 µm edge length. **b, c** Thickness adjustment in the spin-coating process of active layers on the different substrate materials for single active layers (b) and double active layers (c). (Graphs **a** and **b** adapted from [113])

spin-coated directly on the glass substrate, the following three active layers are spin-coated right on top of the other active layers. [113]

For the thickness adjustment of both, the single and double layers, a number of layers with different spin speeds were produced on each substrate material. The thickness was measured at a small scratch in each layer with an atomic force microscope.

An empiric model, developed in [127] was applied to link the coating thickness d (mean and standard deviation of each parameter set) to the spin speed ω_{spin} and the concentration C as

$$d = D \cdot C^{\alpha} \cdot \omega_{\text{spin}}^{\beta} \tag{4.1}$$

with the empirically determined parameters D, α and β. For the purpose of linking spin speed to final thickness, it is sufficient to fit the parameters $D \cdot C^{\alpha}$ as one variable. [113]

Figure 4.4b and c show the performed thickness adaption for each substrate, TiO_2, glass and an active layer, for the single and double active layers, respectively. The adaption on glass for the double active layer reference samples was omitted because the layer thickness of the references is not as crucial and from the adaption of the single active layers it was evident that the resulting thickness is almost identical for the TiO_2 and glass substrate.

The mean of all standard deviations from this analysis of the active layer thickness on TiO_2 are 4.2 nm (from 18 measurements in total) for the single layer and 4.1 nm (from 15 measurements in total) for the double layer. As the calculated values of the two different types of layers are so close, only one value of 4.15 nm is implemented in simulation, representing both types of active layers. This deviation corresponds to a 1.3% for a 315 nm thin layer.

4.1.6. Refractive index

The refractive index was analyzed using spectral ellipsometry (Methods Section 3.2.2). I chose to fit the active layer with a simple absorbing Cauchy model with a surface roughness [121]. For the wavelengths 1700 nm to 2000 nm, the refractive index data was extrapolated using a Cauchy model. This polymer-nanoparticle composite material with various low absorbing spectral regions is very difficult to fit and a more complex model did neither improve the quality of the fit nor the reliability of the result. The roughness thickness was in the range of 5 nm, slightly less but in agreement with the roughness determined in atomic force microscopy measurements. With this model, a good agreement of fit and measurement was found, both thickness and real refractive index were well determined with a mean square error of 13.6 for a 241.6 nm thin layer (Fig. 4.5a). I assume that the determined real refractive

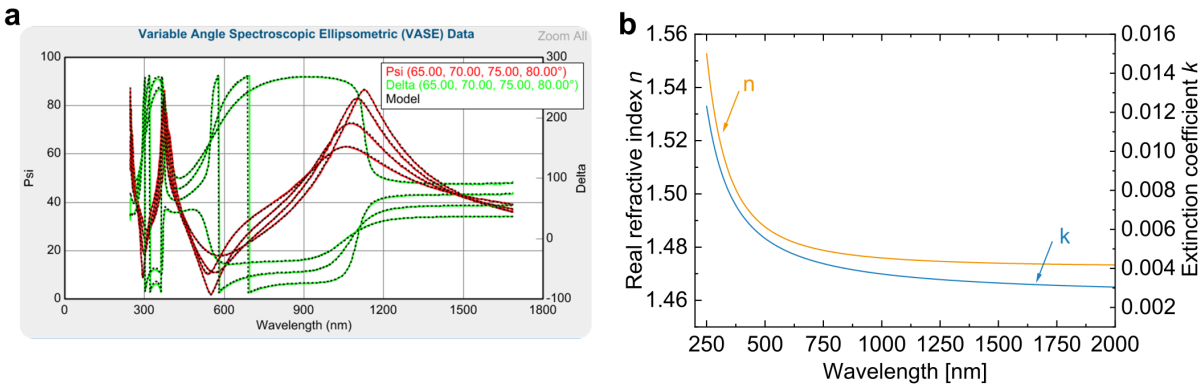

Figure 4.5.: Ellipsometry data analysis for refractive index and extinction coefficient of the active layer material, PMMA with embedded upconverter nanoparticles. a Fit on ellipsometry measurement data of one active layer with a Cauchy model. **b** Refractive index and extinction coefficient (b from [113]).

index n is very precise, with a value of 1.474 at 1523 nm, shown in Fig. 4.5b. It also matches the refractive index of the upconverter material well with $n \approx 1.5$ [124]. However, the extinction coefficient cannot be determined precisely with this model. The absorption is very low and has a complex pattern with various absorbing regions within the upconverter material. Also from photospectrometer measurements, it is known that the absorptance of the utilized UCNPs is quite low, even in the main region of interest around 1523 nm. In fact, the precise value could not be determined. Considering the absorption coefficient of a bulk upconverter material [28], the absorptance of one active layer can be estimated to be below 0.01%. Therefore, as input in simulations, only the real refractive index is used, while the absorption is neglected, setting $k = 0$ for the simulation of the energy density within the Bragg structure. For a later application, however, this means that the number of layers and the loading of UCNPs in the layer would need to increase. [113]

4.2. Design of high refractive index layers

4.2.1. Layer composition

The high refractive index layer in the Bragg structures has to fulfill a number of requirements: *i)* it should be transparent in the absorption and emission range of the upconverter. *ii)* the highest possible refractive index because the photonic effects within the Bragg structure are strongest when the refractive index contrast between the high and low refractive index layer material is largest. *iii)* excellent layer uniformity and thickness control. The optical thickness of the high refractive index layer is even more vulnerable to production inaccuracies than the low refractive index layer, which has a larger effect on the optical properties of the final Bragg structure. *iv)* fabrication needs to be compatible with the organic contents in the active layer material, therefore only low temperature processes are possible.
A very good choice that almost ideally fulfills these requirements is TiO_2 fabricated with atomic layer deposition (ALD) (Methods Section 3.2.1). A low temperature deposition at only 100°C was used to insure compatibility with PMMA in the active layers. In the following, the layer characterization and thickness adaption is presented.

4.2.2. Crystallinity

The following passage is partly taken from my own publication ref. [113]. At the low deposition temperature of 100°C within the ALD process, the TiO_2 layers are expected to be amorphous. Compared to crystalline thin layers, an amorphous thin layer is expected to depict the lowest surface roughness.
Therefore, I analyzed single TiO_2 layers and also the final Bragg structures with respect to their crystallinity using X-Ray diffraction (XRD) (Methods Section 3.2.2). Figure 4.6 shows the measurement of a plain glass substrate (***i***), glass with one active layer (***ii***), glass with one TiO_2 layer (***iii***) and a Bragg structure with 4 layers of TiO_2 and 3 active layers (***iv***). For anatase TiO_2, usually forming at temperatures above 200°C, a dominant reflection on the A101 bulk anatase plane around 25.5° [128–132] is expected. Both, the single TiO_2 layer (c) and the Bragg structure (d) do not depict this reflection and the TiO_2 films are amorphous, as expected for our low deposition temperature. The broad peak around 22°, which is visible in all four graphs, stems from the borosilicate glass substrate [133]. The narrow peaks around 53° and 17° can be attributed to reflection on the 100- and 211-crystal plane of β-$NaYF_4$:Er^{3+}, according to the JCPDS card (No.28-1192) [134]. These peaks are visible in graph (***ii***) where the measured sample contains one active layer, and more pronounced in graph (***iv***) where the measured sample contains three active layers.

4.2.3. Refractive index

Spectroscopic ellipsometry measurements on thin TiO_2 layers were carried out on a silicon substrate (Methods Section 3.2.2). To fit the data, I applied a Cody-Lorentz model [121], as it describes amorphous materials with a broad Lorentzian absorption. In the model, a surface roughness that was fitted to 1 nm to 2 nm is included, which is in good agreement with a measured surface roughness of $\approx$ 2 nm in atomic force microscopy topography

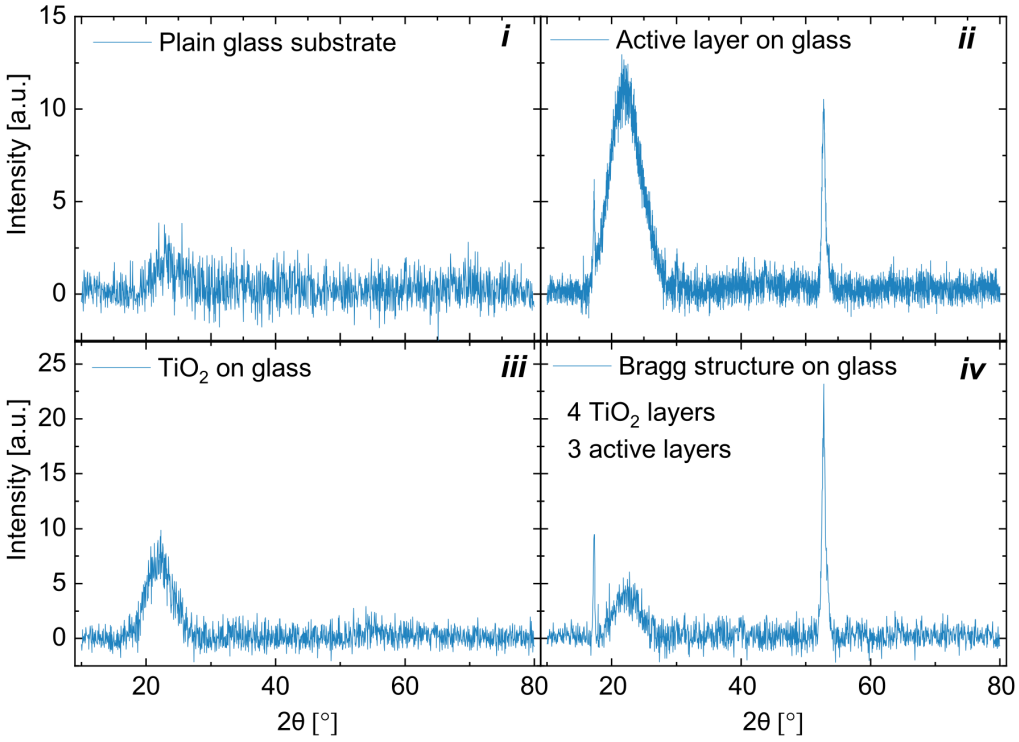

Figure 4.6.: Determination of TiO_2 crystalinity. X-ray diffraction measurements of only a glass substrate (***i***), one active layer on glass (***ii***), one TiO_2 layer on glass (***iii***) and a Bragg structure made up of four TiO_2 layers and three intermediate active layers on glass (***iv***). [113]

measurements. The fit describes the measured data very well with a mean square error of 6.0 for a 202.0 nm thin TiO_2 film (Fig. 4.7a). The applied model allows for a very precise fit of

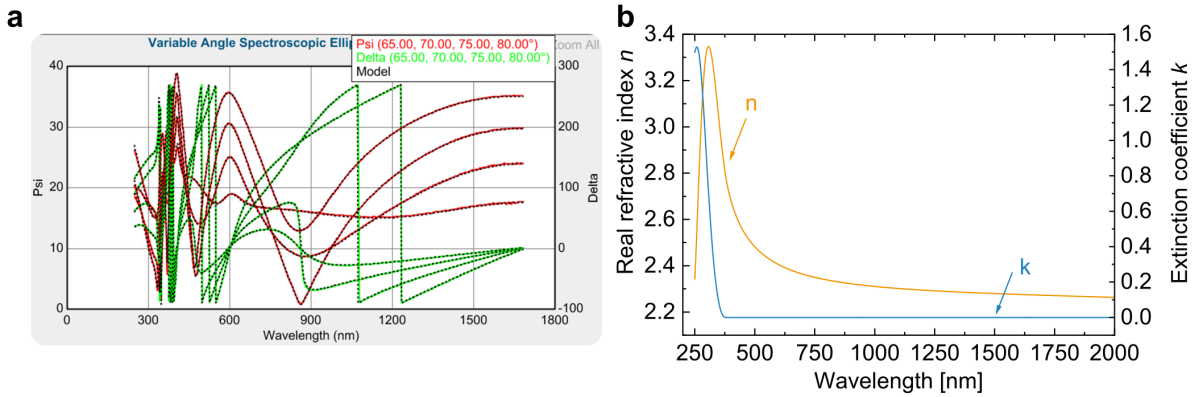

Figure 4.7.: Ellipsometry data analysis for refractive index and extinction coefficient of TiO_2. a Fit on ellipsometry measurement data of one TiO_2 layer with a Cody Lorentz model.**b** Refractive index and extinction coefficient. (Graph **b** adapted from [113])

both refractive index and layer thickness. Figure 4.7 shows the fitted refractive index. The real refractive index features n = 2.279, the extinction coefficient k = 0 at 1523 nm wavelength. Considering the low deposition temperature of only 100°C, the refractive index n = 2.279 is

relatively high. In the final Bragg structures the large refractive index contrast between low and high refractive index layer is expected to show well detectable, high photonic effects.

4.2.4. Layer thickness adaption

The layer thickness of TiO_2 was determined in spectroscopic ellipsometry measurements. In the atomic layer deposition (ALD) chamber, 30 glass substrates of 25 mm times 25 mm size were placed on an 8 inch silicon support wafer (Fig. 4.8). The resulting TiO_2 thickness

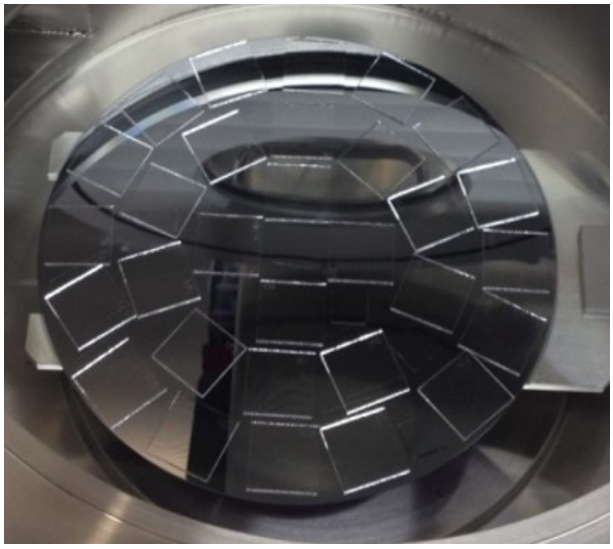

Figure 4.8.: Sample positioning in atomic layer deposition chamber for production of TiO_2 layers. [113]

in one deposition run was determined at two points b and d on each sample (Fig. 4.9a). Within the deposition chamber, the TiO_2 layer thickness was found to vary slightly in the range from 189 nm to 213 nm. This stable inhomogeneity was favorable because it allowed for a controlled production of different Bragg structure designs in one deposition run. [113]

In simulation, the layer thickness variation is included. The input parameter was determined as the standard deviation of the TiO_2 layer thickness on the silicon support wafer, measured with spectroscopic ellipsometry. As the most reliable thickness fits are obtained on a silicon substrate, a new silicon substrate wafer was used for each deposition run in the Bragg structure fabrication (except the first, when the approach had not yet been decided). At one distinct point in the deposition chamber, the layer thickness was measured on all four substrate wafers. Mean and standard deviation were drawn from the four measurements. In total, 16 positions within the deposition chamber were analyzed separately and subsequently the mean of all standard deviations was calculated.

This mean standard deviation of 1.53 nm, corresponding to 0.8%, calculated from 64 measurements in total, served as input in simulations for the standard deviation of the Gaussian distribution in the layer thickness variation [113].

4.3. Design of optimized Bragg structures

Composition of the multilayer structure

The fabrication of Bragg structure samples, was carried out by alternating the processes of atomic layer deposition for TiO_2 and spin-coating for active layers in one glovebox in Argon atmosphere to reduce contamination of the samples. Each sample was placed at a distinct position in the atomic layer deposition chamber (see Fig. 4.8) and for each precisely determined layer thickness of TiO_2 (Section 4.2), the matching active layer thickness was spin-coated to gain the same optical thickness of both layers and therefore a defined design wavelength within the Bragg structure. In total, 30 Bragg structure samples were fabricated. 11 of the samples were made with smaller UCNPs (purchased from CANdots), to test whether these would result in a more homogeneous active layer with less roughness than the larger custom made UCNPs. However, the UC signal from the purchased UCNPs was so small that they were not further characterized. 19 Bragg structure samples were made with the custom made, highly efficient UCNPs (Section 4.1), 9 with three active layers and 10 with four active layers, to compare the strength of the photonic effects. In the samples with only three active layers, the photonic effects are visible. However, as expected, they are much more pronounced and hence better to characterize in the Bragg structures with four active layers. Therefore, in this thesis, only the characterization of eight fabricated Bragg structure samples with four active layers is presented (two of this batch were used for other characterization). The presented optimized Bragg structures are made of five TiO_2 layers and four intermediate active layers. The simulated maximum UCPL enhancement, due to the photonic effects of the Bragg structure, appears at 1855 nm design wavelength. The corresponding layer thicknesses are 203 nm for TiO_2 and 315 nm for the active layers. The eight samples with four active layers are designed with target design wavelengths right at, as well as longer and shorter than the expected maximum enhancement (see Fig. 6.3).

4.3.1. Composition of reference samples

Each reference is composed of a multilayer stack of only the active layers of the corresponding Bragg structure. This way, the reference contains the same amount of upconverter material without the photonic structure around it. The reference samples are fabricated by spin-coating the active layers of the corresponding Bragg structure right on top of each other. Thereby, the target thickness of the active layers in Bragg structure and reference are identical. The spin-coating parameters were adapted for each substrate material separately (Fig. 4.4). [26]

4.3.2. Design wavelength determination

The following passage is partly taken from my publications ref. [26] and ref. [113]. For this study, the most important properties of the Bragg structure are the existence and position of the photonic bandgap, represented by the characteristic reflectance (Fig. 4.9b). The position of the reflectance peak, and therewith the first photonic bandgap, is determined by the design wavelength (λ_{design}) that defines the thickness $d_i = \lambda_{\text{design}}/4n_i$ of each layer i with

refractive index n_i. The λ_{design} slightly varies throughout each sample. Therefore, on each of the eight Bragg structures, five distinct points were characterized (Fig. 4.9a), such that in total 40 separate designs were analyzed. Figure 4.9b shows the simulated reflectance

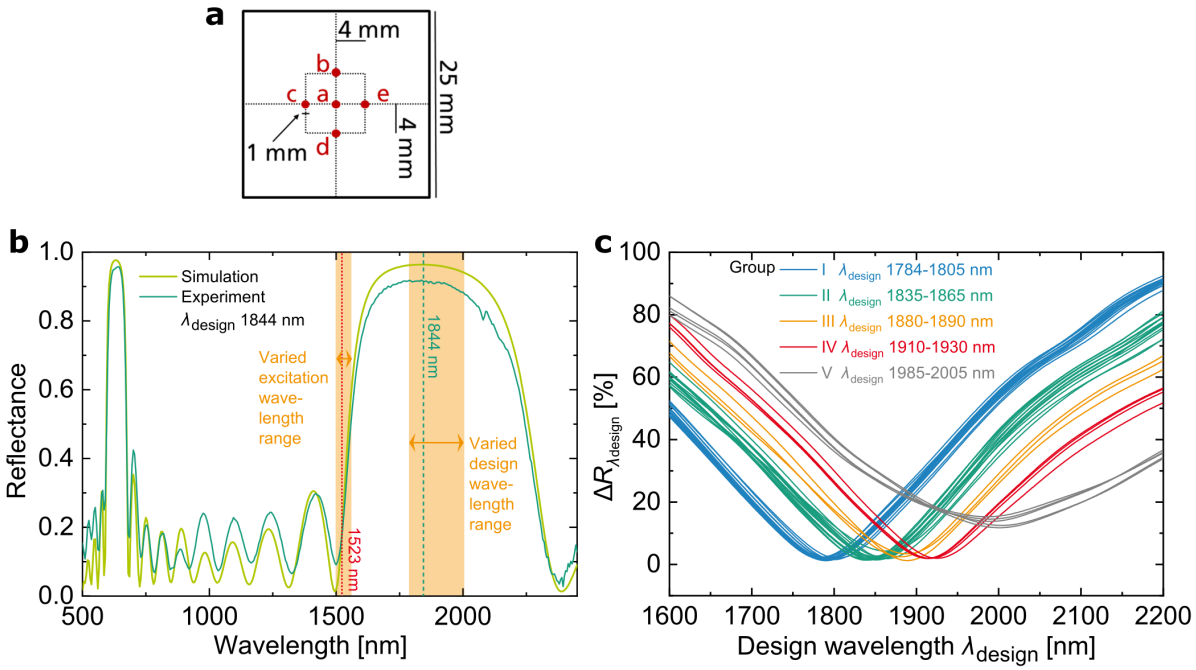

Figure 4.9.: Determination of design wavelength of Bragg structure via reflectance analysis. a Sample dimensions and measurement areas of the five small analyzed points a-e. **b** Reflectance of a fabricated Bragg structure with the matched simulated reflectance at a design wavelength λ_{design} = 1844 nm. The 40 investigated sample designs range from an 1784 nm $\leq \lambda_{\text{design}} \leq$ 2005 nm. For UCPL measurements, the excitation wavelength is varied from 1500 nm to 1560 nm. **c** Square difference $\Delta R_{\lambda_{\text{design}}}$ of the simulated and measured reflectance for the design wavelength determination of each sample and measured points a-e. For all 40 investigated designs, a distinct minimum was found and thus a λ_{design} could be determined. (Figure adapted from [113])

for an exemplary Bragg structure with a determined λ_{design} = 1844 nm. The position of the reflectance peak and side lobes in the measured and simulated reflectance are in good agreement. From this agreement, it can be concluded that the fabricated Bragg structure is indeed very close to the target design. However, there are two slight deviations visible between simulation and experiment. One is the deviation of the side lobes, which stem from slight deviations in the single layer thicknesses in experiment due to small production inaccuracies. The other is the height of the main reflectance peak, which could be due to the choice of white standard in the reflectance measurement. However, this feature is not relevant for this investigation. Fitting the measured to the simulated reflectance, the exact design wavelength of each evaluated sample point was determined. Figure 4.9c shows the squared difference $\Delta R_{\lambda_{\text{design}}}$ (equation 3.44) for all analyzed sample points. All curves show a well-defined minimum that clearly determines the design wavelength of each point on all Bragg structures ($\lambda_{\text{design}}(R_{\text{exp}})$). As can be seen, the sample points with λ_{design} around 2000 nm depict the largest deviation from simulation. This is due to one layer showing a

quite large difference to the target thickness due to a slight instability in the spin-coating process for this layer. However, the overall design wavelength of these Bragg structure can be clearly defined.

With the chosen sample designs, the photonic effects, ranging from the expected maximum with an excitation at the photonic band edge, to an expected suppression can be investigated. The photonic effects on UC in dependence on λ_{design} are presented in Fig. 6.3.

4.3.3. Multilayer uniformity and nanoparticle distribution

Figure 4.10a shows an image of a Bragg structure cross section of a single active layer

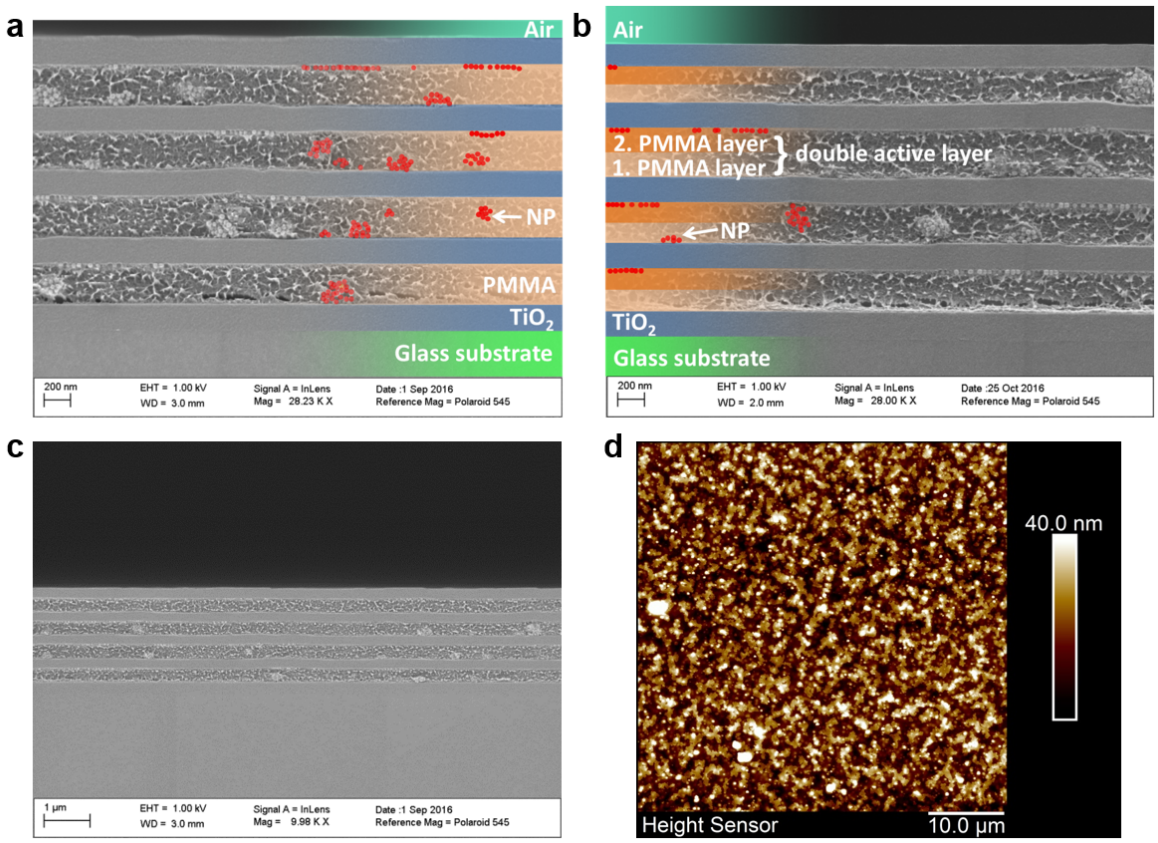

Figure 4.10.: Layer uniformity and roughness of Bragg structures. a,b Scanning electron microscope (SEM) image of realized 1D-photonic structures made of TiO_2 and PMMA with embedded upconverter nanoparticles (UCNPs) as a single active layer (a) and a double active layer (b). **c** SEM image of the single active layer design displaying a large cross section, demonstrating the high uniformity. **d** Atomic force microscopy scan of the Bragg structure surface roughness [113]. (Graph **a** adapted from [26], graphs **c** and **d** adapted from [113])

design, measured with a scanning electron microscope (SEM). In the SEM image, the different constituents as well as the precision of production, layer uniformity and smoothness can be seen very clearly. In the active layers, fringes are visible, which stem from the degradation of PMMA under the electron beam. The UCNPs form small clusters and

some are positioned at the active layer surface. A reason for this behavior could be the polymerization when the layer dries out during the spin-coating process. However, the clusters are small enough to not influence the layer uniformity. The UCNPs at the layer surface represent the roughness that is included in the layer thickness adaption and do not significantly influence the overall Bragg structure design. Overlaying the SEM image with a Bragg structure with the target ratio of low- and high refractive index layer, shows that the relation between the high- and low refractive index layers is very close to the target relation, which again is a proof of quality. [113]

Figure 4.10b shows an SEM image of a Bragg structure with a double active layer design, two layers deposited on top of each other make up each active layer. From the image it is evident that the UCNP distribution within the layer does not significantly differ from the other production method with one single layer. Possibly, a part of the first layer is dissolved to allow a new clustering of UCNPs from the first and second layer. The layer thickness accuracy in this image is not as excellent as in the Bragg structure with single active layers. Still, the double active layers give a high quality active layer. Figure 4.10c displays a Bragg structure cross sectional image on a larger area, demonstrating the very high uniformity in a larger scale.

Finally, the effect of the roughness of each active layer on the overall roughness of a complete Bragg structure was investigated. The SEM images in panels a-c show that the roughness of one active layer evens out throughout the Bragg structure latest with the next active layer. A large area atomic force microscopy scan (Methods Section 3.2.2) confirms this observation. The monolayers of hexagonally organized islands of UCNPs are still visible. There are some clusters visible, higher than one monolayer. However, the roughness of a complete Bragg structure, here measured as 10.1 nm, lies within the same range as the roughness of one single active layer with 5.2 nm (compare to Fig. 4.4a). [113]

4.4. Summary

In this chapter, a thorough analysis of the design of single layers and final Bragg structure samples was presented. The fabrication of the active layers, containing Poly(methyl methacrylate) (PMMA) with embedded upconverter nanoparticles, was done via spin-coating. In the optimized process, a high layer uniformity could be reached with a low surface roughness of 5.2 nm for a 300 nm thin layer, as well as a precise thickness control, showing layer thickness deviations of only 1.3%.

The high refractive index layer was chosen to be TiO_2, fabricated in a low temperature atomic layer deposition process. The resulting amorphous thin TiO_2 films allowed for a very high thickness control with deviations of 0.8% for a 200 nm thin layer and negligible surface roughness. With the chosen materials and fabrication methods, a large contrast in refractive indices could be reached, featuring n_{low} = 1.47 and n_{high} = 2.28 for the active and TiO_2-layer, respectively, at 1523 nm wavelength.

Final Bragg structures were realized with four active layers and five surrounding TiO_2 layers. For the final analysis, 40 different designs on eight separate samples were analyzed. The samples were designed to show photonic effects at and around the expected maximum photonic effects on the main UC emission at 984 nm. Via the reflectance characteristics

of the Bragg structure, the design wavelength of fabricated structures was determined with a precision of 1 nm in design wavelength. Additionally, a high layer uniformity was found as well as a low surface roughness of 10.1 nm on the topmost layer of a complete Bragg structure. Due to a very precise design of the single layers, high quality Bragg structures could be realized.

4.5. Contributions to this chapter

Clarissa L. M. Hofmann (Author)

- planned all experiments
- adapted the spin-coating process and fabricated active layers via spin-coating
- performed the atomic force microscopy measurements
- conceived of the analysis of the TiO_2 layer inhomogineity and of fabricating multiple Bragg structure designs in one atomic layer deposition run
- planned and performed ellipsometry measurements
- performed the ellipsometric data analysis
- conceived of and planned the explicit Bragg structure designs
- fabricated the final Bragg structure samples at the Institute of Nanotechnology, Karlsruhe Nano Micro Facility at Karlsruhe Institute of Technology: spin-coating of active layers, placement of samples, overlooking the production process, whereby Christian Reitz was in charge of the atomic layer deposition process (see below)
- planned and performed spectrophotometer measurements
- performed all experimental data analysis

Stefan Fischer

- fabricated the custom made core-shell upconverter nanoparticles at the Department of Materials Science and Engineering at Stanford University

Christian Reitz

- adapted and was in charge of the atomic layer deposition process for fabrication of the TiO_2 layers of the Bragg structure samples at the Institute of Nanotechnology, Karlsruhe Nano Micro Facility at Karlsruhe Institute of Technology

Measurements:

- Volker Kübler performed the scanning electron microscopy measurements on Bragg structure cross sections at the Fraunhofer Institute of Solar Energy Systems ISE

- Andrew Mondon performed the scanning electron microscopy measurements on single active layer cross sections at the Fraunhofer Institute of Solar Energy Systems ISE
- Nicolo Baroni performed the X-ray diffraction measurements at the Institute of Microstructure Technology at the Karlsruhe Institute of Technology
- Felicia Volle performed repeated spin-coating tasks
- Kristina Winkler and Fabian Gerspacher performed repeated spectroscopic ellipsometer measurements
- Kristina Winkler, Fabian Gerspacher and Felix Martin also performed spectrophotometer measurements

Bryce S. Richards

- conceived of the TiO_2 thin-film deposition process for multilayer-stack production
- significantly contributed to planning and interpreting the experiments,
- gave significant advice on ellipsometric data analysis

Jan Christoph Goldschmidt

- conceived of the research question and the concept of investigating Bragg structures for UC enhancement,
- contributed significantly to planning all experiments and to the interpretation of all experimental data

CHAPTER 5

MODELING PHOTONIC UPCONVERTER DEVICES

The interplay of upconversion (UC) dynamics and a surrounding photonic structure are complex and influenced by a large number of parameters. To understand this interplay and enable an optimization of the photonic structure design to maximize UC efficiency, a modeling framework has been established in the research group over the past 15 years. Within this work, the model has been further developed (Hofmann, Eriksen et al. 2018, Hofmann et al. 2016) and the photonic effects on UC have been experimentally verified in a large parameter scan, published in Nature Communications (Hofmann et al. 2021). Furthermore, within this work, the model has been published open access on the Fraunhofer data platform Fordatis `http://dx.doi.org/10.24406/fordatis/110.2`.
In this chapter, the modeling results are presented. In the first part, the photonic effects within a Bragg structure are analyzed in detail. In the second part, the UC photoluminescence (UCPL) and quantum yield (UCQY) are investigated, in a homogeneous medium and influenced by each photonic effect. Based on these findings, the maximum possible enhancement of UC efficiency with optimized Bragg structures is discussed. Finally, the impact of different Bragg structure materials and simulated production inaccuracies, as they appear in any real device, are analyzed. The parameters, varied in this section are the incident irradiance, the design wavelength and number of layers of the Bragg structure and the refractive indices the structure is made of. Additionally, the production accuracy is varied and its impact on photonic upconverter devices is tested.

This chapter is based on parts of the following publications:

C. L. M. Hofmann, S. Fischer, E. H. Eriksen, B. Bläsi, C. Reitz, D. Yazicioglu, I. A. Howard, B. S. Richards and J. C. Goldschmidt, Experimental validation of a modeling framework for upconversion enhancement in 1D-photonic crystals, *Nature Communications* **12**, 1-10 **(2021)**

C. L. M. Hofmann, E. H. Eriksen, S. Fischer, B. S. Richards, P. Balling, and J. C. Goldschmidt, Enhanced upconversion in 1D photonic crystals: a simulation-based assessment within realistic material and fabrication constraints, *Optics Express* **26**, 7537-7554 **(2018)**

C. L. M. Hofmann, B. Herter, S. Fischer, J. Gutmann, and J. C. Goldschmidt, Upconversion in a Bragg structure: photonic effects of a modified local density of states and irradiance on luminescence and upconversion quantum yield. *Optics Express* **24**, 14895-14914 **(2016)**

Contributions to this chapter of the author, co-authors and others can be found in section 5.4.

5.1. Photonic effects in a Bragg structure

Photonic effects of a Bragg structure influence the UC process: a change in optical local energy density scales all stimulated processes within the UC process. These effects are very sensitive to structural imperfections. Therefore, the effect of different production inaccuracies, as they appear in experiment, are elaborated. The second photonic effect is the modified local density of optical states which alters the probability of all spontaneous emission processes. To be able to tune a photonic structure design in order to maximize the efficiency of an embedded upconverter, these two photonic effects are analyzed in detail in this section.

5.1.1. Optical local energy density

The optical local energy density within the Bragg structure is simulated via the transfer matrix method, as elaborated in Section 3.1.2. All simulations shown in this section are done for the excitation wavelength of 1523 nm, the optimal excitation for ground state absorption ${}^4I_{15/2} \rightarrow {}^4I_{13/2}$ in the upconverter β-$NaYF_4$ doped with 25% Er^{3+}. The corresponding dominant UC emission is the ${}^4I_{11/2} \rightarrow {}^4I_{15/2}$ at 984 nm, which is right above the bandgap of silicon and therefore suitable for a target application in silicon photovoltaics. In this section, the most important parameters defining the optical local energy density enhancement within the active layers of a Bragg structure are investigated: *i)* the design wavelength, which defines the optical thickness of all layers, *ii)* the number of layers in a Bragg structure and *iii)* the difference in refractive indices of the alternating low- and high refractive index layers. After an assessment of ideal Bragg structures, the optical local energy density in Bragg structures with production inaccuracies are investigated.

In an ideal Bragg structure

The local energy density crucially depends on the design wavelength (λ_{design}) of the Bragg structure, which defines the optical thickness of all layers. Therefore, optimizing the design wavelength is of high importance to achieve a high energy density enhancement within the active layers, which contains the upconverter material. Figure 5.1 shows a set of simulations for the experimentally investigated Bragg structure design, build up by four active layers with refractive index n_{low} = 1.47 and five surrounding layers with high refractive index n_{high} = 2.28 (see Chapter 4 and 6). Figure 5.1a shows the average relative energy density ($\bar{u}_{\text{rel}}$) within the active layers for an excitation wavelength $\lambda_{\text{excitation}}$ = 1523 nm, at normal incidence from air in dependence on the design wavelength λ_{design}. The maximum enhancement across all active layers is achieved for λ_{design} = 1855 nm, when the excitation wavelength lies at the photonic band edge, as illustrated in Fig. 5.1b. The high enhancement can be understood when looking at the corresponding energy density distribution $u(x)$ inside the Bragg structure, shown in Fig. 5.1c along with the refractive index profile. All maxima of $u(x)$ are positioned in the active layers. It is well known throughout literature, that high field enhancements occur at the photonic band edge [58, 135]. The enhancement can be explained in the context of photonic crystals as slow light piling up [136] or in a more classical context as the formation of a standing wave due to interference between the forward and backward propagating waves. At the mininum average relative energy density found in Fig. 5.1a at λ_{design} = 1415 nm,

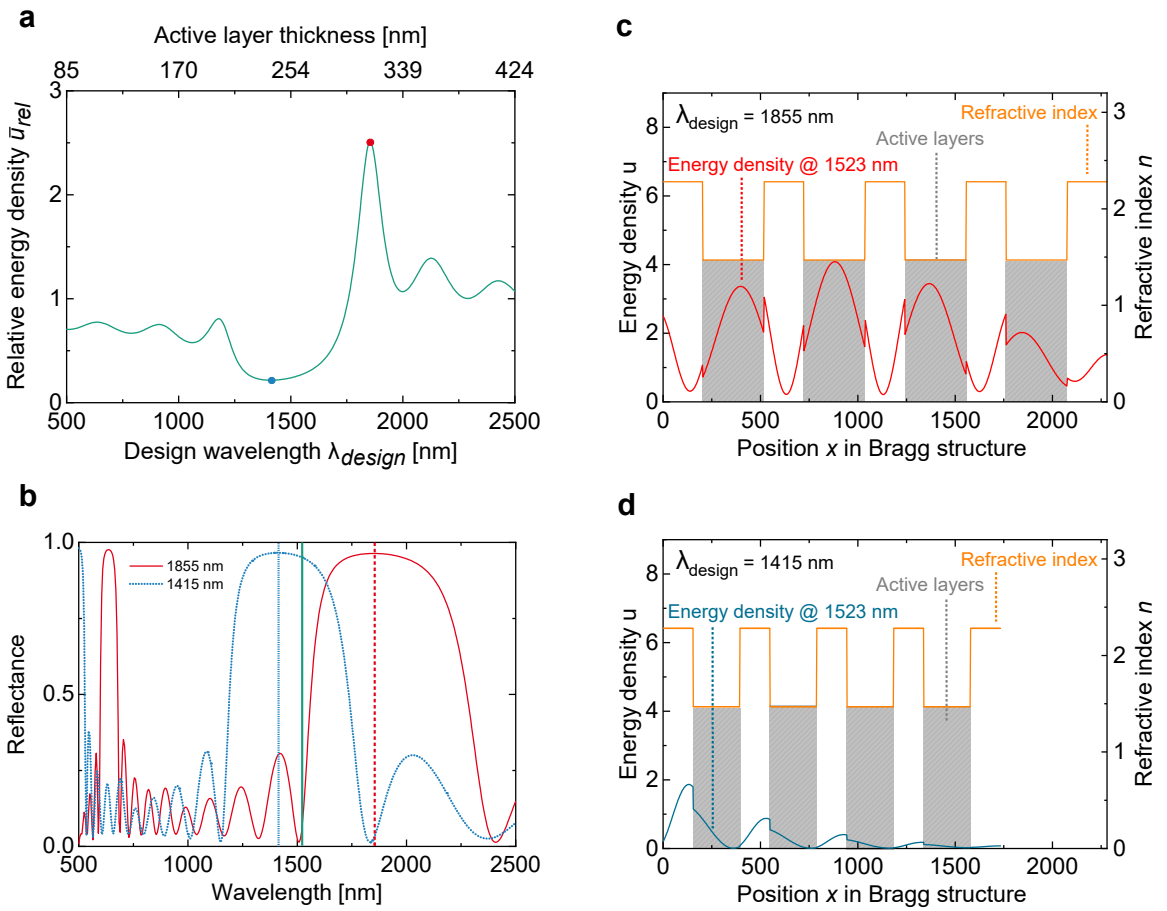

Figure 5.1.: Local energy density in a Bragg structure. **a** Average relative energy density $\bar{u}_{\text{rel}}$ across the active layers as a function of design wavelength λ_{design} for the experimentally investigated Bragg structure design with low refractive index n_{low}= 1.47, high refractive index n_{high}= 2.28 and 4 active layers. The upper x-axis indicates the active layer thickness, $d_{\text{low}} = \lambda_{\text{design}}/(4n_{\text{low}})$. **b** Reflectance of the two example structures at λ_{design} yielding the maximum $\bar{u}_{\text{rel}}$-value ($\lambda_{\text{design}}(u_{\text{rel,max}})$) and minimum $\bar{u}_{\text{rel}}$-value at λ_{design} = 1415 nm, marked by a red and blue circle in panel **a**, respectively. **c**, **d** Spatial energy density distribution inside the Bragg structure for $\lambda_{\text{design}} = \lambda_{\text{design}}(u_{\text{rel,max}})$ and $\lambda_{\text{design}} = 1415$ nm, respectively. Additionally, the refractive index profile is shown.

the incident wave of $\lambda_{\text{excitation}}$ = 1523 nm hits the photonic bandgap (Fig. 5.1b). The small fraction of energy density that enters the structure then exponentially decays, leaving very little energy density in the active layers, as illustrated in Fig. 5.1d.

Figure 5.2 now shows how the peak of the $\bar{u}_{\text{rel}}$- distribution changes, when increasing the number of active layers in the Bragg structure. This analysis has been carried out for a different set of refractive indices n_{low} = 1.5 and n_{high} = 1.8, as in the publication [32]. With the second design parameter, the active layer number of the Bragg structure, the shape of the peak of $\bar{u}_{\text{rel}}$ changes. From the six plotted examples for 4, 12, 20 (Fig. 5.2a) and 40, 70 and 100 (Fig. 5.2b) active layers, it can be seen how an increasing active layer number leads to a higher and spectrally more narrow peak of $\bar{u}_{\text{rel}}$. Figures 5.2c and 5.2d show a summary of the peak values $u_{\text{rel,max}}$ as well as the design wavelengths at which the peak occurs $\lambda_{\text{design}}(u_{\text{rel,max}})$, respectively, for all scanned designs from 4 to 100 active layers. A

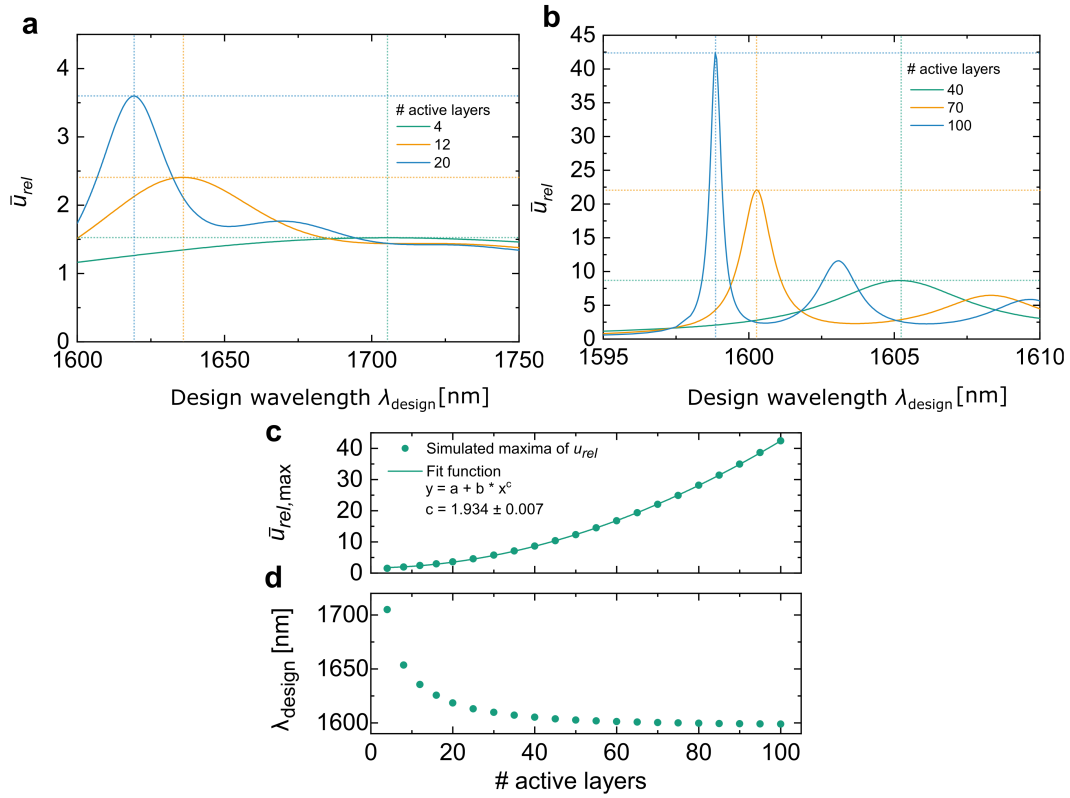

Figure 5.2.: Maximum energy density enhancement ($u_{\mathbf{rel,max}}$) for Bragg structures with a varied number of active layers. The investigated Bragg structure is made up of the low refractive index n_{low} = 1.5 and high refractive index n_{high} = 1.8. **a,b** Average energy density enhancement ($\bar{u}_{rel}$) in dependence on the design wavelength λ_{design}. For an increasing number of active layers, here shown for 4, 12, 20 (**a**) and 40, 70 and 100 (**b**), $u_{rel,max}$ increases and the peak position on the λ_{design} axis ($\lambda_{design}(u_{rel,max})$) moves to shorter λ_{design}. **c** $u_{rel,max}$ is plotted for each simulated active layer number. A fit on all determined $u_{rel,max}$ shows that it increases quadratically with an increasing the number of active layers. **d** With an increasing number of active layers, photonic band edge of the design that yields maximum enhancement $\lambda_{design}(u_{rel,max})$, converges towards the excitation wavelength.

fit on the points of all maxima shows that $u_{rel,max}$ increases quadratically with an increasing active layer number. Thus, very high energy density enhancement factors can be reached. As the number of layers increases, the higher frequency photonic band edge of the design that yields $u_{rel,max}$, converges towards the excitation wavelength. Consequently, the peak value $u_{rel,max}$ gets higher but also reduces in spectral width.

Including production inaccuracies

In this section the experimental feasibility of high enhancement Bragg structures is discussed. No experimental production method is ideal, every method and process has a certain production accuracy. This deviation from the ideal structure has an impact on the appearing photonic effects. To take into account production tolerances, a Monte Carlo method as described in section 5.1.1 is applied. The thickness of each layer in the Bragg structure is modified with a random value drawn from a Gaussian distribution with a defined standard

deviation σ. The production accuracy of the experimentally realized Bragg structures in this work is 4.15 nm (1.3%) for the active layers, produced via spin-coating (see Section 4.1) and 1.53 nm (0.8%) for the TiO_2-layers, produced via atomic layer deposition (see Section 4.2). Figure 5.3 shows the simulated energy density enhancement for the experimentally realized

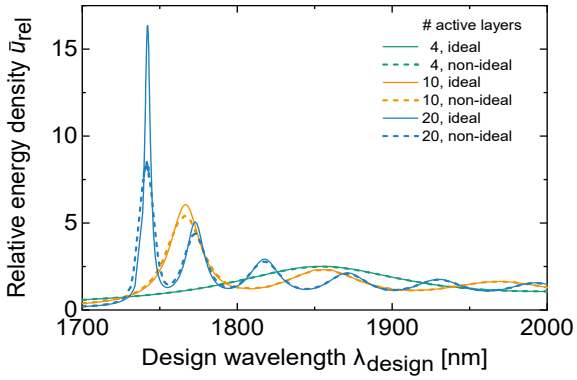

Figure 5.3.: Impact of production inaccuracies on the relative energy density for Bragg structures with examplary 4, 10 and 20 active layers. Average relative energy density ($\bar{u}_{rel}$) in the active layers of Bragg structures with low refractive index n_{low} = 1.47, high refractive index n_{high} = 2.28 and production accuraries simulated with σ = 4.15 nm and 1.53 nm for the low- and high refractive index layers, respectively. For four active layers, the production inaccuracy has nearly no impact, compared to the ideal structure, while for more complex designs with 10 and 20 active layers, $\bar{u}_{rel}$ is strongly reduced.

Bragg structures with four active layers with ideal accuracy (meaning no deviation from the target thickness of each layer) and including the above given production inaccuracies. For a simple design with only four active layers, the production accuracy reached in experiment is sufficient to be able to observe the photonic effects with nearly no reduction. For more complex designs with 10 active layers, the peak enhancement $u_{rel,max}$ is significantly reduced to 90%, while for 20 active layers $u_{rel,max}$ is reduced to 50% of the ideal peak enhancement.

Hence, the impact of production inaccuracies strongly depends on the number of layers in the Bragg structure: high, narrow enhancement peaks are strongly reduced. Another parameter that is decisive for the strength of photonic effects is the difference in refractive indices between the low- and high refractive index layer. Figure 5.4 shows the impact of different production inaccuracies on the maximum average relative energy density enhancement $\bar{u}_{rel}$ for a large scan of design parameters. The range of considered structures for the difference in refractive indices is $1.5 < n_{high} \leq 4.0$, while n_{low} always resembles 1.5. The active layer number is scanned from 1 to 50. Each structure is evaluated at the design wavelength $\lambda_{design}(u_{rel,max})$ at which the highest enhancement $u_{rel,max}$ for this particular structure, with set refractive indices and a set active layer number, appears. Figure 5.4a shows $u_{rel,max}$ with ideal production accuracy (σ = 0). As the number of active layers and/or the refractive index contrast increases, the photonic effects become stronger and $u_{rel,max}$ increases. The associated decrease in spectral width of the peak on the λ_{design} axis with respect to the layer thickness causes a correspondingly increasing sensitivity to structural imperfections. To obtain the maximum $u_{rel,max} \approx 400$, as shown in Fig. 5.4a, a subatomic production accuracy is required. The peak of $\bar{u}_{rel}$ on the λ_{design} axis then reaches a spectral width in the sub-Ångstrøm-range, which cannot be realistically be exploited in experiment as such

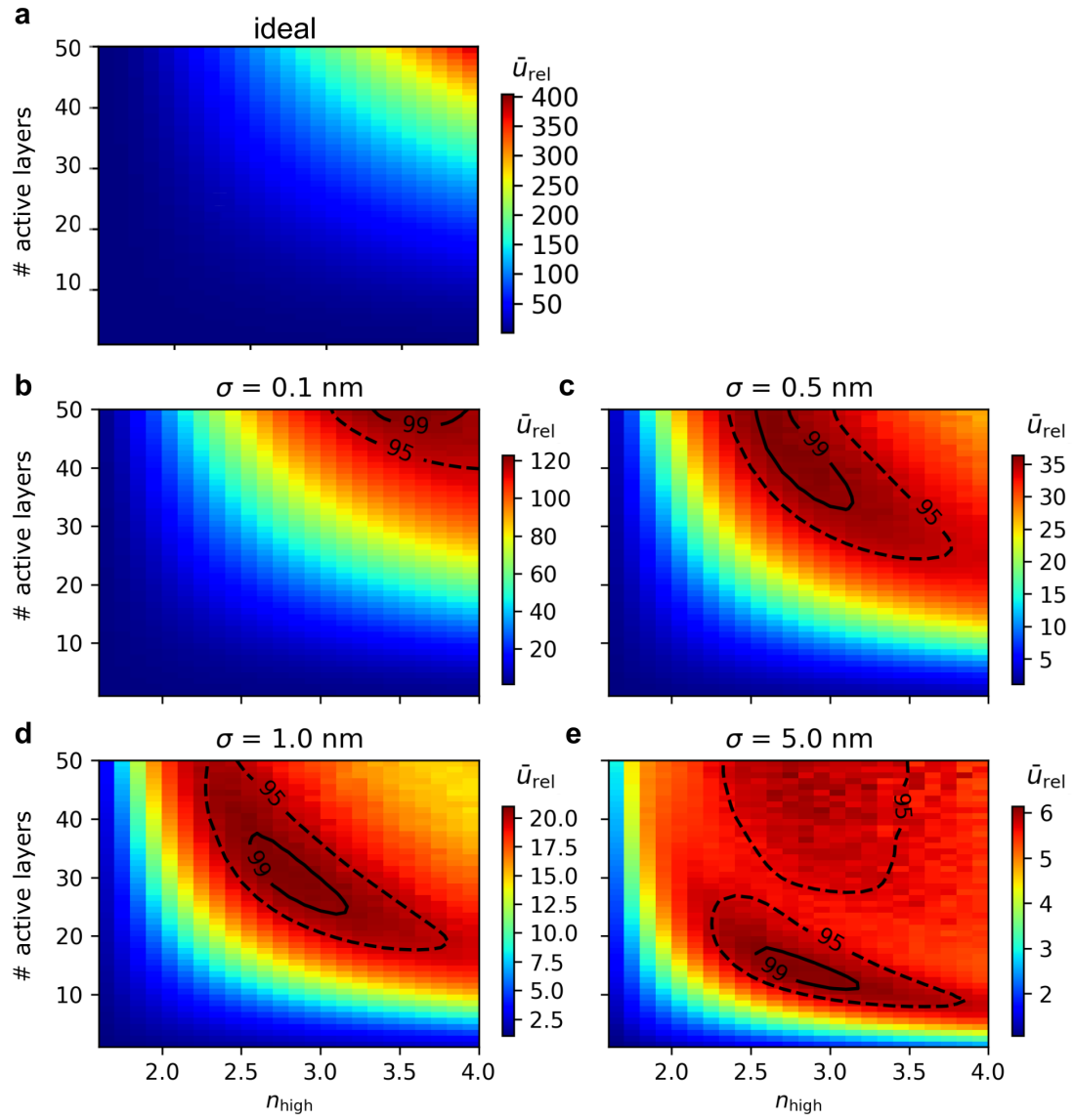

Figure 5.4.: Impact of production inaccuracies on the maximum average relative energy density $u_{\text{rel,max}}$ across the active layers of a Bragg structure as a function of the high refractive index n_{high} and active layer number. The low refractive index is n_{low} = 1.5. **a** the maximum relative energy density $u_{\text{rel,max}}$ for the ideal production accuracy. **b-e** $u_{\text{rel,max}}$ for four different production accuracies, simulated using a Monte Carlo method. The black contours indicate 99% (solid line) and 95% (dashed line) of the maximum. The panels show σ-values of 0.1 nm (**b**), 0.5 nm (**c**), 1.0 nm (**d**), and 5.0 nm (**e**). (Figure adapted from [34])

accuracy can never be realized. As can be seen, the non-zero production tolerances limit the realistically achievable value of $u_{\text{rel,max}}$ severely. Even with Ångstrøm precision, as displayed in Fig. 5.4b, corresponding to the thickness of a single atomic layer, $u_{\text{rel,max}}$ drops to around 125. With 0.5 nm and 1 nm precision, Figs. 5.4c and 5.4d, the maximum decreases further to values around 35 and 20, respectively. For $\sigma = 5$ nm, Fig. 5.4e, the maximum region in

the 2D scan moves further down, particularly to fewer active layers, and the maximum value drops to around 6. Hence, to obtain high enhancement factors, high-precision manufacturing is of uttermost importance. [34]

5.1.2. Local density of optical states

A modification in the local density of optical states (LDOS) has an impact on the probability of spontaneous emission processes, as discussed in Section 5.1.2 and 3.1.6. Therefore, when wanting to model the probability of a spontaneous emission processes in the context of UC, one has to consider the LDOS at the positions of the upconverter material in a photonic structure.

Figure 5.5 shows the photonic band structure and relative LDOS ($LDOS_{rel}$) for two ex-

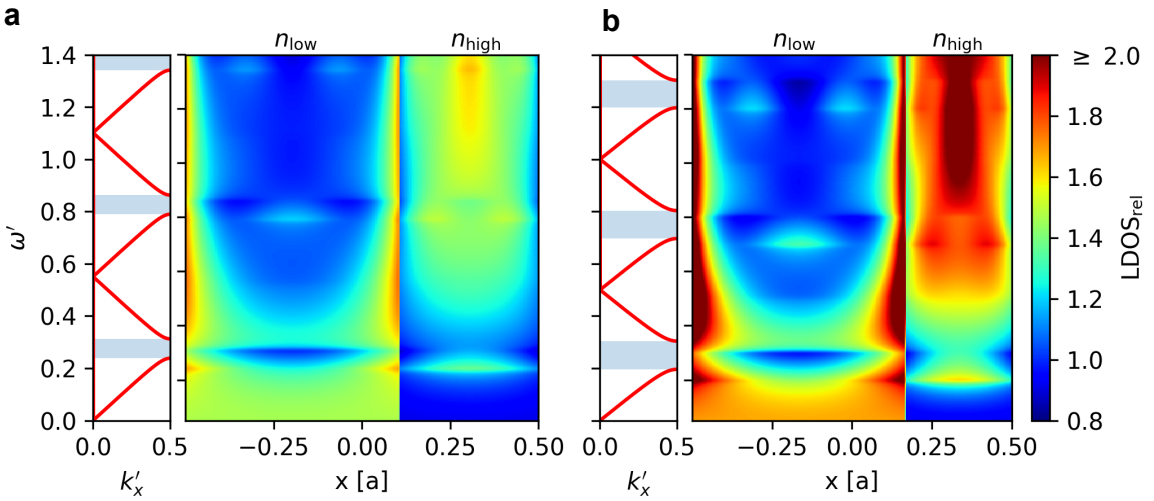

Figure 5.5.: Photonic band structure and relative local density of optical states ($LDOS_{rel}$). Band structure and $LDOS_{rel}$ for the low refractive index n_{low} = 1.5 and high refractive index n_{high} = 2.3 (**a**) or n_{high} = 3.0 (**b**), along with the associated photonic band structure for $k'_y = 0$. The regions of n_{high} and n_{low}, the latter being the active layer, in which the upconverter is positioned, within the Wigner-Seitz unit cell are indicated on the top. The bandgaps are marked by blue shadings. To avoid washing out features in the left panel, the scale is truncated at 2.0 even though the maximum value in the right panel is 2.5. [34]

emplary high refractive index materials n_{high} = 2.3 (Fig. 5.5a) and n_{high} = 3.0 (Fig. 5.5b). For both panels, the low refractive index material is set to n_{low} = 1.5. The band structure is plotted within the First Brillouin Zone. The bands show a linear dispersion relation, which deviates from linearity at the edge of the First Brillouin Zone where the bandgaps are formed. The modification of the LDOS is plotted relative to the homogeneous reference medium with refractive index 1.5. $LDOS_{rel}$ is shown within the Wigner-Seitz unit cell *a* with the n_{low} and n_{high} regions indicated on the top, both featuring the same optical thickness. From the two example structures, a compression of the band structure along the frequency axis can be observed with increasing n_{high}, which is due to the increasing effective refractive index. Furthermore, as due to the increase in refractive index contrast, the features of the LDOS become more pronounced and the size of the bandgaps increases.

The relative change of the LDOS is implemented in the UC rate equation model, featuring each spontaneous emission separately (see section 3.1.6). The UC process regarded in this work, features two dominant spontaneous emission processes: the UC emission is almost exclusively caused by the spontaneous emission at 984 nm between the states ${}^4I_{11/2} \rightarrow {}^4I_{15/2}$, while the radiative losses are dominated by the 1558 nm emission between the states ${}^4I_{13/2} \rightarrow {}^4I_{15/2}$, as demonstrated in Fig. 5.9a. To allow for a simple assessment on the UC process affected by the LDOS of different structures, I define the mean relative LDOS within the active layers of the Bragg structure ($\overline{\text{LDOS}}_{\text{rel}}$). The ratio between the $\overline{\text{LDOS}}_{\text{rel}}$ for the 984 nm main UC emission ($\overline{\text{LDOS}}_{\text{rel}}$(984 nm)) and the 1558 nm loss emission ($\overline{\text{LDOS}}_{\text{rel}}$(1558 nm)) is plotted in Fig. 5.6. [34]

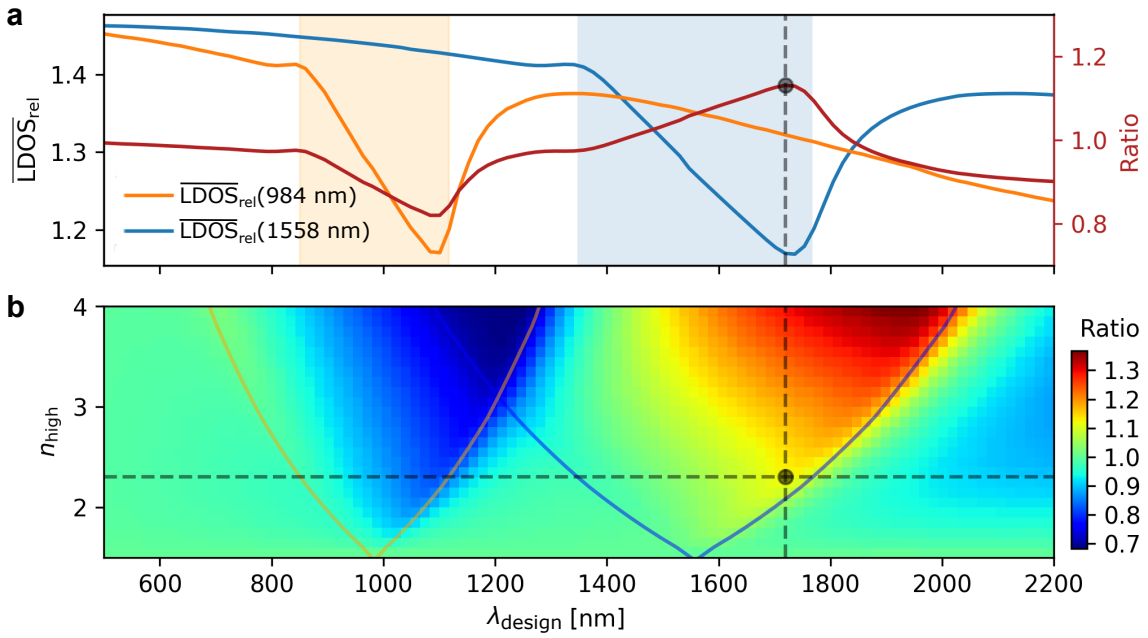

Figure 5.6.: Effect of the mean relative local density of optical states ($\overline{\text{LDOS}}_{\text{rel}}$) on spontaneous emission probabilities for the main upconversion (UC) emission at 984 nm ($\overline{\text{LDOS}}_{\text{rel}}$(984 nm)) and the main loss emission at 1558 nm ($\overline{\text{LDOS}}_{\text{rel}}$(1558 nm)). a $\overline{\text{LDOS}}_{\text{rel}}$(984 nm) and $\overline{\text{LDOS}}_{\text{rel}}$(1558 nm), as well as their ratio $\overline{\text{LDOS}}_{\text{rel}}$(984 nm)/$\overline{\text{LDOS}}_{\text{rel}}$(1558 nm) for an example structure with low refractive index n_{low} = 1.5 and high refractive index n_{high} = 2.3 as a function of the design wavelength λ_{design}. The shaded regions indicate where the respective transition lies within the first photonic bandgap. **b** Ratio of $\overline{\text{LDOS}}_{\text{rel}}$(984 nm)/$\overline{\text{LDOS}}_{\text{rel}}$(1558 nm) as a function of n_{high} and λ_{design}. The solid lines indicate where the respective transition lies within the first photonic bandgap. The ratio is highest when $\overline{\text{LDOS}}_{\text{rel}}$(1558 nm) is in the photonic bandgap, at the lower band edge and increases with a higher contrast in refractive indices. [34]

This ratio should be as high as possible, as the ideal case features an enhancement of the UC emission and a suppression of the loss emission. In Fig. 5.6a, $\overline{\text{LDOS}}_{\text{rel}}$ is plotted for an example structure with n_{high} = 2.3. The x-axis of Fig. 5.6 shows the design wavelength λ_{design}, which is scaling the unit cell in position space. The orange and blue shaded regions indicate the λ_{design} region, in which the main UC emission at 984 nm and the loss emission at 1558 nm are within the first photonic bandgap, respectively. The $\overline{\text{LDOS}}_{\text{rel}}$ is strongly reduced when the respective emission is found within the first photonic bandgap.

However, as the reference consists only of the low refractive index material, there are more photonic states in the Bragg structure, and $\overline{\text{LDOS}}_{\text{rel}}$ is always above one. The maximum ratio $\overline{\text{LDOS}}_{\text{rel}}$(984 nm)/$\overline{\text{LDOS}}_{\text{rel}}$(1558 nm) is observed when the emission 1558 nm is within the photonic bandgap and therefore, $\overline{\text{LDOS}}_{\text{rel}}$(1558 nm) is reduced. The corresponding design wavelength, where the ratio $\overline{\text{LDOS}}_{\text{rel}}$(984 nm)/$\overline{\text{LDOS}}_{\text{rel}}$(1558 nm) is at its maximum, is very close to the design wavelength $\lambda_{\text{design}}(u_{\text{rel,max}})$ that maximizes the relative energy density $\bar{u}_{\text{rel}}$. It is important to note that the emission wavelength of 1558 nm is significantly stokes-shifted relative to the excitation wavelength at 1523 nm. Therefore, the excitation wavelength can be efficiently coupled into the structure at the edge of the first photonic bandgap, while the probability of an emission process at 1558 nm is reduced in the first photonic bandgap. In Fig. 5.6b, n_{high} is varied on the y-axis. The grey dashed lines indicate the example structure shown in Fig. 5.6a. The orange and blue lines indicate the edges of the first photonic bandgap for the main UC emission at 984 nm and loss emission at 1558 nm, respectively. For all n_{high}, the behavior is similar to Fig. 5.6a. The ratio is small when the UC emission at 984 nm falls into the first photonic bandgap and large when the loss emission at 1558 nm lies in the region of maximum suppression in the first photonic bandgap. Additionally, the ratio increases with increasing n_{high}. This can be understood from Fig. 5.5. As n_{high} increases, the features of the LDOS become more pronounced. Thereby, the contrast in $\overline{\text{LDOS}}_{\text{rel}}$ increases between the region of the first photonic bandgap and the band edges surrounding the first photonic bandgap. Consequently, the most favorable design is obtained by placing the loss emission at 1558 nm in the first photonic bandgap while utilizing materials with the largest possible refractive index contrast. [34]

5.1.3. Fractional local density of optical states

To analyze the directionality of emission of the upconverted photons, the fractional local density of optical states (FLDOS) is introduced in section 5.1.3. It allows for analyzing the fraction of photons that are coupled out of the photonic-upconverter into air that can be detected within a detection cone with half angle θ_d that is tilted with respect to the surface normal by a half angle ϕ_d. The simulations for this section are performed for the angle θ_d = 0.5°. Figure 5.7 shows the normalized fractional density of optical states ($\text{FDOS}_{\text{norm}}$) (equations 3.20 and 3.23). $\text{FDOS}_{\text{norm}}$ displays the fraction of out-coupled modes from the active layer into each angle ϕ_d normalized by the LDOS of the active layer, that contains all modes. The small half angle of the detection cone of θ_d = 0.5° allows for a fine analysis of each emission angle. However, the choice of a small half angle also results in the low number of modes in each cone in the range of 10^{-5} relative to all emitted modes. In Fig. 5.7a, the unitless frequency is plotted as the x-axis. Within the bandgaps, there are no modes and an increased number of modes is visible at the band edges, especially at the higher frequency band edge. Towards higher detection angles, the band splitting of the two polarizations of modes becomes evident at the band edges (see e.g. [36]). Figure 5.7b displays $\text{FDOS}_{\text{norm}}$ for the design wavelength λ_{design} = 1735 nm for which the effect of the LDOS on UC is at its maximum [1]. For this choice of design, the x-axis scales to the emission wavelength. The maximum effect is mainly caused by the suppression of the

[1] In this thesis, the analysis of the maximum LDOS effect is shown for a different set of refractive indices in Fig. 5.10. The analysis for the current set of refractive indices is presented in Fig. 3, Hofmann *et al.* 2021 [26]

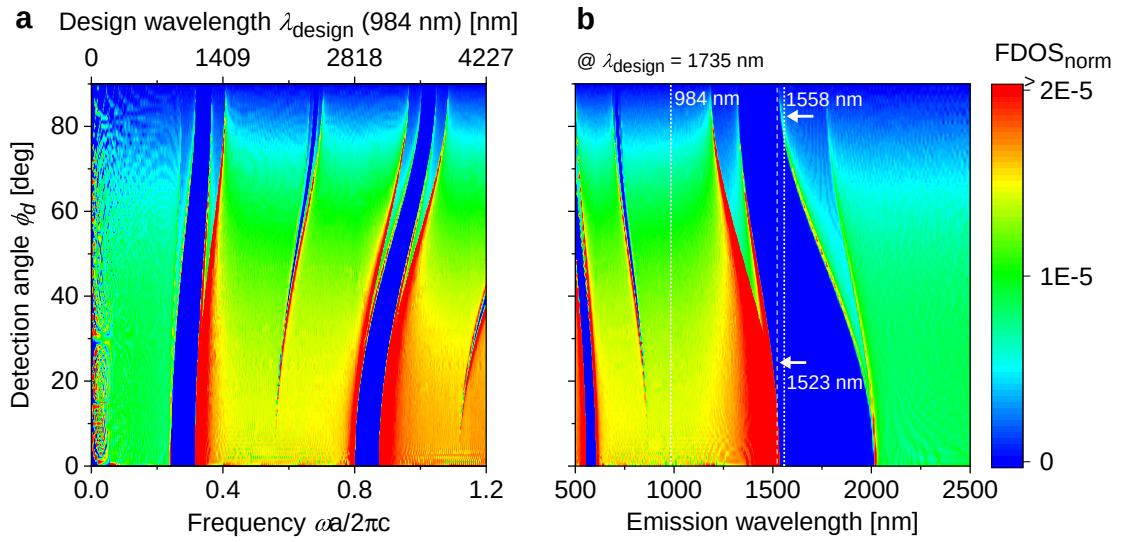

Figure 5.7.: Normalized fractional density of optical states (FDOS$_{norm}$). FDOS$_{norm}$ for the low refractive index n_{low} = 1.47, high refractive index n_{high} = 2.28 and surrounding medium air ($n = 1.0$). Each detection angle ϕ_d is calculated for a detection half cone of 0.5 °. **a** FDOS$_{norm}$ plotted against the unitless frequency, with the top x-axis indicating the respective design wavelength λ_{design} for the main upconversion (UC) emission at 984 nm. **b** FDOS$_{norm}$ scaled to the design wavelength λ_{design} = 1735 nm at which the LDOS effect is at its maximum. The main UC emission at 984 nm is far from the bandgaps and the majority of the modes are directed into small ϕ_d.

loss emission at 1558 nm, which lies within the photonic bandgap in almost the complete detection angle range. Because of the significant red-shift of the emission relative to the excitation of the first excited state, the excitation wavelength of 1523 nm is positioned at the band edge, where optical energy density enhancement effects occur (compare to Fig. 5.1) [2]. The main UC emission at 984 nm lies in a region far from the bandgaps. Thus, the emission characteristics are not much altered by the photonic structure, but feature a similar behavior as in the reference sample: the majority of the out-coupled modes are directed into small angles relative to the surface plane. This is favorable for an application in photovoltaics, where the solar cell is placed above of the photonic-upconverter, able to absorb the majority of the out-coupled modes.

To understand how the UC emission is altered in a Bragg structure relative to the reference structure, FDOS$_{rel}$ (equations 3.20 and 3.24) is shown in Fig. 5.8. For most of the spectral region off the bandgaps, FDOS$_{rel}$ is close to unity, best visible in Fig. 5.8a. This means that the sum of out-coupled modes into each detection angle is almost identical in Bragg structure and reference. Merely at the band edges, significant enhancements of out-coupled modes can be found in the Bragg structure. As can be seen from Fig. 5.8b, also FDOS$_{rel}$ of the main UC emission at 984 nm is close to unity at all detection angles.

[2] Note that the excitation at 1523 nm is not effected by the LDOS, or FLDOS. The wavelength is only highlighted to demonstrate that the excitation at 1523 nm can be positioned at the band edge, while the red-shifted emission at 1558 nm is positioned in the photonic bandgap and is thus suppressed. It is a trade-off between reaching an enhancement of the excitation up to high incident angles and reaching a suppression of the loss emission already at small emission angles.

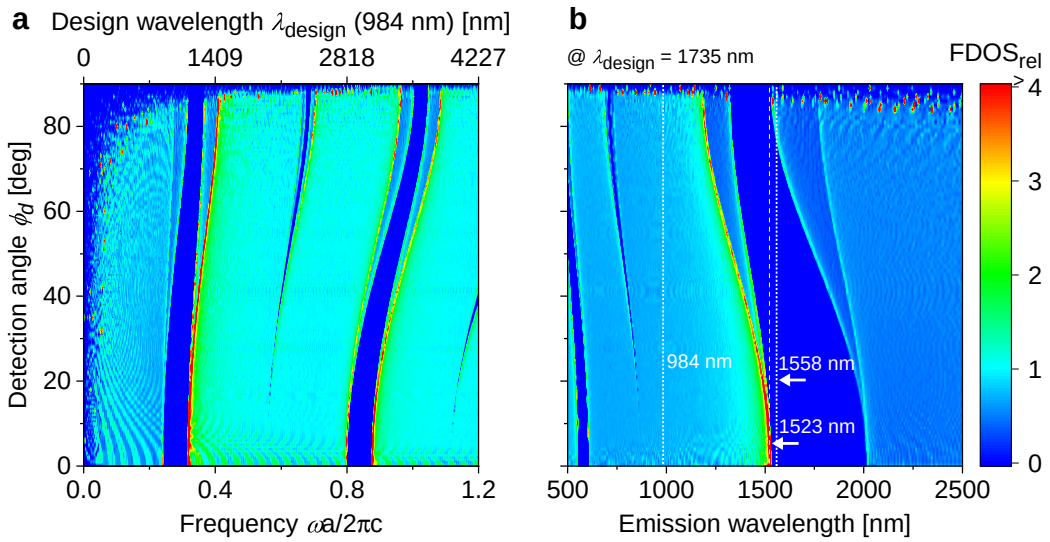

Figure 5.8.: Relative fractional density of optical states (FDOS$_{rel}$). FDOS$_{rel}$ for the low refractive index n_{low} = 1.47, high refractive index n_{high} = 2.28 and surrounding medium air ($n = 1.0$). Each detection angle ϕ_d is calculated for a detection half cone of 0.5 °. **a** FDOS$_{rel}$ plotted against the unitless frequency, with the top x-axis indicating the respective design wavelength λ_{design} for the main upconversion (UC) emission at 984 nm. **b** FDOS$_{rel}$ scaled to the design wavelength λ_{design} = 1735 nm at which the LDOS effect is at its maximum. In all regions far from the bandgaps, FDOS$_{rel}$ is close to unity.

5.2. Upconversion photoluminescence and quantum yield

5.2.1. Homogeneous media

The reference structure is simulated as the UC process in a homogeneous medium, without the influence of any photonic effects. A comprehensive description of the UC process and the simulation model can be found in Sections 2.2.2 and 3.1.5, respectively. The investigated upconverter material is β-$NaYF_4$ doped with 25% Er^{3+}. The light is incident into the upconverter material from air with refractive index 1.0.

Figure 5.9 shows the simulated UC process in the reference upconverter material. Figure 5.9a depicts the simulated absorption and emission rates for an excitation at 1523 nm (see Fig. 2.6 for comparison that illustrates the energy levels), normalized such that the absorption features unity at the highest simulated irradiance. Absorption is plotted as the sum of ground state absorption (GSA) and excited state absorption (ESA), showing a linear dependence on the incident irradiance. The dominant emission process is the stokes shifted photoluminescence at 1558 nm, the direct de-excitation of the first excited state. The dominant UC process is the UC photoluminescence (UCPL) at 984 nm. In the regime of very low incident irradiance, the probability of an UC process is very low because two or more excited ions are needed in close vicinity in space and time to take part in an energy transfer UC process (ETU). Towards higher irradiances, this probability increases, as there are more excited Er^{3+} ions available. As the probability for UCPL increases towards higher irradiances, the direct de-excitation at 1558 nm becomes less probable. As plotted in Fig. 5.9b, the UCQY of the 984 nm emission has a characteristic maximum at 12000 W m^{-2}. Past this

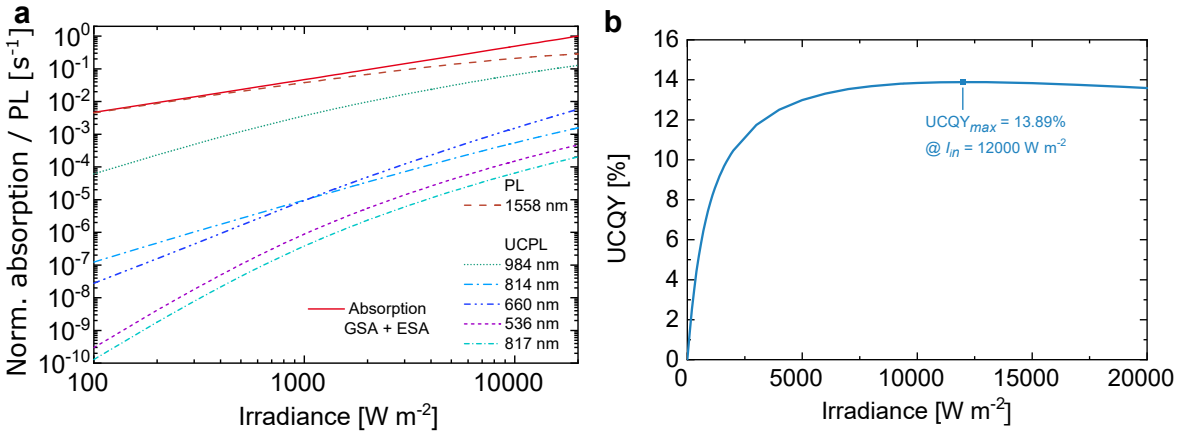

Figure 5.9.: Modeled upconversion (UC) dynamics in β-NaYF$_4$ doped with 25% Er^{3+}. a Simulated absorption and radiative emission processes photoluminescence (PL) and upconversion photoluminescence (UCPL) as a function of the incident irradiance I_{in}. **b** Simulated UC quantum yield (UCQY) of the 984 nm UC emission.

maximum, the UCQY of this particular UC emission decreases again, as UC emissions from higher energy levels become more likely. In the following, photonic effects on the 984 nm UCPL under 1523 nm excitation are investigated, as these are the relevant transitions for an application of UC in silicon photovoltaics.

5.2.2. Impact of photonic effects

The photonic structure surrounding the UC material has an impact on the UC process, as discussed in sections 2.2.4 and 3.1.6. The change in local optical energy density scales all stimulated processes, while the modified LDOS affects spontaneous emission probabilities. The photonic effects have been analyzed in Section 5.1. In a real photonic structure, the two effects will always occur together. However, in simulation there is the possibility of clarifying the contribution of each effect by 'switching on' only one effect and setting the relative change of the other effect to unity. Elaborating the contribution of each photonic effect on UC is subject of this section.

The two investigated parameters, that the UC efficiency shows a strong dependence on, are the incident irradiance I_{in} and the design wavelength λ_{design} of the Bragg structure. The analysis is performed at the optimal excitation wavelength $\lambda_{\text{excitation}}$ = 1523 nm for the upconverter material Er^{3+} and at normal incidence. The analysis in this section is based on the publication Hofmann *et al.* 2016 [32], where the refractive indices n_{low} = 1.5 and n_{high} = 1.8 where investigated, based on a material system that was experimentally investigated at that time. The Bragg structures investigated in this section therefore feature the same refractive indices n_{low} = 1.5 and n_{high} = 1.8. A layer of undoped PMMA of half the thickness $d = \lambda_{\text{design}}/8$ is added in front and behind the Bragg structure in order to reduce side lobes in the reflectance and thus efficiently couple in the excitation beam. In the following, the effect of the $\overline{\text{LDOS}}_{\text{rel}}$ on the UC process is investigated, while the relative energy density $\bar{u}_{\text{rel}}$ is set to unity. Figure 5.10a shows a 2D scan of the UCQY, with only the LDOS effect

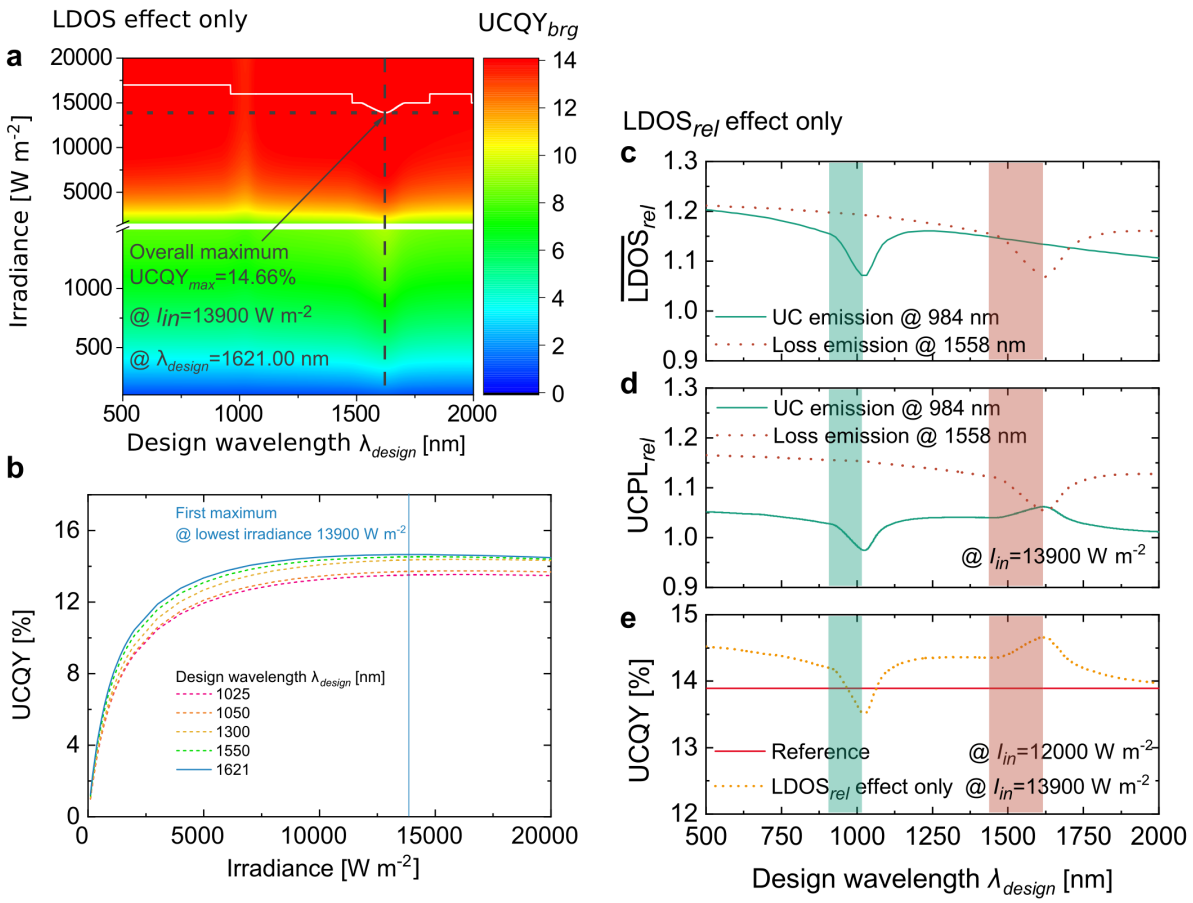

Figure 5.10.: Photonic effect of only the local density of optical states (LDOS) on upconversion (UC) by setting the energy density enhancement to unity. The Bragg structure is simulated as an infinite photonic crystal with low refractive index n_{low} = 1.5 and high refractive index n_{high} = 1.8. **a** UC quantum yield (UCQY) in dependence on design wavelength λ_{design} and incident irradiance I_{in}. The white line indicates the maximum UCQY at each λ_{design}. When scanning the I_{in} axis, the first maximum UCQY (UCQY$_{\text{first,max}}$) of 14.66% is reached at I_{in}(UCQY$_{\text{first,max}}$) = 13900 W m^{-2} and λ_{design}(UCQY$_{\text{first,max}}$) = 1621 nm. UCQY$_{\text{first,max}}$ is also the highest UCQY found in the scanned region. **b** UCQY as a function of I_{in} (cuts through graph **a**) for a selection of λ_{design} values, including λ_{design}(UCQY$_{\text{first,max}}$). **c** Average relative LDOS for the main UC emission at 984 nm ($\overline{\text{LDOS}}_{\text{rel}}$(984 nm)) and loss emission at 1558 nm ($\overline{\text{LDOS}}_{\text{rel}}$(1558 nm)). **d** Relative photoluminescence at 1558 nm (PL$_{\text{rel}}$(1558 nm)) and UC photoluminescence at 984 nm (UCPL$_{\text{rel}}$(984 nm)). **e** UCQY of the main UC emission at 984 nm in dependence on λ_{design} (cut through graph **a** at I_{in}(UCQY$_{\text{first,max}}$)).

considered. The general trends in the 2D scan can be understood easiest when looking at cuts along the irradiance axis. Exemplary cuts at different λ_{design} are presented in Fig. 5.10b. Every cut features a curve with a similar shape to the reference UCQY (compare to Fig. 5.9b). However, the curve is slightly compressed or stretched along the irradiance axis, such that the maximum always lies at a different position on the x-axis. Thereby the maximum UCQY gradually increases when going from λ_{design} = 1025 nm to λ_{design} = 1621 nm. This observation is explained later in panel f. The white line in Fig. 5.10a represents the position of the maximum UCQY on the irradiance axis at each λ_{design}. [3] When scanning

[3] The large steps in the white line are due to a large binning of 1000 W m^{-2} from 15000 W m^{-2} to 20000 W m^{-2}.

the irradiance axis from zero to higher values, the first maximum UCQY ($UCQY_{first,max}$) is found at $I_{in}(UCQY_{first,max})$ = 13900 W m^{-2} for the cut at $\lambda_{design}(UCQY_{first,max})$ = 1605.35 nm (Fig. 5.10a). The $UCQY_{first,max}$ is also the overall maximum found in the scanned region. This finding is adressed again in the discussion of panel f. The trends of the UCQY along the λ_{design} axis can be understood by the change in the LDOS for the main UC emission ($\overline{LDOS}_{rel}$) (Fig. 5.10c, compare to Fig. 5.6a) and the resulting change in photoluminescence for the two most important spontaneous emission processes: the main UC emission at 984 nm ($UCPL_{rel}$(984 nm)) and the loss emission at 1558 nm (PL_{rel}(1558 nm)) (Fig. 5.10d, compare to Fig. 5.9a). Figure 5.10c demonstrates how $\overline{LDOS}_{rel}$(984 nm) of the main UC

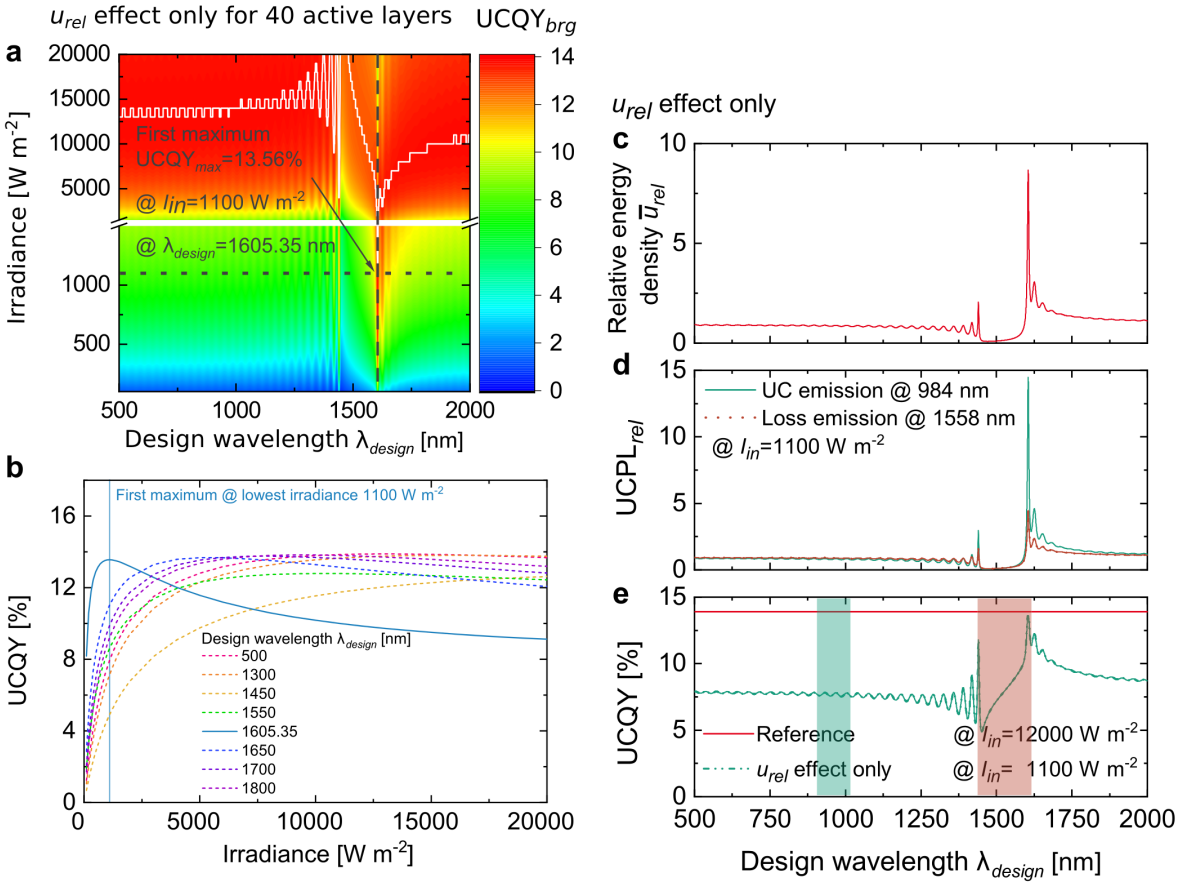

Figure 5.11.: Photonic effect of only the energy density enhancement on upconversion (UC) by setting the local density of optical states (LDOS) to unity. The investigated Bragg structure consists of 40 active layers with low refractive index n_{low} = 1.5 and high refractive index n_{high} = 1.8. **a** UC quantum yield (UCQY) in dependence on design wavelength λ_{design} and incident irradiance I_{in}. The white line indicates the maximum UCQY at each λ_{design}. When scanning the I_{in} axis, the first maximum UCQY ($UCQY_{first,max}$) of 13.56% is already reached at $I_{in}(UCQY_{first,max})$ = 1100 W m^{-2} and $\lambda_{design}(UCQY_{first,max})$ = 1605.35 nm. **b** UCQY as a function of I_{in} (cuts through graph **a**) for a selection of λ_{design} values, including $\lambda_{design}(UCQY_{first,max})$. **c** Average relative energy density $\bar{u}_{rel}$ across the active layers of the Bragg structure for an excitation wavelength $\lambda_{excitation}$ = 1523 nm. **d** Relative photoluminescence at 1558 nm (PL_{rel}(1558 nm)) and UC photoluminescence at 984 nm ($UCPL_{rel}$(984 nm)). **e** UCQY of the main UC emission at 984 nm in dependence on λ_{design} (cut through graph **a** at $I_{in}(UCQY_{first,max})$).

emission and $\overline{LDOS}_{rel}$(1558 nm) of the loss emission is suppressed when the respective

emission falls into the photonic bandgap (highlighted regions). [4] Figure 5.10d shows the relative photoluminescence influenced by only the LDOS effect. The trend of PL_{rel}(1558 nm) is mainly influenced by the LDOS of the corresponding emission $\overline{LDOS}_{rel}$(1558 nm). The net effect of the LDOS on $UCPL_{rel}$(984 nm), however, is a complex, non-linear superposition of $\overline{LDOS}_{rel}$(984 nm) and $\overline{LDOS}_{rel}$(1558 nm). An increase in $\overline{LDOS}_{rel}$(984 nm) linearly increases the UC efficiency in $UCPL_{rel}$(984 nm). However, an increase in $\overline{LDOS}_{rel}$(1558 nm) non-linearly decreases UC efficiency in $UCPL_{rel}$(984 nm). Finally, Fig. 5.10e shows the UCQY as a cut through Fig. 5.10a at $I_{in}(UCQY_{first,max})$ = 13900 W m^{-2}. The UCQY is proportional to the UC luminescence (see equation 3.40) and thus follows the trend of $UCPL_{rel}$(984 nm) (Fig. 5.10d). The LDOS effect has a maximum positive impact on the UCQY when the loss emission at 1558 nm falls into the photonic bandgap. In this region there are fewer photonic states available for the loss photoluminescence at 1558 nm relative to an increase in the photonic states being available for an UC emission at 984 nm. The same trend along the λ_{design} axis can be seen at every irradiance in Fig. 5.10a. Consequently, the $UCQY_{first,max}$ also represents the overall maximum in the scanned region. A comparison to the reference and other effects is drawn in Fig. 5.13.

The second photonic effect is the modified local energy density. Figure 5.11 shows the detailed analysis of the energy density effect for a Bragg structure with 40 active layers, in the same manner as the LDOS effect is investigated in Fig. 5.10. Figure 5.11a again depicts the 2D scan of the UCQY for a varied λ_{design} and I_{in}. The white line indicates the maximum of each cut along the irradiance axis. Figure 5.11b shows a selection of these cuts. The major change, compared to the investigation of the LDOS effect, is that $UCQY_{first,max}$ is already found at a very low irradiance $I_{in}(UCQY_{first,max})$ = 1100 W m^{-2}. Thereby, $UCQY_{first,max}$ of 13.56% is slightly lower than the reference maximum UCQY of 13.89%, which is discussed again later. At the same time, the trend along the λ_{design} axis shows more pronounced features. The cut through (Fig. 5.11a along the λ_{design} axis at $I_{in}(UCQY_{first,max})$ is plotted in Fig. 5.11e. The average relative energy density $\bar{u}_{rel}$ within the active layers of the Bragg structure (Fig. 5.11c) depicts a sharp peak at the photonic band edge at $\lambda_{design}(u_{rel,max})$ = 1605.2 nm, reaching a value of 8.7. This increase in the energy density linearly increases the absorption, and therefore approximately linearly increases the loss emission PL_{rel}(1558 nm). The UC emission $UCPL_{rel}$(984 nm), however, is increased non-linearly, reaching a peak enhancement of 14.5. (Fig. 5.11d). The shape of the UCQY in Fig. 5.11e is given by the ratio of $UCPL_{rel}$(984 nm) and the absorption enhancement, which is identical to $\bar{u}_{rel}$ (see equation 3.36).

Finally, Fig. 5.12 demonstrates how UC efficiency is influences by the combined photonic effects. Figure 5.12a shows the 2D scan of the UCQY, now influenced by both, the LDOS effect and the energy density enhancement. Fig. 5.12b depicts the cuts along the I_{in} axis, including a cut at $\lambda_{design}(UCQY_{first,max})$, which is now found at $I_{in}(UCQY_{first,max})$ = 1290 W m^{-2}. Figures 5.12c and d again show $\bar{u}_{rel}$ and $\overline{LDOS}_{rel}$, respectively. Looking at $UCPL_{rel}$ (Fig. 5.12e) and the UCQY cut along the λ_{design} axis (Fig. 5.12f), it becomes evident that the dominant photonic effect on UC efficiency is the energy density enhancement.

The UCQY cuts along the I_{in} and λ_{design} axis at $UCQY_{first,max}$ of each 2D scan (Figs. 5.10, 5.11 and 5.12) are summarized in Fig. 5.13 together with the reference UCQY. Figure

[4] In the Fig. 5.6a $\overline{LDOS}_{rel}$(984 nm) and $\overline{LDOS}_{rel}$(1558 nm) are plotted in an identical way, however, the simulated n_{high} differes. In Fig. 5.6a n_{high} = 2.3, in Fig. 5.10c, n_{high} = 1.8.

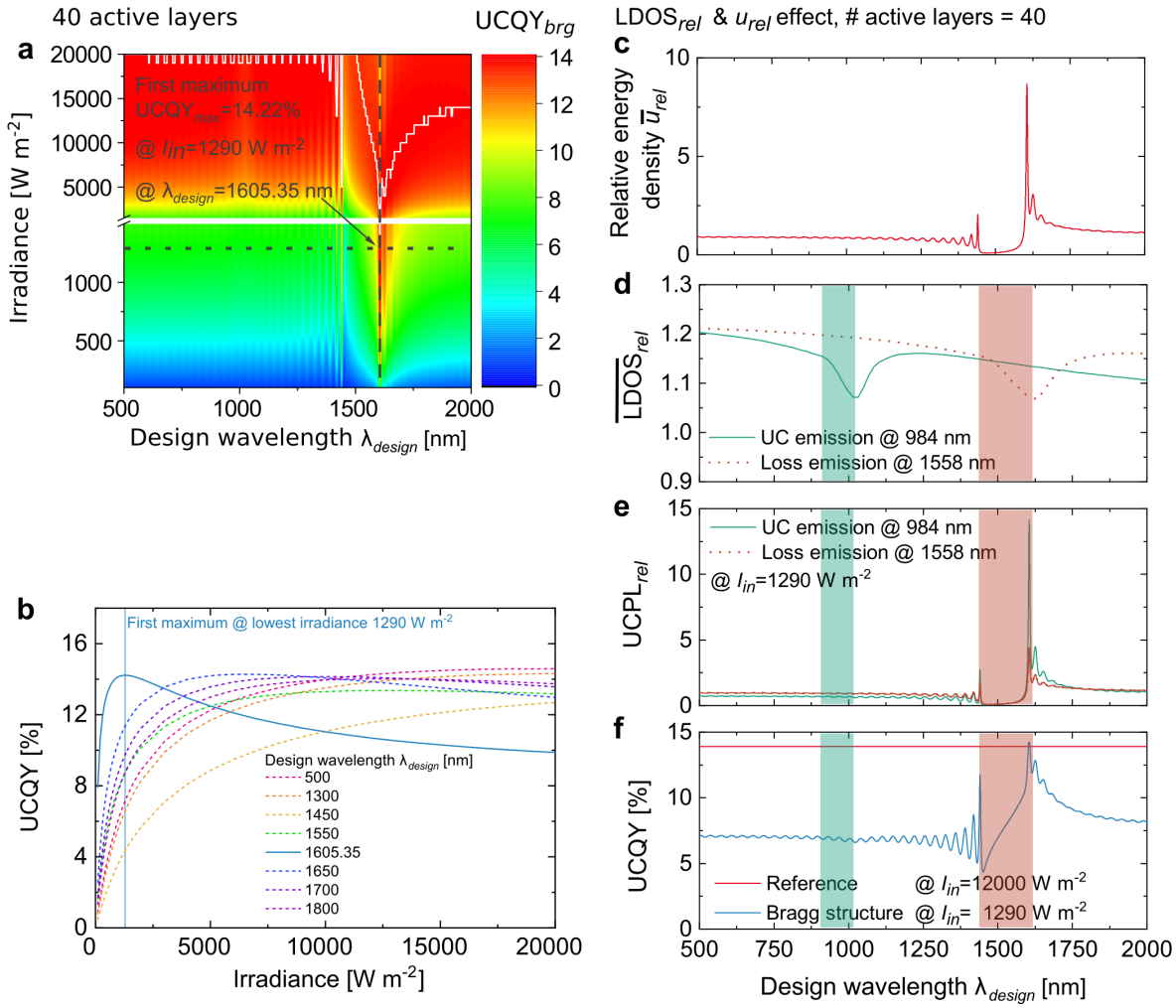

Figure 5.12.: Photonic effects on upconversion (UC) including both photonic effects, the local density of optical states (LDOS) and energy density enhancement. The investigated Bragg structure consists of 40 active layers with low refractive index n_{low} = 1.5 and high refractive index n_{high} = 1.8. **a** UC quantum yield (UCQY) in dependence on design wavelength λ_{design} and incident irradiance I_{in}. The white line indicates the maximum UCQY at each λ_{design}. When scanning the I_{in} axis, the first maximum UCQY ($\text{UCQY}_{\text{first,max}}$) of 14.22% is already reached at $I_{\text{in}}(\text{UCQY}_{\text{first,max}})$ = 1290 W m^{-2} and $\lambda_{\text{design}}(\text{UCQY}_{\text{first,max}})$ = 1605.35 nm. **b** UCQY as a function of I_{in} (cuts through graph **a**) for a selection of λ_{design} values, including $\lambda_{\text{design}}(\text{UCQY}_{\text{first,max}})$. **c** Average relative energy density $\bar{u}_{\text{rel}}$ across the active layers of the Bragg structure for an excitation wavelength $\lambda_{\text{excitation}}$ = 1523 nm. **d** Average relative LDOS for the main UC emission at 984 nm ($\overline{\text{LDOS}}_{\text{rel}}$(984 nm)) and loss emission at 1558 nm ($\overline{\text{LDOS}}_{\text{rel}}$(1558 nm)). **e** Relative photoluminescence at 1558 nm (PL_{rel}(1558 nm)) and UC photoluminescence at 984 nm (UCPL_{rel}(984 nm)). **f** UCQY of the main UC emission at 984 nm in dependence on λ_{design} (cut through graph **a** at $I_{\text{in}}(\text{UCQY}_{\text{first,max}})$).

5.13a shows how the maximum possible UCQY is increased from 13.89% in the reference structure to 14.66% when including the effect of the LDOS. The reason is that there are less photonic states available for the loss emission at 1558 nm relative to the photonic states that are available for an UC emission at 984 nm. At the same time, the maximum is shifted to a slightly higher irradiance. When only the effect of the relative energy density $\bar{u}_{\text{rel}}$ is

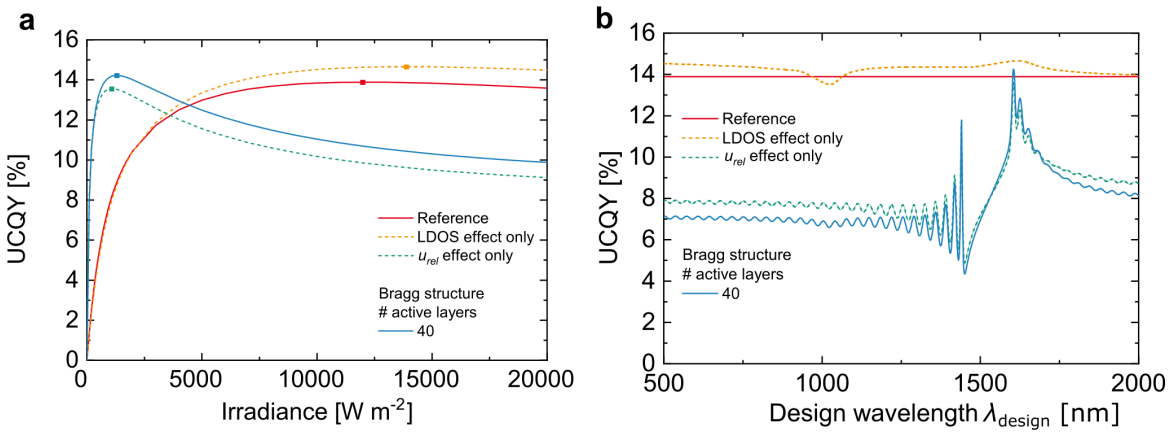

Figure 5.13.: Summary of photonic effects on upconversion (UC), only the local density of optical states (LDOS), only the energy density enhancement and both effects in comparison to the reference. The investigated Bragg structure consists of 40 active layers with low refractive index n_{low} = 1.5 and high refractive index n_{high} = 1.8.**a** UC quantum yield (UCQY) of the main UC emission at 984 nm as a function of incident irradiance (I_{in}). Each curve is given at the design walelength (λ_{design}) at which the first maximum UCQY ($\text{UCQY}_{\text{first,max}}$) occurs $\lambda_{\text{design}}(\text{UCQY}_{\text{first,max}})$. **b** UCQY in dependence on λ_{design}, each plotted at $I_{\text{in}}(\text{UCQY}_{\text{first,max}})$ at which $\text{UCQY}_{\text{first,max}}$ occurs.

investigated, the UCQY curve is compressed along the x-axis. Consequently, $\text{UCQY}_{\text{first,max}}$ is already reached at a much lower $I_{\text{in}}(\text{UCQY}_{\text{first,max}})$ = 1100 W m^{-2}, compared to the reference structure, where the maximum is only reached at I_{in} = 12000 W m^{-2}. The local irradiance at the position of the upconverter material, is given by the product of incident irradiance I_{in} and local energy density $u(x)$. At any maximum UCQY, this local irradiance approximately features the optimal irradiance of 12000 W m^{-2}. However, because $u(x)$ is oscillating in the Bragg structure (compare to Fig. 5.1c), the optimal irradiance can never be reached at all positions of upconverter material. Consequently, the UCQY is slightly lower than in the reference. Finally, when both photonic effects are included in simulation, the compression of the UCQY curve due to an increaes in local energy density appears, as well as the increase of the maximum UCQY due to the modified LDOS. The $\text{UCQY}_{\text{first,max}}$ of 14.22% is therefore reached at $I_{\text{in}}(\text{UCQY}_{\text{first,max}})$ = 1290 W m^{-2}, which is almost by a factor of ten lower than I_{in} of the reference maximum UCQY. Figure 5.13b depicts the λ_{design} dependence for each effect. When only the LDOS effect is considered, the UCQY outperforms the reference, expect for the spectral region around 1000 nm, where the UC emission lies within the photonic bandgap. The maximum UCQY appears in a broad spectral range, when the loss emission is in the photonic bandgap. When the effect of the energy density $\bar{u}_{\text{rel}}$ is included, the shape and position of the peak enhancement of $\bar{u}_{\text{rel}}$ defines the UCQY. Consequently, the maximum UCQY appears only in a narrow spectral range. For all other λ_{design}, the UCQY is much lower than the reference UCQY because of the low $I_{\text{in}}(\text{UCQY}_{\text{first,max}})$ that the cuts are plotted for.

5.2.3. Analysis of maximum upconversion efficiency

When the photonic effects on UC are understood, the design of the photonic structure can be optimized to maximally enhance UC efficiency. In the previous section 5.2.2, the photonic effects on UCQY and UCPL were investigated in dependence on the design wavelength λ_{design} and the incident irradiance I_{in}. In this section, the number of layers within the Bragg structure is additionally varied and an optimum design wavelength λ_{design} is identified that yields a peak UCQY enhancement at a certain incident irradiance I_{in}. Furthermore, design parameters to gain a maximum UCPL are found. The simulations are performed for the same refractive indices as in Section 5.2.2, n_{low} = 1.5 and n_{high} = 1.8. The outermost layers of the Bragg structures feature undoped PMMA with a thickness $d = \lambda_{\text{design}}/8$ to improve coupling in the excitation beam at 1523 nm.

Figure 5.14a-d shows the UCQY in a 2D scan of λ_{design} and I_{in} for four exemplary Bragg

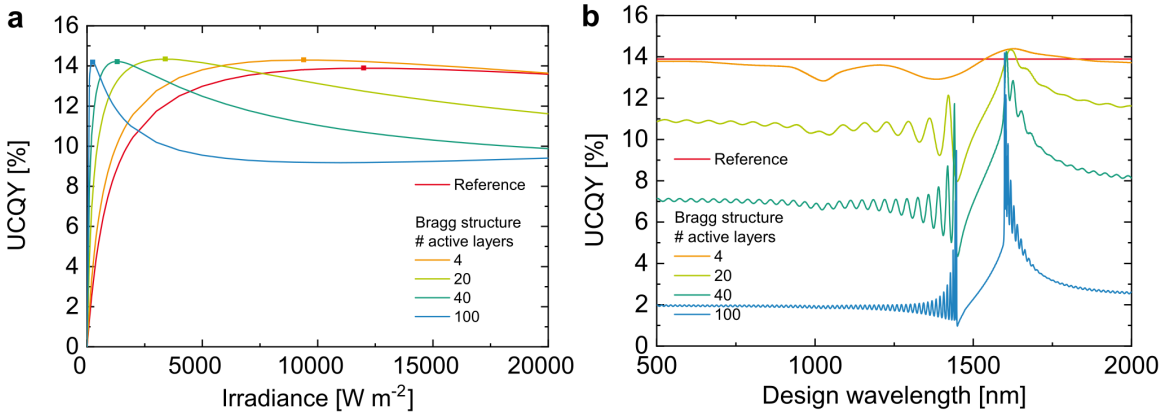

Figure 5.14.: 2D-scan of the upconversion quantum yield ($\text{UCQY}_{\text{first,max}}$) for Bragg structures with 4, 20, 40 and 100 active layers. The investigated Bragg structures are made of the low refractive index n_{low} = 1.5 and high refractive index n_{high} = 1.8. **a-d** Upconversion quantum yield (UCQY) in dependence on design wavelength λ_{design} and incident irradiance I_{in} for Bragg structures with 4, 20, 40 and 100 active layers, respectively. The white line indicates the maximum UCQY at each λ_{design}. $\text{UCQY}_{\text{first,max}}$ is identified in each scan as the maximum UCQY at the lowest I_{in}.

structure designs with 4, 20, 40 and 100 active layers, respectively. The white line indicates the irradiance I_{in} at which the maximum UCQY is reached for each simulated λ_{design} (a more comprehensive explanation is given in the discussion of Fig. 5.10a). The position of the maxima is strongly dependent on the energy density enhancement within each particular structure (as closely investigated in Fig. 5.11 and Fig. 5.12).

The maximum that characterizes each structure is the first maximum UCQY ($\text{UCQY}_{\text{first,max}}$) that appears at the lowest I_{in} ($I_{\text{in}}(\text{UCQY}_{\text{first,max}})$). Figures 5.15a and b show the cuts along the I_{in} and λ_{design} axis, respectively, at $\text{UCQY}_{\text{first,max}}$ in each 2D scan. As the layer number increases, and therewith the energy density enhancement increases, the first maximum UCQY moves to lower I_{in}. On the λ_{design} axis, the peak enhancement around the maximum UCQY reduces in spectral width as the layer number increases and moves to lower λ_{design}.

From an application point of view, it is important to understand at which irradiance a photonic upconverter device depicts a high efficiency. Or to find a photonic upconverter

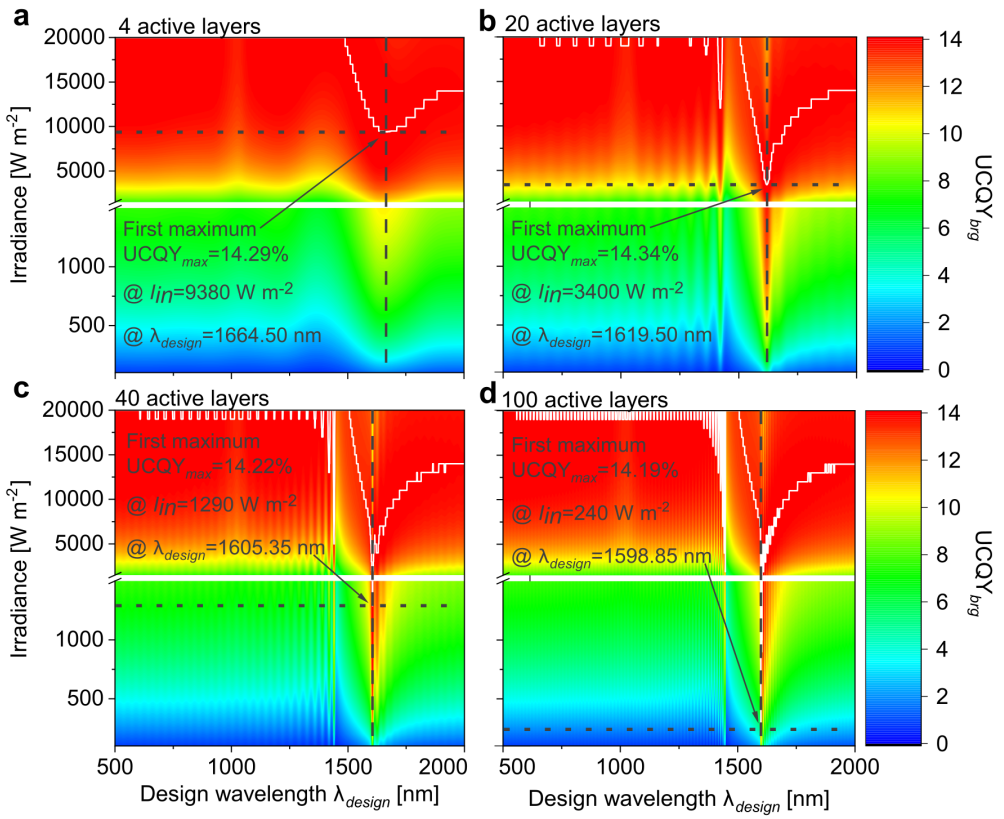

Figure 5.15.: First maximum upconversion quantum yield (UCQY$_{\mathbf{first,max}}$) for Bragg structures with 4, 20, 40 and 100 active layers. The investigated Bragg structures are made of the low refractive index n_{low} = 1.5 and high refractive index n_{high} = 1.8. **a** Cuts along the I_{in} axis at λ_{design}(UCQY$_{\text{first,max}}$). As the layer number increases, UCQY$_{\text{first,max}}$ gradually moves to lower I_{in}. **b** Cuts along the λ_{design} axis at I_{in}(UCQY$_{\text{first,max}}$). The peak gets sharper and moves to lower λ_{design} as the active layer number increases.

device that has a high efficiency at a given irradiance for a specific application. In the same way as in Fig. 5.14, 2D scans were carried out for Bragg structures with 4 to 16 active layers in steps of 4 and 20 to 100 active layers in steps of 5. Figure 5.16 shows the summary of all optimizations.

For each investigated active layer number, UCQY$_{\text{first,max}}$ is plotted (Fig. 5.16a), together with the corresponding incident irradiance I_{in}(UCQY$_{\text{first,max}}$) (Fig. 5.16b) and design wavelength λ_{design}(UCQY$_{\text{first,max}}$) (Fig. 5.16c). The result demonstrates that a maximum UCQY between 14.1% and 14.4% can be reached with all investigated Bragg structure designs ranging from 4 to 100 active layers. These reached maximum UCQY values are significantly higher than the 13.89% maximum UCQY of the reference. The most important finding, however, is that a maximum UCQY can be found at incident irradiances ranging from 200 W m^{-2} to 10000 W m^{-2}(Fig. 5.16b). Consequently, a maximum UCQY can be found at almost any incident irradiance I_{in} when a suitable Bragg structure design is chosen. The reference upconverter material reaches its maximum UCQY at 12000 W m^{-2}. In a Bragg structure with 4 active layers, a low energy density enhancement occurs, such that UCQY$_{\text{first,max}}$ is shifted to a slightly lower I_{in}(UCQY$_{\text{first,max}}$) = 9380 W m^{-2}. As the active layer number increases,

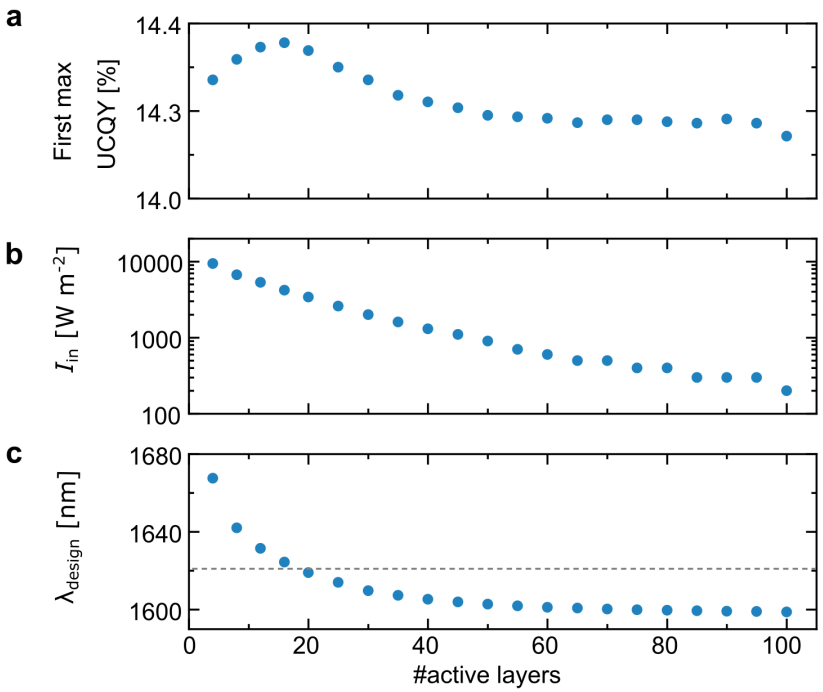

Figure 5.16.: First maximum upconversion quantum yield ($UCQY_{first,max}$) in dependence on the number of active layers. The investigated Bragg structures are made of the low refractive index n_{low} = 1.5 and high refractive index n_{high} = 1.8. **a** The $UCQY_{first,max}$ for each investigated active layer number, together with the corresponding incident irradiance $I_{in}(UCQY_{first,max})$ (**b**) and design wavelength $\lambda_{design}(UCQY_{first,max})$ (**c**) at each $UCQY_{first,max}$. With a suitable Bragg structure design, a UCQY close to the possible maximum of around 14.4% can be reached in a large irradiance range from 10000 W m^{-2} down to 240 W m^{-2} within the scanned parameter range.

the energy density enhancement in the Bragg structure increases and $UCQY_{first,max}$ gradually moves to lower I_{in}, reaching 240 W m^{-2} with 100 active layers. The convergence of $\lambda_{design}(UCQY_{first,max})$ (Fig. 5.16c) towards $\lambda_{design} \sim$ 1598.85 nm is already clearly visible in Fig. 5.15b. The excitation wavelength experiences the highest photonic enhancement effects when it is spectrally positioned at the photonic band edge. As the number of active layers in the Bragg structure increases, the peak of the energy density enhancement spectrally reduces in width and λ_{design}, which defines the position of the photonic bandgap, converges such that the excitation wavelength is placed right at the photonic band edge. The peak in the curve of all $UCQY_{first,max}$-values around 16 active layers can also be understood from the trend of the corresponding design wavelengths $\lambda_{design}(UCQY_{first,max})$: the LDOS effect has a maximally positive impact on the UCQY at λ_{design} = 1621 nm (see Fig. 5.10). The Peak in the $UCQY_{first,max}$-values occurs around the design of 16 active layers, where $\lambda_{design}(UCQY_{first,max})$ is closest to 1621 nm. At smaller and larger λ_{design}, $UCQY_{first,max}$ drops to slightly lower values.

As a conclusion for Fig. 5.16, I want to provide a short "how-to" when one wants to find a suitable design for a specific application with a fix incident irradiance: Fig. 5.16 shows that at basically any incident irradiance, a Bragg structure design can be found that yields a UCQY close to the possible maximum UCQY. Fig. 5.16b links the given incident irradiance to an active layer number. For this active layer number, the corresponding design wavelength

and expected first maximum UCQY can then be extracted from Fig. 5.16a and Fig. 5.16c, respectively. Because the curves in all three graphs are smooth, I expect that interpolation is possible to find optimal designs for incident irradiances that were not specifically found in this optimization.

It is important to note that the method applied in this analysis identifies the simplest possible Bragg structure with the fewest active layers that reaches its first maximum UCQY at a particular incident irradiance I_{in}. Other Bragg structure designs could be found that yield a similar UCQY at the same I_{in}. However, the enhancement will not be at the maximum energy density enhancement $u_{\text{rel,max}}$, but at a lower value of $\bar{u}_{\text{rel}}$ (compare to Fig. 5.1). Depending on the experimental circumstances, like available production accuracy and needed amount of upconverter material, a simple structure with few layers can be favorable, or a structure with more layers that demands a much higher production accuracy (compare to Fig. 5.3) but also allows for more embedded upconverter material.

Depending on the application, the UCPL enhancement can be of more interest than the UCQY. Figure 5.17a-d therefore depicts the UCPL enhancement (UCPL_{rel}) of the main UC

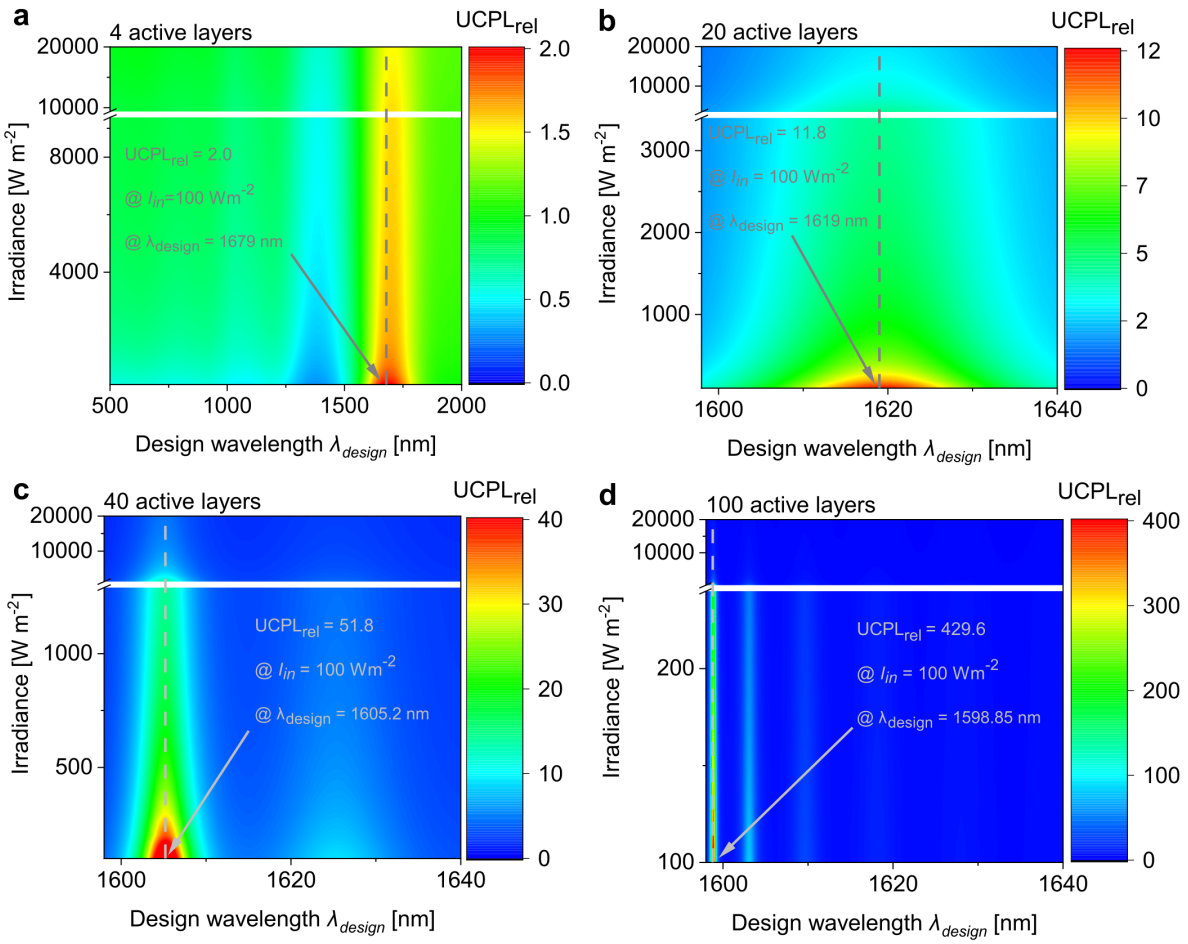

Figure 5.17.: 2D-scan of the relative upconversion (UC) photoluminescence UCPL_{rel} of the main UC emission at 984 nm. The investigated Bragg structures are made of the low refractive index n_{low} = 1.5 and high refractive index n_{high} = 1.8. **a-d** The UCPL_{rel} in dependence on design wavelength λ_{design} and incident irradiance I_{in} for Bragg structures with 4, 20, 40 and 100 active layers, respectively.

emission at 984 nm, again scanning λ_{design} and I_{in} for the same exemplary Bragg structures with 4, 20, 40 and 100 active layers, respectively. Note that the axes are scaled differently in all graphs to get a clear visualization of each individual 2D scan. The spectral position and shape of the UCPL enhancement is strongly related to the energy density enhancement (compare to Fig. 5.1). As the number of active layers increases, the enhancement peak gets spectrally more narrow. At the same time, the enhancement factor largely increases with more complex Bragg structure designs. While for 4 active layers $UCPL_{rel}$ = 2, 100 active layers yield $UCPL_{rel}$ = 430 at I_{in} = 100 W m^{-2}. Especially in comparison to the maximum UCQY, it is important to understand that the highest $UCPL_{rel}$ is always found at the lowest investigated I_{in}.

Figure 5.18 shows the cuts at λ_{design} that yields the highest $UCPL_{rel}$ in each panel a-d at

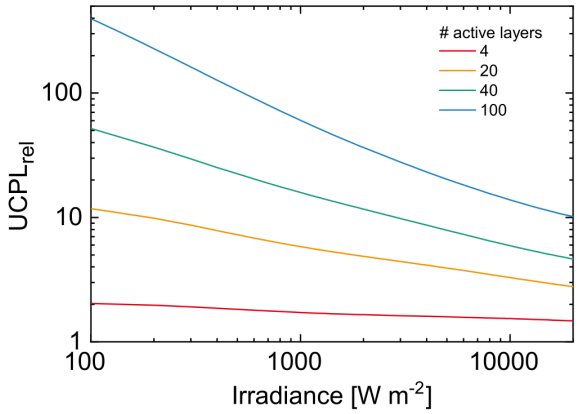

Figure 5.18.: Maximum relative upconversion (UC) photoluminescence $UCPL_{rel}$ of the main UC emission at 984 nm. The investigated Bragg structures are made of the low refractive index n_{low} = 1.5 and high refractive index n_{high} = 1.8. The cuts along the I_{in} axis at the design wavelength $\lambda_{design}(UCPL_{rel,max})$, at which the maximum $UCPL_{rel}$ occurs at the lowest investigated I_{in} = 100 W m^{-2} for 4, 20, 40 and 100 active layers. The highest $UCPL_{rel}$ is always found in the Bragg structure with the most active layers.

an exemplary incident irradiance I_{in} = 100 W m^{-2}. The cuts clearly show that the highest UCPL enhancement is always reached in the Bragg structure with the most layers.

5.2.4. Impact of Bragg structure materials and fabrication constraints

This subsection is largely based on my own publication ref. [34]. Next to the design wavelength λ_{design} and the active layer number that were investigated in the previous section, another important design parameter of a Bragg structure are the refractive indices of the two alternating layers. Therefore, in this section an analysis of varying the high refractive index layer of the Bragg structure is presented. The range of $1.5 \leq n_{high} \leq 4.0$ which is experimentally relevant is scanned. Furthermore, the active layer number is varied. A production accuracy of $\sigma = 1$ nm is assumed for this analysis (see Section 5.1.1), which is realistically attainable with current high-precision manufacturing methods.

To limit the parameter space, in this analysis λ_{design} is fixed at $\lambda_{design}(u_{rel,max})$, the design wavelength for which the enhancement of the energy density is at its maximum (see Fig. 5.2). For low irradiances, this is a reasonable approximation, as the energy density enhancement is the most important effect in this regime. Additionally, as discussed in section

5.2.2,$\lambda_{\text{design}}(u_{\text{rel,max}})$ is typically close to the λ_{design} for which the benefit of the LDOS, i.e. the ratio between the relative LDOS for the main UC emission and main loss emission $\overline{\text{LDOS}}_{\text{rel}}$(984 nm)/$\overline{\text{LDOS}}_{\text{rel}}$(1558 nm) is at its maximum. Since the peak of this ratio in λ_{design} space is much broader than that of $\bar{u}_{\text{rel}}$, $\lambda_{\text{design}}(u_{\text{rel,max}})$ will typically yield a UCQY value close to the maximum possible value.

In this section, the reference is simulated as a fully homogeneous medium. The simulations presented in all other sections were performed later when the simulation model was adapted such that the light is incident from air with $n = 1.0$. This leads to a difference in the irradiance of the reference maximum UCQY, which is identified as 11600 W m^{-2} in this section and 12000 W m^{-2} in all other. Figure 5.19 illustrates the basic dependence of the UCQY on the

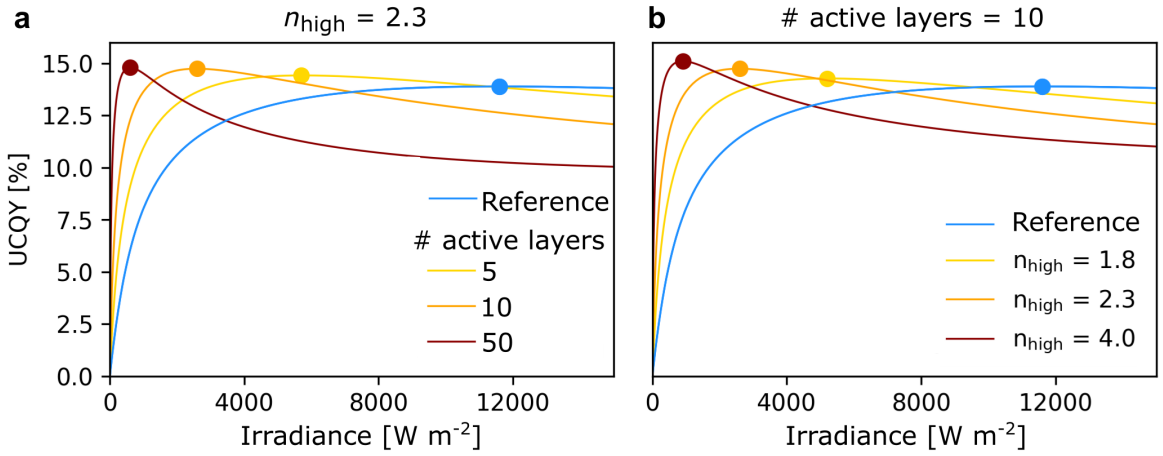

Figure 5.19.: Upconversion quantum yield (UCQY) as a function of incident irradiance I_{in} for exemplary families of Bragg structures. a UCQY for the high refractive index n_{high} fixed at 2.3 while the active layer number of the Bragg structure is varied and **b** for fixed 10 active layers while n_{high} is varied. The low refractive index n_{low} = 1.5. The analysis is performed at the design wavelength λ_{design}that yields the maximum energy density enhancement $\lambda_{\text{design}}(u_{\text{rel,max}})$ and for a layer thickness accuracy of σ = 1 nm. For the Bragg structures, higher UCQY values at much lower I_{in} are achievable. The maximum for each design is marked with a large dot. [34]

high refractive index n_{high} and the active layer number as a function of the incident irradiance I_{in}. In Fig. 5.19a, n_{high} is fixed at 2.3 while the active layer number is varied. This allows for studying the effect of $\bar{u}_{\text{rel}}$, as the calculated LDOS varies only slightly with the active layer number due to the change in $\lambda_{\text{design}}(u_{\text{rel,max}})$. The maximum UCQY for the reference is found at an irradiance of 11600 W m^{-2}. For the Bragg structures, the UCQY curve is compressed along the irradiance axis, as comprehensively discussed in Section 5.2.2. Fig. 5.4d showed that for n_{high} = 2.3, $\bar{u}_{\text{rel}}$ increases when the active layer number increases. Therefore, the compression of the UCQY curve on the irradiance axis is stronger for a higher layer number. Additionally, the maxima for the Bragg structures are slightly higher than for the reference due to the modified LDOS, as discussed in Section 5.2.2. In Fig. 5.19b, the active layer number is fixed at 10, while n_{high} is varied. Fig. 5.4d demonstrated that for 10 active layers, $\bar{u}_{\text{rel}}$ increases with increasing n_{high}. That is, as the refractive index contrast increases, fewer layers are needed to reach the same energy density enhancement. Similar to the case of increasing the active layer number, a compression along the irradiance axis

occurs. Additionally, the maximum UCQY moves to higher values with increasing n_{high} due to the increasing strength of the LDOS modification as illustrated in Figs. 5.5 and 5.6.

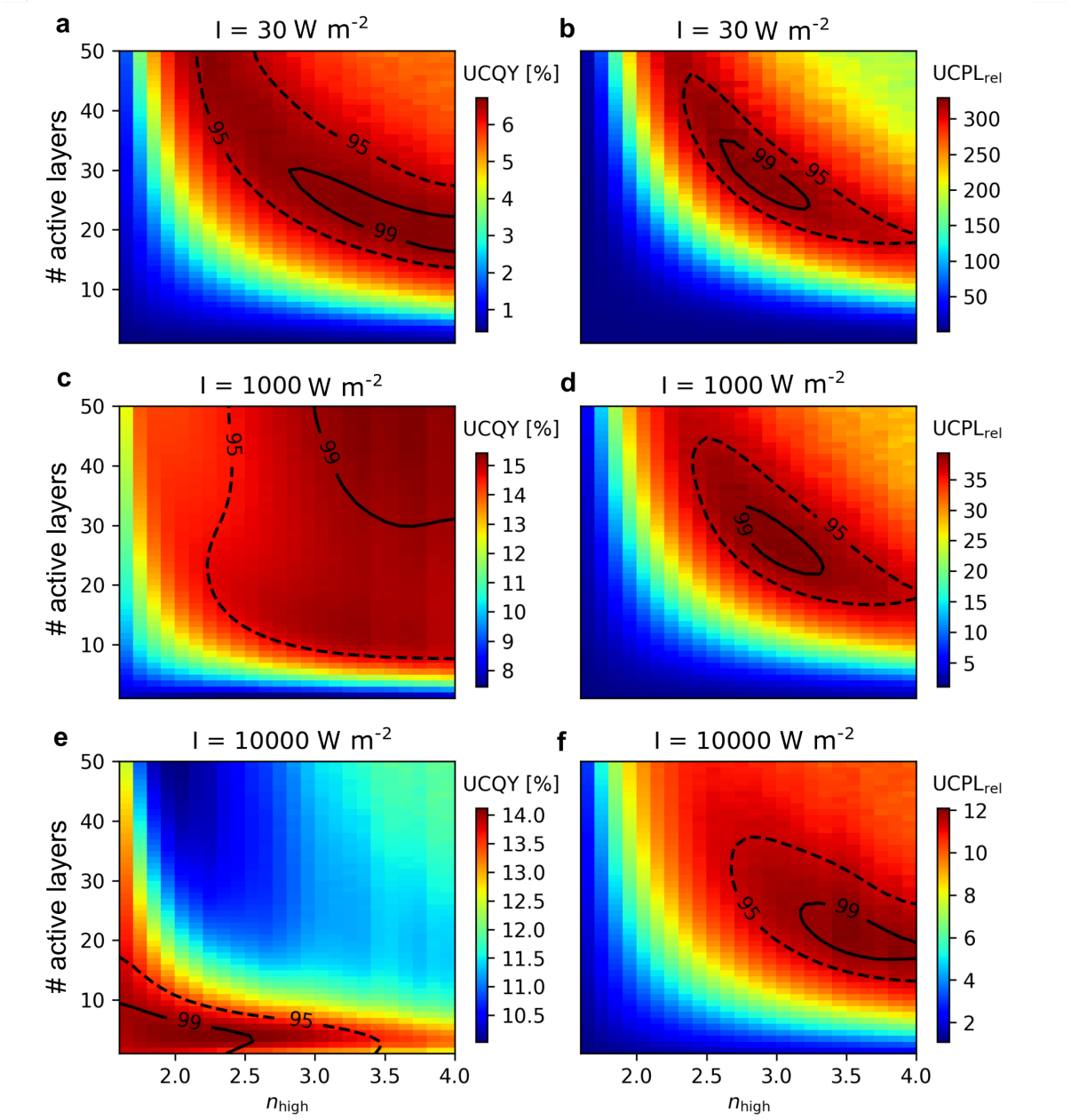

Figure 5.20.: Upconversion quantum yield (UCQY) (left) and relative upconversion photoluminescence (UCPL) of the main UC emission at 984 nm (UCPL_{rel}(984 nm)) (right) as a function of high refractive index (n_{high}) and the number of active layers in the Bragg structure. The low refractive index n_{low} = 1.5. The analysis is performed at the design wavelength λ_{design} that yields the maximum energy density enhancement $\lambda_{\text{design}}(u_{\text{rel,max}})$ and for a layer thickness accuracy of σ = 1 nm. The black contour lines indicate 99% (solid line) and 95% (dashed line) of the maximum UCQY in each plot. The rows show different incident irradiance scenarios of I_{in} = 30 W m^{-2}, 1000 W m^{-2}, and 10000 W m^{-2} (1 W cm^{-2}). [34]

To enable an assessment of structural designs in two dimensions, the dimensionality of the

parameter space is reduced by fixing the irradiance at specific application scenarios. For non-concentrated sunlight, the irradiance available from the air-mass 1.5 global spectrum within the absorption range of Er^{3+} (from 1450 nm to 1600 nm) is approximately 30 W m^{-2} [137]. A higher incident irradiance case of 1000 W m^{-2} could be reached by combined spectral and geometrical concentration [138]. To also investigate the photonic upconverter system in the high irradiance regime, the case of 10000 W m^{-2} (1 W cm^{-2}) is considered as well.

For each scenario, the UCQY is shown as a function of n_{high} and the active layer number in the left panels of Fig. 5.20. In the first panel, I_{in} = 30 W m^{-2}, the incident irradiance is so low, that the UCQY is determined almost exclusively by the energy density enhancement. This explains the structural resemblance of Fig. 5.20a to Fig. 5.4d. The highest UCQY reached for this irradiance is 6.7%. At I_{in} = 1000 W m^{-2}, Fig. 5.20c, UCQY values up to 15.4% become possible. With n_{high} = 2.3, 95% of this maximum value can be reached with 20 layers, while for n_{high} = 3.0 only 10 layers are needed. Because of the saturation of the UCQY that is clearly visible in Fig. 5.19 for the reference, the UCQY does not feature a strong dependence on the irradiance. Hence, the observed maximum of the UCQY is rather broad. Going to even higher I_{in}, Fig. 5.20e, saturation occurs and the UCQY starts decreasing (see also Fig. 5.19). Hence, in concentrated-solar applications, the benefit of the Bragg structure decreases regarding the UCQY. However, it should be noted that higher UCQY values than shown are possible by tuning λ_{design}. In the case of a very high I_{in}, the assumption of $\lambda_{\text{design}} = \lambda_{\text{design}}(u_{\text{rel,max}})$ being an almost ideal choice for maximizing the UCQY, is no longer valid. For some applications, the UCPL is of more interest than the UCQY. Therefore, also the relative UCPL (UCPL_{rel}) for the main UC emission at 984 nm is investigated. The analysis is shown in the right panels of Fig. 5.20, again as a function of n_{high} and the active layer number. While the absorption enhancement is directly given by the energy density enhancement, the UCPL depends non-linearly on the local energy density. This non-linearity saturates to linearity at a characteristic irradiance threshold. Therefore, at low irradiances far from saturation, the UCPL can be increased by orders of magnitude compared to the performance of the reference. For the very low irradiance of I_{in} = 30 W m^{-2}, Fig. 5.20b, the Bragg structure enables a 330-fold UCPL enhancement, even with the assumed production inaccuracy of $\sigma = 1$ nm. At I_{in} = 1000 W m^{-2}, Fig. 5.20d, the maximum UCPL enhancement has decreased to $\approx$ 40-fold. At this irradiance, the relative effect of the Bragg structure is lower because the UCQY of the reference is already much higher. Proceeding to the case of I_{in} = 10000 W m^{-2} (1 W cm^{-2}) plotted in Fig. 5.20f, the enhancement factor drops further to a maximum of $\approx$ 12. At this high irradiance, the UCQY is in fact lower for some Bragg structures compared to the reference, which causes the UCPL enhancement to drop below the energy density enhancement. In consequence, the ideal design for the UCPL enhancement is a different one than for the UCQY enhancement.

5.2.5. Directionality of emission

Particularly for a target application in photovoltaics, it is important to understand the directionality of the UC emission. The photonic-upconverter needs to be positioned such that a large part of the out-coupled upconverted photons can reach the solar cell. Therefore, the directionality of UC emission is investigated in this section.

Figure 5.21 shows the fractional UC photoluminescence $\text{UCPL}_{\text{FDOS}}$ (equation 3.42) for the

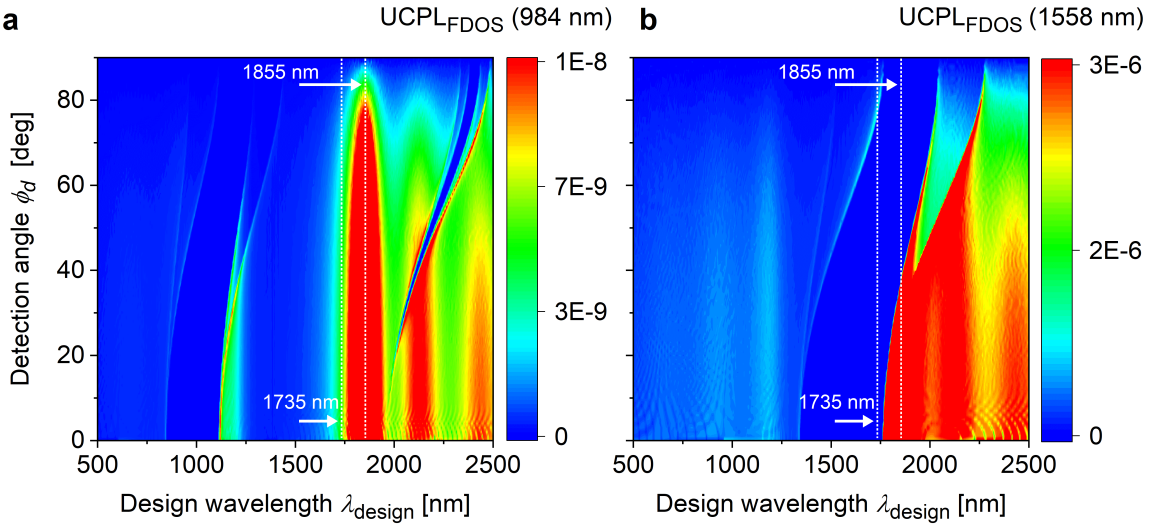

Figure 5.21.: Fractional upconversion photoluminescence (UCPL$_{FDOS}$). The UCPL is calculated for an incident irradiance of 30 W cm^{-2} at 1523 nm excitation wavelength at normal incidence. FDOS$_{norm}$ is simulated for the low refractive index n_{low} = 1.47, high refractive index n_{high} = 2.28 and surrounding medium air (n = 1.0). Each detection angle ϕ_d is calculated for a detection half cone of 0.5 °. **a** UCPL$_{FDOS}$ for the main UC emission at 984 nm, plotted against the design wavelength λ_{design}. **b** UCPL$_{FDOS}$ for the loss emission at 1558 nm. The optimal λ_{design} for the LDOS effect at λ_{design} = 1735 nm and for a maximal UCPL$_{rel}$ at λ_{design} = 1855 nm are indicated as a white dashed line. At the optimal λ_{design} = 1855 nm, the majority of the main UC emission is detected at small angles. Consequently, a large part of the out-coupled UC emission can reach a solar cell placed above the photonic-upconverter.

main UC emission at 984 nm (UCPL$_{FDOS}$(984 nm)) and the main loss emission at 1558 nm (UCPL$_{FDOS}$(1558 nm)). UCPL$_{FDOS}$ describes the fraction of the total UC emission that is coupled out of the photonic structure and detected at an angle ϕ_d in a detection cone with half angle θ_d. The features of FDOS$_{norm}$ (see 5.7) are again visible in the UCPL$_{FDOS}$, overlaid with the enhancement effects of the optical energy density enhancement in the Bragg structure. The peak of UCPL$_{FDOS}$(984 nm) at the design wavelength λ_{design} = 1855 nm, caused by the optical energy density enhancement, dominates the net effect at all detection angles (Fig. 5.21a). In the λ_{design}-range around 1855 nm, the UCPL$_{FDOS}$(984 nm) does not coincide with a photonic bandgap. A large part of the modes are directed into small angles, such that a large fraction of the UC emission can reach a solar cell placed above the photonic-upconverter. UCPL$_{FDOS}$(1558 nm) (Fig. 5.21b), however, lies at the photonic band edge in the λ_{design}-range around 1855 nm. At λ_{design} = 1735 nm, UCPL$_{FDOS}$(1558 nm) coincides with the photonic bandgap for all detection angles. Moving towards larger λ_{design}, UCPL$_{FDOS}$(1558 nm) reaches the band edge at small detection angles and is thus enhanced. However, this effect is not decisive for the emission characteristics of the main UC emission UCPL$_{FDOS}$(984 nm).

Figure 5.22 depicts the fractional relative UC photoluminescence UCPL$_{rel,FDOS}$, the out-coupled emission from the Bragg structure, relative to the out-coupled emission from the reference structure (equation 3.43). Again, the features of the FDOS$_{rel}$, shown in Fig. 5.8, are clearly visible, in superposition with the optical energy density enhancement. In the

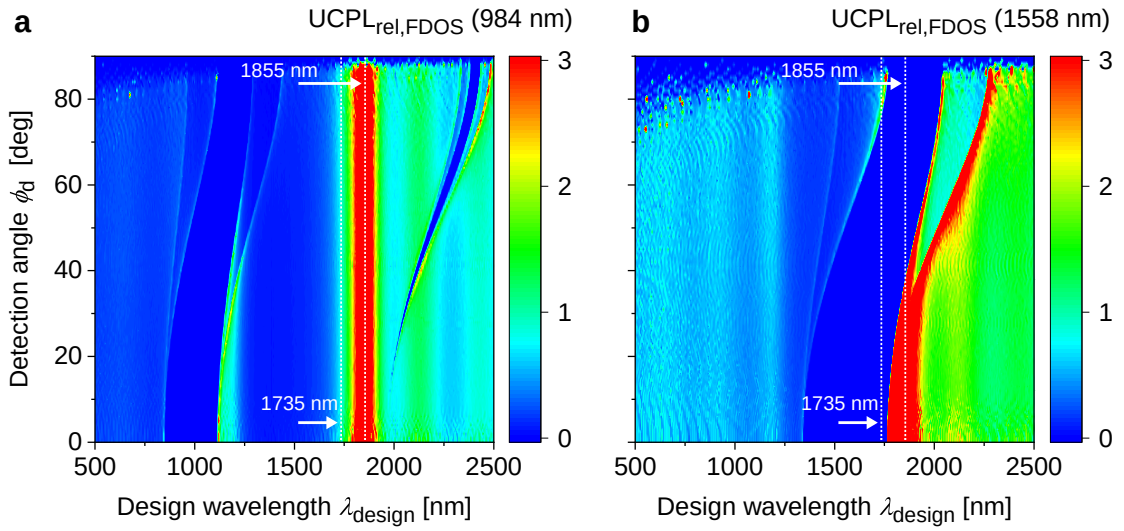

Figure 5.22.: Fractional relative upconversion photoluminescence (UCPL$_{rel,FDOS}$). The UCPL is calculated for an incident irradiance of 30 W cm^{-2} at 1523 nm excitation wavelength at normal incidence. FDOS$_{norm}$ is simulated for the low refractive index n_{low} = 1.47, high refractive index n_{high} = 2.28 and surrounding medium air ($n = 1.0$). Each detection angle ϕ_d is calculated for a detection half cone of 0.5 °. **a** UCPL$_{FDOS}$ for the main UC emission at 984 nm, plotted against the design wavelength λ_{design}. **b** UCPL$_{FDOS}$ for the loss emission at 1558 nm. The optimal λ_{design} for the LDOS effect at λ_{design} = 1735 nm and for a maximal UCPL$_{rel}$ at λ_{design} = 1855 nm are indicated as a white dashed line. Differences in the emission characteristics of Bragg structure and reference occur in the spectral regions in and around the bandgaps.

spectral regions off the bandgaps, the features are almost constant over all detection angles, showing that the emission characteristics of the Bragg structure are almost identical to the reference in these spectral regions. Features that vary along the detection angle axis are, as expected, in the spectral regions within the bandgaps and at the band edges. However, UCPL$_{rel,FDOS}$(984 nm) is nearly constant over all detection angles for the λ_{design}-range of interest around 1855 nm.

5.3. Summary

In this chapter, a comprehensive study of modeling photonic effects of a Bragg structure on UC within β-NaYF$_4$:Er^{3+} was presented. Firstly, the two photonic effects were modeled on their own. The enhancement peak of the optical local energy density was found at the higher frequency band edge of the first photonic bandgap. Production inaccuracies, as they occur in any experiment, were found to be crucial to be included in simulation. They drastically diminish the maximum enhancement, especially for more complex designs with a high active layer number. The other photonic effect, the local density of optical states (LDOS), grows stronger with an increasing refractive index contrast. As a figure of merit, the ratio of relative LDOS enhancement of the main UC emission divided by the main loss emission, showed a maximum in the spectral range where the loss emission is placed in the first photonic

bandgap.

In a second step, the dynamics of the UC process were analyzed in a reference structure versus a Bragg structure. Additionally, the impact of only one photonic effect on UC was studied by setting the enhancement of the other photonic effect to unity. The LDOS effect was found to increase the maximum possible UCQY from 13.89% in the reference, to 14.66%, because there are less photonic states available for the loss emission relative to the states available for an UC emission to take place. The energy density enhancement effect compresses the UCQY curve along the irradiance axis, such that the maximum UCQY, that is found at 12000 W m^{-2} in the reference, can already be found at much lower incident irradiance values. A scan of the active layer number, incident irradiance and design wavelength revealed that a UCQY close to the maximum possible UCQY can be found for any incident irradiance between 200 W m^{-2} to 10000 W m^{-2} using designs between 4 and 100 active layers. This finding demonstrates the necessity of actually optimizing a photonic structure design for a particular application. The enhancement of the UCPL, for ideal Bragg structures however, is always highest in the Bragg structure design with most layers and always increases towards lower incident irradiances.

In a third step, the benefit of photonic effects for the UCQY and UCPL was investigated, including a production inaccuracy of σ = 1 nm. Thereby, the interdependence of the active layer number and refractive index contrast was analyzed in a 2D-scan. It was shown that the incident irradiance is decisive for the choice of a best design: at a low incident irradiance of 30 W m^{-2} (one sun), complex designs with many layers are favorable to yield a higher UCQY. At an intermediate irradiance of 1000 W m^{-2}, a large range of designs from 10 active layers and a high refractive index of 2.0 onward, all yield similar UCQY values. For a high incident irradiance of 10000 W m^{-2}, simple designs below 10 active layers are favorable to maximize the UCQY. For the case of the UCPL including production inaccuracies, different from the case of an ideal structure, it is not the most complex design that yields the highest enhancement factors. The enhancement factor itself drops from 330-fold at a low incident irradiance of 30 W m^{-2} to 12-fold for a high incident irradiance of 10000 W m^{-2}. However, the best performing designs are nearly the same for all tested incident irradiances. Therefore, the optimal design is closely linked to the set production inaccuracy.

Finally, the directionality of the emitted modes was analyzed by means of the fractional local density of optical states. It was found that the UC emission mainly differs from modes coupled out of the reference at the band edges, where they are enhanced, and in the bandgaps, where they are suppressed. For the designs of interest in this work, the UC emission is in a spectral region far from the bandgaps. Therefore, the emission characteristics and the modes that are coupled out, are very similar to the characteristics in the reference structure. Consequently, a large part of the emitted light could reach a solar cell placed above the photonic upconverter.

5.4. Contributions to this chapter

Clarissa L. M. Hofmann (Author)

- conceived of the research questions and planned the according simulations

- implemented most simulations, except the ones implemented by E. H. Eriksen (see below)
- interpreted all simulations - some in joint effort with E. H. Eriksen (see below)
- planned and designed most figures (except for the ones designed by E. H. Eriksen in the joint publication Hofmann, Eriksen *et al.* [34])

Emil H. Eriksen

- implemented the simulations and figures for the joint publication with shared first authorship Hofmann, Eriksen *et al.* [34]. Simulations and Figures of this publication are used in Figs. 5.4, 5.5, 5.6, 5.19, 5.20 of this thesis
- interpreted the simulation results of Hofmann, Eriksen *et al.* [34] in joint efforts with C. L. M. Hofmann

Benedikt Bläsi

- significantly contributed to the discussion of results

Bryce S. Richards

- significantly contributed to the discussion of results

Jan Christoph Goldschmidt

- conceived of research questions that the simulations of this work are based on
- discussion of all simulation results

CHAPTER 6

COMPARISON OF MODEL AND EXPERIMENT

This chapter presents the analysis of upconversion photoluminescence (UCPL) in experimentally realized photonic upconverter devices drawing a comparison between model and experiment. Photonic effects are investigated in 40 different sample designs and large parameter scans, varying the excitation wavelength, incident irradiance and angle of incidence, comprising of 2480 separate parameter combinations. This chapter introduces the UCPL measurements as well as the varied parameters with respect to their relevance in an application in photovoltaics. Subsequently, all parameter scans are presented in a comparison of model and experiment.

This chapter is based on parts of the following publication and its supplementary information:

C. L. M. Hofmann, S. Fischer, E. H. Eriksen, B. Bläsi, C. Reitz, D. Yazicioglu, I. A. Howard, B. S. Richards and J. C. Goldschmidt, Experimental validation of a modeling framework for upconversion enhancement in 1D-photonic crystals, *Nature Communications* **12**, 1-10 **(2021)**

Contributions to this chapter of the author, co-authors and others can be found in section 6.9.

6.1. Upconversion photoluminescence in Bragg structure and reference

To quantify the effect of a photonic structure on UC, the UC photoluminescence (UCPL) of a Bragg structure is investigated relative to its corresponding reference (Fig. 6.1). A

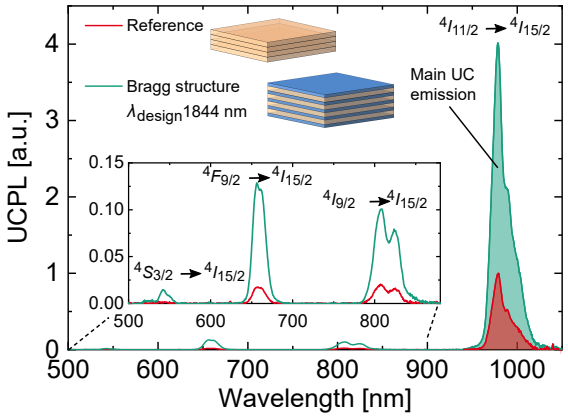

Figure 6.1.: upconversion photoluminescence (UCPL) of a Bragg structure and reference. Measured UCPL under 1523 nm excitation at 1.48 W cm^{-2} irradiance using an integrating sphere to collect the integrated light from all detection angles. Due to the photonic effects on upconversion (UC), in the Bragg structure all UC emission is significantly enhanced. The relative enhancement of the main UCPL at 984 nm ($UCPL_{rel}$) in the Bragg structure compared to the reference is 4.1. [26]

description of the measurement setup as well as calibration and measurement details can be found in Section 3.2.3. As a reference, I choose one active layer on glass, featuring the same thickness as the sum of all active layers of the corresponding Bragg structure (see section 4.3). The main UC emission around 984 nm, which stems from the electronic transition $^4I_{11/2} \rightarrow {}^4I_{15/2}$, contains 94% of the measured total UCPL. The emission intensity, corresponding to this transition is enhanced in the Bragg structure by a factor of 4.1 due to the photonic effects. The $^4I_{9/2} \rightarrow {}^4I_{15/2}$ transition can be seen in the 814 nm UC emission, with an enhancement factor of 5.2. The 3-photon processes $^4F_{9/2} \rightarrow {}^4I_{15/2}$ at 660 nm and $^4S_{3/2}$ combined with $^4H_{3/2} \rightarrow {}^4I_{15/2}$ at 536 nm are enhanced by a factor of 7.3 and 8.9, respectively. [26]

6.2. Upconversion for photovoltaics —introduction of varied parameters

The target application photovoltaics requires the specific understanding of a number of parameters, illustrated in Fig. 6.2. *i*) Fig. 6.2a: the design wavelength of a Bragg structure specifies the spectral position at which the photonic effects occur. Therefore, the design wavelength needs to be tuned such that the photonic effects enhance wanted transitions within the UC process and suppress unwanted transitions. *ii*) Fig. 6.2b: the irradiance incident on the photonic-upconverter has a large impact on the appearing enhancement

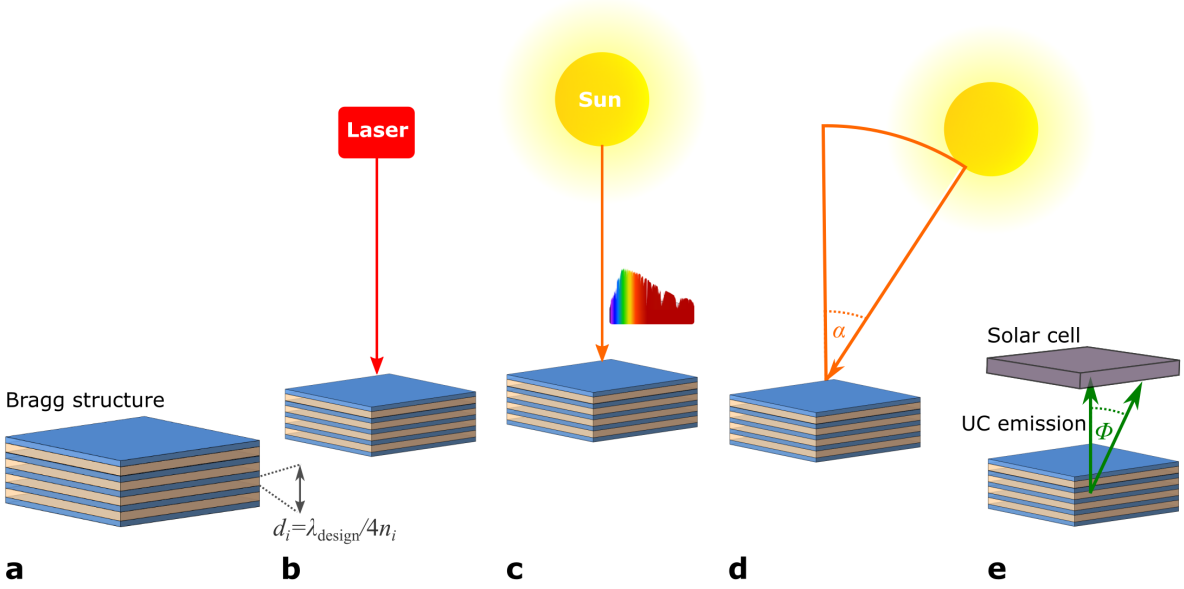

Figure 6.2.: Sketch of the varied parameters in this work that are relevant for an application in photovoltaics. a The design wavelength defines the single layer thicknesses and the spectral position of the photonic effects. **b** The incident irradiance is decisive for the efficiency of the non-linearly dependent upconversion (UC) process. **c** To feature a broadband excitation source as the sun, the laser irradiance is scanned through the core domain of the upconverter absorption spectrum. **d** The incident angle is varied to understand the in-coupling efficiency at different angles. **e** The directionality of emission and out-coupling efficiency is analyzed to understand which part of the upconverted photons from a photonic upconverter could reach a solar cell placed above.

factors of UC relative to a reference sample. In the simulation chapter 5 of this work, the dependence of UC on the incident irradiance has already been analyzed thoroughly. In this work, the measurements are performed in an irradiance regime as low as possible, between 60 and 500 suns irradiance to be of relevance for a target application in photovoltaics that operates in the low irradiance regime. Thereby, the definition of one sun illumination is defined as the irradiance in the absorption range of the upconverter Er^{3+} (1450 nm to 1600 nm) being 3 mW cm^{-2} [137]. *iii*) Fig. 6.2c: the sunlight is not monocromatic but a broadband excitation source. Therefore, the spectral width of the photonic effects needs to be analyzed. In the experiments of work, this is realized by scanning through the core-domain of the upconverter Er^{3+} excitation spectrum from 1500 nm to 1560 nm excitation wavelength with a monochromatic laser. *iv*) Fig. 6.2d: photonic structures are highly angle dependent, however, each type of photonic structure depicts a different angle dependence. The incident angle of the sun onto a photovoltaic module changes throughout the day and concentrated photovoltiacs couple in light from a specific angle cone. Therefore the experiments of this work also cover an incident angle scan and comparison to the modeling framework. *v*) Fig. 6.2e: photonic structures are not only angle dependent in the in-coupling of light but also in the directionality of emission. For a photonic-upconverter it is therefore important to understand which part of the upconverted photons is coupled out of the photonic structure and into which detection angle. The theoretical analysis presented in section 5.2.5 showed that the directionality of emission of the Bragg structure is almost identical for to

the directionality of emission in the reference structure for the investigated UC emission around 984 nm. Preliminary experiments support the findings from theory and no further investigations have been carried out in the scope of this thesis. The experimental analysis of points *i*) to *iv*) is discussed in the following sections 6.3 to 6.6.

6.3. Design wavelength

40 fabricated sample designs are analyzed to investigate the dependence of the photonic effects on UC with a varied design wavelength λ_{design} of the photonic-upconverter (see section 4.3). The designs are chosen around the maximum UCPL enhancement expected from theory. Thereby, the enhancement factor, the relative UCPL ($UCPL_{rel}$, see equation 3.41) is given by the UC signal in the Bragg structure, relative to the UC signal in the corresponding reference structure. The measurements were performed at an irradiance around 500 suns in order to ensure a good signal-to-noise ratio, which was not feasible at only one sun illumination. Fig. 6.3 shows the $UCPL_{rel}$ of the 40 investigated photonic-upconverter designs

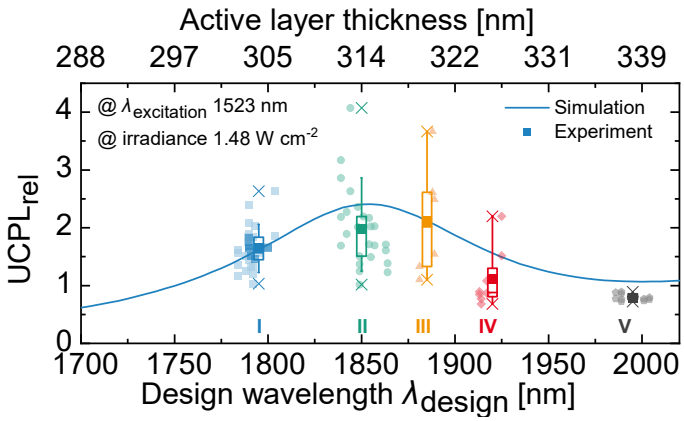

Figure 6.3.: Effect of a varied design wavelength on the relative upconversion photoluminescence ($UCPL_{rel}$) - comparison of simulation and experiment. The dependence of $UCPL_{rel}$ on the design wavelength λ_{design} is investigated using 40 sample designs around the expected maximum UC enhancement, sorted into five groups (I-V) of similar λ_{design}. Two measurements of each investigated design are plotted, the boxes contain 50%, the whiskers 80% of the data points within each group. Point and horizontal line represent mean and median, respectively. [26]

compared to the respective simulation. The simulation takes into account the reduction of the photonic effects due to production inaccuracies. As presented in sections 4.1.5 and 4.2.4, the experimentally measured standard deviations of the single layer production accuracies for the active and TiO_2-layers is 4.2 nm and 1.5 nm, respectively. The average energy density enhancement over 1000 separate calculations enters the simulation (see methods section 3.1.2 and results section 3.1.2).

For evaluation, the data is sorted into five groups (I-V) of similar λ_{design}. Both, the active- and TiO_2 layer are scaled to match the desired design wavelength λ_{design} (see section 4.3). The corresponding active layer thickness is shown in the top x-axis of Fig. 6.3. The simulated $UCPL_{rel}$ includes the standard deviation of the layer thicknesses and both photonic effects (see section). In experiment the photonic effects increase the UC signal for λ_{design}

around the simulated maximum $UCPL_{rel}$ at 1855 nm. In group II and III, at and close to the simulated maximum, respectively, the highest mean measured $UCPL_{rel}$ is found, while group III slightly outperforms group II. Moving further away from the maximum, the experimentally measured $UCPL_{rel}$ is lower (group I and IV), and finally suppressed when the $\lambda_{excitation}$ falls into the photonic bandgap (group V). One explanation for the variation of the single $UCPL_{rel}$ measurements, also within the same design wavelength, are slight thickness variations of the single layers in each stack that appear due to production inaccuracies (see Sections 4.1 and 4.2). Despite these thickness variations of single layers, a defined design wavelength can be assigned to each investigated sample (see Fig. 4.9). In simulation, the impact of the production inaccuracy on $UCPL_{rel}$ is taken into account. However, the simulation features the mean expected reduction over 1000 separate calculations. Most random thickness variations of single layers lead to a decrease in energy density in the active layers and therefore to a reduced $UCPL_{rel}$. For particular designs though, non-periodic thickness variations of single layers can lead to an additional strong increase of the energy density in the active layers [139], which consequently leads to an additional increase in $UCPL_{rel}$. This might contribute to a maximum measured enhancement of 4.1 for λ_{design} = 1844 nm. A closer analysis of the impact of the non-periodicity within each single Bragg structure design, was out of scope of this work. [26]

6.4. Excitation wavelength

The spectral width of photonic effects on UC is decisive for applications with a broad band excitation source, such as photovoltaics. In this work, the effect of a varied excitation wavelength $\lambda_{excitation}$ is investigated by monochromatically scanning through the upconverter absorption spectrum (compare to Fig. 4.1). In experiment, the experimentally feasible core domain of the Er^{3+} absorption spectrum is covered with 1500 nm< $\lambda_{excitation}$ < 1560 nm. Figure 6.4 shows the UCPL of an exemplary Bragg structure with λ_{design} = 1844 nm and

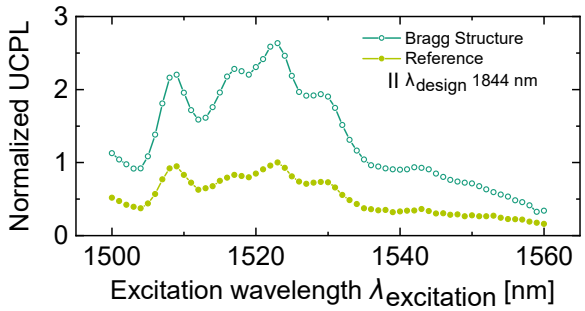

Figure 6.4.: upconversion photoluminescence (UCPL) of an exemplary Bragg structure and reference sample under a varied excitation wavelength ($\lambda_{excitation}$). A significant enhancement of UCPL can be seen in the Bragg structure throughout the complete scanned range.

its corresponding reference, normalized to unity at the maximum of the reference signal. The peaks in the UCPL coincide with the peaks in the absorption (compare to Fig. 4.1c), however, in the UCPL the peaks are larger, due to the non-linear dependence of UC on

an increased absorption. Furthermore, the UCPL is significantly increased in the Bragg structure, throughout the complete measured range.

The same measurement was performed on all 40 sample designs. To evaluate the relative enhancement of the UCPL, the data was again sorted into the same five groups as in Fig. 6.3. Figure 6.5 presents the evaluation of mean and standard deviation of $UCPL_{rel}$ within each

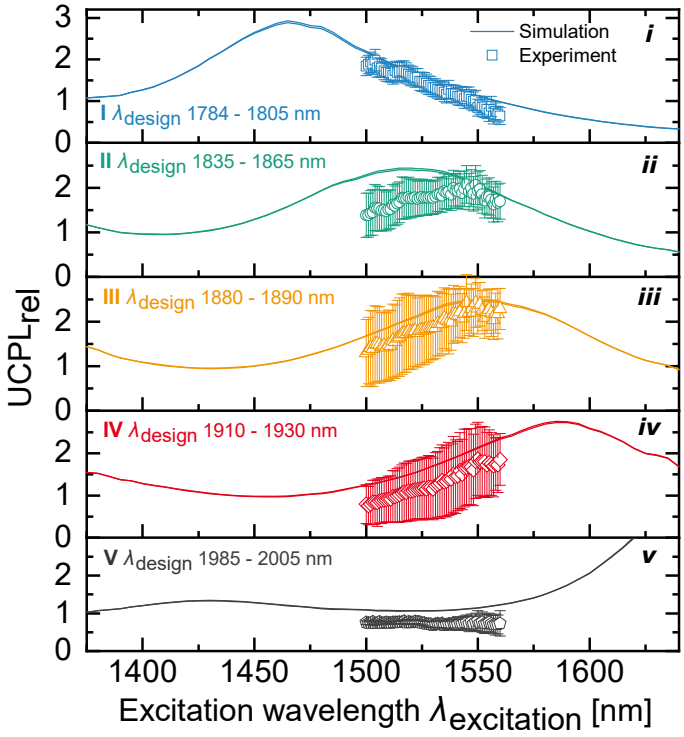

Figure 6.5.: Effect of a varied excitation wavelength ($\lambda_{excitation}$) on the relative upconversion photoluminescence ($UCPL_{rel}$) of the main UC emission around 984 nm - comparison of simulation and experiment. Scanning $\lambda_{excitation}$, the mean and standard deviation of $UCPL_{rel}$ within each group I-V is plotted. The applied irradiance in experiment lies between 1.57 W cm^{-2} at $\lambda_{excitation}$ = 1500 nm and 1.38 W cm^{-2} at $\lambda_{excitation}$ = 1560 nm. The simulation is plotted for the center λ_{design} of each group at these two boundary irradiances and takes into account the reduction of photonic effects due to experimental production inaccuracies. The two simulated curves are very close to each other, such that they appear as one curve. [26]

group. In simulation, the excitation wavelength scan is performed throughout the complete absorption spectrum of the upconverter material Er^{3+} with 1375 nm < $\lambda_{excitation}$< 1650 nm. For comparison to each group in Fig. 6.5, the simulation is carried out for the center λ_{design} of each group. As described for Fig. 6.3, the simulation includes the reduction of photonic effects due to experimental production inaccuracies.

Group II shows a broad plateau for $\lambda_{excitation}$ around 1523 nm. This corresponds to the expectation that for λ_{design} = 1855 nm, $UCPL_{rel}$ peaks at $\lambda_{excitation}$ = 1523 nm. For group I, the maximum enhancement is expected at a shorter $\lambda_{excitation}$ = 1465 nm, for group III, IV and V at longer $\lambda_{excitation}$ of 1555 nm, 1585 nm and 1645 nm, respectively. Consequently, in the investigated $\lambda_{excitation}$ range, the dependence of $UCPL_{rel}$ on $\lambda_{excitation}$ corresponds to a falling flank (group I), a rising flank (group III and IV) or a rather flat region (group V). The slope expected from simulation, which characterizes the Bragg structures effects, is very well

visible in the experimental data in all five groups. Consequently, with a suitable design for a specific application, $UCPL_{rel}$ can be increased in any desired spectral region. In the optimum design range (group II), the complete core domain of the Er^{3+} absorption spectrum between about 1475 nm to 1575 nm can be significantly enhanced, with a simulated peak $UCPL_{rel}$ of 2.4 at an incident irradiance of 1.48 W cm^{-2}. At the outer ranges of the absorption domain (visible particularly in group I and IV), the enhancement factors are slightly higher. This is because in spectral regions where very little light is absorbed, the photonic enhancement has a larger impact on UC efficiency than in spectral regions with higher absorptance. [26]

To quantify how experiment and simulation match for all the different parameter combinations, I define a mean agreement of the measured and simulated $UCPL_{rel}$ (see section 3.2.3). To calculate the mean agreement, for the excitation wavelength scan, as shown in Fig. 6.5, the simulation is carried out at each $\lambda_{excitation}$, each featuring the exact irradiance of the experiment (Fig. 3.6b).

To calculate the agreement between measurement and simulation, I divided the measured $UCPL_{rel}$ by the simulated values. In the mean of all 2440 separate parameter combinations in the excitation wavelength scan, the mean agreement of measurement and simulation lies at 81.8$\pm$23.9%. For such a large number of measurements, one could expect, that the mean of experiment and simulation should match, especially because reductions of UC enhancement due to production inaccuracies are already taken into account. There are two obvious reasons for this additional reduction of $UCPL_{rel}$ that can be seen in the mean of all measurements: *i)* the distribution of upconverter nanoparticles within the active layers, and *ii)* the surface roughnesses in the Bragg structure. The photonic effects are strongest in the center of the active layer. However, the upconverter nanoparticles are not evenly distributed in the active layer, they are rather positioned at the outer ranges (compare to Fig. 4.10a and b). Additionally, the layers of the Bragg structure feature a roughness of around 10 nm (Fig. 4.10d), which introduces additional scattering that most probably leads to a reduction of the overall photonic effects on $UCPL_{rel}$, which is currently not accounted for in the model. [26]

In addition to the main UC emission at 984 nm, the UC emission from higher energy levels has also been investigated in this work. However, not in the same depth as the main UC emission of interest. Figure 6.6 presents the measured and simulated $UCPL_{rel}$ of the 814 nm UC emission. The simulation was carried out the same way as for the analysis shown in Fig. 6.5. In simulation, the $UCPL_{rel}$ was calculated from the sum of the UCPL of the ${}^4I_{9/2} \rightarrow {}^4I_{15/2}$ transition at 814 nm and the ${}^4S_{3/2} \rightarrow {}^4I_{13/2}$ transition at 817 nm because of the spectral overlap in experiment. Experiment and simulation show a good agreement, also for this higher UC emission. This shows that the modeling framework is also able to describe the higher two-photon UC process. However, the slight overestimation of the $UCPL_{rel}$ in the 984 nm emission (Fig. 6.5) is not visible in the 814 nm emission in Fig. 6.6 but on the contrary a slight underestimation of the $UCPL_{rel}$. In the model, the overestimation of the 984 nm emission represents a slightly higher probability for the main UC emission. Consequently, fewer photons are available to take part in higher UC processes. The model, being consistent within itself, would have to be slightly adapted to resemble the probabilities found in experiment.

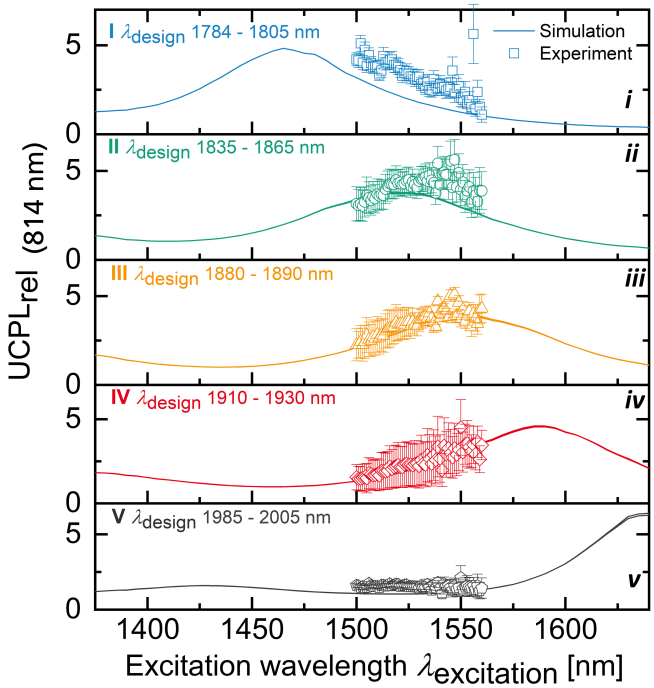

Figure 6.6.: Effect of a varied excitation wavelength ($\lambda_{excitation}$) on the relative upconversion photoluminescence (UCPL$_{rel}$) of the UC emission around 814 nm - comparison of simulation and experiment. Scanning $\lambda_{excitation}$, the mean and standard deviation of UCPL$_{rel}$ within each group I-V is plotted. The applied irradiance in experiment lies between 1.57 W cm^{-2} at $\lambda_{excitation}$ = 1500 nm and 1.38 W cm^{-2} at $\lambda_{excitation}$ = 1560 nm. The simulation is plotted for the center λ_{design} of each group at these two boundary irradiances and takes into account the reduction of photonic effects due to experimental production inaccuracies. Graph from [113]

6.5. Irradiance

The irradiance, incident on a photonic-upconverter largely influences the observed enhancement factors. Within this work, this dependence has been analyzed exhaustively in simulation, as presented in Fig. 5.17 and Fig. 5.20. In Fig. 6.7, the dependence of the photonic effects on the irradiance are demonstrated experimentally for a sample of group III with λ_{design} = 1888 nm. Fig. 6.7a shows the UCPL of Bragg structure and corresponding reference sample, normalized to unity at the maximum of the reference signal. The non-linear dependence of UC on the irradiance is visible. In Fig. 6.7b, the slope of UCPL$_{rel}$ is compared to simulation. Again, the simulation includes the experimental production inaccuracies, same as for Fig. 6.3. As comprehensively discussed in section 5.2.2, in simulation it is possible to switch on the photonic effects one by one, simply by setting the relative enhancement factor of the other photonic effect to unity. The simulation is therefore plotted with only the effect of the energy density $\bar{u}_{rel}$ taken into account, only the LDOS effect, and finally including both photonic effects.

Considering only the effect of the energy density, results in a falling curve for UCPL$_{rel}$ towards higher irradiances. In the low irradiance regime, in which the reference performs poorly, an increase in energy density, followed by a stronger absorption, largely increases

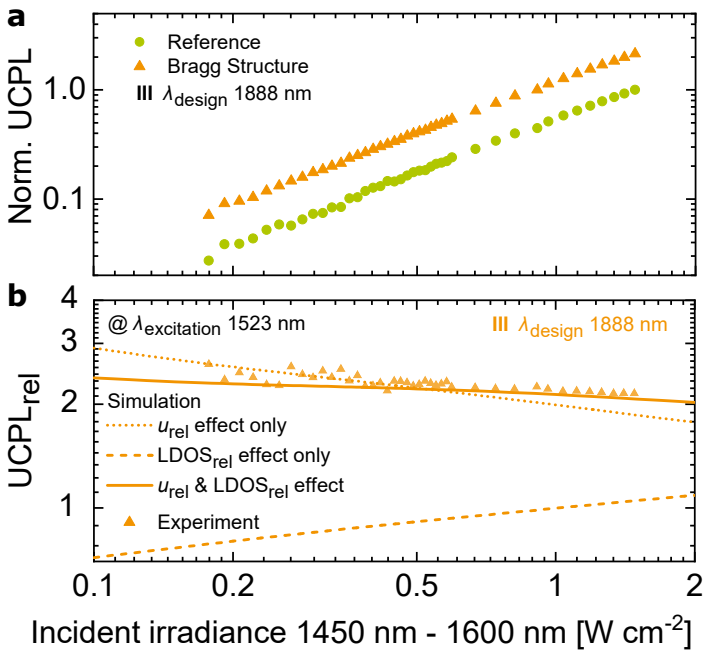

Figure 6.7.: Effect of a varied incident irradiance I_{in} on the relative upconversion photoluminescence ($UCPL_{rel}$) - comparison of simulation and experiment. a measured upconversion photoluminescence (UCPL) of a sample design of group III, and its corresponding reference sample. The data is normalized to unity at the maximum of the reference. **b** measured $UCPL_{rel}$ (from graph **a**) compared to the simulated $UCPL_{rel}$, including only one photonic effect of the changed local energy density $\bar{u}_{rel}$, or the modified local density of optical states $\overline{LDOS}_{rel}$, or both effects. (Graph **b** adapted from [26])

the probability of an energy transfer UC process to take place, resulting in a high $UCPL_{rel}$. At higher irradiances, energy transfer UC to yet higher energy levels becomes more probable, which decreases the probability of the main UC emission at 984 nm, thus decreasing $UCPL_{rel}$. In direct comparison with experiment, one can see that the absolute value of $UCPL_{rel}$ is reproduced, but that the effect of a falling $UCPL_{rel}$ towards higher irradiances is exaggerated. However, the negative effect of the LDOS is stronger in the low irradiance regime, as can be seen from the curve showing only the LDOS effect. Thus, when both effects are taken into account, the experimental data clearly follows the slope of the simulation, accurately reproducing the simulated $UCPL_{rel}$. [26]

The calculation the mean agreement of experiment and simulation (see section 3.2.3) for the 41 measurements contained in the irradiance scan in Fig. 6.7 shows that the experiment reaches 104.5±11.6% of the simulated $UCPL_{rel}$. For the final quantification, the mean agreement of experiment and simulation (see section 3.2.3) is calculated for all measurements with different parameter combinations: all measurements of the excitation wavelength scan (Fig. 6.5) and all (except one) measurements of the irradiance scan (Fig. 6.7). The design wavelength scan (Fig. 6.3) is not included as it is a repetition of parameter combinations. For all 2480 separate parameter combinations, the final mean agreement of experiment and simulation yields 82±24%.

6.6. Excitation angle

Photonic structures are highly angle selective, both in the in-coupling and out-coupling of light. To examine the angle dependence of light coupled into the Bragg structure, and the subsequent efficiency of the UC process, the UCPL was measured for a varied excitation angle α. As the angle selectivity of in-coupled photons is also spectrally selective, additionally the excitation wavelength $\lambda_{excitation}$ was varied in a 2D scan (see methods section 3.2.3 for details). In the photoluminescence measurement setup for a varied excitation angle, the detection unit is placed at 18° off the surface normal, detecting photons within a cone with a half angle of 7°. Therefore, the UCPL within this analysis is referred to as the fractional UCPL ($UCPL_{FDOS}$) and the fractional relative UCPL ($UCPL_{rel,FDOS}$) as described by the equations 3.42 and 3.43 for simulation, respectively.

Figure 6.8 shows the measured $UCPL_{FDOS}$ of an exemplary reference (Fig. 6.8a) and

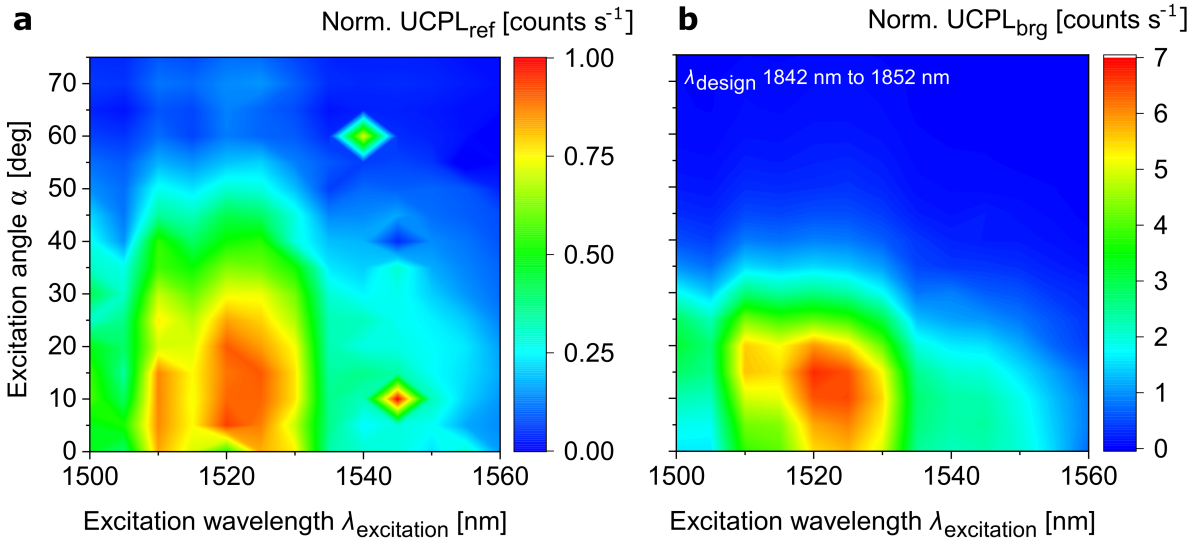

Figure 6.8.: Investigation of the normalized upconversion photoluminescence (UCPL) for a spectrally and angle resolved excitation. In the reference structure (a), the features of the Er^{3+} absorption are clearly visible. In the exemplary Bragg structure (b), an enhancement of UCPL and angle selectivity can be observed.

Bragg structure (Fig. 6.8b). Different from the measurements described in the previous sections, the laser spot is larger in this setup. Therefore, the design wavelength of the measured spot on the Bragg structure cannot be determined as precisely. The range of all λ_{design}-determinations within the laser spot area is given, which is 1842 nm < λ_{design} < 1852 nm for the sample shown in Fig. 6.8b. The measurements are performed at a low irradiance of $I(0°) = 0.2546$ W cm^{-2}, corresponding to 85 suns irradiance within the absorption range of Er^{3+}. Each column (*i-iii*) presents the analysis of a separate sample, whereby the sample designs are chosen from group *i*), *ii*) and *v*) introduced in Fig. 6.5, such that the spectral position of the photonic effects is significantly different between the three samples.

The position of the photonic bandgap changes with a varied incident angle according to equation 2.25. When moving to larger incident angles α, the photonic bandgap is blue shifted, which is clearly visible in the reflectance spectrum of a Bragg structure.

Therefore, Fig. 6.9a shows the simulated reflectance for each Bragg structure design *i-iii*). Figure 6.9b zoomes into the simulated reflectance in the excitation wavelength range 1500 nm < $\lambda_{excitation}$ < 1560 nm, used for $UCPL_{rel,FDOS}$ measurements. In the zoom, the large shift of the bandgap within this small spectral region is clearly visible, as well as the difference between the three evaluated designs.

Figures 6.9c and d depict the simulated $UCPL_{rel,FDOS}$ for the upper (c) and lower (d) limit of the measured λ_{design} on each of the investigated samples. Also the simulated $UCPL_{rel,FDOS}$ data is corrected to feature common conditions with the measured $UCPL_{rel,FDOS}$ (see section 3.2.3) The simulated enhancement peak of $UCPL_{rel,FDOS}$ is at the lower photonic band edge and thus also moves towards lower $\lambda_{excitation}$ with an increasing incident angle. While there are only small differences visible in the spectral position of the enhancement peak between the maximum (row c) and minimum (row d) λ_{design}, the difference in the $UCPL_{rel,FDOS}$ peak position between the samples (columns *i-iii*) is significant.

Finally, Fig. 6.9e shows the measured $UCPL_{rel,FDOS}$ for all three samples. In experiment, the $UCPL_{rel,FDOS}$ enhancement is clearly visible in the simulated expected spectral range. Furthermore, the shift of the enhancement peak clearly follows the expected trend from simulation for all three investigated sample designs.

To be able to compare the data to simulation, both, experimental and simulated data were corrected to feature the same conditions (for details see section 3.2.3). Subsequently, simply for better comparison of Bragg structure and reference in Fig. 6.8, the $UCPL_{FDOS}$ signal was normalized to the maximum measured signal of the reference sample. In the measured $UCPL_{FDOS}$ of the reference structure (Fig. 6.8a), the features of the Er^{3+} absorption spectrum are clearly visible, as well as the expected cosine decay towards higher excitation angles. In $UCPL_{FDOS}$ of the Bragg structure (Fig. 6.8b), an enhancement is visible and the spectral and angle dependent characteristics are altered.

To analyze the appearing effects in the Bragg structure, a detailed analysis of the shift of the photonic bandgap and resulting $UCPL_{rel,FDOS}$ is shown in Fig. 6.9. Each column (*i-iii*) presents the analysis of a separate sample, whereby the sample designs are chosen from group *i*), *ii*) and *v*) introduced in Fig. 6.5, such that the spectral position of the photonic effects is significantly different between the three samples.

The position of the photonic bandgap changes with a varied incident angle according to equation 2.25. When moving to larger incident angles α, the photonic bandgap is blue shifted, which is clearly visible in the reflectance spectrum of a Bragg structure. Therefore, Fig. 6.9a shows the simulated reflectance for each Bragg structure design *i-iii*). Figure 6.9b zoomes into the simulated reflectance in the excitation wavelength range 1500 nm < $\lambda_{excitation}$ < 1560 nm, used for $UCPL_{rel,FDOS}$ measurements. In the zoom, the large shift of the bandgap within this small spectral region is clearly visible, as well as the difference between the three evaluated designs.

Figures 6.9c and d depict the simulated $UCPL_{rel,FDOS}$ for the upper (c) and lower (d) limit of the measured λ_{design} on each of the investigated samples. Also the simulated $UCPL_{rel,FDOS}$ data is corrected to feature common conditions with the measured $UCPL_{rel,FDOS}$ (see section 3.2.3) The simulated enhancement peak of $UCPL_{rel,FDOS}$ is at the lower photonic band edge and thus also moves towards lower $\lambda_{excitation}$ with an increasing incident angle. While there are only small differences visible in the spectral position of the enhancement peak between

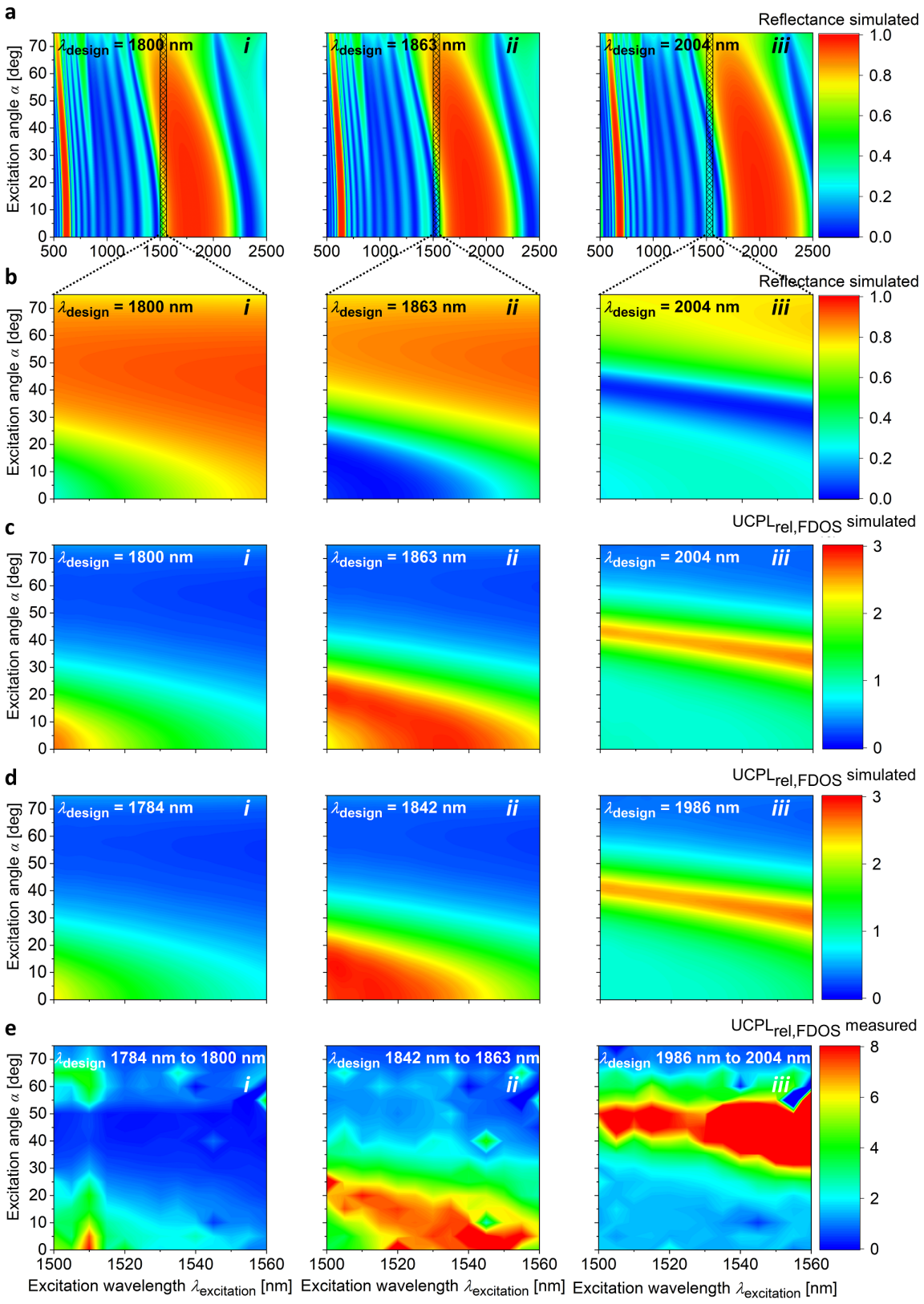

Figure 6.9.: Investigation of the relative upconversion photoluminescence ($UCPL_{rel,FDOS}$) in different Bragg structure designs for a spectrally and angle resolved excitation. a, simulated reflectance

for three different experimentally investigated Bragg structure designs to illustrate the shift of the photonic bandgap. The maximum design wavelengths λ_{design} measured on each sample is displayed (*i-iii*). **b** Simulated reflectance, zoomed in into the experimentally investigated spectral range. **c** Simulated $UCPL_{rel,FDOS}$ for the maximum measured λ_{design}. The maximum $UCPL_{rel,FDOS}$ shifts along with the photonic band edge towards smaller wavelengths at higher incident angles α. **d** Simulated $UCPL_{rel,FDOS}$ for the minimum measured λ_{design}. **e** Measured $UCPL_{rel,FDOS}$ on three different experimentally investigated Bragg structure designs. The measured λ_{design}-range on each sample is indicated in the graph. The trend for each sample in comparison to the simulation of the maximum (c) and minimum (d) measured λ_{design}, is in good agreement. Efficient in-coupling of light is possible out of a large angle range, up to about 30° (for design ii). [113]

the maximum (row c) and minimum (row d) λ_{design}, the difference in the $UCPL_{rel,FDOS}$ peak position between the samples (columns *i-iii*) is significant. Finally, Fig. 6.9e shows the measured $UCPL_{rel,FDOS}$ for all three samples. In experiment, the $UCPL_{rel,FDOS}$ enhancement is clearly visible in the simulated expected spectral range. Furthermore, the shift of the enhancement peak clearly follows the expected trend from simulation for all three investigated sample designs.

With a design shown in Fig. 6.9e,*ii*, optimal for coupling in the light around 1523 nm, an enhancement of $UCPL_{rel,FDOS}$ up to an incident angle of about 30° is observed. Consequently, light can efficiently be coupled into the Bragg structure from a large range of incident angles, up to approximately 30°. Furthermore, as can be seen from the results of the three different designs *i-iii*), both the spectral and incident angle range that is coupled in efficiently can be tuned by adapting the design wavelength of the Bragg structure.

The analysis of the varied incident angle has been carried out towards the end of this work. Therefore, it is not as precisely worked out as the other parameter scans presented in Fig. 6.3, 6.5 and 6.7 that were published in [26]. In the analysis presented in Fig. 6.9, the enhancement factors of $UCPL_{rel,FDOS}$ in simulation and experiment vary significantly. It is possible, that the experimental setup was not calibrated precise enough with respect to the power incident on the sample and especially the illuminated area, which has a large impact on the measured enhancement factor. However, the angle dependent characteristics are clearly visible in the performed parameter scans for all three samples.

6.7. Discussion of results in the context of literature

It is difficult to draw a detailed comparison to literature for results of this work. As discussed in section 2.2.5, there is no standardized way of carrying out an analysis of photonic structure enhanced UC. Highly important factors vary between different reports in literature, like the choice of reference and the measurement setup, such as the applied irradiance, the angle of incidence and angle of detection and additionally, the details are often not fully reported. Furthermore, the quality, form and possibly co-doping of the investigated upconverter material all influence the outcome of a measured UC luminescence enhancement factor significantly. A detailed overview over a selection of important reports is given in Tables 2.1 - 2.4 with respect to the design of the photonic structure, upconverter material and experimental details. However, the maximum UCPL enhancement factor of 4.1 at 1.48 W m^{-2} irradiance that was measured in this work, is a good achievement for the simplicity of the regarded Bragg structures, particularly because it was measured integrated over all detection angles.

Often in literature, the maximum UCPL enhancement factor is reported, that was measured at one distinct detection angle. A very high UCPL enhancement of 10^4 was reported by Lin *et al.* in a waveguide structure [100] (see Table 2.3). This enhancement factor, however, was measured only in a very narrow detection angle range of about 1°. Off this optimum angle, the UCPL enhancement is reported to drop rapidly by three orders of magnitude. Consequently, this type of structure is not favorable for broad-band applications with a varying angle of incidence, such as photovoltaics.

Johnson *et al.* also investigated a Bragg structure of Er^{3+}-doped porous silicon. Under 1550 nm excitation and a high irradiance, they report a 26.5 and 5-fold enhancement of the green and 980 nm UC emission, respectively, for a structure similar to what we define a 30 active layer structure [58] (see Table 2.4). The enhancement occurs in an incident angle range of approximately 4°. They mention difficulties in controlling the layer thickness, which crucially diminishes the photonic effects. This report agrees well with the simulation in this work, including the correct refractive indices and a large layer thickness variation and pronounces the importance of including fabrication inaccuracies: a precise 4-active layer stack can reach an effect close to an imprecise 30-active layer stack. The amount of upconverter material, of course, also needs to be considered: while the design used by Johnson *et al.* features a total thickness of all upconverter-doped layers of as much as 15 µm, the Bragg structures investigated in this work with four active layers feature a summed up active layer thickness of about 1.3 µm. [26]

Rojas-Hernandez *et al.* report a 25-fold enhancement of the green UCPL under 975 nm excitation in a microcavity structure of 21 layers of TiO_2 and Tb^{3+}/Yb^{3+}-doped aluminosilicate glass. The structure features a summed up active layer thickness of about 1 µm and the measurement is performed at a distinct detection angle [101] (see Table 2.4). To draw a comparison to the simulations in my work, a Bragg structure with 10 active layers (in total 21 layers) can be taken, using the production accuracy, reached in the experiments of my work. The simulated UCPL enhancement is a factor of 4.3 at a relatively high irradiance of 1.48 W cm^{-2} and 27 at a low irradiance of one sun. The enhancement factor is in a similar range as reported by Rojas-Hernandez, however, one needs to be careful when comparing these results because of the difference in excitation and emission wavelength.

6.8. Summary

In this chapter, a thorough comparison of model and experiment was drawn. The measured enhancement of the UC photoluminescence ($UCPL_{rel}$) was compared to simulation within large parameter scans, comprising of 5225 measurements with separate parameter combinations.

The maximum measured enhancement of the main UC emission around 984 nm under excitation at 1523 nm was a factor of 4.1 for a Bragg structure with a design wavelength of 1844 nm, close to the expected maximum enhancement at 1855 nm. Key parameters for an application in photovoltaics were scanned: 40 different sample designs were analyzed in a scan of the excitation wavelength, sorted into 5 groups of similar design wavelength. Thereby, the groups were chosen in the region of maximum expected $UCPL_{rel}$, closely around that region and within the region of no expected enhancement. Within each group,

the mean and standard deviation of the measured $UCPL_{rel}$ clearly followed the slope of the simulated $UCPL_{rel}$ with a mean agreement of experiment and simulation of 81.8±23.9%. In a scan of the incident irradiance, the measured $UCPL_{rel}$ clearly reproduced the trend of the simulated $UCPL_{rel}$ including the influence of both photonic effects with a mean agreement of experiment and simulation of 104.5±11.6%. A simulation only including one photonic effect, the enhanced optical energy density or the local density of optical states, depicts a significantly different slope than the experimental data of the irradiance scan. For all separate 2480 parameter combinations in the excitation wavelength and irradiance scan, the mean agreement of experiment and simulation with respect to the $UCPL_{rel}$ lies at 82.2±24.0%. Thereby, the simulations for all the above comparison to experiment were performed for the exact experimental conditions, including the production inaccuracies from experiment.

Furthermore, in a 2D-scan of the incident angle and excitation wavelength, the experiment clearly reproduced the trends from simulation for three different sample designs. Thereby, efficient in-coupling of photons was found up to an incident angle of about 30°. This analysis proved that both the spectral and angle range that is coupled into the photonic upconverter, can be tuned to match the needs of a specific application by choosing a suitable design wavelength.

6.9. Contributions to this chapter

Clarissa L. M. Hofmann (Author)

- conceived of the research questions and planned the according measurements
- performed the first measurements for the scan of design wavelength, excitation wavelength and incident irradiance
- performed all experimental data analysis
- implemented all simulations for comparison with experiments
- planned and designed all figures

Deniz Yazicioglu

- constructed the setup for UC photoluminescence measurements for a varied incident angle and performed UC photoluminescence measurements at this setup
- performed repeated UC photoluminescence measurements at the integrating sphere setup for the scan of design wavelength, excitation wavelength and incident irradiance

Benedikt Bläsi

- gave significant advice to the photoluminescence setup and UC photoluminescence data interpretation

Ian A. Howard

- gave significant advice on calibration of photoluminescence measurements

- gave significant advice on planning and interpretation of photoluminescence measurements

Bryce S. Richards

- significantly contributed to planning the experiments
- significantly contributed to the UC photoluminescence data interpretation

Jan Christoph Goldschmidt

- conceived of research questions that the experiments of this work are based on
- significantly contributed to the planning of photoluminescence measurements
- discussion of all experimental results

CHAPTER 7
CONCLUSION AND OUTLOOK

7.1. Conclusion

This work was comprised of three key aspects: *i*) to understand the interplay of photonic effects of a 1D-photonic structure and upconversion (UC) dynamics in the embedded upconverter β-$NaYF_4$:Er^{3+} in a simulation-based assessment, *ii*) to experimentally realize optimized photonic upconverters in high precision and *iii*) to reach an exact experimental validation of the comprehensive modeling framework.

Simulation

In the scope of the simulation-based analysis, the influence of photonic effects either on the UC photoluminescence (UCPL) or the UC quantum yield (UCQY) was thoroughly analyzed. In literature, the position of the photonic bandgap is often used to define an optimal design of a photonic structure. However, based on the findings of this work, it can be concluded that the position of the photonic bandgap is not sufficient, but the spectral width of the peak energy density enhancement has to be known, which occurs at the photonic band edge. The highest UCPL enhancement always occurs very close to the peak energy density enhancement and increases towards lower incident irradiances. Therefore, when wanting to optimize the UCPL, the simulation of the energy density enhancement is a good estimate to find the optimal photonic structure design. However, if a photonic upconverter should operate at its maximum UCQY, it is of crucial importance to include not only the local enhancement in energy density but also the modified local density of optical states (LDOS) and the internal UC dynamics. The UCQY curve depicts a characteristic maximum at a material specific incident irradiance. A detailed analysis within this work (for an ideal Bragg structure with low- and high refractive index layer featuring n_{low} = 1.5 and n_{high} = 1.8) showed that the effect of the LDOS increases the maximum UCQY from 13.9% in the reference, to 14.7% because in the Bragg structure there are less photonic states available for the main loss emission to take place, relative to the photonic states available for an UC emission to take place. Additionally, the photonic effect of the energy density enhancement compresses the UCQY curve along the irradiance axis, such that the maximum UCQY occurs at a much

lower incident irradiance. In fact, scanning through Bragg structure designs of up to 100 active layers showed that at any incident irradiance down to 200 W m^{-2}, a Bragg structure design can be found that yields close to the maximum possible UCQY. For other irradiance values, the UCQY drops. Therefore, to optimize the UCQY, it is very important to thoroughly optimize the photonic structure design for the intended application, especially considering the irradiance of the target application.

The photonic effects of the Bragg structure can be tuned by adapting the refractive index contrast of the two alternating layers as well as the number of layers. With an increasing number of layers, the peak energy density enhancement gets significantly higher but at the cost of a reduced spectral width. Therefore, the width and height of the enhancement are always a trade-off. It is, however, always favorable to choose the highest possible refractive index contrast, as this enhances the photonic effects. Consequently, with a higher refractive index contrast, a high peak enhancement can be reached with only few layers, allowing for a high but also spectrally broad enhancement peak.

The peak energy density enhancement is also highly sensitive to layer thickness variations of the single layers within the Bragg structure. Also for other photonic structure designs, the exact periodicity of refractive indices is highly important. Deviations from this periodicity, as they occur in any fabrication process, most often diminish the photonic effects. Therefore, within this work, the layer thickness variations were accounted for in simulation as set production inaccuracies, representing random deviations of the single layer thicknesses, drawn from a Gaussian distribution in a Monte-Carlo approach. In simulations of this work, it was found that the production inaccuracies increasingly diminish the peak energy density enhancement for an increasing refractive index contrast and particularly for an increasing layer number of photonic structure design. For a set production accuracy, the enhancement can actually decrease again for Bragg structures with more layers or a higher refractive index contrast, such that a precise 10-active layer Bragg structure can reach stronger photonic effects than a slightly less precise 50-active layer Bragg structure. From this analysis it can be concluded that the production accuracy should be optimized with emphasis. Subsequently, an analysis should be carried out with respect to which photonic structure complexity is most suitable for the reached production accuracy, thus reaching the highest enhancement factors. Because for real, non-ideal photonic structures, the most complex design is not necessarily the best performing design.

Experimental realization and comparison of model and experiment

To reach an experimental validation of the modeling framework, optimized photonic upconverters (based on the simulation) were fabricated with high precision. Subsequently, a thorough comparison of the measured and simulated UCPL enhancement was drawn. The modeling framework, on the one hand, combines a number of theories to describe the different parts, the energy density enhancement, the modified local density of optical states and the UC dynamics. The experimentally realized photonic upconverters, on the other hand, are highly sensitive to imperfections in the single layer thicknesses, to scattering within the layers and at surfaces. Furthermore, the design of Bragg structures is highly sensitive to the refractive indices of the single layers. The precise fabrication of Bragg structures with embedded upconverter nanoparticles allowed for detecting the photonic effects in the

measured UCPL enhancement nearly without reduction (compared to the expected photonic effects from simulation) due to the careful optimization of single layers and high accuracy in fabrication of the final multilayer stacks. In all performed parameter scans, comprising of 5225 separate parameter combinations, good agreement was found for the measured and simulated trends of the UCPL enhancement. The very precise analysis of the design wavelength scan, the excitation wavelength scan and the incident irradiance scan comprises of 2480 separate parameter combinations, whereby the mean agreement of experiment and simulation was found to be $82\pm24\%$. Considering the complexity of both model and experiment, this agreement of experiment and simulation within one standard deviation is an excellent achievement.

Bragg structures for photovoltaic applications

Within this work, I chose to investigate a Bragg structure, because its simplicity allows for understanding all appearing photonic effects on the UC process. The careful preparation of fabricating the single layers in high precision and thickness control, along with a detailed optical analysis allowed for a very precise experimental realization of the final Bragg structures with embedded upconverter nanoparticles. Thereby, the production accuracy was high enough to detect all the appearing photonic effects on the UCPL. In comparison to literature, it is evident that Bragg structures are not the photonic structures that have the potential to reach the highest possible UC enhancement factors. However, Bragg structures have many favorable features for an application in photovoltaics: *i*) High UCPL enhancement effects can be found especially in the low irradiance regime. *ii*) The amount of embedded upconverter material is flexible within a Bragg structure. The amount of upconverter material and therewith its total absorption, can be tuned by adding more layers to the stack. *iii*) Photonic structure enhancement effects on UC can be designed to appear in a broad spectral range, covering the core domain of the Er^{3+} absorption spectrum. *iv*) Light can efficiently be coupled into the Bragg structure up to a large half angle of about 30°. This is important for broad-band and wide-angle applications, such as photovoltaics: a simple photovoltaic system without tracking has the light incident from various angles during the day. In a concentrator system using tracking, the consequence of concentration is that the incident angle of the light onto the solar cell is increased.

From the findings of this work it can be concluded that it is of crucial importance to include the given parameters of a target application when wanting to choose and optimize a photonic structure design. The incident irradiance has a major impact on the UCQY, as well as on the UCPL enhancement. Furthermore, the spectral width of the photonic enhancement effects and angle dependent characteristics need to be matched to the requirements of the specific target application. Furthermore, the production accuracy that can be reached in experiment needs to be taken into account, such that the realized photonic upconverter devices are operating at their maximum photonic effects with the given accuracy. A more complex design can result in significantly decreasing photonic effects, which is not favorable.

Theoretical optimization in literature and contribution of this work

Looking at literature, it is evident that the importance of optimizing photonic structure designs for UC enhancement is more and more accounted for. In an increasing number of literature reports, a careful design optimization is included [97–99, 102]. However, especially comprehensive models of the UC dynamics are not used. Only simplified rate equation models, that have mainly been developed for analyzing plasmonic effects on UC are lately being converted to be used in the context of photonic structure enhanced UC [99, 103]. The main contribution of this work to the research community is therefore to provide, open access and fully available, an experimentally validated comprehensive theoretical modeling framework that enables a knowledge-based optimization of photonic upconverter devices. It can now be used to optimize 1D-photonic structure designs for UC enhancement in β-$NaYF_4$:Er^{3+}. The model can be easily expanded to other 2D- and 3D-photonic structure designs, because the way the photonic effects act on the UC process is identical as for a 1D-photonic structure. Furthermore, the basic findings of this work can be applied to any upconverter material with a similar set of energy levels and the parameters of the UC dynamics can be adapted easily when the required experimental parameters of another upconverter material are available. Within the model, the design optimization can be carried out within parameter ranges that are relevant for the target application, which is not limited to photovotaics, but for any application.

7.2. Outlook

It is still a long way to go to achieve a significant improvement of silicon solar cell efficiencies by the use of UC. This is due to multiple properties of the UC process and currently available upconverter materials. In a very recent paper, Richards *et al.* critically and comprehensively reviewed the potential of UC for photovoltaic applications [1]. The fundamental limiting factor, is the low efficiency of the available rare earth ion-based upconverter materials, particularly a very low absorption cross section but also a low energy transfer rate, as well as quenching effects on material surfaces or impurities. Based on a simplified simulation model describing the UC process [140], Richards *et al.* find that an increase in the generation rate, intermediate state lifetime or energy transfer rate by 1-2 orders of magnitute is needed to achieve efficient UC for solar applications. The efficiency of an upconverter can be improved in several ways:

i) As investigated in this thesis, photonic structures can gain a significant enhancement of UC efficiency, both via a locally enhanced energy density and increasing the UCQY via modifying the local density of optical states. Using this approach, enhancements of the local energy density of up to 20 are well achievable [1]. From my findings and literature research, the reported UC emission enhancement factors range from 2 to 100 or more, however care must be taken how to interpret the results due to choice of reference and measurement setup.

ii) Plasmonic structures have been investigated thoroughly and gain high field enhancements, however over a very small area and at the cost of quenching effects [85, 86]. Also plasmonic-photonic hybrid structures have been shown to improve UC efficiency [106]

iii) Applying cosensitizer materials and/or organic dyes to spectrally concentrate a larger part of the silicon sub-bandgap region into the absorption range of the upconverter. This

would increase the spectral fraction of the upconverted light and additionally the irradiance acting on the upconverter, which in turn enhances the UC efficiency at low incident irradiance levels [82–84]. It is estimated that down-shifting the complete spectral range below the silicon bandgap into the Er^{3+} absorption range could increase the current enhancement in a silicon solar cell by as much as a factor of three, compared to a purely Er^{3+}-based upconverter system [141]. This could increase the generation rate by maximally a factor of four [1]. In fact, superior UC properties have been reported for hybrid upconverter materials composed of lanthanide-doped upconverter nanoparticles and organic dyes that function as a sensitizer with a significantly higher absorption, and have been applied to photovoltaics systems [4]. Down-shifting organic dyes can be applied either separately next to an upconverter material or as a hybrid material design. Hybrid materials are UCNPs decorated with organic dyes that usually absorb light in the range between 700 nm to 850 nm. This approach is expected to realistically increase the absorption of the upconverter by a factor of three to four. However, the dyes can also introduce severe surface quenching, which diminishes a part of the UC enhancement effect.

iv) Concentration optics could be applied to allow for the system to operate in an irradiance regime, in which the upconverter features a significantly higher UCQY. Particularly for silicon-based tandem solar cell designs, if the silicon bottom cell limits the overall current, this approach could significantly improve the overall performance. Different approaches have been investigated, modules with concentrator optics that are specifically designed for UC [81] and microlens arrays for UC enhancement [142]. Furthermore, Liang *et al.* [143] demonstrated UC emission enhancement of UC nanoparticles applying superlensing microbeads. Thereby, spherical microbeads can exhibit about half the maximum possible concentration of sunlight [1] and therefore potentially significantly increase UC effiency. However, care must be taken with this approach, as the UC material needs to exhibit a sufficient thickness for absorption of a significant fraction of the concentrated light beam [1].

Going one step back, one should also consider rethinking the upconverter material itself. Currently, the highest UCQY values of rare earth ion-based upconverter materials range around 15%. It is difficult to isolate the material properties and find specific reasons for these low efficiencies. Richards *et al.* conclude that if an environment was found that exhibits weak quenching of UC emissive states as well as a fast radiative relaxation from the UC emissive states to the ground state, this could potentially lead to a new generation of UC materials [1].

While none of the above approaches reaches the required enhancement in generation rate by a stable factor of one to two by itself, a combination of various approaches could be successful. If, in future research, new upconverter materials are combined with spectral concentration and photonic structures, or plasmonic photonic hybrid structures, this could lead to a major shift in efficiency. Nonetheless, an application in mass market photovoltaic technologies seems improbable due to the complexity and therefore high production costs of upconverter devices. For other applications, however, photonic UC could still be highly interesting. In anticounterfeiting, e.g. high complexity and customizability are positive features, and in theranostics dose effect relationship could be improved with photonics. For such and any other future applications, the findings and methods developed in this work will help a knowledge-based optimization.

APPENDIX A

APPENDIX

A.1. Experimental parameters of the rate equation model

This section is the summary of all experimental parameters that enter the rate equation model. All measurements are performed for an excitation wavelength of 1523 nm, for which the main UC emission lies at 984 nm.

Squared dipole matrix elements in units of [A^2 s^2 m^2] determined experimentally by Fischer [63]

$$|\hat{\mu}|^2 = 10^{-62} \cdot \begin{bmatrix} - & 7.19 & 2.04 & 0.12 & 2.56 & 1.10 \\ 7.19 & - & 5.59 & 3.50 & 0.53 & 0.36 \\ 2.04 & 5.59 & - & 0.79 & 6.50 & 0.38 \\ 0.12 & 3.50 & 0.79 & - & 0.54 & 2.13 \\ 2.56 & 0.53 & 6.50 & 0.54 & - & 1.37 \\ 1.10 & 0.36 & 0.38 & 2.13 & 1.37 & - \end{bmatrix} \tag{A.1}$$

Material constants for multi-phonon relaxation, determined from a fit on the experimental data by Fischer *et al.* Details can be found in ref. [28]

$$\begin{aligned} C_{\text{MPR}} &= 1 \cdot 10^8 \ \text{s}^{-1} \\ \kappa &= 2.15 \cdot 10^{20} \ \text{J}^{-1} \end{aligned} \tag{A.2}$$

Angular frequencies of emission in units of [s^{-1}], determined experimentally in an unpublished

work by Fröhlich *et al.* [1].

$$\omega_{\text{emission}} = 10^5 \cdot \begin{bmatrix} - & 1.209 & 1.914 & 2.314 & 2.852 & 3.515 \\ - & - & 0.705 & 1.105 & 1.643 & 2.306 \\ - & - & - & 0.400 & 0.938 & 1.601 \\ - & - & - & - & 0.538 & 1.201 \\ - & - & - & - & - & 0.663 \\ - & - & - & - & - & - \end{bmatrix} \tag{A.3}$$

Fit parameters K_{if} in units of [s] to describe absorption and stimulated emission, determined by Fischer [63]

$$\begin{aligned} K_{12} &= 1.7 \cdot 10^{-14} & K_{21} &= 7.1 \cdot 10^{-15} \\ K_{24} &= 1.3 \cdot 10^{-11} & K_{42} &= 0 \\ K_{46} &= 5.7 \cdot 10^{-15} & K_{64} &= 0 \end{aligned} \tag{A.4}$$

The refractive index used for all calculations in the rate equation model as a good approxiation of the upconverters real refractive index is

$$n = 1.5 \tag{A.5}$$

The distance between the Er^{3+} ions is defined in equation 3.35. The Erbium doping concentration c_{Er} can be varied within the modeling framework. The lattice parameters $\mathcal{A}$ and $\mathcal{C}$ are taken as [55]

$$\begin{aligned} 0 < c_{\text{Er}} &< 1 \\ \mathcal{A} &= 5.9757 \ \mathring{A} \\ \mathcal{C} &= 3.5305 \ \mathring{A}. \end{aligned} \tag{A.6}$$

The integral overlap of the line shape functions for all energy transfer upconversion (ETU) processes and cross relaxation processes (CR), determined by Fischer [63] are given in table A.1

[1] Note that these frequencies are different from the ones published by Fischer in [63].

ETU	ETU	CR	CR
Process	κ_{ET} [J^{-1}]	Process	κ_{ET} [J]
(2,2)→(1,4)	$6.1 \cdot 10^{19}$	(4,1)→(2,2)	$5.0 \cdot 10^{17}$
(2,4)→(1,6)	$3.3 \cdot 10^{17}$	(6,1)→(4,2)	$2.6 \cdot 10^{19}$
(4,4)→(2,6)	$8.6 \cdot 10^{18}$	(6,2)→(4,4)	$7.2 \cdot 10^{18}$
(3,3)→(1,6)	$3.6 \cdot 10^{22}$	(6,1)→(3,3)	$3.5 \cdot 10^{14}$
(4,2)→(1,6)	$2.0 \cdot 10^{18}$	(6,1)→(2,4)	$9.0 \cdot 10^{20}$
(5,3)→(2,6)	$1.7 \cdot 10^{19}$	(6,2)→(3,5)	$7.7 \cdot 10^{24}$
(3,5)→(2,6)	$3.6 \cdot 10^{19}$	(6,2)→(5,3)	$4.2 \cdot 10^{24}$
(3,2)→(1,5)	$2.01 \cdot 10^{20}$	(5,1)→(2,3)	$3.7 \cdot 10^{13}$
(4,3)→(2,5)	$3.0 \cdot 10^{22}$	(5,2)→(3,4)	$1.4 \cdot 10^{23}$

Table A.1.: Integral overlap κ_{ET} of the line shape functions for all energy transfer upconversion (ETU) processes and cross relaxation processes (CR).

LIST OF SYMBOLS

Symbol	Description	Unit
A_{FWHM}	Full width half maximum region of the laser spot area in the photoluminescence measurement setup	m^2
$A_i f$	Einstein coefficient of spontaneous emission	s^{-1}
$\mathcal{A}$	Lattice constant of β-$NaYF_4$	m
B_{if}^{STE}	Einstein coefficient of induced emission	$m^3\ J^{-1}\ s^{-2}$
B_{if}^{ABS}	Einstein coefficient of absorption	$m^3\ J^{-1}\ s^{-2}$
$\mathcal{B}$	Lattice constant of β-$NaYF_4$	m
C_{MPR}	Empirical material specific parameter for multi-phonon relaxation	s^{-1}
$\mathcal{C}$	Lattice constant of β-$NaYF_4$	m
DOS3D	Analytical 3D density of optical states	
E_m^+	Electric field amplitude in transfer matrix formalism, wave traveling in forward direction on left side of interface	
E_m^-	Electric field amplitude in transfer matrix formalism, wave traveling in backward direction on left side of interface	
$E_m'^+$	Electric field amplitude in transfer matrix formalism, wave traveling in forward direction on right side of interface	
$E_m'^-$	Electric field amplitude in transfer matrix formalism, wave traveling in backward direction on right side of interface	
$\mathrm{FDOS}_{\mathrm{norm,brg}}$	Fractional density of optical states from the active layers of the Bragg structure	
$\mathrm{FDOS}_{\mathrm{norm,ref}}$	Fractional density of optical states from the reference structure	
$\mathrm{FDOS}_{\mathrm{rel}}$	Relative fractional density of optical states from the active layers of the Bragg structure	
FLDOS	Fractional local density of optical states	
H	Perturbation Hamiltonian	

Symbol	Description	Unit
I_{in}	Incident irradiance, in experiment, the full width half maximum region is taken	W m^{-2}
$I_{\text{in,FWHM}}$	Laser irradiance within the full width half maximum region in photoluminescence measurements	W m^{-2}
J	Total angular momentum	
J_{SC}	Short circuit current	mA cm^{-2}
K_{if}	Fit parameter in rate equation model	s
L	angular orbital momentum	
LDOS	Local density of optical states	
$LDOS_{brg}$	Local density of optical states in the Bragg structure	
$LDOS_{ref}$	Local density of optical states in the reference structure	
$LDOS_{rel}$	Relative local density of optical states	
$\overline{LDOS}_{rel}$	Mean relative local density of optical states in the active layers of the Bragg structure	
M_{ABS}	Matrix, describing change of occupation of energy levels due to absorption processes in rate equation model	s^{-1}
M_{ESA}	Matrix, describing change of occupation of energy levels due to excited state absorption processes in rate equation model	s^{-1}
M_{GSA}	Matrix, describing change of occupation of energy levels due to ground state absorption processes in rate equation model	s^{-1}
M_{MPR}	Matrix, describing change of occupation of energy levels due to multi phonon relaxation processes in rate equation model	s^{-1}
M_{SPE}	Matrix, describing change of occupation of energy levels due to spontaneous emission processes in rate equation model	s^{-1}
M_{STE}	Matrix, describing change of occupation of energy levels due to stimulated emission processes in rate equation model	s^{-1}
N_j	Occupation of energy level j	
P_{if}	Transition rate between two energy eigenstates i and f	
P_{SPE}	Probability of spontaneous emission	
P_{MPR}	Probability of multi phonon relaxation	
$P^{(if,i'f')}_{\text{(ET,dd)}}$	Probability of the electric dipole-dipole transition	
P_{FWHM}	Laser power in the full width half maximum region in the photoluminescence measurement setup	W
P_{total}	Total laser power in the photoluminescence measurement setup	W
PL	Photoluminescence	s^{-1}
PL_{rel}	Relative photoluminescence	
R	Reflectivity	

Symbol	Description	Unit
R_{exp}	Measured reflectance of a Bragg structure	
R_{sim}	Simulated reflectance of a Bragg structure	
S	Spin momentum	
T	Transmittivity	
$\mathcal{T}$	Temperature	K
UCPL	Upconversion photoluminescence, integrated over all detection angles	s^{-1}
$UCPL_{rel}$	Relative upconversion photoluminescence, integrated over all detection angles	
$UCPL_{FDOS}$	Upconversion photoluminescence, at a specific detection angle	s^{-1}
$UCPL_{rel,FDOS}$	Relative upconversion photoluminescence, at a specific detection angle	
$UCPL_{rel,max}$	Maximum relative upconversion photoluminescence	
UCQY	Upconversion quantum yield	%
$UCQY_{rel}$	Relative upconversion quantum yield	
$UCQY_{first,max}$	Maximum upconversion quantum yield at a specific design wavelength in a Bragg structure at the lowest possible incident irradiance	%

Symbol	Description	Unit
a	Size of Wigner-Seitz unit cell	m
b	Band index	
c_0	Speed of light in vacuum	m s^{-1}
c	Speed of light in medium	m s^{-1}
c_{Er}	Doping concentration of Erbium atoms in host material	
d_i	Thickness of a thin layer	m
d_{high}	Layer thickness of high index medium	m
d_{low}	Layer thickness of low index medium	m
d_{Er}	Distance of erbium ions in host material	m
f	Final state	
g_f	Degeneracy of final state f	
g_i	Degeneracy of initial state i	
g_A^{abs}	Spectral line shape function of the acceptor absorption	s
g_D^{em}	Spectral line shape function of the donor emission	s
i	Initial state	
k	Imaginary refractive index	
k_B	Boltzmann constant	J K^{-1}
l_a	Arc length for FLDOS calculation	m
l_c	Circumference length for FLDOS calculation	m
m	integer number	
n	Real refractive index	
n_i	Refractive index of the medium from which the light is incident from	
n_{eff}	Effective refractive index	
n_{low}	Real refractive index of low index medium	
n_{high}	Real refractive index of high index medium	
n_t	Refractive index of the medium from which the light is transmitted into	
r_s	Fresnel coefficient of reflection of s-polarized modes	
r_p	Fresnel coefficient of reflection of p-polarized modes	
$r_{m-1,m}$	Fresnel coeffient of reflection at the mth interface in the transfer matrix formalism	
t	Time	s
t_s	Fresnel coefficient of transmission of s-polarized modes	
t_p	Fresnel coefficient of transmission of p-polarized modes	
$t_{m-1,m}$	Fresnel coeffient of transmission at the mth interface in the transfer matrix formalism	
$u(x)$	Local energy density	J s m^{-3}
u_{rel}	Relative energy density in the active layers of the Bragg structure	
$\bar{u}_{\mathrm{rel}}$	Relative mean energy density in the active layers of the Bragg structure	
$u_{\mathrm{rel,max}}$	Maximum relative mean energy density in the active layers of the Bragg structure	J s m^{-3}
x	Spatial direction of periodicity of the Bragg structure	m

Symbol	Description	Unit
$\mathbf{D}_{m-1,m}$	Transmission matrix through the mth interface in the Transfer matrix formalism	
$\mathbf{E}$	Electrical field strength	V m^{-1}
$\mathbf{E}_{\text{loc}}$	Local field correction factor	V m^{-1}
$\mathbf{H}$	Magnetic field strength	A m^{-1}
$\mathbf{j}$	Electrical current density	A m^{-2}
$\mathbf{k}$	Reciprocal wave vector	m^{-1}
$\mathbf{k}_{\parallel}$	Reciprocal wave vector parallel to the interface	m^{-1}
$\mathbf{k}_{\perp}$	Reciprocal wave vector perpendicular to the interface	m^{-1}
$\mathbf{k}_i$	Reciprocal wave vector in the incident medium	m^{-1}
$\mathbf{k}_t$	Parallel reciprocal wave vector in the transmitted medium	m^{-1}
$\dot{\mathbf{n}}$	Occupation vector of energy levels in rate equation model	
$\mathbf{P}_{m-1}$	Propagation matrix of the (m-1)th layer in the Transfer matrix formalism	
$\mathbf{T}$	Transfer matrix	
$\mathbf{u}_{b,\mathbf{k}}(\mathbf{r})$	Bloch function	A m^{-1}
$\mathbf{r}$	Position vector	m

Symbol	Description	Unit
α	Excitation angle	degrees
α_{trans}	Pre factor for transition matrices of stimulated processes in the rate equation model	
δ	phase difference	
δd	Modification of the Bragg structures layer thickness, drawn from Gaussian distribution	m
$\Delta R(\lambda_{\text{design}})$	Difference of measured and simulated reflectance	
ε	Electrical permittivity	F m^{-1}
$\varepsilon(\mathbf{r})$	Relative permittivity	
ε_0	Vacuum permittivity	F m^{-1}
θ_d	Detection cone half angle	degrees
$\hat{\Theta}$	Hermitian operator of master equation	
κ	Empirical material specific parameter for multi-phonon relaxation	J^{-1}
κ_{ET}	Spectral overlap integral for energy transfer processes, fit parameter in rate equation model	J^{-1}
$\lambda_{\text{excitation}}$	Wavelength	m
λ_{design}	Design wavelength of the Bragg structure	m
$\lambda_{\text{design}}(u_{\text{rel,max}})$	Design wavelength of the Bragg structure at which the maximum mean relative energy density enhancement is reached	m
μ_{if}	Electric dipole operator for the transition from energy level i to f	A s m
$\mu(\mathbf{r})$	Relative magnetic permeability	
μ	Magnetic permeability	H m^{-1}
$\mu(\mathbf{r})$	Relative permeability	
μ_0	Vacuum permeability	H m^{-1}
ν_{ETU}	Vector describing change of occupation of energy levels due to energy transfer upconversion processes in rate equation model	
$\rho(\omega)$	Density of optical states	
$\rho(\mathbf{r},\omega)$	Local density of optical states	
σ	Standard deviation of the Gaussian distribution for random layer thickness variations of the Bragg structure's layers	m
ϕ_d	Detection angle	degrees
ω	Angular frequency	s^{-1}
ω_{if}	Frequency of a transition from an initial to a final state	s^{-1}
ω_{spin}	Spin speed in the spin-coating process	s^{-1}
$\hbar$	Reduced Planck constant	J s

LIST OF ACRONYMS

Abbreviation	Description
CR	Cross relaxation
DOS	Density of optical states
ESA	Excited state absorption
ET	Energy transfer
ETU	Energy transfer upconversion
FBZ	First Brillouin zone
FLDOS	Fractional local density of optical states
GSA	Ground state absorption
LDOS	Local density of optical states
REM	Rate equation model
SPE	Spontaneous emission
STE	Stimulated emission
UC	Upconversion
UCPL	Upconversion photoluminescence
UCQY	Upconversion quantum yield (internal)
WSC	Wigner-Seitz unit cell

LIST OF FIGURES

LIST OF TABLES

BIBLIOGRAPHY

[1] Richards, B. S., Hudry, D., Busko, D., Turshatov, A. & Howard, I. A. Photon upconversion for photovoltaics and photocatalysis: A critical review. *Chemical Reviews* **121**, 9165–9195 (2021).

[2] Yoshikawa, K. *et al.* Silicon heterojunction solar cell with interdigitated back contacts for a photoconversion efficiency over 26%. *Nature energy* **2**, 1–8 (2017).

[3] Green, M. A. *et al.* Solar cell efficiency tables (version 58). *Progress in Photovoltaics: Research and Applications* **29**, 657–667 (2021).

[4] Wen, S. *et al.* Future and challenges for hybrid upconversion nanosystems. *Nature Photonics* **13**, 828–838 (2019).

[5] Safdar, M., Ghazy, A., Lastusaari, M. & Karppinen, M. Lanthanide-based inorganic-organic hybrid materials for photon-upconversion. *Journal of Materials Chemistry C* **8**, 6946–6965 (2020).

[6] Zhou, J., Liu, Q., Feng, W., Sun, Y. & Li, F. Upconversion luminescent materials: advances and applications. *Chemical reviews* **115**, 395–465 (2015).

[7] Chen, G., Ågren, H., Ohulchanskyy, T. Y. & Prasad, P. N. Light upconverting core-shell nanostructures: nanophotonic control for emerging applications. *Chemical Society Reviews* **44**, 1680–1713 (2015).

[8] Schulze, T. F. & Schmidt, T. W. Photochemical upconversion: present status and prospects for its application to solar energy conversion. *Energy & Environmental Science* **8**, 103–125 (2015).

[9] Huang, X., Han, S., Huang, W. & Liu, X. Enhancing solar cell efficiency: the search for luminescent materials as spectral converters. *Chemical Society Reviews* **42**, 173–201 (2013).

[10] Madsen, S. *et al.* Improving the efficiency of upconversion by light concentration using nanoparticle design. *Journal of Physics D: Applied Physics* **53**, 073001 (2019).

[11] Richter, A., Hermle, M. & Glunz, S. W. Reassessment of the limiting efficiency for crystalline silicon solar cells. *IEEE Journal of Photovoltaics* **3**, 1184–1191 (2013).

[12] Veith-Wolf, B. A., Schäfer, S., Brendel, R. & Schmidt, J. Reassessment of intrinsic lifetime limit in n-type crystalline silicon and implication on maximum solar cell efficiency. *Solar Energy Materials and Solar Cells* **186**, 194–199 (2018).

[13] Auzel, F. Upconversion and anti-stokes processes with f and d ions in solids. *Chemical reviews* **104**, 139–174 (2004).

[14] Dong, H., Sun, L.-D. & Yan, C.-H. Energy transfer in lanthanide upconversion studies for extended optical applications. *Chemical Society Reviews* **44**, 1608–1634 (2015).

[15] Liu, G. Advances in the theoretical understanding of photon upconversion in rare-earth activated nanophosphors. *Chemical Society Reviews* **44**, 1635–1652 (2015).

[16] Wang, X. *et al.* Dye-sensitized lanthanide-doped upconversion nanoparticles. *Chemical Society Reviews* **46**, 4150–4167 (2017).

[17] Liu, X. *et al.* Probing the nature of upconversion nanocrystals: instrumentation matters. *Chemical Society Reviews* **44**, 1479–1508 (2015).

[18] Wang, Y. *et al.* Remote manipulation of upconversion luminescence. *Chemical Society Reviews* **47**, 6473–6485 (2018).

[19] Gnach, A., Lipinski, T., Bednarkiewicz, A., Rybka, J. & Capobianco, J. A. Upconverting nanoparticles: assessing the toxicity. *Chemical Society Reviews* **44**, 1561–1584 (2015).

[20] Tu, L., Liu, X., Wu, F. & Zhang, H. Excitation energy migration dynamics in upconversion nanomaterials. *Chemical Society Reviews* **44**, 1331–1345 (2015).

[21] Chen, X., Peng, D., Ju, Q. & Wang, F. Photon upconversion in core–shell nanoparticles. *Chemical Society Reviews* **44**, 1318–1330 (2015).

[22] Li, X., Zhang, F. & Zhao, D. Lab on upconversion nanoparticles: optical properties and applications engineering via designed nanostructure. *Chemical Society Reviews* **44**, 1346–1378 (2015).

[23] Wen, S. *et al.* Advances in highly doped upconversion nanoparticles. *Nature communications* **9**, 1–12 (2018).

[24] Sun, T. *et al.* Integrating temporal and spatial control of electronic transitions for bright multiphoton upconversion. *Nature communications* **10**, 1–7 (2019).

[25] Hudry, D., Howard, I. A., Popescu, R., Gerthsen, D. & Richards, B. S. Structure-property relationships in lanthanide-doped upconverting nanocrystals: Recent advances in understanding core-shell structures. *Advanced Materials* **31**, 1900623 (2019).

[26] Hofmann, C. L. M. *et al.* Experimental validation of a modeling framework for upconversion enhancement in 1D–photonic crystals. *Nature Communications* **12**, 1–10 (2021).

[27] Johnson, C. M. & Conibeer, G. J. Limiting efficiency of generalized realistic c-si solar cells coupled to ideal up-converters. *Journal of Applied Physics* **112**, 103108 (2012).

[28] Fischer, S., Steinkemper, H., Löper, P., Hermle, M. & Goldschmidt, J. C. Modeling upconversion of erbium doped microcrystals based on experimentally determined Einstein coefficients. *Journal of Applied Physics* **111**, 13109 (2012).

[29] Fischer, S. *et al.* Plasmon enhanced upconversion luminescence near gold nanoparticles - simulation and analysis of the interactions. *Optics Express* **20**, 271–282 (2012).

[30] Fischer, S. *et al.* Plasmon enhanced upconversion luminescence near gold nanoparticles – simulation and analysis of the interactions: Errata. *Optics Express* **21**, 10606–10611 (2013).

[31] Herter, B. *et al.* Increased upconversion quantum yield in photonic structures due to local field enhancement and modification of the local density of states - a simulation-based analysis. *Optics Express* **21**, A883–A900 (2013).

[32] Hofmann, C. L. M., Herter, B., Fischer, S., Gutmann, J. & Goldschmidt, J. C. Upconversion in a Bragg structure: photonic effects of a modified local density of states and irradiance on luminescence and upconversion quantum yield. *Optics Express* **24**, 14895–14914 (2016).

[33] Gutmann, J., Zappe, H. & Goldschmidt, J. C. Quantitative modeling of fluorescent emission in photonic crystals. *Physical Review B* **88**, 205118 (2013).

[34] Hofmann, C. L. M. *et al.* Enhanced upconversion in one-dimensional photonic crystals: a simulation-based assessment within realistic material and fabrication constraints. *Optics Express* **26**, 7537–7554 (2018).

[35] Hofmann, C. L. M. *et al.* remUCPS–rate equation model of upconversion dynamics including photonic structure effects (2020). URL `https://doi.org/10.24406/fordatis/110.2`.

[36] Joannopoulos, J. D., Johnson, S. G., Winn, J. N. & Meade, R. D. *Photonic crystals: molding the flow of light* (Princeton university press, 2011).

[37] Johnson, S. G. & Joannopoulos, J. D. Block-iterative frequency-domain methods for Maxwell's equations in a planewave basis. *Optics Express* **8**, 173–190 (2001).

[38] Demtröder, W. *Experimentalphysik 3: Atome, Moleküle und Festkörper* (Springer-Verlag, 2016).

[39] Johnson, S. G. & Joannopoulos, J. D. Block-iterative frequency-domain methods for maxwells equations in a planewave basis. *Optics express* **8**, 173–190 (2001).

[40] Pavarini, E. *et al.* Band structure and optical properties of opal photonic crystals. *Physical Review B* **72**, 045102 (2005).

[41] Born, M. & Wolf, E. *Principles of optics* (Cambridge university press, 2019).

[42] Busch, K. & John, S. Photonic band gap formation in certain self-organizing systems. *Physical Review E* **58**, 3896 (1998).

[43] Barnett, S. M. & Loudon, R. Sum rule for modified spontaneous emission rates. *Physical review letters* **77**, 2444 (1996).

[44] Scheel, S. Sum rule for local densities of states in absorbing dielectrics. *Physical Review A* **78**, 013841 (2008).

[45] Peters, I. M. Photonic concepts for solar cells. *Universität Freiburg, Freiburg, Germany* (2009).

[46] Demtröder, W. *Elektrizität und Optik*, vol. 2 (Springer, 2009).

[47] Solé, J., Bausa, L. & Jaque, D. *An introduction to the optical spectroscopy of inorganic solids* (John Wiley & Sons, 2005).

[48] Henderson, B. & Imbusch, G. F. *Optical spectroscopy of inorganic solids*, vol. 44 (Oxford University Press, 2006).

[49] Auzel, F. E. Materials and devices using double-pumped-phosphors with energy transfer. *Proceedings of the IEEE* **61**, 758–786 (1973).

[50] Judd, B. R. Optical absorption intensities of rare-earth ions. *Phys. Rev.* **127**, 750–761 (1962).

[51] Ofelt, G. S. Intensities of crystal spectra of rare-earth ions. *The Journal of Chemical Physics* **37**, 511–520 (1962).

[52] Thoma, R., Insley, H. & Hebert, G. The sodium fluoride-lanthanide trifluoride systems. *Inorganic chemistry* **5**, 1222–1229 (1966).

[53] Suyver, J. F. *et al.* Upconversion spectroscopy and properties of $NaYF_4$ doped with Er^{3+}, Tm^{3+} and/or Yb^{3+}. *Journal of Luminescence* **117**, 1–12 (2006).

[54] Auzel, F. & Pecile, D. Absolute efficiency for ir to blue conversion materials and theoretical prediction for optimized matrices. *journal of Luminescence* **11**, 321–330 (1976).

[55] Krämer, K. W. *et al.* Hexagonal sodium yttrium fluoride based green and blue emitting upconversion phosphors. *Chemistry of materials* **16**, 1244–1251 (2004).

[56] Snoeks, E. *et al.* Cooperative upconversion in erbium-implanted soda-lime silicate glass optical waveguides. *JOSA B* **12**, 1468–1474 (1995).

[57] Polman, A. Erbium implanted thin film photonic materials. *Journal of applied physics* **82**, 1–39 (1997).

[58] Johnson, C., Reece, P. & Conibeer, G. Theoretical and experimental evaluation of silicon photonic structures for enhanced erbium up-conversion luminescence. *Solar Energy Materials and Solar Cells* **112**, 168–181 (2013).

[59] Fischer, S., Johnson, N. J., Pichaandi, J., Goldschmidt, J. C. & van Veggel, F. C. Upconverting core-shell nanocrystals with high quantum yield under low irradiance: On the role of isotropic and thick shells. *Journal of applied physics* **118**, 193105 (2015).

[60] Einstein, A. Zur Quantentheorie der Strahlung. *Physikalische Zeitschrift* **18**, 121–128 (1917).

[61] Sprik, R., Van Tiggelen, B. & Lagendijk, A. Optical emission in periodic dielectrics. *EPL (Europhysics Letters)* **35**, 265 (1996).

[62] Dowling, J. P. & Bowden, C. M. Atomic emission rates in inhomogeneous media with applications to photonic band structures. *Physical Review A* **46**, 612 (1992).

[63] Fischer, S. Upconversion of sub-band-gap photons for silicon solar cells. *PhD thesis, Freiburg im Breisgau* (2014).

[64] Weber, M. J. Probabilities for radiative and nonradiative decay of Er^{3+} in LaF_3. *Physical Review* **157**, 262–272 (1967).

[65] Weber, M. Radiative and multiphonon relaxation of rare-earth ions in Y_2O_3. *Physical Review* **171**, 283–291 (1968).

[66] Riseberg, L. A. & Moos, H. Multiphonon orbit-lattice relaxation of excited states of rare-earth ions in crystals. *Physical Review* **174**, 429–438 (1968).

[67] Shalav, A., Richards, B. & Green, M. Luminescent layers for enhanced silicon solar cell performance: Up-conversion. *Solar energy materials and solar cells* **91**, 829–842 (2007).

[68] Förster, T. Zwischenmolekulare Energiewanderung und Fluoreszenz. *Annalen der physik* **437**, 55–75 (1948).

[69] Dexter, D. L. A theory of sensitized luminescence in solids. *The journal of chemical physics* **21**, 836–850 (1953).

[70] Pollnau, M., Gamelin, D., Lüthi, S., Güdel, H. & Hehlen, M. Power dependence of upconversion luminescence in lanthanide and transition-metal-ion systems. *Physical Review B* **61**, 3337–3346 (2000).

[71] Suyver, J., Grimm, J., Krämer, K. & Güdel, H.-U. Highly efficient near-infrared to visible up-conversion process in $NaYF_4$: Er^{3+}, Yb^{3+}. *Journal of luminescence* **114**, 53–59 (2005).

[72] Shockley, W. & Queisser, H. J. Detailed balance limit of efficiency of p-n junction solar cells. *Journal of Applied Physics* **32**, 510–519 (1961).

[73] Richards, B. Enhancing the performance of silicon solar cells via the application of passive luminescence conversion layers. *Solar energy materials and solar cells* **90**, 2329–2337 (2006).

[74] Trupke, T., Green, M. & Würfel, P. Improving solar cell efficiencies by down-conversion of high-energy photons. *Journal of Applied Physics* **92**, 1668–1674 (2002).

[75] Trupke, T., Shalav, A., Richards, B., Würfel, P. & Green, M. Efficiency enhancement of solar cells by luminescent up-conversion of sunlight. *Solar Energy Materials and Solar Cells* **90**, 3327–3338 (2006).

[76] Gibart, P., Auzel, F., Guillaume, J.-C. & Zahraman, K. Below band-gap ir response of substrate-free gaas solar cells using two-photon up-conversion. *Japanese journal of applied physics* **35**, 4401 (1996).

[77] Strümpel, C. *et al.* Modifying the solar spectrum to enhance silicon solar cell efficiency - an overview of available materials. *Solar Energy Materials and Solar Cells* **91**, 238–249 (2007).

[78] Shalav, A., Richards, B., Trupke, T., Krämer, K. & Güdel, H.-U. Application of $NaYF_4$: Er^{3+} up-converting phosphors for enhanced near-infrared silicon solar cell response. *Applied Physics Letters* **86**, 013505 (2005).

[79] Richards, B. S. & Shalav, A. Enhancing the near-infrared spectral response of silicon optoelectronic devices via up-conversion. *IEEE Transactions on Electron Devices* **54**, 2679–2684 (2007).

[80] Fischer, S., Favilla, E., Tonelli, M. & Goldschmidt, J. C. Record efficient upconverter solar cell devices with optimized bifacial silicon solar cells and monocrystalline BaY_2F_8:30% Er^{3+} upconverter. *Solar Energy Materials and Solar Cells* **136**, 127–134 (2015).

[81] Arnaoutakis, G. E. *et al.* Enhanced energy conversion of up-conversion solar cells by the integration of compound parabolic concentrating optics. *Solar energy materials and solar cells* **140**, 217–223 (2015).

[82] Strümpel, C., McCann, M., Del Cañizo, C., Tobias, I. & Fath, P. Erbium-doped up-converters of silicon solar cells: assessment of the potential. In *Proceedings of the 20th European photovoltaic solar energy conference*, 43–46 (2005).

[83] Goldschmidt, J. C. *et al.* Advanced upconverter systems with spectral and geometric concentration for high upconversion efficiencies. In *2008 Conference on Optoelectronic and Microelectronic Materials and Devices*, 307–311 (IEEE, 2008).

[84] Goldschmidt, J., Löper, P. & Peters, M. Solarelement mit gesteigerter Effizienz und Verfahren zur Effizienzsteigerung. *Deutsches Patent* (2007).

[85] Park, W., Lu, D. & Ahn, S. Plasmon enhancement of luminescence upconversion. *Chemical Society Reviews* **44**, 2940–2962 (2015).

[86] Wu, D. M., García-Etxarri, A., Salleo, A. & Dionne, J. A. Plasmon-enhanced upconversion. *The journal of physical chemistry letters* **5**, 4020–4031 (2014).

[87] De Dood, M., Knoester, J., Tip, A. & Polman, A. Förster transfer and the local optical density of states in erbium-doped silica. *Physical Review B* **71**, 115102 (2005).

[88] Blum, C. *et al.* Nanophotonic control of the Förster resonance energy transfer efficiency. *Physical Review Letters* **109**, 203601 (2012).

[89] Andrew, P. & Barnes, W. L. Förster energy transfer in an optical microcavity. *Science* **290**, 785–788 (2000).

[90] Rabouw, F. T., Den Hartog, S. A., Senden, T. & Meijerink, A. Photonic effects on the Förster resonance energy transfer efficiency. *Nature Communications* **5** (2014).

[91] Spallek, F. & Wellens, T. *Personal communication* (2017).

[92] Shi, Y. *et al.* Upconversion fluorescence enhancement of $NaYF_4$: Yb/Re nanoparticles by coupling with SiO_2 opal photonic crystals. *Journal of Materials Science* **54**, 8461–8471 (2019).

[93] Niu, W. *et al.* 3-dimensional photonic crystal surface enhanced upconversion emission for improved near-infrared photoresponse. *Nanoscale* **6**, 817–824 (2014).

[94] Yin, Z. *et al.* Remarkable enhancement of upconversion fluorescence and confocal imaging of PMMA Opal/$NaYF_4$:Yb^{3+}, Tm^{3+}/Er^{3+} nanocrystals. *Chemical Communications* **49**, 3781–3783 (2013).

[95] Xu, S. *et al.* $NaYF_4$:Yb,Tm nanocrystals and TiO_2 inverse opal composite films: a novel device for upconversion enhancement and solid-based sensing of avidin. *Nanoscale* **6**, 5859–5870 (2014).

[96] Zhang, F., Deng, Y., Shi, Y., Zhang, R. & Zhao, D. Photoluminescence modification in upconversion rare-earth fluoride nanocrystal array constructed photonic crystals. *Journal of Materials Chemistry* **20**, 3895–3900 (2010).

[97] Wang, H. *et al.* Remarkable enhancement of upconversion luminescence on 2–D anodic aluminum oxide photonic crystals. *Nanoscale* **8**, 10004–10009 (2016).

[98] Würth, C. *et al.* Metasurface enhanced sensitized photon upconversion: Toward highly efficient low power upconversion applications and nanoscale E-field sensors. *Nano Letters* **20**, 6682–6689 (2020).

[99] Mao, C. *et al.* Enhanced upconversion luminescence by two-dimensional photonic crystal structure. *ACS Photonics* **6**, 1882–1888 (2019).

[100] Lin, J. H. *et al.* Giant enhancement of upconversion fluorescence of $NaYF_4$: Yb^{3+}, Tm^{3+} nanocrystals with resonant waveguide grating substrate. *ACS Photonics* **2**, 530–536 (2015).

[101] Rojas-Hernandez, R. E., Santos, L. F. & Almeida, R. M. Photonic crystal assisted up-converter based on Tb^{3+}/Yb^{3+}–doped aluminosilicate glass. *Optical Materials* **83**, 61–67 (2018).

[102] Lin, J. H. *et al.* Giant enhancement of upconversion fluorescence of $NaYF_4$:Yb^{3+},Tm^{3+} nanocrystals with resonant waveguide grating substrate. *ACS Photonics* **2**, 530–536 (2015).

[103] Shao, B. *et al.* Au nanoparticles embedded inverse opal photonic crystals as substrates for upconversion emission enhancement. *Journal of the American Ceramic Society* **100**, 988–997 (2017).

[104] Eriksen, E. H. *et al.* Enhanced upconversion via plasmonic near-field effects: role of the particle shape. *Journal of Optics* **21**, 035004 (2019).

[105] Lu, D. *et al.* Plasmon enhancement mechanism for the upconversion processes in $NaYF_4$: Yb^{3+}, Er^{3+} nanoparticles: Maxwell versus Förster. *ACS nano* **8**, 7780–7792 (2014).

[106] Gao, Y. *et al.* Enhancing upconversion photoluminescence by plasmonic-photonic hybrid mode. *Optics express* **28**, 886–897 (2020).

[107] Ma, Y. *et al.* Improving upconversion emission of $NaYF_4$: Yb^{3+}, Er^{3+} nanoparticles by coupling au nanoparticles and photonic crystals: The detection enhancement of rhodamine b. *Journal of Alloys and Compounds* **788**, 1265–1273 (2019).

[108] Wang, H. *et al.* Remarkable enhancement of upconversion luminescence on cap-Ag/PMMA ordered platform and trademark anticounterfeiting. *ACS applied materials & interfaces* **9**, 37128–37135 (2017).

[109] Zhou, D. *et al.* Synergistic upconversion enhancement induced by multiple physical effects and an angle-dependent anticounterfeit application. *Chemistry of Materials* **29**, 6799–6809 (2017).

[110] Yin, Z. *et al.* Local field modulation induced three-order upconversion enhancement: combining surface plasmon effect and photonic crystal effect. *Advanced Materials* (2016).

[111] Liao, J. *et al.* Upconversion emission enhancement of $NaYF_4$: Yb, Er nanoparticles by coupling silver nanoparticle plasmons and photonic crystal effects. *The Journal of Physical Chemistry C* **118**, 17992–17999 (2014).

[112] Xu, W. *et al.* A novel strategy for improving upconversion luminescence of $NaYF_4$: Yb, Er nanocrystals by coupling with hybrids of silver plasmon nanostructures and poly (methyl methacrylate) photonic crystals. *Nano Research* **6**, 795–807 (2013).

[113] Hofmann, C. L. M. *et al.* Experimental validation of a modeling framework for upconversion enhancement in 1D–photonic crystals - supplementary information. *Nature Communications* **12** (2021).

[114] Eriksen, E. H. tmmpy (2018). URL `https://zenodo.org/record/1344878`.

[115] Eriksen, E. H. *Modelling nanostructure-enhanced upconversion for photovoltaic applications*. Ph.D. thesis, Aarhus University, Department of Physics and Astronomy (2018).

[116] Katsidis, C. C. & Siapkas, D. I. General transfer-matrix method for optical multilayer systems with coherent, partially coherent, and incoherent interference. *Appl. Opt.* **41**, 3978–3987 (2002).

[117] Macleod, H. A. *Thin-film optical filters, fourth edition* (CRC press, 2010).

[118] Bendickson, J. M., Dowling, J. P. & Scalora, M. Analytic expressions for the electromagnetic mode density in finite, one-dimensional, photonic band-gap structures. *Physical Review E* **53**, 4107–4121 (1996).

[119] Yeganegi, E., Lagendijk, A., Mosk, A. P. & Vos, W. L. Local density of optical states in the band gap of a finite one-dimensional photonic crystal. *Physical Review B* **89**, 045123 (2014).

[120] Gutmann, J. *Photonic luminescent solar concentrators*. Ph.D. thesis, Albert-Ludwigs University Freiburg, Technical Faculty (2014).

[121] Company, J. A. W. CompleteEASE software manual version 3.18 (2014).

[122] Fischer, S. *et al.* Plasmon enhanced upconversion luminescence near gold nanoparticles–simulation and analysis of the interactions. *Optics Express* **20**, 271–282 (2012).

[123] Burns, J. H. Crystal structure of hexagonal sodium neodymium fluoride and related compounds. *Inorganic Chemistry* **4**, 881–886 (1965).

[124] Thoma, R. E., Insley, H. & Hebert, G. M. The sodium fluoride-tanthanide trifluoride systems. *Inorganic Chemistry* **5**, 1222–1229 (1966).

[125] Fröhlich, B. Charakterisierung von Hochkonvertermaterialien für die Photovltaik. *Diploma thesis, University of Freiburg* (2014).

[126] Homann, C. *et al.* $NaYF_4$: Yb, Er/$NaYF_4$ core/shell nanocrystals with high upconversion luminescence quantum yield. *Angewandte Chemie International Edition* **57**, 8765–8769 (2018).

[127] Walsh, C. B. & Franses, E. I. Ultrathin PMMA films spin-coated from toluene solutions. *Thin Solid Films* **429**, 71–76 (2003).

[128] Yang, H. G. *et al.* Anatase TiO_2 single crystals with a large percentage of reactive facets. *Nature* **453**, 638–641 (2008).

[129] Pore, V. *et al.* Atomic layer deposition of photocatalytic TiO_2 thin films from titanium tetramethoxide and water. *Chemical Vapor Deposition* **10**, 143–148 (2004).

[130] Lee, C.-S., Kim, J., Son, J., Choi, W. & Kim, H. Photocatalytic functional coatings of TiO_2 thin films on polymer substrate by plasma enhanced atomic layer deposition. *Applied Catalysis B: Environmental* **91**, 628–633 (2009).

[131] Ma, X. Y. *et al.* Fabrication of uniform anatase TiO_2 particles exposed by $\{001\}$ facets. *Chemical communications* **46**, 6608–6610 (2010).

[132] Kartini, I. *et al.* Hydrothermal seeded synthesis of mesoporous titania for application in dye-sensitised solar cells (DSSCs). *Journal of Materials Chemistry* **14**, 2917–2921 (2004).

[133] Gautam, C., Madheshiya, A., Kumar Singh, A., Kishor Dey, K. & Ghosh, M. Synthesis, optical and solid NMR studies of strontium titanate borosilicate glasses doped with TeO_2. *Results in Physics* **16**, 102914 (2020).

[134] Tong, L. *et al.* $NaYF_4$:Sm^{3+}/Yb^{3+}@$NaYF_4$:Er^{3+}/Yb^{3+} core-shell structured nanocalorifier with optical temperature probe. *Optics Express* **25**, 16047–16058 (2017).

[135] Johnson, C. M., Reece, P. J. & Conibeer, G. J. Slow-light-enhanced upconversion for photovoltaic applications in one-dimensional photonic crystals. *Optics Letters* **36**, 3990–3992 (2011).

[136] Krauss, T. F. Slow light in photonic crystal waveguides. *Journal of Physics D: Applied Physics* **40**, 2666 (2007).

[137] Fischer, S., Fröhlich, B., Steinkemper, H., Krämer, K. W. & Goldschmidt, J. C. Absolute upconversion quantum yield of β-$NaYF_4$ doped with Er^{3+} and external quantum efficiency of upconverter solar cell devices under broad-band excitation considering spectral mismatch corrections. *Solar Energy Materials and Solar Cells* **122**, 197–207 (2014).

[138] Goldschmidt, J. C. *et al.* Advanced upconverter systems with spectral and geometric concentration for high upconversion efficiencies. In *Conference on Optoelectronic and Microelectronic Materials and Devices*, 307–311 (IEEE, 2008).

[139] Spallek, F., Buchleitner, A. & Wellens, T. Optimal trapping of monochromatic light in designed photonic multilayer structures. *Journal of Physics B: Atomic, Molecular and Optical Physics* **50**, 214005 (2017).

[140] Joseph, R. E. *et al.* Critical power density: a metric to compare the excitation power density dependence of photon upconversion in different inorganic host materials. *The Journal of Physical Chemistry A* **123**, 6799–6811 (2019).

[141] Goldschmidt, J. C. *et al.* Record efficient upconverter solar cell devices. In *Proc. 29th European Photovoltaic Solar Energy Conference and Exhibition (EUPVSEC)*, 1–4 (2014).

[142] Liu, Q. *et al.* Microlens array enhanced upconversion luminescence at low excitation irradiance. *Nanoscale* **11**, 14070–14078 (2019).

[143] Liang, L. *et al.* Upconversion amplification through dielectric superlensing modulation. *Nature communications* **10**, 1–9 (2019).